Top-antitop energy asymmetry in jet-associated top-quark pair production at ATLAS

Dissertation submitted

for the award of the title

Doctor of Natural Sciences

to the Faculty of Physics, Mathematics, and Computer Science
of Johannes Gutenberg University Mainz

Alexander Basan

Born in Mainz

Mainz, October 18th, 2022

First reviewer: Prof. Dr. Lucia Masetti
Second reviewer: - removed from the electronic version for privacy reasons -
Third reviewer: - removed from the electronic version for privacy reasons -
Date of oral examination: April 26th, 2023
Dissertation at the Johannes Gutenberg University Mainz (D77)

Affidavit

I confirm that I wrote this dissertation personally using only the sources and aids cited. I am aware of the stipulations for the safeguarding of good academic practice in research and teaching and the consequences of academic misconduct. This dissertation has not been submitted as part of another qualification, neither in this nor in a similar form.

Alexander Basan
Mainz, October 18th, 2022

Alexander Basan
ETAP - Institute for experimental particle and astroparticle physics
Faculty of Physics, Mathematics, and Computer Science
Staudingerweg 7
Johannes Gutenberg University Mainz
D-55128 Mainz

We may reflect that physics and philosophy are at most a few thousand years old, but probably have lives of thousands of millions of years stretching away in front of them. They are only just beginning to get under way, and we are still, in Newton's words, like children playing with pebbles on the sea-shore, while the great ocean of truth rolls, unexplored, beyond our reach.

Sir James Jeans, 1942 [1]

Kurzfassung

Das Standardmodell (SM) der Teilchenphysik stellt unser aktuelles Verständnis elementarer Teilchen und ihrer Wechselwirkungen dar und liefert korrekte Vorhersagen mit erstaunlicher Präzision für zehntausende Messungen. Verbleibende offene Fragen wie die beobachtete Asymmetrie zwischen Materie und Antimaterie in unserem Universum sowie Beobachtungen, die auf die Existenz dunkler Materie hinweisen, deuten auf neue Physik jenseits des Standardmodells hin. Observablen im Top-Quark-Sektor sind besonders gut geeignet, um das SM und viele seiner Erweiterungen auf der elektroschwachen symmetriebrechenden Skala und darüber hinaus zu untersuchen.

An Proton-Proton-Collidern ist die Produktion von Top-Antitop-Quark-Paaren in führender Ordnung der Quantenchromodynamik symmetrisch unter dem Austausch der Top- und Antitop-Quarks, während Interferenzen höherer Ordnungen bei der Quark-Antiquark-Annihilation eine Asymmetrie erzeugen. Diese Ladungsasymmetrie kann sensitive Proben für viele Modelle jenseits des SM, wie etwa massive Farboktettzustände, Extradimensionen, flavour-verletzende Eichbosonen oder Axigluonen, liefern. Bei jet-assoziierter Top-Quark-Paar Produktion tritt diese Asymmetrie bereits in führender Ordnung bei Quark-Gluon-Wechselwirkungen auf. Darüber hinaus ermöglichen die Endzustände die Definition einer neuen Observablen, der Energieasymmetrie, welche die unterschiedliche Wahrscheinlichkeit widerspiegelt, dass Top- oder Antitop-Quarks die höhere Energie haben.

Das ATLAS Experiment am Large Hadron Collider am CERN nahm während Run 2 im Datenerfassungszeitraum 2015–2018 Proton-Proton-Kollisionsdaten mit einer integrierten Luminosität von $139\,\mathrm{fb}^{-1}$ bei einer Schwerpunktsenergie von 13 TeV auf, was die Möglichkeit bietet, weniger häufige Prozesse wie die jet-assoziierte Top-Quark-Paar Produktion und weitestgehend alle Wechselwirkungen des Top-Quarks mit hoher statistischer Präzision zu untersuchen.

Diese Dissertation stellt die erste Messung der Energieasymmetrie vor, welche im semi-leptonischen Zerfallskanal in jet-assoziierten Top-Quark-Paar-Ereignissen in der so genannten Boosted-Topologie, in der das hadronisch zerfallende Top-Quark einen transversalen Impuls von über 350 GeV hat, durchgeführt und mit der Fully Bayesian Unfolding (FBU) Methode hinsichtlich Detektoreffekten korrigiert wurde. Die gemessene Asymmetrie stimmt in allen drei Bins des Jetstreuwinkels mit der Standardmodellvorhersage auf nächstführender Ordnung überein. Die gemessene Energieasymmetrie von -0.043 ± 0.020 in der zentralen Region, in welcher die erwartete Asymmetrie am größten ist, stimmt mit der SM-Vorhersage von -0.037 ± 0.003 überein.

Die Standardmodell Effektive Feldtheorie (SMEFT) stellt ein modellunabhängiges Framework für neue physikalische Interpretationen dar, worin die Energieasymmetrie besonders sensitiv gegenüber der chiralen und der Farbstruktur von Vier-Quark-Operatoren ist. Die Sensitivität der Energieasymmetrie wird in den aus Fits der erwarteten zur gemessenen Asymmetrie bestimmten Grenzen von Wilson-Koeffizienten dargestellt und erweist sich als vergleichbar mit und komplementär zu der anderer Observablen im Top-Quark-Sektor und wird somit einen wertvollen Beitrag zu globalen SMEFT-Fits liefern.

Abstract

The Standard Model (SM) of particle physics, representing our current understanding of fundamental particles and their interactions, gives correct predictions with an astonishing precision for tens of thousands of measurements. Remaining open questions, like the observed matter-antimatter asymmetry in our universe and observations hinting at the existence of dark matter point to new physics beyond the Standard Model. Observables in the top-quark sector are particularly well suited to probe the SM and many extensions thereof at the electroweak symmetry-breaking scale and beyond.

At proton-proton colliders, top-antitop-quark pair production is symmetric at leading order in quantum chromodynamics under the exchange of the top and antitop quarks, while interferences at higher orders in quark-antiquark annihilation create an asymmetry. This charge asymmetry can provide sensitive probes for many models beyond the SM like massive colour-octet states, extra dimensions, flavour-violating gauge bosons or axigluons. In jet-associated top-quark pair production, this asymmetry arises already at leading order in quark-gluon interactions. Furthermore, the final states in jet-associated top-antitop events allow for the definition of a new observable, the energy asymmetry, reflecting the different probability of top and antitop quarks to have the higher energy.

The ATLAS experiment at the Large Hadron Collider at CERN collected $139\,\mathrm{fb}^{-1}$ of proton-proton collision data at a centre-of-mass energy of 13 TeV during Run 2 in the data-taking period 2015–2018, providing the possibility to study less frequent processes like jet-associated top-quark pair production as well as essentially all interactions of the top quark with high statistical precision.

This thesis presents the first measurement of the energy asymmetry, performed in the semi-leptonic decay channel in jet-associated top-quark pair events in the so called boosted topology, requiring the hadronically decaying top quark to have a transverse momentum above 350 GeV, and corrected for detector effects with the Fully Bayesian Unfolding (FBU) method. The measured asymmetry is found to be in agreement with the SM prediction at next-to-leading order accuracy in all three bins of the jet-scattering angle. In the central region, where the energy asymmetry is expected to be the highest, the energy asymmetry is measured to be -0.043 ± 0.020, in agreement with the SM prediction of -0.037 ± 0.003.

The Standard Model Effective Field Theory (SMEFT) represents a model-independent framework for new physics interpretations. Within the SMEFT framework, the energy asymmetry is especially sensitive to the chiral and colour structure of four-quark operators. The sensitivity of the energy asymmetry is presented in the bounds on Wilson coefficients obtained from one and two-dimensional fits of the predicted to the measured asymmetry. The sensitivity of the energy asymmetry is found to be comparable to that of other observables in the top-quark sector as well as to resolve blind directions in current LHC fits and will thus provide a valuable new input for global SMEFT fits.

Contents

1. Introduction

Particle physics addresses the questions humanity has always been puzzled about: "What is the universe made of?" and "What holds the world together at its core?".

The ancient Greeks imagined all matter of the universe to consist of the four elements air, water, fire and earth; Leukippus and Democritus [2] introduced the idea of indivisible atoms in an empty space around 400 BC. Around 2 300 years later, in 1869, D. Mendeleev presented a classification of the then known elements according to their chemical properties in the periodic table of elements [3], which now contains more than 110 elements. The lightest negatively charged elementary particle, the electron, was discovered by J.J. Thomson [4] in 1897 via the deflection of cathode rays in a magnetic field. E. Rutherford found that the positive charge of an atom is concentrated in a nucleus by scattering ionised helium atoms in a thin sheet of gold foil in 1911 [5]; the lightest one, the so called proton, was found to be part of larger atomic nuclei in 1919 [6]. The discovery of the neutron, an uncharged nucleus, in 1932 by J. Chadwick [7] in the scattering of ionised helium atoms with beryllium completed the proton-neutron model of the nucleus [8]. All known matter could be explained to be formed by atoms consisting of "heavy-weight" baryons (protons and neutrons) and "light-weight" leptons (electrons). The positron, the antiparticle of the electron with the same mass but oppositely charged, predicted in the relativistic quantum theory by P. Dirac [9], was discovered in cosmic rays by C.D. Anderson [10] in 1933. The pion, a "mid-weight" meson, expected to be the mediator of the very short ranged strong force holding together the nucleus by H. Yukawa [11], was discovered in cosmic rays in 1947 [12]. The neutrino, a very light and charged neutral particle predicted by W. Pauli [13] to ensure energy conservation in nuclear beta decays, was detected in a tank of water near a nuclear reactor by F. Reines and C.L. Cowan [14] in 1953.

The discovery of many more baryons and mesons lead to the development of the quark model by M. Gell-Mann and O.W. Greenberg in 1964 [15–17], which proposed that all hadrons (baryons and mesons) are composed of more elementary constituents, the so called quarks, bound together by the strong interaction acting on a new type of charge, today known as colour charge. Deep inelastic electron-proton and photon-proton scattering experiments at the Stanford Linear Accelerator Center (SLAC) in 1969 confirmed the quark model by revealing the inner structure of the proton [18–20].

The mediator of the strong force, the gluon, was discovered at the Deutsche Elektronen-Synchrotron (DESY) [21–24] in 1979. During 1959–1967, S. Glashow [25], A. Salam [26] and S. Weinberg [27] developed a theory for electroweak interactions via exchange of intermediate $W^{\pm}$ and Z bosons, both of which were discovered at the Super Proton Synchrotron proton-antiproton collider at CERN in 1983 [28–31]. All fundamental particles acquire their mass via the Higgs mechanism postulated by P. Higgs, F. Englert and R. Brout in 1964 [32, 33], the corresponding Higgs boson was observed by the ATLAS [34] and CMS [35] collaborations at the proton-proton collider at CERN in 2012.

This interplay between experimental observations and theoretical predictions led to the development of the Standard Model (SM) [36] of elementary particle physics, representing our current understanding of subatomic particles and their interactions. The SM describes matter to consist of three generations of each two quarks and leptons, governed by the three fundamental electromagnetic, weak and strong interactions, which are mediated by photons, $W^{\pm}$ and Z bosons and gluons, respectively.

The SM is an extremely impressive theory with verified highest-precision predictions in tens of thousands of measurements [36]. Nevertheless, the SM leaves many fundamental questions unanswered. It does not provide an unification of gravity, the most evident interaction in daily life and on astronomic scales, but negligible on subatomic scales, with quantum field theory. There are many free parameters such as coupling constants and fermion masses and no explanation for the matter-antimatter asymmetry observed in our matter dominated universe. Beyond the Standard Model (BSM) theories like supersymmetry [37–39], string theory [40–42] and many others try to provide answers to these questions.

The top quark, observed at the Collider Detector at the Fermi National Laboratory (CDF) in 1995 [43], is particularly well suited to probe the Standard Model and many extensions thereof at the electroweak symmetry-breaking scale and beyond. It is by far the heaviest fermion in the Standard Model and has a Yukawa coupling to the Higgs boson close to one; with a mass of approximately 173 GeV [44] it is about 30 times heavier than the next heaviest fermion, the bottom quark, and nearly as heavy as a gold atom. The large dataset collected during Run 2 (2015–2018) at the Large Hadron Collider (LHC), a proton-proton accelerator at CERN, allows for the examination of essentially all top-quark interactions at the highest yet reached energy scales and precision in prediction and measurement to search for deviations from SM predictions in the presence of new physics [45–53].

The charge asymmetry in inclusive top-quark pair production, defined as the asymmetry under charge conjugation in the final state, provides sensitive probes for many BSM models such as massive colour-octet bosons [54], extra dimensions [55], grand unification [56], and axigluons [57]. At leading order in the strong coupling constant, top-quark pair production, dominated by gluon-gluon fusion at the LHC, is predicted to be symmetric under the exchange of the top and antitop quarks, while interferences at next-to-leading order (NLO) in quark-gluon fusion produce an asymmetry [58]. The charge asymmetry was found to be in good agreement with the SM prediction in measurements of the forward-backward asymmetry at Tevatron [59, 60] and of the rapidity asymmetry at ATLAS [61–66] and CMS [64, 67, 68].

In jet-associated top-quark pair production, the asymmetry arises already at leading order in quark-gluon interactions [69–72]. The additional jet in the final state allows for the definition of a new observable, the energy asymmetry [73, 74], expressed in terms of the energy difference between the top and antitop quarks. With the dataset collected at the LHC during Run 2 the measurement of the energy asymmetry with a high statistical significance comes into reach [74]; concrete predictions for the measurement taking into account effects of the parton shower, hadronisation and detector efficiencies were published in reference [75]. Similar as in inclusive $t\bar{t}$ production, the charge asymmetry in jet-associated top-quark pair production is sensitive to BSM models such as colour-octet states [76], top-flavour violating resonances [77], extra dimensions [78], and axigluons [79].

The Standard Model Effective Field Theory (SMEFT) framework provides a model-independent treatment of BSM effects by introducing effective couplings that modify and extend the interactions of SM particles at energies within reach of the LHC [80–82]. The energy asymmetry in jet-associated top-quark pair production is a complementary observable to the cross section and rapidity asymmetry that is sensitive to new combinations of effective interactions that are not accessible in inclusive top-quark pair production.

This thesis presents both the measurement of the energy asymmetry in jet-associated top-quark pair production in proton-proton collision data collected by the ATLAS experiment during Run 2 in 2015–2018 of the LHC as well as its interpretation in the SMEFT framework. Chapter 2 introduces the theoretical aspects of the Standard Model, the top-quark charge asymmetry and BSM physics. The experimental aspects of the Large Hadron Collider, the ATLAS experiment and Monte Carlo simulations are presented in chapter 3. Chapters 4 and 5 define the physics objects used in this analysis and the applied event selection and reconstruction criteria, respectively. The data, signal and background samples used in this analysis are presented in chapter 6. The unfolding method and the theoretical and systematic uncertainties are explained in chapters 7 and 8, respectively. The expected and observed results of the energy asymmetry measurement are presented in chapter 9. Chapter 10 shows the interpretation of the measured energy asymmetry in terms of the Standard Model Effective Field Theory. A summary and an outlook are given in chapter 11.

The key results of this thesis were published in reference [83]; feasibility studies and a comparison with the rapidity asymmetry measurement were published in references [75] and [66], respectively. The author of this thesis is the main person responsible for the analysis work in the first two of these publications. The measurement of the energy asymmetry was performed within the ATLAS collaboration which collected the collision data and provided a common software framework. The author's contributions include the SM and SMEFT predictions of the energy asymmetry described in sections 2.3.4 and 2.4.3, the simulation of $t\bar{t}j$ events described in section 6.2, and the estimation of fake and non-prompt lepton events discussed in section 6.3.2. The author optimised the event selection and reconstruction described in chapter 5 for the inclusion of an associated jet as explained further in section 9.2. He implemented the code for the unfolding procedure described in chapter 7 from data preparation, asymmetry extraction and uncertainty estimation discussed in sections 8.3.1 to 8.4. The author was responsible for all steps of the energy asymmetry measurement and SMEFT interpretation described in chapters 9 and 10, respectively. He presented the results to a public audience at the 148th LHCC meeting [84] and at the LHC Top Working Group meeting [85].

2. Theoretical aspects of particle physics

Section 2.1 reviews the key aspects of the Standard Model relevant for this thesis like its particle content, fundamental interactions and electroweak symmetry breaking; the theory description is largely based on reference [86]. Subsequently, the production and decay of top quarks are explained in section 2.2. A description of the top-quark charge asymmetries follows in section 2.3. Finally, an overview of conceptual problems and an outlook on physics beyond the Standard Model is given in section 2.4.

2.1. The Standard Model of elementary particle physics

The Standard Model (SM) is a relativistic quantum field theory describing elementary particles as representations of symmetry groups and their interactions via the action principle. The symmetry group of the SM is the direct product of a space-time symmetry group, the Poincaré group, $\mathrm{ISO}(1,3)$, and an internal symmetry group, $\mathrm{SU}(3)_\mathrm{C} \times \mathrm{SU}(2)_\mathrm{L} \times \mathrm{U}(1)_\mathrm{Y}$, called the gauge group:

$$\mathrm{ISO}(1,3) \times \mathrm{SU}(3)_\mathrm{C} \times \mathrm{SU}(2)_\mathrm{L} \times \mathrm{U}(1)_\mathrm{Y} \tag{2.1}$$

The Poincaré group, $\mathrm{ISO}(1,3)$, is the group of all distance-preserving transformations in Minkowski space, namely translations and Lorentz transformations. The internal symmetry groups $\mathrm{SU}(3)_\mathrm{C}$, $\mathrm{SU}(2)_\mathrm{L}$, and $\mathrm{U}(1)_\mathrm{Y}$ correspond to the colour space of strong interactions, the space of left-handed particles also called weak isospin space, and the hypercharge space, respectively. The electroweak symmetry group $\mathrm{SU}(2)_\mathrm{L} \times \mathrm{U}(1)_\mathrm{Y}$ is spontaneously broken to the electromagnetic group $\mathrm{U}(1)_\mathrm{EM}$ via the Higgs mechanism, giving mass to the weak gauge bosons.

The dynamics of particles are governed by the action, defined as the space-time integral over the Lagrangian $\mathcal{L}(\psi, \partial_\mu \psi)$, which is a functional of fields ψ and their first derivates:

$$S = \int d^4x \mathcal{L}(\psi, \partial_\mu \psi) \tag{2.2}$$

The action is symmetric under the symmetry group in eq. 2.1 and the key ingredient used to calculate cross sections and decay rates as described in section 2.1.2. The equations of motions are the Euler-Lagrange equations derived by the principle of least action:

$$\frac{\partial \mathcal{L}}{\partial \psi} - \partial_\mu \frac{\partial \mathcal{L}}{\partial(\partial_\mu \psi)} = 0 \tag{2.3}$$

Noether's theorem [87] states that each continuous symmetry of the theory leads to a conserved quantity. Space-time symmetries thus lead to conservation of 4-momenta and angular momenta, including spin, while internal symmetries lead to conserved quantum numbers, called charges. Global U(1) symmetries yield baryon and lepton number conservation. The conservation of momenta and charges allows for the reconstruction of unstable particles from their decay products.

2.1.1. Particle content

In the Standard Model, particles correspond to (infinite-dimensional) representations of the direct product of the Poincaré group $\mathrm{ISO}(1,3)$ and the gauge group $\mathrm{SU(3)_C} \times \mathrm{SU(2)_L} \times \mathrm{U(1)_Y}$ in eq. 2.1.

Each particle is uniquely classified by its mass m, a non-negative real number, its spin J, a non-negative half integer, and charges corresponding to the internal symmetry groups. For each mass m and spin J, there are $2J+1$ independent spin states for massive particles with $m > 0$ and $2J$ spin states for massless particles, corresponding to linearly independent polarizations.

The particle spectrum in the Standard Model consists of twelve spin-1/2 fermions, twelve spin-1 vector or gauge bosons and one spin-0 scalar Higgs boson. Table 2.1 summarises the Lagrangian densities and equations of motion for these three representations.

Table 2.1.: Particle representations of the Poincaré group in the Standard Model, classified by spin J, with the corresponding Lagrangian $\mathcal{L}$ and equations of motion (EOM) for free fields [86]. The equations of motions for scalar bosons, fermions and vector bosons are known as Klein-Gordon, Dirac and Proca equations, respectively.

Particle	Spin J	$\mathcal{L}$	EOM
Scalar boson	0	$\frac{1}{2}(\partial_\mu\phi)(\partial^\mu\phi) - \frac{1}{2}m^2\phi^2$	$(\partial_\mu\partial^\mu + m^2)\phi = 0$
Spinor fermion	1/2	$\bar{\psi}(i\gamma^\mu\partial_\mu - m)\psi$	$(i\gamma^\mu\partial_\mu - m)\psi = 0$
Vector boson	1	$(-\frac{1}{4}F^{\mu\nu}F_{\mu\nu} + \frac{1}{2}m^2A_\mu A^\mu)$	$\partial_\mu F^{\mu\nu} + m^2A^\nu = 0$

The fundamental building blocks of all visible matter in the universe are the twelve fermion fields with spin 1/2, subject to the Pauli exclusion principle [88, 89], which states that two identical fermions cannot occupy the same state. The fermions can be divided into quarks, which participate in the strong interaction, and leptons, which do not. Both, quarks and leptons, take part in the electroweak interaction. They are further divided into three generations also referred to as "flavours" with identical charges, but different masses. Particles of the second and third generation, except neutrinos, are unstable and decay into first generation particles via weak interaction. Quarks have baryon number +1/3 and leptons lepton number +1, additionally there is one lepton number for each lepton generation.

There are two two-dimensional representations with spin 1/2 transforming equally under rotations, but differently under Lorentz boosts. These so called left- and right-handed spinor representations are related by parity transformation, such that a relativistic theory necessarily includes both in the Dirac spinor representation.

The spin-1 vector bosons, also called gauge bosons, arise as connections allowing the comparison of field values at different space-time points and act as mediators of three of the four fundamental forces. The electroweak interactions are mediated via $W^\pm$-, Z- and γ-boson exchange, while the eight gluons are the carrier of the strong interaction.

Finally, the Higgs boson, which gives mass to the $W^\pm$ and Z gauge bosons via the Higgs mechanism described in section 2.1.3, is a scalar spin-0 particle and thus invariant under Lorentz transformations.

Antiparticles have the same mass and spin as particles, but opposite charges under internal symmetries. Unless explicitly indicated otherwise, the terms "particle" and "antiparticle" are used synonymously in this thesis.

The Standard Model thus contains 6 leptons and 6 quarks with 3 colour options each, their corresponding antiparticles, as well as 12 gauge bosons and 1 Higgs boson, totalling in 61 particles. Table 2.2 summarises the particle content of the SM with the corresponding masses, lifetimes and charges.

Table 2.2.: Particle content of the Standard Model. Quarks, leptons and bosons with mass, lifetime, electric charge Q_e and colour charge Q_c. Quarks carry a colour charge $c \in \{$"red" r, "green" g, "blue" $b\}$ and thus participate in the strong interaction, while leptons do not. Additionally, quarks have baryon number $+1/3$ and leptons lepton number $+1$, respectively. The 8 gluons carry combinations of colour-anticolour ($c\bar{c}'$) charges. Due to the confinement property of QCD, quarks and gluons appear only in colour neutral combinations as hadrons. Antiparticles have the same mass, but carry opposite charges as particles. The masses and lifetimes were taken from the Particle Data Group (PDG) [36].

	Particle	Mass	Lifetime	Q_e $[e]$	Q_c
Quarks	Up u	$2.2^{+0.5}_{-0.3}\,\mathrm{MeV}$	-	$+2/3$	$c \in \{r, g, b\}$
	Down d	$4.7^{+0.5}_{-0.2}\,\mathrm{MeV}$	-	$-1/3$	
	Charm c	$1.27 \pm 0.02\,\mathrm{GeV}$	-	$+2/3$	
	Strange s	$93^{+9}_{-3}\,\mathrm{MeV}$	-	$-1/3$	
	Top t	$172.7 \pm 0.3\,\mathrm{GeV}$	$4.6 \cdot 10^{-25}\,\mathrm{s}$	$+2/3$	
	Bottom b	$4.18^{+0.03}_{-0.02}\,\mathrm{GeV}$	-	$-1/3$	
Leptons	Electron e	$0.511\,\mathrm{MeV}$	stable	-1	-
	Electron neutrino ν_e	$< 1.1\,\mathrm{eV}$	-	0	
	Muon μ	$105.66\,\mathrm{MeV}$	$2.2 \cdot 10^{-6}\,\mathrm{s}$	-1	
	Muon neutrino ν_μ	$< 0.19\,\mathrm{MeV}$	-	0	
	Tau τ	$1776.9 \pm 0.1\,\mathrm{MeV}$	$290 \cdot 10^{-15}\,\mathrm{s}$	-1	
	Tau neutrino ν_τ	$< 18.2\,\mathrm{MeV}$	-	0	
Gauge	Gluon g	0	-	0	$c\bar{c}'$
	$W^\pm$ boson	$80.38 \pm 0.01\,\mathrm{GeV}$	$3.2 \cdot 10^{-25}\,\mathrm{s}$	± 1	-
	Z boson	$91.188 \pm 0.002\,\mathrm{GeV}$	$2.6 \cdot 10^{-25}\,\mathrm{s}$	0	-
	Photon γ	0	stable	0	-
	Higgs boson h	$125.25 \pm 0.17\,\mathrm{GeV}$	$2.1 \cdot 10^{-22}\,\mathrm{s}$	0	-

2.1.2. Fundamental interactions

Based on current knowledge, there are four fundamental interactions in the universe. Gravity is most evident in daily life and on astronomic scales, but it is by far the weakest interaction and does not play any role on subatomic scales, which are dominated by the electromagnetic, weak and strong interaction. Their mediator particles,

relative strengths and ranges are listed in table 2.3. Quantum electrodynamics (QED) describes processes like Coulomb repulsion and attraction, pair production and annihilation of charged leptons and Compton scattering via photon exchange between electrically charged particles. Quantum chromodynamics (QCD) is used to describe the strong force binding together colour-charged quarks and gluons in hadrons and is mediated by gluon exchange. All quarks and leptons interact via the weak interaction, mediated by $W^{\pm}$ and Z bosons. Neutral currents account for processes like neutrino-electron scattering and contribute to non-flavour-changing processes, while charged currents change the flavour of fermions.

Table 2.3.: Mediator, coupling, relative strength and range for the fundamental interactions [90, 91]. Gravity with its hypothetical mediator, the graviton, is not yet included in the Standard Model.

Interaction	Mediator	Coupling	Strength	Range
Strong	Gluons g	colour charge	10	$\approx 10^{-15}$ m
Electromagnetic	Photon γ	electric charge	10^{-2}	∞
Weak	$W^{\pm}, Z$	weak charge	10^{-13}	$\ll 10^{-15}$ m
Gravity	Graviton?	mass	10^{-42}	∞

Structure of the SM Lagrangian

The gauge principle states that the theory described by a Lagrangian must be invariant under global

$$\psi(x) \to U\psi(x), \quad U = e^{i\alpha^a T^a} \in \mathrm{SU}(N) \tag{2.4}$$

as well as local

$$\psi(x) \to U(x)\psi(x), \quad U(x) = e^{i\alpha^a(x) T^a} \in \mathrm{SU}(N) \tag{2.5}$$

gauge transformations, where T^a are the generators of $\mathrm{SU}(N)$ and α is an arbitrary parameter. Lagrangians are the sum of several terms combining fields and their derivatives multiplied by a so-called coupling constant. The most general renormalisable (see section 2.1.5) locally $\mathrm{SU}(N)$ invariant Lagrangian for N matter fields ψ and N^2-1 gauge bosons A can be written as:

$$\mathcal{L} = -\frac{1}{4} F^a_{\mu\nu} F^{a,\mu\nu} + \sum_{i,j=1}^{N} \bar{\psi}_i (\delta_{ij} i\partial\!\!\!/ + g A\!\!\!/^a T^a_{ij} - m\delta_{ij})\psi_j + \theta \epsilon^{\mu\nu\alpha\beta} F^a_{\mu\nu} F^a_{\alpha\beta} \tag{2.6}$$

where $F_{\mu\nu} = (\partial_\mu A_\nu - \partial_\nu A_\mu) - ig[A_\mu, A_\nu]$ is the field strength with $A_\mu \equiv A^a_\mu T^a$ and $A\!\!\!/ \equiv \gamma^\mu A_\mu$.

The first term proportional to $F_{\mu\nu}F^{\mu\nu}$ is the kinetic term for the gauge fields. For abelian theories like the electromagnetic gauge group $\mathrm{U}(1)_{\mathrm{EM}}$, it contains only terms quadratic in A_μ, describing freely propagating fields. In non-abelian theories like the strong interaction with gauge group $\mathrm{SU}(3)_{\mathrm{C}}$, however, also higher order terms appear, corresponding to self-interactions of the gauge bosons important for the concept of confinement described in section 2.1.4.

The second term describes the propagation of matter fields ψ with mass m as well as interactions between the matter fields ψ and the gauge bosons A with coupling constant g. In a chiral theory, however, the mass term violates SU(2) invariance and is thus forbidden.

The last term, $\theta\epsilon^{\mu\nu\alpha\beta}F^a_{\mu\nu}F^a_{\alpha\beta}$, which can be written as $\mathcal{L}_\theta = \bar{\theta}\frac{\alpha_s}{16\pi}\epsilon^{\mu\nu\alpha\beta}G^a_{\mu\nu}G^a_{\alpha\beta}$ with colour field strength tensor $G^{\mu\nu}$ in the SM, is violating the CP invariance in strong interactions. The strong CP problem addresses the question why the strong CP phase $\bar{\theta}$, constrained to be smaller than 10^{-10} [92] from limits on the electric dipole moment of neutrons [93] and mercury [94], has such a small value close to 0.

Cross sections for particle decays and scattering processes

Elementary particle interactions can be probed in bound states, particle decays and scattering processes. Quantum field theory is particularly well suited to describe particle decays and scattering processes.

In quantum mechanics, the probability of an initial state $|i, t_i\rangle$ at time t_i to be measured in the final state $|f, t_f\rangle$ at time t_f is given by the squared modulus of the inner product of those states, $|\langle f; t_f|i; t_i\rangle|^2$. In colliding experiments, asymptotic states at times $t = \pm\infty$ are assumed to be free of interactions. The S-matrix is defined as the time evolution operator from $t = -\infty$ to $t = +\infty$ in the Heisenberg picture:

$$\langle f|S|i\rangle_{\text{Heisenberg}} = \langle f; \infty|i; -\infty\rangle_{\text{Schrödinger}} \tag{2.7}$$

The elements of this matrix can be calculated by the Dyson series [86, 95]

$$S = T\left[e^{i\int d^4x\mathcal{L}_{\text{int}}}\right] \tag{2.8}$$

where the T is the time-ordering operator and $\mathcal{L}_{\text{int}}$ the interacting part of the Lagrangian in the interaction picture. The matrix element $\mathcal{M}$ contains all dynamic information and is implicitly defined via:

$$S = 1 + i(2\pi)^4\delta^4(\sum_{i=1}^{m} p_i - \sum_{f=1}^{n} p_f)\mathcal{M} \tag{2.9}$$

where p_i and p_j denote the four-momenta of the m initial and n final state particles.

Scattering processes can be described by the cross section, a measure of the interaction strength, defined as the quantum mechanical probability of scattering P divided by the flux Φ and interaction time T:

$$d\sigma = \frac{1}{T}\frac{1}{\Phi}dP \tag{2.10}$$

The differential cross section in a scattering process with two particles a and b in the initial state and n particles in the final state with momenta p_a, p_b and $\{p_i\}, j \in \{1, ..., n\}$, respectively, can be written as:

$$d\sigma(p_a + p_b \to \{p_i\}) = \frac{1}{(2E_a)(2E_b)|\vec{v}_a - \vec{v}_b|}|\mathcal{M}(p_a + p_b \to \{p_i\})|^2 d\Phi \tag{2.11}$$

with the Lorentz-invariant phase space element:

$$d\Phi = \prod_{i=1}^{n}\frac{d^3p_i}{(2\pi)^3}\frac{1}{2E_{p_i}}(2\pi)^4\delta^4\left(p_a + p_b - \sum_{i=1}^{n} p_i\right) \tag{2.12}$$

The decay rate or decay width Γ is the probability for a particle to decay per unit time, $\Gamma = d\tilde{P}/dt$, where $d\tilde{P}$ is the differential probability that the particle decays within the infinitesimal time interval dt. The probability $P(t)$ for the particle to survive at time t satisfies the differential equation $dP = -\Gamma P dt$, leading to an exponential decrease of the surviving probability, $P(t) = P(0)e^{-\Gamma t}$, with mean lifetime $\tau = 1/\Gamma$. For multiple decay modes i with total decay width $\Gamma_{\text{tot}} = \sum_i \Gamma_i$, the branching ratio $\text{BR}_i = \Gamma_i/\Gamma_{\text{tot}}$ defines the probability of the particle to decay into a specific mode i.

The differential decay rate of a particle i with momentum p_i to decay into n particles with momenta $\{p_j\}, j \in \{1, ..., n\}$, can be written as:

$$d\Gamma(p_i \to \{p_j\}) = \frac{1}{2E_i}|\mathcal{M}(p_i \to \{p_j\})|^2 d\Phi \tag{2.13}$$

Typical decay times for the strong, electromagnetic and weak interaction are 10^{-23} s, 10^{-16} s and 10^{-13} s to 15 min [91], respectively.

Feynman diagrams

Feynman diagrams are a pictorial representation of particle interactions used to calculate the matrix element $\mathcal{M}$ in perturbation theory. The visualisation of particles is shown in figure 2.1, fermions are drawn as straight lines, photons, W and Z bosons as wavy lines, scalar particles as dashed lines and gluons as curly lines. Double fermion lines indicate heavy-flavour (b and t) quarks. In the Feynman diagrams used in this thesis, the time axis points from left to right and the vertical axis represents space. Arrows on fermion lines point forward (backward) in time for particles (anti-particles). All interactions in the electroweak interaction and QCD can be described by the fundamental vertices shown in figure 2.2.

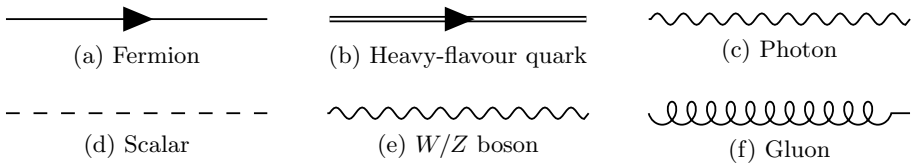

Figure 2.1.: Visualisation of particles in Feynman diagrams.

2.1.3. The Glashow-Weinberg-Salam model

The Glashow-Weinberg-Salam (GWS) model [27, 96, 97] unifies electromagnetic and weak interactions in the gauge group:

$$\text{SU}(2)_\text{L} \times \text{U}(1)_\text{Y} \tag{2.14}$$

with massless gauge bosons W^1, W^2, W^3, and B, which is spontaneously broken via the Higgs mechanism to the electromagnetic gauge group $\text{U}(1)_\text{EM}$ with massive gauge bosons $W^\pm$ and Z and a massless photon A.

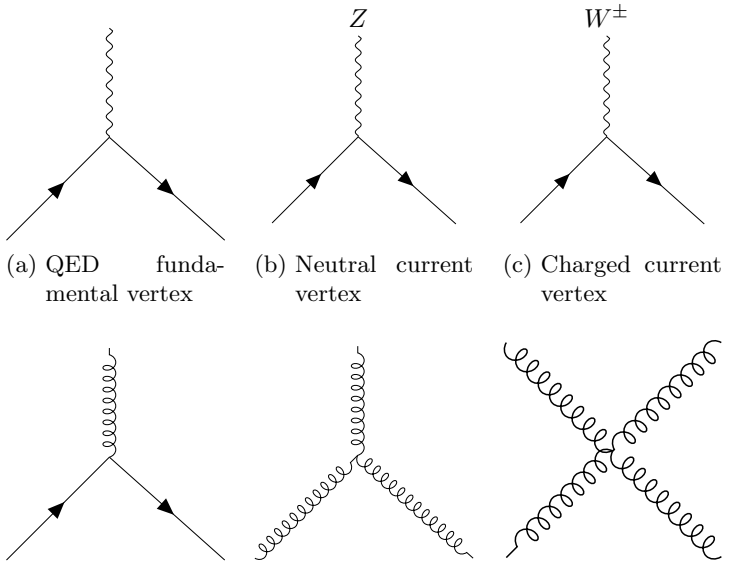

(a) QED fundamental vertex (b) Neutral current vertex (c) Charged current vertex

(d) QCD fundamental vertex (e) QCD three gluon vertex (f) QCD four glouon vertex

Figure 2.2.: Representation of electroweak (top row) and QCD (bottom row) fundamental vertices in Feynman diagrams.

Lepton and quark fields

The GWS model is a chiral and maximally parity-violating theory in which the $\mathrm{SU(2)_L}$ gauge bosons only couple to left-handed fermions and right-handed antifermions. Left-handed leptons and quarks are arranged in $\mathrm{SU(2)_L}$ doublet pairs L^i and Q^i with weak isospin $I = 1/2$, where i denotes the generation. Right-handed leptons e^i_R, ν^i_R and quarks u^i_R, d^i_R are singlets under $\mathrm{SU(2)_L}$ and thus have weak isospin $I = 0$. These multiplets with the corresponding charges are shown in table 2.4. Right-handed neutrinos and left-handed antineutrinos have not yet been observed since they are singlets under weak interaction and charge-less in electromagnetic interaction; they are thus referred to as sterile neutrinos.

The electroweak Lagrangian $\mathcal{L}_{\mathrm{EW}}$ reads:

$$\mathcal{L}_{\mathrm{EW}} = \mathcal{L}_{\mathrm{EW,g}} + \mathcal{L}_{\mathrm{EW,f}} \tag{2.15}$$

where $\mathcal{L}_{\mathrm{EW,g}}$ describes the dynamics of the gauge fields,

$$\mathcal{L}_{\mathrm{EW,g}} = -\frac{1}{4} W^a_{\mu\nu} W^{a,\nu\mu} - \frac{1}{4} B_{\mu\nu} B^{\mu\nu} \tag{2.16}$$

and $\mathcal{L}_{\mathrm{EW,f}}$ the coupling of fermions to the gauge fields:

$$\begin{aligned} \mathcal{L}_{\mathrm{EW,f}} =& i\bar{L}^i(\partial\!\!\!/ - igW\!\!\!/^a\tau^a - ig'Y_L B\!\!\!/)L^i + i\bar{Q}^i(\partial\!\!\!/ - igW\!\!\!/^a\tau^a - ig'Y_Q B\!\!\!/)Q^i \\ &+ i\bar{e}^i_R(\partial\!\!\!/ - ig'Y_e B\!\!\!/)e^i_R + i\bar{\nu}^i_R(\partial\!\!\!/ - ig'Y_\nu B\!\!\!/)\nu^i_R \\ &+ i\bar{u}^i_R(\partial\!\!\!/ - ig'Y_u B\!\!\!/)u^i_R + i\bar{d}^i_R(\partial\!\!\!/ - ig'Y_d B\!\!\!/)d^i_R \end{aligned} \tag{2.17}$$

where τ^a are the generators of $\mathrm{SU(2)_L}$, g and g' the couplings of the $\mathrm{SU(2)_L}$ and $\mathrm{U(1)}_Y$ gauge groups, respectively, and Y_i the hypercharges.

Table 2.4.: Electroweak quantum numbers of leptons, quarks and the Higgs doublet. [86]

Type	Multiplet	I	I_z	Y	Q_e
Leptons	$L^i = \begin{pmatrix}\nu_{eL}\\ e_L\end{pmatrix}, \begin{pmatrix}\nu_{\mu L}\\ \mu_L\end{pmatrix}, \begin{pmatrix}\nu_{\tau L}\\ \tau_L\end{pmatrix}$	$1/2$	$+1/2$ $-1/2$	$-1/2$	0 -1
	$e_R^i = \{e_R, \mu_R, \tau_R\}$	0	0	-1	-1
	$\nu_R^i = \{\nu_{eR}, \nu_{\mu R}, \nu_{\tau R}\}$	0	0	0	0
Quarks	$Q^i = \begin{pmatrix}u_L\\ d_L\end{pmatrix}, \begin{pmatrix}c_L\\ s_L\end{pmatrix}, \begin{pmatrix}t_L\\ b_L\end{pmatrix}$	$1/2$	$1/2$ $-1/2$	$+1/6$	$2/3$ $-1/3$
	$u_R^i = \{u_R, c_R, t_R\}$	0	0	$+2/3$	$+2/3$
	$d_R^i = \{d_R, s_R, b_R\}$	0	0	$-1/3$	$-1/3$
Higgs	$H = \begin{pmatrix}H^+\\ H^0\end{pmatrix}$	$1/2$	$+1/2$ $-1/2$	$+1/2$	$+1$ 0

Higgs mechanism

The Lagrangian for the gauge fields in eq. 2.16 does not contain any mass terms $mA^\mu A_\mu$ for the gauge bosons, as they are not invariant under $\mathrm{SU(2)_L}$ transformations and thus forbidden.

In the Higgs mechanism [32], the electroweak symmetry group $\mathrm{SU(2)_L} \times \mathrm{U(1)_Y}$ with massless gauge bosons W^1, W^2, W^3 and B is spontaneously broken to the electromagnetic gauge group $\mathrm{U(1)_{EM}}$ with massive gauge bosons $W^\pm$ and Z and a massless photon A. This is realised by introducing a complex scalar doublet Higgs field $H = (H^+, H^0)^\top$ with a symmetric potential $V(H)$:

$$V(H) = -\mu^2 H^\dagger H + \lambda (H^\dagger H)^2, \quad \mu^2 > 0, \lambda > 0 \tag{2.18}$$

that induces a non-zero vacuum expectation value (VEV) $v = \mu/\sqrt{\lambda}$. In unitary gauge, the Higgs doublet can be expanded around the VEV with a real scalar field h as:

$$H = \begin{pmatrix} 0 \\ v/\sqrt{2} + h/\sqrt{2} \end{pmatrix} \tag{2.19}$$

Plugging this into the kinetic part $\mathcal{L}_{H,\mathrm{kin}}$ of the Higgs Lagrangian $\mathcal{L}_H$,

$$\mathcal{L}_H = \mathcal{L}_{H,\mathrm{kin}} + V(H) \tag{2.20a}$$

$$\mathcal{L}_{H,\mathrm{kin}} = (D_\mu H)^\dagger (D^\mu H), \quad D_\mu H = (\partial_\mu - igW_\mu^a \tau^a - \frac{1}{2} ig' B_\mu) H \tag{2.20b}$$

yields mass terms for the gauge bosons. These can be diagonalised by linear combinations and rotations of the gauge bosons:

$$W_\mu^\pm = \frac{1}{\sqrt{2}} (W_\mu^1 \mp W_\mu^2) \tag{2.21a}$$

$$\begin{pmatrix} Z_\mu \\ A_\mu \end{pmatrix} = \begin{pmatrix} \cos\theta_\mathrm{W} & -\sin\theta_\mathrm{W} \\ \sin\theta_\mathrm{W} & \cos\theta_\mathrm{W} \end{pmatrix} \begin{pmatrix} W_\mu^3 \\ B_\mu \end{pmatrix} \tag{2.21b}$$

with the weak mixing angle θ_W. The electric charge e can be identified with $g \sin\theta_\mathrm{W} = g' \cos\theta_\mathrm{W}$.

Current measurements yield masses of $80.377 \pm 0.012\,\text{GeV}$ and $91.1876 \pm 0.0021\,\text{GeV}$ for the $W^{\pm}$ and Z boson, respectively [36]. A particle consistent with the Higgs boson predicted by the Standard Model was observed at the ATLAS [34] and CMS [35] experiments at CERN; in October 2013 the nobel prize in physics was awarded to Francois Englert and Peter Higgs "for the theoretical discovery of a mechanism that contributes to our understanding of the origin of mass of subatomic particles" [98]. Current measurements yield a Higgs boson mass of $125.25 \pm 0.17\,\text{GeV}$ [36].

Fermion masses

Mass terms of the form $m_f \bar{\psi}\psi = m_f(\bar{\psi_L}\psi_R + \bar{\psi_R}\psi_L)$ for fermions are not invariant under SU(2)_L transformations and thus forbidden in the SM Lagrangian. However, after electroweak symmetry breaking, Yukawa couplings like

$$\mathcal{L}_\text{Yuk} = -Y^e_{ij}\bar{L}^i H e^j_\text{R} - Y^\nu_{ij}\bar{L} i\sigma_2 H^\star \nu^j_\text{R} - Y^d_{ij}\bar{Q}^i H d^j_\text{R} - Y^u_{ij}\bar{Q}^i i\sigma_2 H^\star u^j_\text{R} + \text{h.c.} \tag{2.22}$$

for charged leptons, neutrinos and quarks generate mass terms with a mass m_f proportional to the coupling to the Higgs boson. The top quark, which is by far the heaviest fermion, is thus most sensitive to the mechanism of electroweak symmetry breaking. Current measurements and limits of the fermion masses are summarised in table 2.2. Neutrinos may acquire mass also in a second way by Majorana mass terms if they are their own antiparticles. In this thesis, neutrinos are considered to be massless.

After electroweak symmetry breaking, the relevant part of the Lagrangian from equations 2.17 and 2.22 for quark masses and electroweak interactions reads:

$$\begin{aligned}\mathcal{L} = &- m^d_j \left(\bar{d}^j_\text{L} d^j_\text{R} + \bar{d}^j_\text{R} d^j_\text{L}\right) - m^u_j(\bar{u}^j_\text{L} u^j_\text{R} + \bar{u}^j_\text{R} j^j_\text{L}) \\ &+ \frac{e}{\sqrt{2}\sin\theta_w}\left[W^+_\mu \bar{u}^i_\text{L}\gamma^\mu (V)^{ij} d^j_\text{L} + W^-_\mu \bar{d}^i_\text{L}\gamma^\mu (V^\dagger)^{ij} u^j_\text{L}\right]\end{aligned} \tag{2.23}$$

where the complex unitary Cabibbo-Kobayashi-Maskawa (CKM) matrix V with four degrees of freedom, three angles and one CP-violating phase, describes quark mixing.

Current measurements yield the following numerical values and uncertainties for the magnitudes of the CKM matrix elements [36]:

$$\begin{pmatrix} |V_{ud}| & |V_{us}| & |V_{ub}| \\ |V_{cd}| & |V_{cs}| & |V_{cb}| \\ |V_{td}| & |V_{ts}| & |V_{tb}| \end{pmatrix} = \begin{pmatrix} 0.97373(31) & 0.2243(8) & 0.00382(20) \\ 0.221(4) & 0.975(6) & 0.0408(14) \\ 0.0086(2) & 0.0415(9) & 1.014(29) \end{pmatrix} \tag{2.24}$$

The largest relevant matrix-element for the top quark, $|V_{tb}|$, is close to one and thus leads to a decay probability of a top quark into a bottom quark of almost 100%. The production and decay of top quarks is described in more detail in section 2.2.

2.1.4. Quantum chromodynamics

The strong interaction is based on the symmetry group $\mathrm{SU(3)_C}$ and described by the theory of quantum chromodynamics (QCD) with the following Lagrangian:

$$\mathcal{L}_{\mathrm{QCD}} = \mathcal{L}_{\mathrm{QCD,g}} + \mathcal{L}_{\mathrm{QCD,f}} = -\frac{1}{4} G^a_{\mu\nu} G^{a\mu\nu} + \sum_q \bar{\psi}_{q,i} (\delta_{ij} i\partial\!\!\!/ - g_s A\!\!\!/^a T^a_{ij}) \psi_{q,j} \tag{2.25}$$

where ψ_i are the quark fields with colour $i, j \in \{r, g, b\}$ index and flavour q index, and A^a, $a \in \{1, ..., 8\}$, the gluon fields with their corresponding field strengths G^a. Quarks carry a charge called colour charge which exists in three types named red, green and blue (r, g, b). Antiquarks carry the opposite charges antired, antigreen and antiblue $(\bar{r}, \bar{g}, \bar{b})$. Gluons carry combinations of colour-anticolour charges $(c\bar{c}')$. Since the $\mathrm{SU(3)_C}$ symmetry group is not broken in the Standard Model, gluons are massless and the colour charge is conserved.

Hadrons

The confinement property of QCD discussed in section 2.1.5 implies that quarks are always observed to be confined to bound colour-neutral states. These states are called hadrons and the most common ones can be approximately described as quark-antiquark pairs (mesons) and three-quark bound states (baryons) [99]. Mesons can be divided into two nonets of pseudoscalar and vector mesons with spin $J = 0$ and $J = 1$, respectively. Each nonet $3 \times \bar{3} = 1 \oplus 8$ consists of one singlet state and 8 mixed symmetry states. Baryons are classified via $3 \times 3 \times 3 = 10 \oplus 8 \oplus 8 \oplus 1$ in a symmetric decuplet with spin $J = 3/2$, two octets with spin $J = 1/2$ and mixed symmetry and one singlet state. The proton is a spin $J = 1/2$ baryon consisting of two up quarks and one down quark. In the Standard Model, protons are stable since baryon number is conserved and protons are the lightest baryons. The spectra of bound quark states like charmonium $c\bar{c}$ and bottonium $b\bar{b}$ can be calculated with the so-called Cornell potential [100, 101]:

$$V(r) = -\frac{4}{3}\frac{\alpha_S}{r} + \sigma r + \mathrm{const.} \tag{2.26}$$

that incorporates a small-distance behaviour $\propto 1/r$ calculable in perturbation theory due to the asymptotic freedom of QCD discussed in section 2.1.5 and a long-distance behaviour $\propto r$ that can be obtained from non-perturbative phenomenological models such as the String Model [102].

Jets

Jets are collimated collections of particles emerging in high-energy colliders. In the parton shower model [86] partons, i.e. quarks and gluons, moving out from the collision point radiate gluons which split into other gluons and quark-antiquark pairs. In the process of hadronisation, these gluons and quarks hadronise into colour-neutral objects due to the confinement property of QCD. This process, described in more detail in section 3.3.1, takes place several times, breaking the system into particles with lower and lower energies until hadrons are formed, which may decay further into stable hadrons, leptons and photons. The resulting collimated collections of particles called "jets" do usually form a cone-like shape due to the Lorentz boost into the direction of the originating parton.

2.1.5. Renormalisation and running coupling constants

The cross sections for scattering processes and decay rates in equations 2.11 and 2.13, respectively, are typically calculated from a perturbative expansion in powers of the electromagnetic, $\alpha_e = g_e^2/4 = e^2/4\pi$, and strong, $\alpha_s = g_s^2/4\pi$, coupling constants. Next-to-leading order corrections to the QED coupling between a photon and a charged fermion are illustrated in the Feynman diagrams in figure 2.3. The calculation of these diagrams involves the integration over the four-momenta of the particles in the loop and lead to ultraviolet-divergent results. These infinities are isolated in some well-defined manner in a mathematical procedure called "regularisation" and absorbed in the parameters, i.e. coupling constants and masses, of the theory by means of "renormalisation" [103–108]. The Standard Model is a "renormalisable" theory in which the adjustment of a finite number of parameters is sufficient to cancel all divergences and to yield finite results to all orders of perturbation theory.

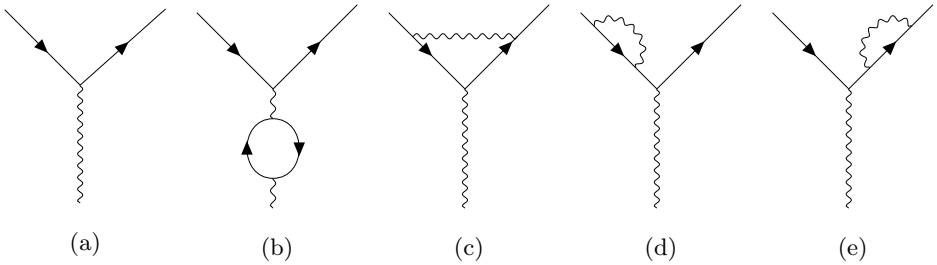

Figure 2.3.: QED coupling between a photon and a charged fermion (a) with photon propagator (b), vertex (c) and fermion-propagator corrections (d)-(e). The effects from the vertex and fermion-propagator corrections cancel exactly to all orders in perturbation theory [109–111].

The renormalisation procedure for the electromagnetic and strong coupling constants is illustrated in figures 2.4 and 2.5, respectively. Virtual lepton, quark and gluon pairs created in the photon or gluon exchange as well as corrections to the vertices and propagators lead to divergences that are regularised by introduction of a regularisation parameter Λ and absorbed in the bare coupling constants α_e and α_s that become infinite. The summation of all diagrams with bare coupling constants corresponds to the one-photon and one-gluon exchange with finite effective coupling constants $\alpha_e(Q^2)$ and $\alpha_s(Q^2)$, respectively, dependent on the momentum transfer Q^2 and Λ. The dependence of these so-called "running" coupling constants on the regularisation parameter is eliminated by expressing the coupling constant at the scale Q^2 in dependence of the coupling constant at some other scale μ_R^2, the so-called renormalisation scale. The electromagnetic and strong coupling constants can then be written as [99]:

$$\alpha_e(Q^2) = \frac{\alpha(\mu_R^2)}{1 - [\alpha(\mu_R^2)/3\pi]\ln(Q^2/\mu_R^2)} \tag{2.27}$$

$$\alpha_s(Q^2) = \frac{\alpha_s(\mu_R^2)}{1 + [\alpha_s(\mu_R^2)/12\pi](33 - 2n_f)\ln(Q^2/\mu_R^2)} \tag{2.28}$$

with n_f flavours contributing to the process at the scale Q^2.

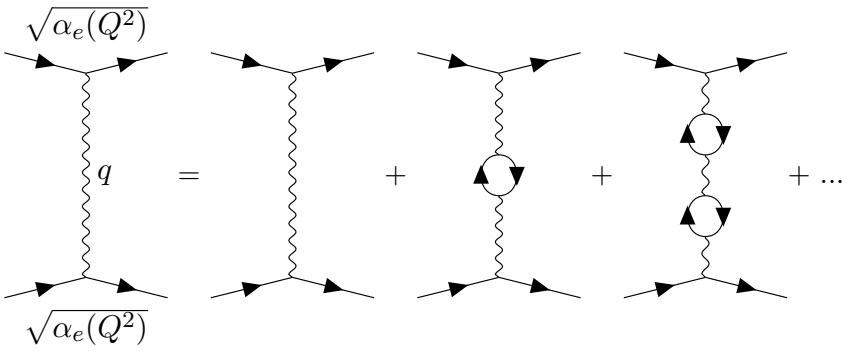

Figure 2.4.: Renormalisation in QED. The summation of all diagrams with bare coupling constant α_e corresponds to the one-photon exchange with a running coupling constant $\alpha_e(Q^2)$ dependent on the momentum transfer $Q^2 = -q^2$ with photon four-momentum q.

The strong coupling constant is typically expressed in terms of the scale Λ^2_{QCD}, defined as the scale Q^2 at which the denominator in eq. 2.28 becomes zero:

$$\alpha_s(Q^2) = \frac{12\pi}{(33 - 2n_f)\ln(Q^2/\Lambda^2_{\mathrm{QCD}})} \tag{2.29}$$

These dependencies of the coupling constants on the momentum scale Q^2 are illustrated in figure 2.6. The QED coupling constant $\alpha_e(Q^2)$ is found to increase slowly with Q^2, i.e. for higher energies and smaller distances. This can be understood pictorially in terms of e^+e^- pairs screening the electron charge; higher values of Q^2 correspond to shorter photon wavelengths and thus higher resolutions of the screening charges. In contrast to the abelian gauge group U(1) for electromagnetic interactions, the SU(3) gauge group is non-abelian, resulting in self-coupling interactions of the gluon fields, corresponding to the fact that gluons carry a colour charge. Thus, in addition to the shielding effect of quark-antiquark pairs, there are also anti-shielding effects from the charged gluons. For large $Q^2 \to \infty$ much larger than Λ_{QCD^2} and thus short distances, the effective coupling becomes very small, leading to an asymptotically free theory. For $Q^2 \approx \Lambda^2_{\mathrm{QCD}}$ corresponding to distances of 1 fm, however, the effective coupling becomes very large, leading to confinement, i.e. the prevention of the existence of free quarks and gluons, and the breakdown of perturbation theory.

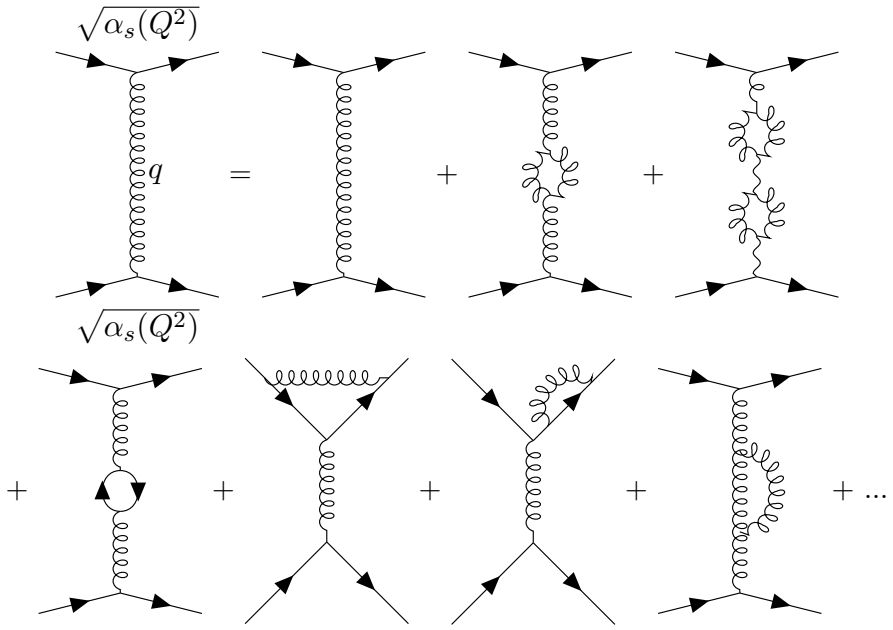

Figure 2.5.: Renormalisation in QCD. The summation of all diagrams with bare coupling constant α_s corresponds to the one-gluon exchange with a running coupling constant $\alpha_s(Q^2)$ dependent on the momentum transfer $Q^2 = -q^2$ with gluon four-momentum q.

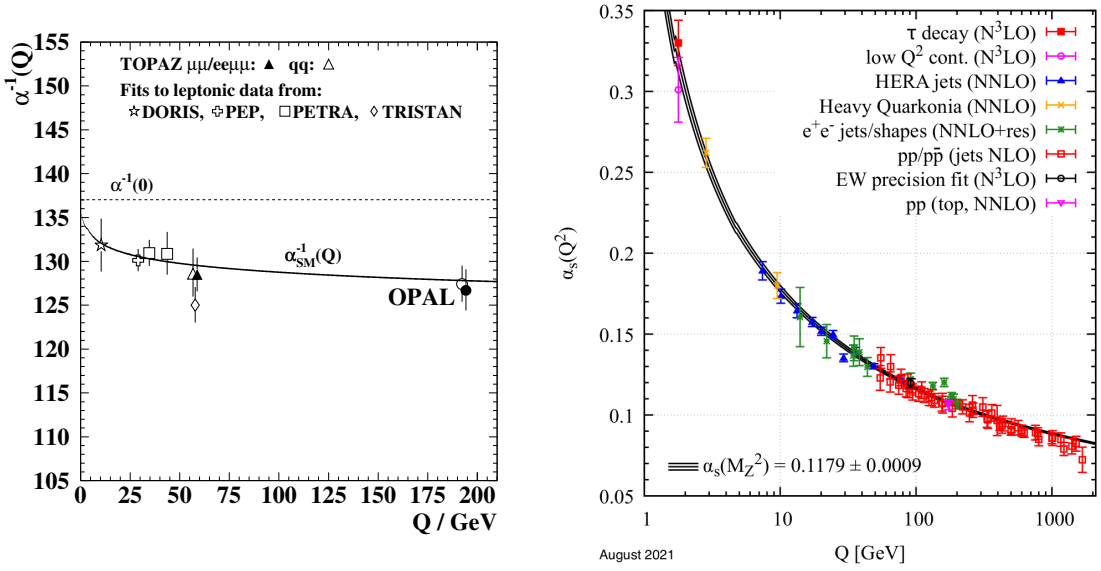

Figure 2.6.: Measurements of the electromagnetic α_e [112] (left) and strong α_S [36] (right) coupling constants as a function of the energy scale Q.

2.2. Top-quark pair production and decay

In this thesis, the energy asymmetry is measured in jet-associated top-quark pair events produced at the LHC in proton-proton collisions. Since the top quarks decay immediately, the energies of the top and antitop quarks are reconstructed from their decay products as explained in section 5.

Section 2.2.1 describes general scattering processes at hadron colliders. The production of inclusive and jet-associated top-quark pair events is explained in section 2.2.2. The top-quark decay is described in section 2.2.3.

2.2.1. Scattering processes at hadron colliders

In collider experiments, the rate of scattered events $\dot{N}$ for a given process is given by the product of the cross section σ and the instantaneous luminosity L:

$$\dot{N} = L\sigma \tag{2.30}$$

where the cross section is a process-specific measure for the probability of an event to occur and the luminosity is a collider-specific expression for the intensity of the colliding beams. The total number of scattered events is given by integrating eq. 2.30 over time:

$$N = \int \sigma L dt = \sigma \mathcal{L} \tag{2.31}$$

where the quantity $\mathcal{L} = \int L dt$ is called the integrated luminosity. With two bunches consisting of n_1 and n_2 particles colliding at a frequency f, the instantaneous luminosity in collider experiments can be expressed as:

$$L = f \frac{n_1 n_2}{4\pi \sigma_x \sigma_y} \tag{2.32}$$

with horizontal and vertical beam sizes σ_x and σ_y, respectively. For two colliding particles a and b with four-momenta p_a and p_b, the centre-of-mass energy $\sqrt{s}$, defined via the Lorentz invariant quantity $s = (p_a + p_b)^2$, represents the available energy for the creation of new particles.

The Large Hadron Collider (LHC) described in section 3.1 is a proton-proton collider. According to the parton model introduced by Feynman [113] and Bjorken [20], protons are composite objects consisting of three valence quarks, two up quarks and one down quark, bound together by the exchange of gluons, which split into virtual quark-antiquark pairs, the so called sea quarks, or radiate further gluons. Figure 2.7a illustrates these processes. All the gluons, valence and sea quarks in the proton are referred to as "partons". The probability to find a parton of type a with momentum fraction x_a in a hadron A is given by the parton distribution function (PDF) $f_{a/A}(x_a, \mu_F)$ depending on the factorisation scale μ_F, which can be thought of as a scale that separates short- and long-distance processes. The splitting of quarks and gluons into each other leads to infrared divergences that are absorbed into running parton densities which form a set of coupled differential equations depending on the factorisation scale μ_F; the so called the Dokshitzer-Gribov-Lipatov-Altarelli-Parisi (DGLAP) [114–117] equations. Figure 2.8 shows the PDFs extracted from experiments by the NNPDF collaboration [118] at $\mu_F^2 = 10\,\mathrm{GeV}^2$ and $\mu_F = 10^4\,\mathrm{GeV}^2$. With increasing μ_F^2, the PDFs

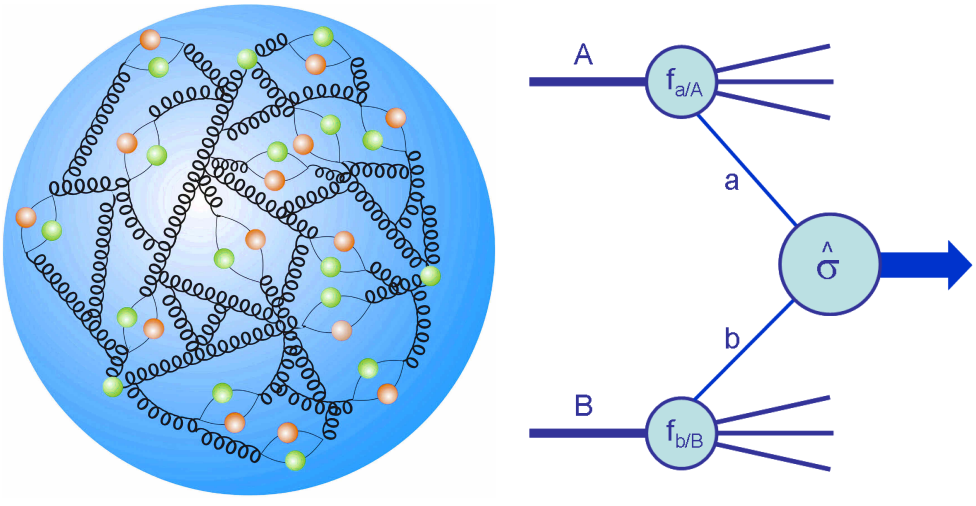

(a) (b)

Figure 2.7.: Schematic view of the proton structure [122] (a) and of proton-proton collisions [121] (b). The proton consists of three valence quarks, bound together by the exchange of gluons, which can split into quark-antiquark pairs, the so called valence quarks, or radiate further gluons. In the collision of two protons A and B the partons a and b scatter in the so called hard-scattering process with cross section $\hat{\sigma}$. The probabilities to find these carrying a momentum fraction x_a and x_b inside the protons A and B are given by the parton distribution functions $f_{a/A}$ and $f_{b/B}$, respectively.

are found to increase at small x and decrease at large x. Qualitatively, higher energy scales μ_F^2 correspond to smaller distances and thus better resolutions, increasing the number of observed partons sharing the same proton momentum [91].

Factorisation theorems [119, 120] state that any scattering process involving protons can be computed by combining the same universal non-perturbative PDFs with perturbative short-distance calculations in QCD. The cross section for the proton-proton scattering process $AB \to X$ illustrated in figure 2.7b can thus be written as [121]:

$$\sigma_{AB\to X} = \sum_{a,b} \int_0^1 dx_a \int_0^1 dx_b f_{a/A}(x_a, \mu_F) f_{b/B}(x_b, \mu_F) \hat{\sigma}_{ab\to X}(\mu_R) \tag{2.33}$$

where $\hat{\sigma}_{ab\to X}(\mu_R)$ denotes the hard-scattering cross section of the partonic subprocess $ab \to X$ depending on the renormalisation scale discussed in section 2.1.5 and the sum runs over all possible parton types. Formally, the cross section calculated to all orders in perturbation theory is independent of the choice of the scales μ_F and μ_R; to finite order, different choices yield differing numerical values, resulting in uncertainties on the prediction discussed in section 8.1 which decrease for higher orders in perturbation theory. Typically, these scales are chosen of the order of the typical momentum scales of the hard scattering process, e.g. $\mu_F = \mu_R = m_t$ in top-quark pair production.

Predictions for various cross sections in proton-proton scattering processes are shown in figure 2.9.

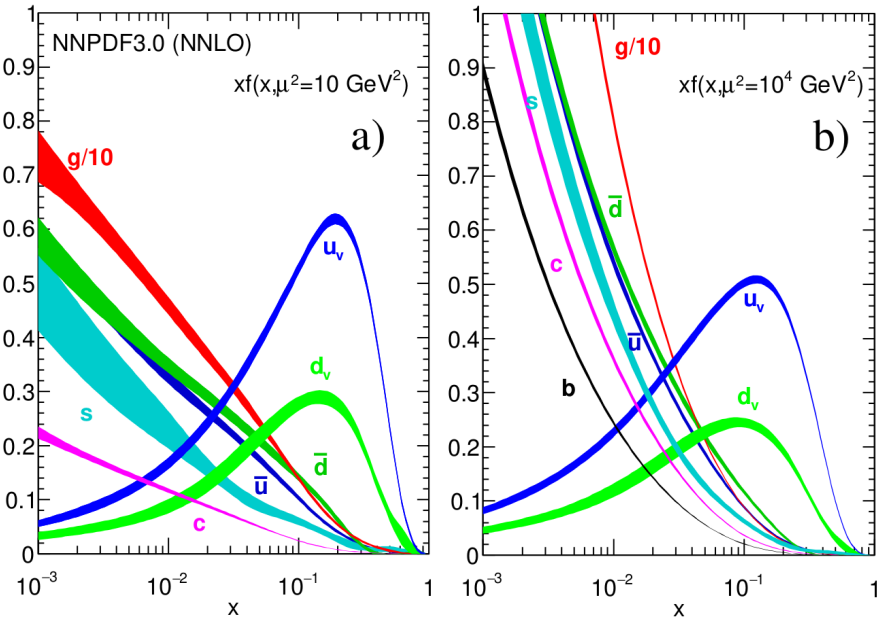

Figure 2.8.: Parton distribution functions (PDFs) obtained in the NNLO NNPDF3.0 global analysis [92, 118] at $\mu_F^2 = 10\,\mathrm{GeV}^2$ (left) and $\mu_F^2 = 10^4\,\mathrm{GeV}^2$ (right).

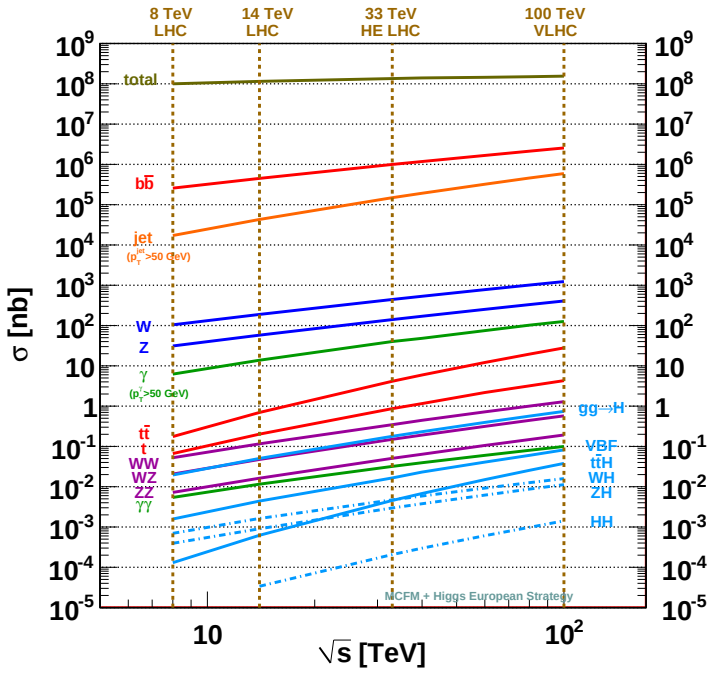

Figure 2.9.: Predicted cross sections for various production processes in proton-proton collisions as a function of the centre-of-mass energy $\sqrt{s}$. [123]

2.2.2. Top-quark pair production

At hadron colliders, top quarks are dominantly produced in pairs via gluon-gluon fusion $gg \to t\bar{t}$ and quark-antiquark annihilation $q\bar{q} \to t\bar{t}$ [36]. Feynman diagrams at leading order (LO) in QCD for these processes are shown in figure 2.10. At the LHC at a centre-of-mass energy of $\sqrt{s} = 13\,\text{TeV}$ about 90% of the production originates from gluon-gluon fusion.

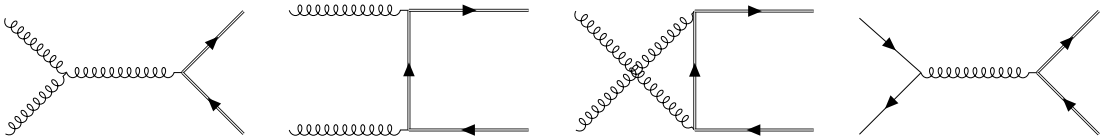

Figure 2.10.: Feynman diagrams for leading order $t\bar{t}$ production in gluon-gluon fusion in the s-, t- and u-channel and quark-antiquark annihilation.

Assuming a top-quark mass of 172.5 GeV, the theoretical prediction for the cross section at next-to-next-to leading order (NNLO) is $\sigma_{t\bar{t}} = 831.8^{+19.8+35.1}_{-29.2-35.1}\,\text{pb}$ [36] at $\sqrt{s} = 13\,\text{TeV}$, where the uncertainties are due to scale dependence and parton distribution functions, respectively. Recent measurements at ATLAS [124] and CMS [125] find $\sigma_{t\bar{t}} = 830.4 \pm 0.4(\text{stat})^{+38.2}_{-37.0}(\text{syst})$ and $\sigma_{t\bar{t}} = 803 \pm 2(\text{stat}) \pm 25(\text{syst}) \pm 20(\text{lumi})$, respectively. Figure 2.11 shows the measured and predicted cross sections as a function of the centre-of-mass energy $\sqrt{s}$.

Top-quark pairs in association with a high transverse momentum jet are predominantly produced via gluon-gluon fusion which contributes for about 70% to the LO cross section. In contrast to inclusive top-quark pair production, quark-gluon scattering appears already at LO and thus gives a significant contribution of about 22%. Figure 2.12 shows exemplary Feynman diagrams for $t\bar{t}j$ production in gluon-gluon fusion, quark-antiquark annihilation and quark-gluon scattering.

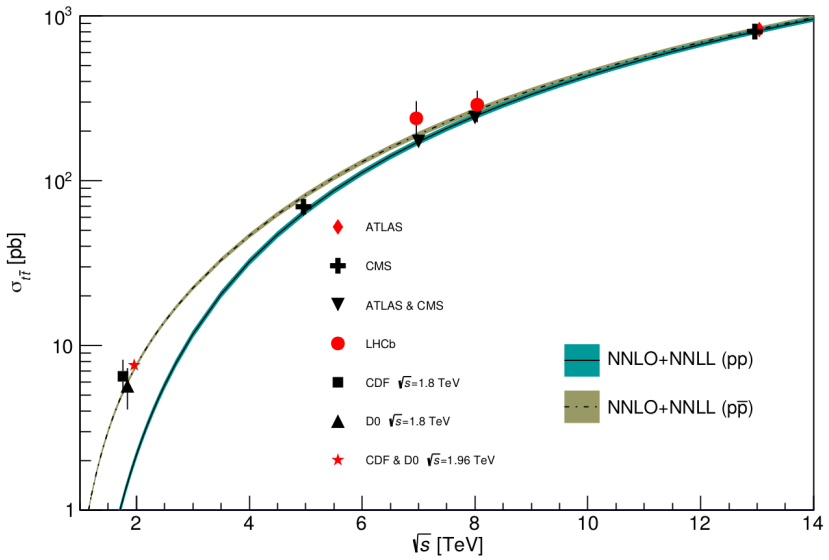

Figure 2.11.: Measured and predicted $t\bar{t}$ production cross section as a function of the centre-of-mass energy $\sqrt{s}$. [92]

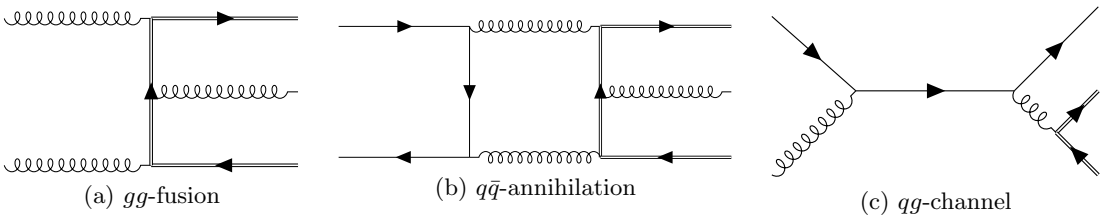

(a) gg-fusion (b) $q\bar{q}$-annihilation (c) qg-channel

Figure 2.12.: Exemplary Feynman diagrams for $t\bar{t}j$ production in gluon-gluon fusion (a), quark-antiquark annihilation (b) and quark-gluon scattering (c).

Table 2.5.: Predicted cross sections for inclusive $t\bar{t}$ production at NNLO [36, 126] with scale and PDF uncertainties and for $t\bar{t}j$ production at NLO [71] with numerical and scale uncertainties for various p_T requirements on the associated jet, assuming a top-quark mass of 172.5 GeV and 174 GeV, respectively, and a centre-of-mass energy $\sqrt{s}$ of 14 TeV.

Process	$t\bar{t}$	$t\bar{t}j$		
		$p_T > 20\,\text{GeV}$	$p_T > 50\,\text{GeV}$	$p_T > 100\,\text{GeV}$
σ[pb]	$984.5^{+23.2+41.3}_{-34.7-41.3}$	$692(3)^{+40}_{-62}$	$376.2(6)^{+17}_{-48}$	$175.0(2)^{+10}_{-24}$

Predictions of the cross sections for inclusive $t\bar{t}$ production at NNLO [126] and for $t\bar{t}j$ production at NLO [71] for different transverse momentum requirements on the associated jet are shown in table 2.5. While the cross section decreases with an increasing associated jet p_T, the energy asymmetry increases [74]. In this analysis, the transverse momentum of the associated jet is required to be larger than 100 GeV; see section 5.1 for details on the event selection.

2.2.3. Top-quark decay

The top quark with a measured mass of $m_t = 172.69 \pm 0.30$ [36] is the only quark that decays into a real W boson and a down-type quark. Due to its short lifetime of $0.5 \cdot 10^{-24}$ s, corresponding to a total decay width of $1.42^{+0.19}_{-0.15}$ GeV, it is expected to decay before hadronisation can occur or $t\bar{t}$-quarkonium-bound states can form [127]. The probability to a decay into a W boson and a bottom quark is close to 100% as the relevant matrix element $|V_{tb}|$ is close to 1, see eq. 2.24. While the bottom quark hadronises and evolves into a jet, the W boson decays either hadronically into an up-type and a down-type quark or leptonically into a charged lepton and a (anti)neutrino.

Depending on its charge, the W boson decays predominantly into the two quark combinations $u\bar{d}$ and $c\bar{s}$ or $\bar{u}d$ and $\bar{c}s$ with three colour options each and three charged lepton-neutrino combinations, yielding branching ratios of approximately 67% and 33% for hadronic and leptonic decays, respectively. The resulting branching ratios for the top-quark decay channels are listed in table 2.6.

The $t\bar{t}$ final states can be divided into three channels: In the all-hadronic channel, both W bosons decay hadronically into quark-antiquark pairs. In the semi-leptonic channel, one of the two W bosons decays into a quark-antiquark pair, while the other

Table 2.6.: Branching ratios for top-quark decays. [92]

Decay channel	BR
$t \to e\nu_e b$	$(11.1 \pm 0.3)\%$
$t \to \mu\nu_\mu b$	$(11.4 \pm 0.2)\%$
$t \to \tau\nu_\tau b$	$(11.1 \pm 0.9)\%$
$t \to q\bar{q}b$	$(66.5 \pm 1.4)\%$

Table 2.7.: Decay channels and branching ratios of top-quark pair decays. Matter-antimatter identities need to be applied depending on the charge of the W boson. [36]

Channel	Decay chain	BR
All-hadronic	$t\bar{t} \to W^+b + W^-\bar{b} \to qq'b + q''q'''b$	45.7%
Semi-leptonic	$t\bar{t} \to W^+b + W^-\bar{b} \to qq'b + l\nu_l b$	43.8%
Di-leptonic	$t\bar{t} \to W^+b + W^-\bar{b} \to l\nu_l b + l'\nu_{l'} b$	10.5%

W boson decays into a charged lepton and a neutrino. In the di-leptonic channel, both W bosons decay leptonically into a charged lepton and a neutrino. The decay channels with the corresponding branching ratio are summarised in table 2.7.

This analysis focuses on semi-leptonic $t\bar{t}$ events including electrons and muons directly originating from the W-boson decay as well as electrons and muons originating from τ decays. Figure 2.13 shows an example of a Feynman diagram for jet-associated top-quark pair production followed by semi-leptonic top-quark decays representing the signal signature selected in this analysis as described in chapter 5.

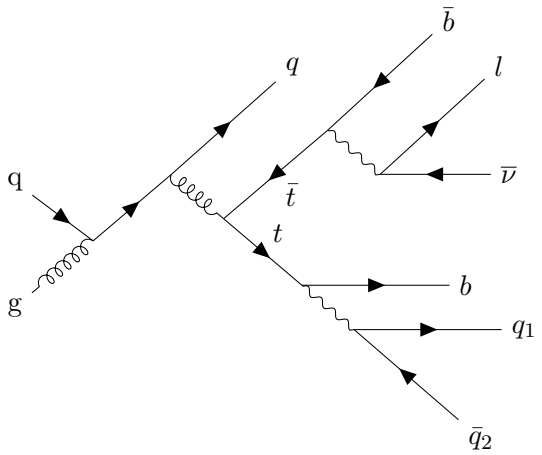

Figure 2.13.: Jet-associated top-quark pair production in the quark-gluon channel followed by semi-leptonic top-quark decays.

2.3. Top-quark charge asymmetry

2.3.1. Charge asymmetry at hadron colliders

Charge asymmetries are defined as asymmetries under charge conjugation in the final state. The leading-order processes for heavy-flavour production, quark-antiquark annihilation, $q\bar{q} \to Q\bar{Q}$, and gluon-gluon fusion, $gg \to Q\bar{Q}$, are symmetric under charge conjugation in the final state and thus yield identical differential cross sections for the production of $Q\bar{Q}$ and $\bar{Q}Q$ states. At next-to-leading order in the strong coupling constant α_S, however, interference terms between amplitudes which are odd under charge conjugation [58] arise due to initial- (ISR) and final-state (FSR) radiative corrections for $q\bar{q}$ annihilation and diagrams involving quark-gluon scattering, $qg \to Q\bar{Q}$. Figures 2.14 and 2.15 show the main Feynman diagrams contributing to the charge asymmetry in $q\bar{q}$ annihilation and qg scattering, respectively. The dominating interferences are depicted in figure 2.16.

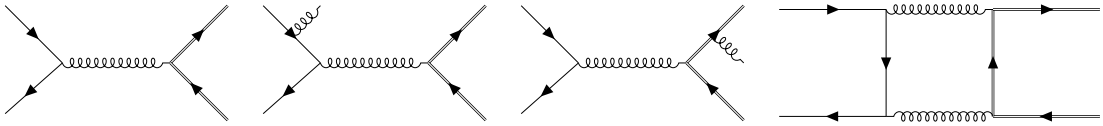

Figure 2.14.: Exemplary Feynman diagrams for heavy-flavour production in quark-antiquark annihilation. Interferences between initial-state (b) and final-state (c) gluon radiation as well as the Born (a) and box (d) diagrams induce a charge asymmetry [58].

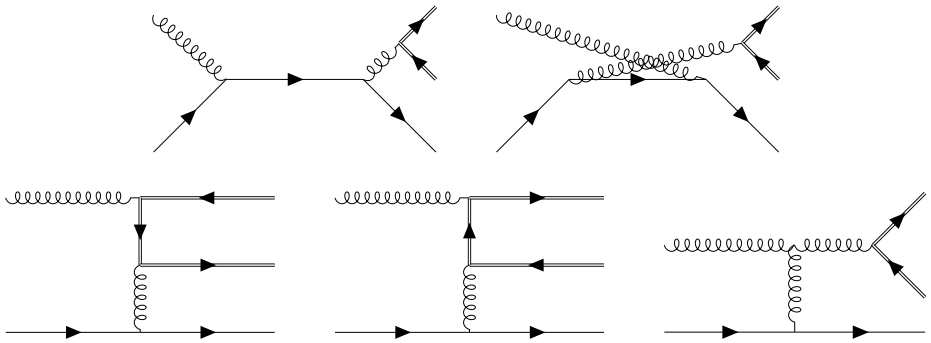

Figure 2.15.: Exemplary Feynman diagrams for heavy-flavour production in quark-gluon scattering, inducing a charge asymmetry [58]. Double fermion lines indicate heavy-flavour quarks.

2.3.2. Forward-backward asymmetry

In proton-antiproton collisions, top quarks are preferentially produced in the direction of the incoming proton. The forward-backward asymmetry A_{FB} is defined as [58, 69]:

$$A_{\mathrm{FB}} = \frac{N(\Delta y > 0) - N(\Delta y < 0)}{N(\Delta y > 0) + N(\Delta y < 0)} \tag{2.34}$$

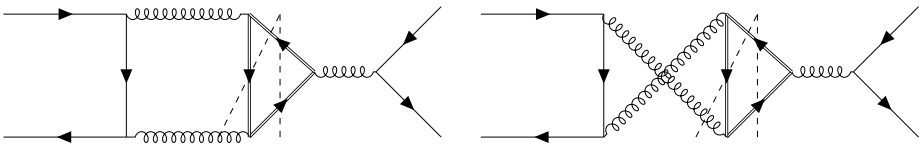

(a) box (b) crossed-box

Figure 2.16.: Dominant contributions to the charge asymmetry from $q\bar{q}$ annihilation. The squared matrix element in eq. 2.11 is visualised by merging the final state particles of the interfering Feynman diagrams separated by dashes. The vertical separations correspond to interferences between the Born and the one loop correction box (a) and crossed-box (b) diagrams. Diagonal separations correspond to interferences between diagrams with initial-state and final-state gluon radiation.

where $\Delta y = y_t - y_{\bar{t}}$ is the rapidity difference between the top and the antitop quark.

Measurements at Tevatron [128] at a centre-of-mass energy of $\sqrt{s} = 1.96\,\text{TeV}$ yield a forward-backward asymmetry of $A_{\text{FB}} = 0.128 \pm 0.025$ consistent with SM predictions.

2.3.3. Rapidity asymmetry

In proton-proton collisions, the colliding beams are symmetric and hence there is no preferential direction of either the top quark or the antitop quark. Since on average the valence quarks in the proton carry a larger fraction of the proton momentum than the sea quarks, there is a momentum imbalance of the initial-state quark and anti-quark in the $q\bar{q}$ annihilation channel. The top quark is preferentially produced in the direction of the initial-state quark and is thus expected to have a higher longitudinal momentum than the antitop quark corresponding to a larger absolute rapidity. The rapidity asymmetry is defined as [129, 130]:

$$A_C = \frac{N(\Delta|y| > 0) - N(\Delta|y| < 0)}{N(\Delta|y| > 0) + N(\Delta|y| < 0)} \tag{2.35}$$

with $\Delta|y| = |y_t| - |y_{\bar{t}}|$.

The rapidity asymmetry was measured at ATLAS [62, 63, 131] and CMS [67, 68] at a centre-of-mass energy of $\sqrt{s} = 8\,\text{TeV}$ and found to be consistent both with 0 and the SM prediction. Current measurements at ATLAS [66] at 13 TeV yield an inclusive rapidity asymmetry of $A_C = 0.0068 \pm 0.0015$ consistent with SM predictions and differing from zero by 4.7 standard deviations.

2.3.4. Energy asymmetry

The availability of an additional jet in jet-associated top-quark pair production allows for the construction of new observables not available in inclusive $t\bar{t}$ production, like the incline and energy asymmetries [73]. In particular, the energies of the top and antitop quarks are identical in a two particle final state due to momentum conservation, which is not the case in the presence of additional jets.

In contrast to inclusive $t\bar{t}$ production, where the charge asymmetry is generated by next-to-leading order corrections in quark-antiquark annihilation and is thus sup-

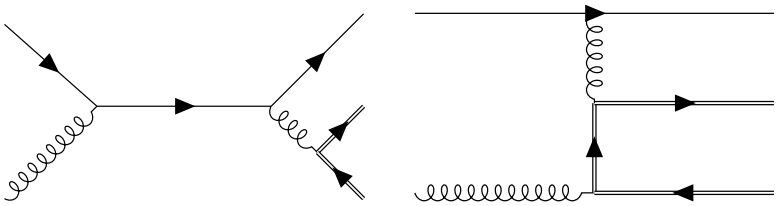

Figure 2.17.: Feynman diagrams for jet-associated top-quark pair production in the quark-gluon channel at leading order (LO) in the strong coupling constant α_S.

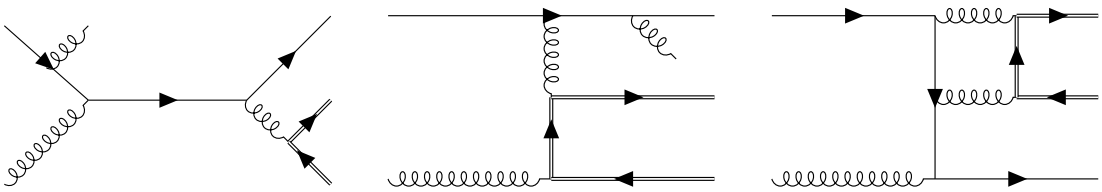

Figure 2.18.: Feynman diagrams for jet-associated top-quark pair production in the quark-gluon channel at next-to-leading order (NLO) in the strong coupling constant α_S.

pressed, the charge asymmetry in inclusive $t\bar{t}j$ production is already generated at leading order in quark-gluon interactions, which are more abundant in high energy collisions than quark-antiquark annihilation. Figures 2.17 and 2.18 show the relevant Feynman diagrams contributing to the charge asymmetry at LO and NLO in inclusive $t\bar{t}j$ production.

The kinematics for the process $p_1 p_2 \to t\bar{t}j$ is shown in figure 2.19, described by the top-quark and jet energies E_t, E_j, the jet scattering angle θ_j with respect to the direction of the incoming parton p_1 and the inclination angle ϕ. The angles ξ and $\bar{\xi}$ between the top and antitop quark, respectively, and the associated jet momenta are fixed by the energies E_t, $E_{\bar{t}}$, E_j and the centre-of-mass energy $\sqrt{\hat{s}} = E_t + E_{\bar{t}} + E_j$.

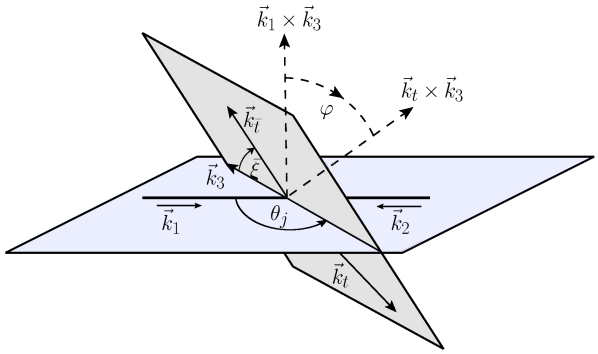

Figure 2.19.: Kinematics of the process $p_1 p_2 \to t\bar{t}p_3$ with jet scattering angle θ_j and inclination angle ϕ. [73]

The energy asymmetry is defined as [73]:

$$A_E(\theta_j) \equiv \frac{\sigma(\theta_j, \Delta E > 0) - \sigma(\theta_j, \Delta E < 0)}{\sigma(\theta_j, \Delta E > 0) + \sigma(\theta_j, \Delta E < 0)} \equiv \frac{\sigma_A(\theta_j)}{\sigma_S(\theta_j)}, \tag{2.36}$$

where $\Delta E = E_t - E_{\bar{t}}$ and θ_j are defined in the $t\bar{t}j$ rest frame, corresponding to the parton centre-of-mass frame at leading order. The asymmetric and symmetric cross sections σ_A and σ_S are defined as the numerator and denominator of the energy asymmetry, respectively. The energy asymmetry is symmetric in $\theta_j \leftrightarrow \pi - \theta_j$ and has a minimum at $\theta_j = \pi/2$ as illustrated in figure 2.21.

The total energy asymmetry at NLO is given by [74]:

$$A_{\mathrm{E}}^{\mathrm{NLO}} \propto \log^{-2}\left(\frac{m_t}{p_T^j}\right)\left[1 + \mathcal{O}(\alpha_s) + \mathcal{O}\left(\alpha_s \log\left(\frac{m_t}{p_T^j}\right)\right)\right] \tag{2.37}$$

and thus increases with the transverse momentum p_T^j of the associated jet and vanishes for $p_T^j \to 0$.

The $t\bar{t}j$ final state can be produced in quark-antiquark annihilation, $q\bar{q} \to t\bar{t}g$, gluon-gluon fusion, $gg \to t\bar{t}g$, which does not contribute to the charge asymmetry, and in the quark-gluon channel, $qg \to t\bar{t}q$, which is neither symmetric nor antisymmetric under charge conjugation. The additional jet is preferentially emitted into the direction of the incoming quark in the qg channel, while the angular jet distribution in the $q\bar{q}$ initial state is symmetric. Contributions from $q\bar{q}$ and $\bar{q}q$ annihilation cancel completely due to the symmetric beam. Individual contributions from qg and gq states, in which the incoming quark momentum is aligned with or opposite to the beam axis, are not symmetric under $\theta_j \leftrightarrow \pi - \theta_j$ due to asymmetric kinematics, while their sum is symmetric. The predicted leading order contributions to the energy asymmetry from gq, qg, $\bar{q}g$ and $g\bar{q}$ initial states at the LHC with a centre-of-mass energy of $\sqrt{s} = 8\,\mathrm{TeV}$ are shown in figure 2.20.

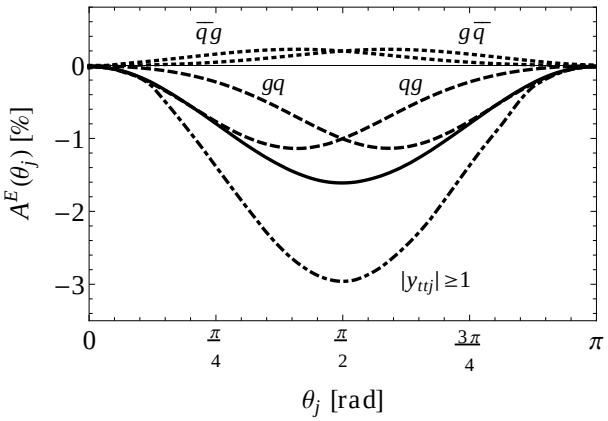

Figure 2.20.: Contributions to the energy asymmetry from gq, qg, $\bar{q}g$ and $g\bar{q}$ initial states at the LHC with a centre-of-mass energy of $\sqrt{s} = 8\,\mathrm{TeV}$ at LO QCD. [73]

Contributions from $\bar{q}g$ and $g\bar{q}$ initial states have the opposite sign than those from qg and gq initial states, but are smaller, since among high-momentum partons in the proton quarks are much more abundant than antiquarks as can be seen from the parton distribution functions in figure 2.8. While it is impossible to disentangle from which of the incoming beams the quark and the gluon originated, it is possible to enhance the asymmetry by combining the maximum contributions from the qg and gq channels by guessing the direction of the incoming quark, since the final state tends to be boosted into the quark direction, as quarks typically carry a larger momentum fraction of the proton than gluons.

The optimised energy asymmetry is defined as [74, 79]:

$$A_E^{\text{opt}}(\theta_j) \equiv \frac{\sigma^{\text{opt}}(\theta_j, \Delta E > 0) - \sigma^{\text{opt}}(\theta_j, \Delta E < 0)}{\sigma^{\text{opt}}(\theta_j, \Delta E > 0) + \sigma^{\text{opt}}(\theta_j, \Delta E < 0)}, \tag{2.38}$$

where $y_{t\bar{t}j}$ is the rapidity of the $t\bar{t}j$ system in the laboratory frame and σ^{opt} is the optimised cross section:

$$\sigma^{\text{opt}}(\theta_j) \equiv \begin{cases} \sigma(\theta_j) & \text{for } y_{t\bar{t}j} > 0 \\ \sigma(\pi - \theta_j) & \text{for } y_{t\bar{t}j} < 0 \end{cases} \tag{2.39}$$

Equivalently, the energy asymmetry can be defined in terms of the number of events N instead of the the cross section σ:

$$A_E^{\text{opt}}(\theta_j) \equiv \frac{N^{\text{opt}}(\theta_j, \Delta E > 0) - N^{\text{opt}}(\theta_j, \Delta E < 0)}{N^{\text{opt}}(\theta_j, \Delta E > 0) + N^{\text{opt}}(\theta_j, \Delta E < 0)}, \tag{2.40}$$

where N^{opt} is the optimised event number:

$$N^{\text{opt}}(\theta_j) \equiv \begin{cases} N(\theta_j) & \text{for } y_{t\bar{t}j} > 0 \\ N(\pi - \theta_j) & \text{for } y_{t\bar{t}j} < 0 \end{cases} \tag{2.41}$$

The optimised energy asymmetry has a predicted minimum around $\theta_j \approx 2\pi/5$ as shown in figure 2.21. NLO corrections are sizeable at low and high jet scattering angles and smaller around the minimum. As they are positive, they reduce the magnitude of the energy asymmetry at the minimum and yield positive asymmetries at low and high jet scattering angles.

The dominant uncertainties on the predictions are missing higher-order QCD corrections, described by renormalisation and factorisation scale dependencies, and PDF uncertainties. The scale uncertainties are sizeable (40% at LO and 10% at NLO) on the cross sections σ_S and σ_S^{opt}, but cancel almost completely out for the energy asymmetry at leading order ($\approx 5\%$) and up to a few percent around the minimum at next-to-leading order.

In the following, the event selection applied in figure 2.21 with requirements on the transverse momentum and pseudorapidity of the associated jet of $p_T(j) > 100\,\text{GeV}$ and $|\eta| < 2.5$ is considered as "loose". In the "boosted" selection, it is additionally required that at least one of the top quarks has a transverse momentum above 300 GeV and $|\eta| < 2.0$. Figure 2.22 shows the SM prediction for the optimised energy asymmetry for the boosted and loose selections obtained from simulation using MADGRAPH5_AMC@NLO 2.6 as described in reference [75].

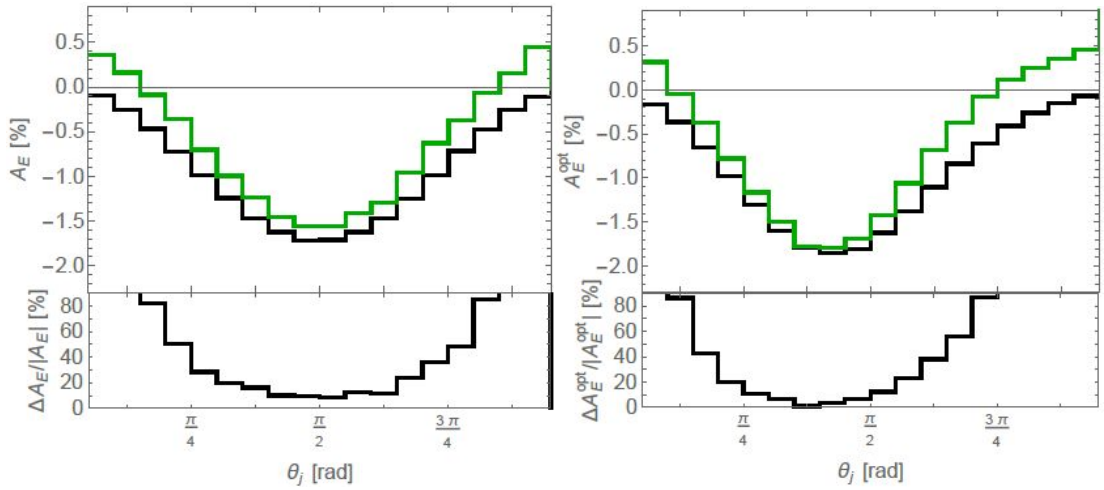

Figure 2.21.: SM prediction of the energy asymmetry (left) and the optimised energy asymmetry (right) in proton-proton collisions at the LHC at $\sqrt{s} = 13\,\text{TeV}$ as a function of the jet scattering angle θ_j [74]. Kinematic cuts of $p_T^j > 100\,\text{GeV}$ and $|y_j| < 2.5$ are applied at leading order (black) and next-to-leading order (green). The minima are at $\theta_j = \pi/2$ and $\theta_j \approx 2\pi/5$ for the energy asymmetry and the optimised energy asymmetry, respectively. The bottom panels show the relative impact of NLO corrections.

The energy asymmetry grows with the absolute value of the top-antitop energy difference $|\Delta E|$ and can be further enhanced by projecting out the central region and thus suppressing the charge symmetric gg background with a cut on the rapidity $y_{t\bar{t}j}$, which reduces the cross section strongly. Figure 2.23 shows the SM prediction at NLO QCD for the optimised differential cross section and the optimised energy asymmetry in a "boosted" selection with high-p_T top quark with different requirements on $|\Delta E|$ and $|y_{ttj}|$.

In this analysis, only the optimised energy asymmetry without cuts on $|\Delta E|$ and $|y_{ttj}|$ is considered and henceforth simply referred to as "energy asymmetry".

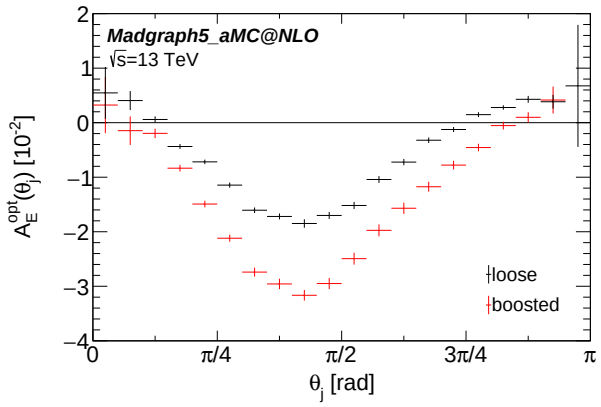

Figure 2.22.: SM prediction for the optimised energy asymmetry at the LHC with $\sqrt{s} = 13\,\text{TeV}$ at NLO QCD in the loose and boosted phase spaces. Vertical markers correspond to the MC statistical uncertainty.

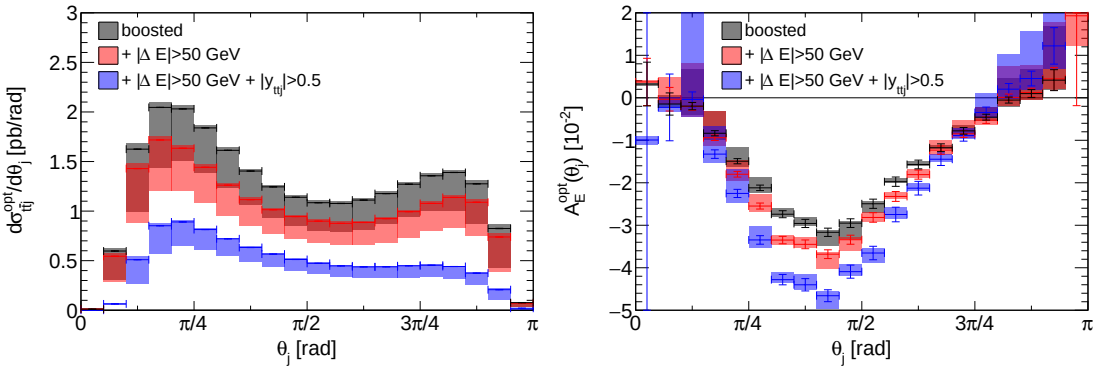

Figure 2.23.: SM prediction for the optimised differential cross section (left) and the optimised energy asymmetry (right) at the LHC with $\sqrt{s} = 13\,\text{TeV}$ at NLO QCD. The MC statistical and scale uncertainties are visualised by vertical markers and coloured bands, respectively. This figure was published as figure 1 in reference [75].

2.4. Physics beyond the Standard Model

2.4.1. Introduction to physics beyond the Standard Model

The Standard Model was found to give correct predictions with an astonishing precision for tens of thousands of measurements in thousands of publications [36]. Despite its impressive success, the Standard Model leaves many fundamental questions unanswered.

The Standard Model contains gauge field patterns and many free parameters such as fermion masses, coupling constants and CKM-matrix elements that cannot be derived from theory, but must be determined from experiments and seem rather arbitrary or fine-tuned [39]. The naturalness or hierarchy problem [39, 132] is that the electroweak mass scale is 16 orders smaller than the Planck scale and that the mass of the Higgs boson is highly sensitive to the couplings to all particles through quantum corrections, such that the entire mass spectrum requires an extensive fine-tuning.

The absence of significant amounts of antimatter in the solar system, direct probes in the form of cosmic rays as well as lacking γ-rays from annihilation processes in other parts of the universe show that the matter-antimatter symmetry is clearly broken in our matter dominated universe [133, 134]. Assuming that the big-bang led to equal amounts of matter and antimatter, Sakharov [135] pointed out that such a baryon-antibaryon asymmetry requires the violation of CP invariance. While the CP symmetry is indeed broken in the Standard Model via the Kobayashi-Maskawa (KM) mechanism [136] which requires at least three generations of matter fields, the amount of CP violation is several orders of magnitude smaller than necessary to explain the observed asymmetry [36].

The observation of rotational curves of galaxies [137] and measurements of the cosmic microwave background (CMB) temperature and lensing-potential power spectra [138] show that baryonic matter accounts for only about 15% of the total matter density in the universe, which in turn accounts for only about 30% of the overall energy density [36]. Only around 1% of the non-baryonic matter content of the universe is known to consist of SM neutrinos. 99% of the non-baryonic matter content is unknown and referred to as Dark Matter (DM) which interacts only via gravity and weak interaction and cannot emit electromagnetic radiation. Dark energy constitutes the remaining 70% of the energy density and is responsible for the accelerating expansion of the universe observed in multiple cosmological measurements of supernovae, baryon acoustic oscillations, weak gravitational lensing and galaxy clusters [139].

Supersymmetry (SUSY) [37–39] aims to solve the hierarchy problem by extending the Poincaré algebra with a symmetry that does not commute with Lorentz transformations and thus relates particles with different spin, turning fermions into bosons and vice versa. The lightest supersymmetric particle (LSP) is stable, interacts only weakly with very small cross sections like neutrinos, and is thus a natural candidate for dark matter.

Most strikingly, the Standard Model does not contain gravity, all attempts to unify quantum field theory and gravity result in non-renormalisable theories and do not yet yield satisfactory results, pointing to new physics at high energy scales.

String Theory [40–42], first proposed as a theory of strong interactions, is a possible candidate of quantum gravity without any free parameters. In String Theory, elementary particles including the graviton are one dimensional strings instead of point-like objects, living in a space-time with more than 4 dimensions, where additional space-time dimensions are compactified.

Many more models aim to answer some of these open questions and to extend the SM. In the following, a small selection of beyond the Standard Model (BSM) models that impact the $t\bar{t}j$ production and may affect the charge asymmetry is presented in more detail.

2.4.2. BSM models and $t\bar{t}j$ production

Heavy-coloured resonances

Massive colour-octet vector bosons can emerge from an enlarged gauge symmetry group $\mathrm{SU(3)_L} \times \mathrm{SU(3)_R}$ in models with chiral colour [140], topcolour [141], or from Kaluza-Klein excitations of the gluon in theories with compactified extra dimensions [142]. Massive colour-octet states are predicted to have large effects on the charge asymmetry and on the cross section in $t\bar{t}j$ production [76, 78, 143].

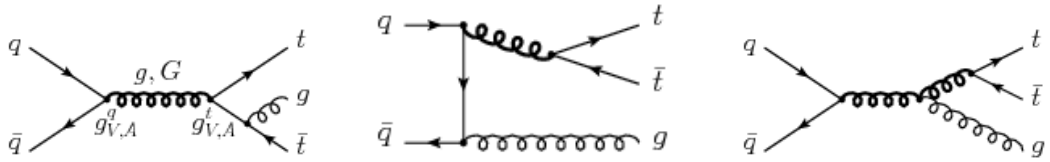

Figure 2.24.: Leading contributions from heavy colour-octet vector bosons (bold curled lines) to the process $q\bar{q} \to t\bar{t}g$. Diagrams for $qg \to t\bar{t}q$ are obtained by substituting $\bar{q} \leftrightarrow g$. [76]

The leading-order contributions to the $q\bar{q} \to t\bar{t}g$ and $qg \to t\bar{t}q$ processes are shown in figure 2.24. In ISR-FSR interference, massive gluons with pure vector couplings generate the charge asymmetry via antisymmetric interference amplitudes with a symmetric colour structure in the same way as gluons in the SM. Massive colour octets with axial-vector couplings generate the asymmetry either with the same mechanism via an antisymmetric amplitude when interacting with itself or via a symmetric amplitude and the antisymmetric colour structure when interacting with the SM gluon or the massive colour octet with vector couplings. Further contributions to the charge asymmetry occur for all remaining combinations of histograms in figure 2.24 via vector-axial-vector interference. The full list of contributions can be found in reference [76].

Top flavour violating resonances

Top flavour violating resonances as studied by Gresham, Kim and Zurek [77] are predicted to be produced in conjunction with another (oppositely charged) top quark and to decay directly into a top or antitop quark and a jet, resulting in a tj or $\bar{t}j$ resonance in $t\bar{t}j$ events. These states have large $\mathcal{O}(1)$ couplings to the top sector and can be very light such that they are expected to be abundantly produced.

Figure 2.25 shows possible leading order $t\bar{t}$ diagrams for $t\bar{t}$ and single-top production involving a top flavour violating resonance M. The new gauge bosons W' and Z' take a down quark to a top quark and an up quark to a top quark, respectively, and the colour triplets or sextets ϕ^a couple up quarks to antitop quarks.

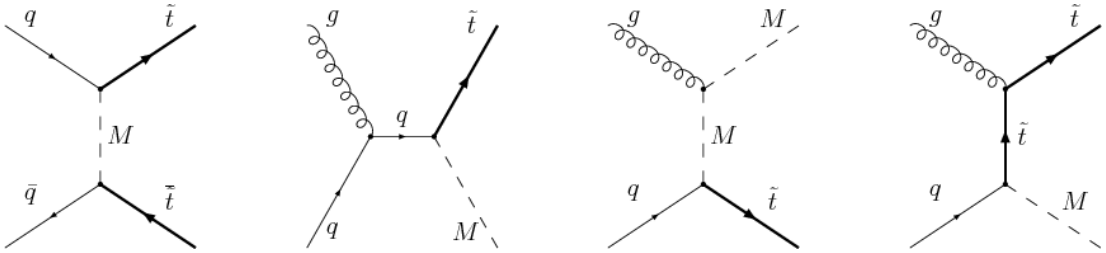

(a) $t\bar{t}$ production (b) s-channel (c) u-channel (d) t-channel

Figure 2.25.: Leading order $t\bar{t}$ production involving a flavour violating mediator M (a) and single M production (b)-(d). $\tilde{t}$ corresponds to the top quark for $M = W', Z'$ and to the antitop quark for $M = \phi^a$. [77]

Axigluons

The chiral colour model first introduced by Frampton and Glashow [140] in 1987 provides an alternative to the Standard Model which is based on the internal symmetry group $\mathrm{SU(3)_L} \times \mathrm{SU(3)_R} \times \mathrm{SU(2)_L} \times \mathrm{U(1)_Y}$ where chiral fermions transform under one or both SU(3) factors. The Higgs mechanism breaks both the chiral colour $\mathrm{SU(3)_L} \times \mathrm{SU(3)_R} \to \mathrm{SU(3)_C}$ and the electroweak $\mathrm{SU(2)_L} \times \mathrm{U(1)_Y} \to \mathrm{U(1)_{EM}}$ gauge groups. This model predicts the existence of an octet of massive coloured axigluons with axial-vector couplings to the SM quarks.

Alte, Berger and Spiesberger [79] investigated the impact of light axigluons in the mass range of 100–400 GeV on the incline, energy and rapidity asymmetries in $t\bar{t}j$ production at the LHC with a centre-of-mass energy of 14 TeV. They find large differences of up to 10%–20% in absolute terms with respect to the SM prediction for all three asymmetries. Particular large differences are found in the differential θ_j distributions, where the SM asymmetries tend to zero for $\theta_j \to 0, \pi$, but large asymmetries appear in the SM extension with axigluons.

Figure 2.26 shows exemplary Feynman diagrams contributing to the partonic processes $q\bar{q} \to t\bar{t}g$ and $qg \to t\bar{t}q$. The predicted impact of axigluons with a mass of $m_A = 400\,\mathrm{GeV}$ on the energy asymmetry is illustrated in figure 2.27.

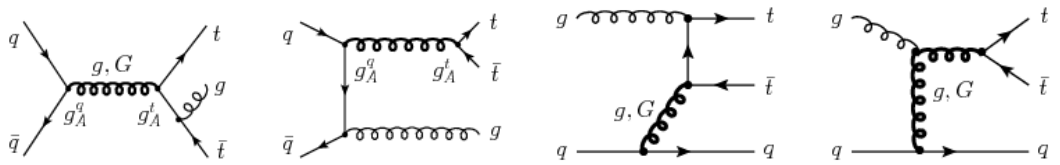

Figure 2.26.: Exemplary Feynman diagrams contributing to the partonic process in the $q\bar{q} \to t\bar{t}g$ and $qg \to t\bar{t}q$ channels in the SM extension with light axigluons. [79]

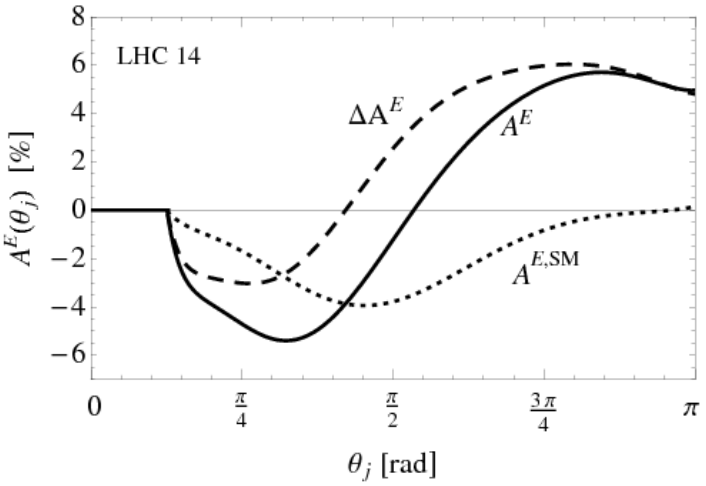

Figure 2.27.: Energy asymmetry as a function of θ_j at the LHC with $\sqrt{s} = 14\,\text{TeV}$ for the SM prediction and a BSM axigluon model with mass $m_A = 400\,\text{GeV}$, an effective coupling to quarks $\alpha_A = g_A^q g_A^t/(4\pi) = 0.032$, and width $\Gamma_A = 40\,\text{GeV}$. The dotted line is the SM prediction and the solid line is the BSM prediction. The dashed line is the difference of the two predictions. Kinematic cuts of $|y_{t\bar{t}j}| \geq 1$ and $|\Delta E| \geq 25\,\text{GeV}$ have been applied. [79]

2.4.3. Standard Model Effective Field Theory

Effective field theories (EFTs) provide a way to compute experimentally measurable quantities without knowing the exact theory in a systematic expansion. In many cases an EFT is the low-energy limit of a more fundamental theory. The Fermi Theory of weak interactions [144] is an example for an EFT at energies below the W- and Z-boson masses. Figure 2.28 shows the leading order Feynman diagrams for the nuclear β decay, in which a neutron decays into a proton, electron and antineutrino in the electroweak theory and in the Fermi Theory, where the W boson and its interactions are replaced by a four-fermion interaction illustrated with a blob.

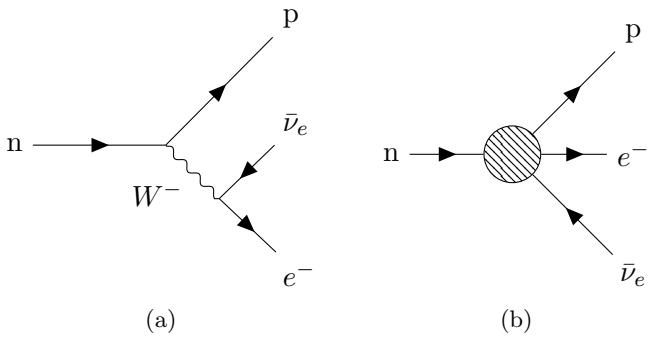

Figure 2.28.: Feynman diagram for the nuclear β decay in the electroweak theory (a) and in the effective Fermi Theory (b). The blob denotes an interaction between four fermions.

The Standard Model Effective Field Theory (SMEFT) is an EFT constructed out of SM fields including the Higgs field and provides a model-independent framework for new-physics interpretations. Extensions to the SM are assumed to involve massive particles heavier than the scale Λ, usually set to 1 TeV. The Lagrangian consists of a series of $\mathrm{SU(3)_C \times SU(2)_L \times U(1)_Y}$ invariant operators [82]:

$$\mathcal{L}_{\mathrm{SMEFT}} = \mathcal{L}_{\mathrm{SM}} + \mathcal{L}^{(5)} + \mathcal{L}^{(6)} + \mathcal{L}^{(7)} + \mathcal{L}^{(8)} + ..., \qquad \mathcal{L}^{(d)} = \sum_{i=1}^{n_d} \frac{C_i^{(d)}}{\Lambda^{d-4}} O^{(d)} \tag{2.42}$$

where $\mathcal{L}_{\mathrm{SM}}$ is the SM Lagrangian and the non-renormalisable higher-dimensional operators $O_i^{(d)}$ with Wilson coefficients $C_i^{(d)}$ are suppressed by Λ^{d-4}. At mass dimension five, there is only one operator which violates lepton-number and generates a Majorana mass term for left-handed neutrinos [80, 145]. At dimension-six, there are 59 independent operators [146]. The number of non-redundant operators increase rapidly for higher dimensions; there are 1542 dimension-seven operators [147], all of which violate either lepton or baryon number, and 44 807 dimension-eight operators. The dominant effects in the top-quark sector can be described by dimension-six operators [53].

This analysis focuses on non-CP violating extensions of the SM, implying real Wilson coefficients. Given that top-quark observables are largely insensitive to the flavour of light quarks, and thus assuming a $U(2)_q \times U(2)_u \times U(2)_d$ flavour symmetry among quarks of the first and second generation, left- and right-handed quarks are denoted by:

$$\begin{aligned} q_i &= (u_L^i, d_L^i), \qquad & u_i &= u_R^i,\, d_i = d_R^i, \qquad & i &= 1,2 \\ Q &= (t_L, b_L), \qquad & t &= t_R,\, b = b_R \end{aligned} \tag{2.43}$$

Under these assumptions, there are 15 independent operators in the so called Warsaw basis [146], the first non-redundant operator basis for $\mathcal{L}^{(6)}$, that affect $t\bar{t}$ and $t\bar{t}j$ production at tree level [75, 148]:

- 8 four-quark operators with Lorentz structures LL and RR,

$$\begin{aligned} O_{Qq}^{1,8} &= (\bar{Q}\gamma_\mu T^A Q)(\bar{q}_i \gamma^\mu T^A q_i), & O_{Qq}^{1,1} &= (\bar{Q}\gamma_\mu Q)(\bar{q}_i \gamma^\mu q_i), \\ O_{Qq}^{3,8} &= (\bar{Q}\gamma_\mu T^A \tau^I Q)(\bar{q}_i \gamma^\mu T^A \tau^I q_i), & O_{Qq}^{3,1} &= (\bar{Q}\gamma_\mu \tau^I Q)(\bar{q}_i \gamma^\mu \tau^I q_i), \\ O_{tu}^{8} &= (\bar{t}\gamma_\mu T^A t)(\bar{u}_i \gamma^\mu T^A u_i), & O_{tu}^{1} &= (\bar{t}\gamma_\mu t)(\bar{u}_i \gamma^\mu u_i), \\ O_{td}^{8} &= (\bar{t}\gamma^\mu T^A t)(\bar{d}_i \gamma_\mu T^A d_i), & O_{td}^{1} &= (\bar{t}\gamma^\mu t)(\bar{d}_i \gamma_\mu d_i) \end{aligned} \tag{2.44}$$

- 6 four-quark operators with Lorentz structures LR and RL,

$$\begin{aligned} O_{Qu}^{8} &= (\bar{Q}\gamma^\mu T^A Q)(\bar{u}_i \gamma_\mu T^A u_i), & O_{Qu}^{1} &= (\bar{Q}\gamma^\mu Q)(\bar{u}_i \gamma_\mu u_i), \\ O_{Qd}^{8} &= (\bar{Q}\gamma^\mu T^A Q)(\bar{d}_i \gamma_\mu T^A d_i), & O_{Qd}^{1} &= (\bar{Q}\gamma^\mu Q)(\bar{d}_i \gamma_\mu d_i), \\ O_{tq}^{8} &= (\bar{q}_i \gamma^\mu T^A q_i)(\bar{t}\gamma_\mu T^A t), & O_{tq}^{1} &= (\bar{q}_i \gamma^\mu q_i)(\bar{t}\gamma_\mu t) \end{aligned} \tag{2.45}$$

- 1 tensor operator that modifies the top-gluon interaction,

$$^{\ddagger}O_{tG} = (\bar{Q}\sigma^{\mu\nu} T^A t)\, \widetilde{\phi}\, G_{\mu\nu}^A \tag{2.46}$$

This analysis focuses on the following six operators, yielding a complete set of chiralities (LL, RR, LR), both for colour singlet and octet operators:

$$O_{Qq}^{1,1}, O_{Qq}^{1,8}, O_{tq}^{1}, O_{tq}^{8}, O_{tu}^{1}, O_{tu}^{8}$$

with corresponding Wilson coefficients denoted by $C_{Qq}^{1,1}$, $C_{Qq}^{1,8}$, C_{tq}^{1}, C_{tq}^{8}, C_{tu}^{1} and C_{tu}^{8}, respectively. In the following, the notations $C_{Qq}^{1,1}$ and C_{Qq}^{11} as well as $C_{Qq}^{1,8}$ and C_{Qq}^{18} are used interchangeably.

The remaining operators differ by their weak gauge structure and/or light quark flavour which would affect the energy asymmetry very similarly. The flavour of the initial quarks, for instance, can be resolved in $t\bar{t}Z$ or $t\bar{t}W$ production in a global analysis [53].

The contributions from four-quark operators can be classified in terms of vector V and axial-vector A currents, which are odd (V) and even (A) under top-quark charge conjugation. The vector and axial-vector combinations for colour-octet operators are defined as [53]:

$$\begin{aligned}
4\,C_{VV}^{u,8} &= C_{Qq}^{1,8} + C_{Qq}^{3,8} + C_{tu}^{8} + C_{tq}^{8} + C_{Qu}^{8} \\
4\,C_{AA}^{u,8} &= C_{Qq}^{1,8} + C_{Qq}^{3,8} + C_{tu}^{8} - C_{tq}^{8} - C_{Qu}^{8} \\
4\,C_{AV}^{u,8} &= -\big(C_{Qq}^{1,8} + C_{Qq}^{3,8}\big) + C_{tu}^{8} + C_{tq}^{8} - C_{Qu}^{8} \\
4\,C_{VA}^{u,8} &= -\big(C_{Qq}^{1,8} + C_{Qq}^{3,8}\big) + C_{tu}^{8} - C_{tq}^{8} + C_{Qu}^{8}
\end{aligned} \tag{2.47}$$

where replacing the index $u \to d$ yields the corresponding combinations for operators with down quarks. The same relations are defined for colour-singlet operators by changing the index $8 \to 1$. A list of all combinations of four-quark operator coefficients that contribute to $t\bar{t}$ and $t\bar{t}j$ production can be found in [75].

Figure 2.29 shows exemplary Feynman diagrams generating the energy asymmetry through initial-state radiation (ISR-ISR) and through the interference of initial- and final-state radiation (ISR-FSR). Charge asymmetric contributions are generated either from an asymmetric Lorentz structure or an asymmetric colour structure of the corresponding matrix elements [76]. In SM QCD, the charge asymmetry is induced from ISR-FSR interferences with an asymmetric Lorentz structure and a colour structure that splits into a symmetric and an asymmetric part. Both the ISR-ISR and FSR-FSR interferences have symmetric Lorentz and colour structures and thus do not contribute to the charge asymmetry [58, 149].

In SMEFT, operator insertions with axial-vector currents can change the Lorentz structure of the ISR-ISR and FSR-FSR matrix elements, for instance via C_{AA}–SM or C_{AA}–C_{VV} interference, and thus induce additional charge asymmetric contributions. In ISR-FSR interference, the charge asymmetry can be generated from vector operators that preserve the asymmetric Lorentz structure, like C_{VV}–C_{VV} interference, or from axial-vector operators with a symmetric Lorentz structure in combination with an asymmetric colour structure, like C_{VV}–C_{AA} interference.

Cross sections for scattering processes can be calculated from the absolute square of the amplitude as described in section 2.1.2. Neglecting flavour violating dimension-five and dimension-seven terms, the Lagrangian of eq. 2.42 leads to an amplitude of the following form [150]:

$$\mathcal{A} \propto A_{\mathrm{SM}} + \frac{A^{(6)}}{\Lambda^2} + \frac{A^{(8)}}{\Lambda^4} + ... \tag{2.48}$$

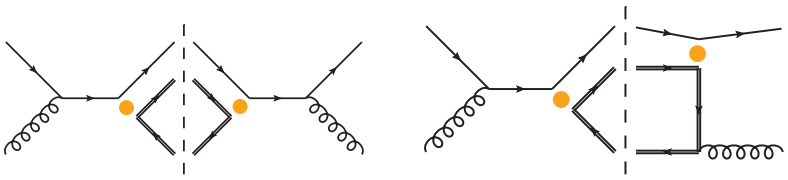

Figure 2.29.: Exemplary Feynman diagrams generating the energy asymmetry through initial-state radiation (ISR-ISR) and through the interference of initial- and final-state radiation (ISR-FSR). Orange dots denote the insertion of a four-quark operator or a gluon, the dashed lines symbolise the interference for the two $gq \to t\bar{t}q$ amplitudes. [75]

where A_{SM} is the SM amplitude and $A^{(6)}$ and $A^{(8)}$ are corrections from dimension-six and dimension-eight operator contributions, respectively. Up to $\mathcal{O}(\Lambda^{-4})$, the squared amplitude contains elements of the following form:

$$|\mathcal{A}|^2 \propto |A_{\mathrm{SM}}|^2 + \frac{A_{\mathrm{SM}} \times A^{(6)}}{\Lambda^2} + \frac{|A^{(6)}|^2}{\Lambda^4} + \frac{A_{\mathrm{SM}} \times A^{(8)}}{\Lambda^4} + \ldots \tag{2.49}$$

where $A \times B = A^\star B + A B^\star$ denote the interference terms between A and B. Considering only dimension-six operators, the cross sections and asymmetries can be written as [75]:

$$\begin{aligned} \sigma &= \sigma_S^{\mathrm{SM}} + \sum_k C_k \sigma_S^k + \sum_{k \le l} C_k C_l \, \sigma_S^{kl} \\ A &= \frac{\sigma_A}{\sigma_S} = \frac{\sigma_A^{\mathrm{SM}} + \sum_k C_k \sigma_A^k + \sum_{k \le l} C_k C_l \, \sigma_A^{kl}}{\sigma_S^{\mathrm{SM}} + \sum_k C_k \sigma_S^k + \sum_{k \le l} C_k C_l \, \sigma_S^{kl}} \end{aligned} \tag{2.50}$$

with Wilson coefficients C_k, C_l in units of $\Lambda^{-2} = 1\,\mathrm{TeV}^{-2}$ and charge-symmetric σ_S^{SM} and -asymmetric σ_A^{SM} cross sections in the Standard Model. The cross sections $\sigma_{S,A}^k$ and $\sigma_{S,A}^{kl}$ correspond to the $A_{\mathrm{SM}} \times A^{(6)}$ and $|A^{(6)}|^2$ interference terms, respectively.

Figures 2.30 and 2.31 show the predicted inclusive energy and rapidity asymmetries as well as the differential energy asymmetry, respectively, as functions of a single Wilson coefficient. The rapidity asymmetry was calculated from the SM prediction at NNLO including electroweak corrections [151] with operator contributions at NLO [152]. The energy asymmetry was simulated at the particle level as described in section 6.2.2 with the event selection explained in chapter 5. The dependencies of the asymmetries vary for different coefficients and between the differential bins illustrating the necessity for simultaneous fits as performed in chapter 10.

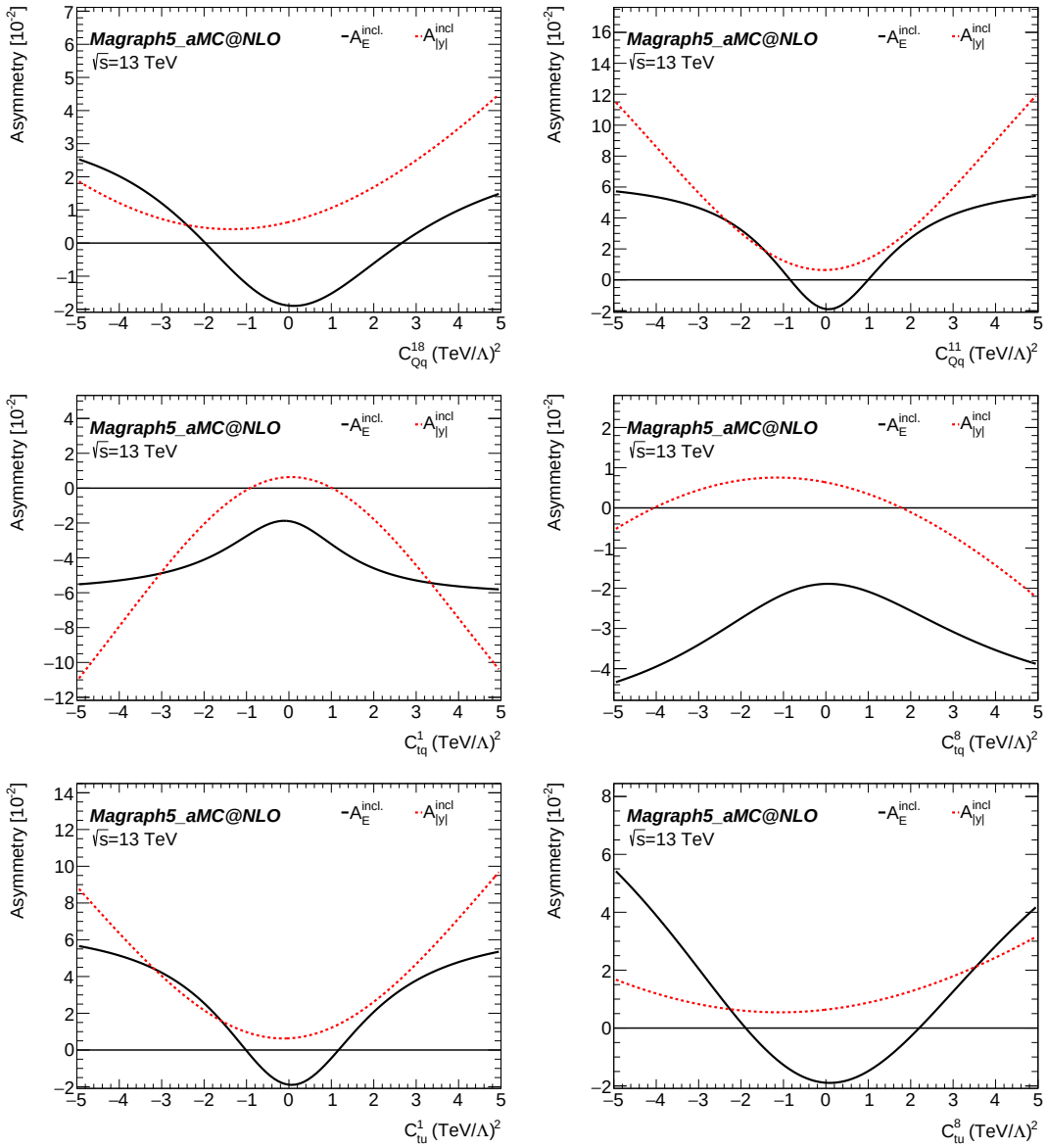

Figure 2.30.: Evolution of the inclusive energy and rapidity asymmetries, $A_E^{\text{incl.}}$ and $A_C^{\text{incl.}}$, as a function of a single Wilson coefficient, with all other coefficients being fixed at 0. The rapidity asymmetry was calculated from the SM prediction at NNLO with electroweak corrections [151] and operator contributions at NLO [152]. The energy asymmetry was simulated at the particle level with MADGRAPH 5 as described in section 6.2.2 with the event selection explained in chapter 5.

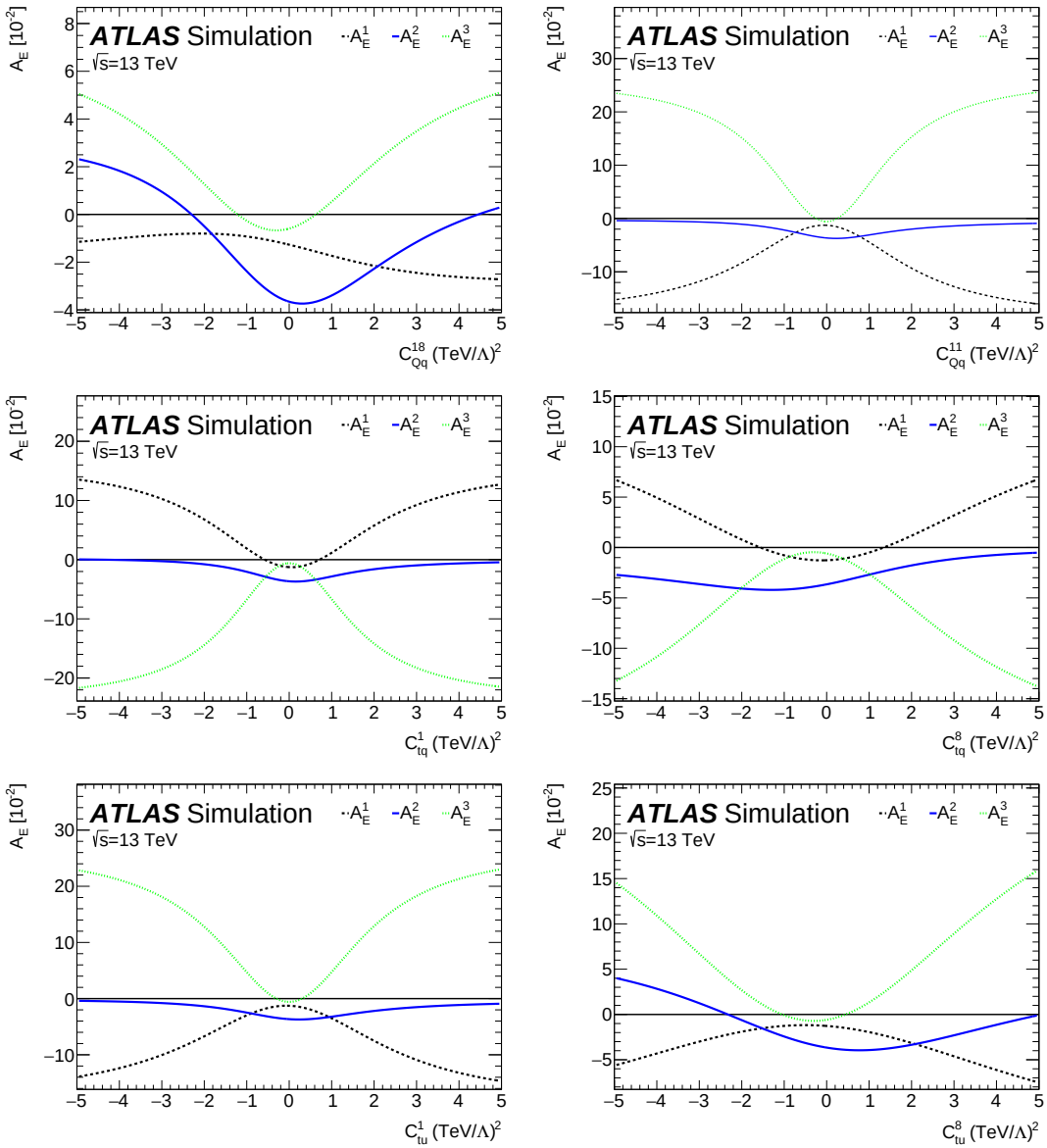

Figure 2.31.: Evolution of the energy asymmetry in three differential θ_j bins, $[0, \pi/4, 3\pi/5, \pi]$, as a function of a single Wilson coefficient, with all other coefficients being fixed at 0. The energy asymmetry was simulated at the particle level using MADGRAPH 5 as described in section 6.2.2 with the event selection explained in chapter 5. This figure was published as figure 8 in reference [83].

3. The Large Hadron Collider and ATLAS

CERN, the European Organization for Nuclear Research or "Conseil Européen pour la Recherche Nucléaire", was founded in 1954 with the goal to establish a world-class fundamental physics research organisation [153]. Today, CERN has 23 member states, about 2 600 staff members and around 12 500 visiting scientists from over 600 institutes and universities around the world from over 70 countries [154, 155].

Section 3.1 gives an overview of the Large Hadron Collider (LHC), the world's largest and most powerful particle accelerator, which provides the high energy proton beams for ATLAS [156], CMS [157], ALICE [158], LHCb [159] and further smaller experiments. The ATLAS detector, one of the two multi-purpose detectors at the LHC, and its components most relevant for this analysis are described in section 3.2. The simulation of signal and background samples used to interpret the observed data is described in section 3.3.

3.1. The Large Hadron Collider

The Large Hadron Collider (LHC) [160], a two-ring superconducting hadron accelerator and collider, was designed to accelerate and collide protons and lead ions with centre-of-mass energies of up to 14 TeV and 1 150 TeV, respectively. Its construction started in 2000 in the 26.7 km long tunnel 45 m to 170 m below the surface, originally hosting the Large Electron-Positron Collider (LEP) [161] machine between 1984 and 1989. The first beam was successfully guided around the accelerator in September 2008 [162].

Starting from a bottle of hydrogen gas the protons are obtained by ionisation and accelerated to an energy of 50 GeV in the Linear Accelerator (LINAC2), followed by acceleration in the Proton Synchrotron Booster (PBS), the Proton Synchrotron (PS), and the Super Proton Synchrotron (SPS) to an energy of 450 GeV before they eventually enter the two beam pipes of the LHC. In the LHC, the protons are further accelerated in superconducting cavities via electromagnetic resonators to a maximum of 7 TeV per beam, running parallel but in opposite direction, yielding a centre-of-mass energy at the collision points of up to 14 TeV.

The protons are kept on the circular trajectory with magnetic fields of 8.3 Tesla, generated by superconducting dipole magnets at a temperature below 2 K, cooled down with superfluid helium. Quadruople mangnets are used to focus the beam vertically or horizontally, compensating the repulsion between the protons, and thus increasing the intensity.

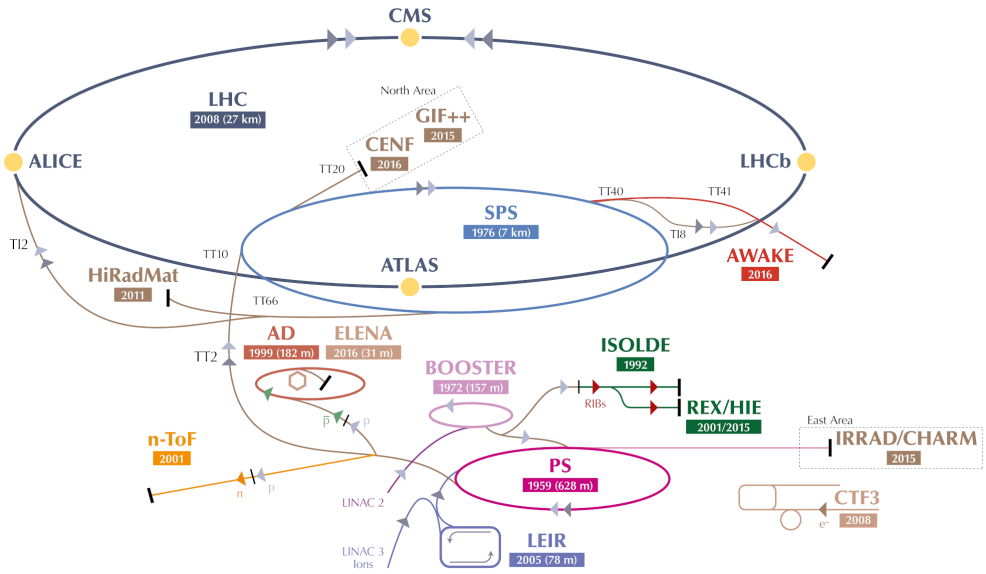

Figure 3.1.: Schematic layout of the CERN accelerator complex, including LINAC2, BOOSTER, PS and SPS which are used as pre-accelerators for the LHC. [163]

An overview of the CERN accelerator complex is shown in figure 3.1. The four largest experiments are located in big caverns at the four crossing points. ATLAS [156] (A Toroidal LHC ApparatuS) and CMS [157] (Compact Muon Solenoid) are independently designed general-purpose detectors for a large range of physics including precision measurements of the Standard Model and the search for BSM physics. ALICE [158] (A Large Ion Collider Experiment) and LHCb [159] (Large Hadron Collider Beauty) have detectors specialised for focusing on specific phenomena like strongly interacting matter and precision measurements of CP violation and rare b-hadron decays, respectively. The smaller experiments TOTEM [164] and LHCf [165] focus on the forward region of LHC collisions with detectors positioned on either side of the CMS and ATLAS interaction points. The TOTEM experiment measures the total pp cross section to understand and study the proton structure, while LHCf measures neutral particles to provide data for hadron interaction model calibration that is used in the study of cosmic rays. The MOEDAL [166] experiment is searching for hypothetical particles with magnetic charge, so called magnetic monopoles, and highly ionising stable or pseudo-stable massive particles (SMPs).

Assuming a Gaussian beam distribution and N_b particles per bunch and n_b bunches per beam, the instantaneous luminosity in eq. 2.32 can be written as [160]:

$$L = \frac{N_b^2 n_b f_{\text{rev}} \gamma_r}{4\pi \epsilon_n \beta^\star} F \tag{3.1}$$

where f_{rev} is the revolution frequency, γ_r the relativistic gamma factor, ϵ_n the normalised transverse beam emittance, corresponding to the bunch area, and $\beta^\star$ the beta function at the collision point. F is a geometric correction factor due to the crossing angle at the interaction point. The rate and number of scattered events are given by equations 2.30 and 2.31, respectively.

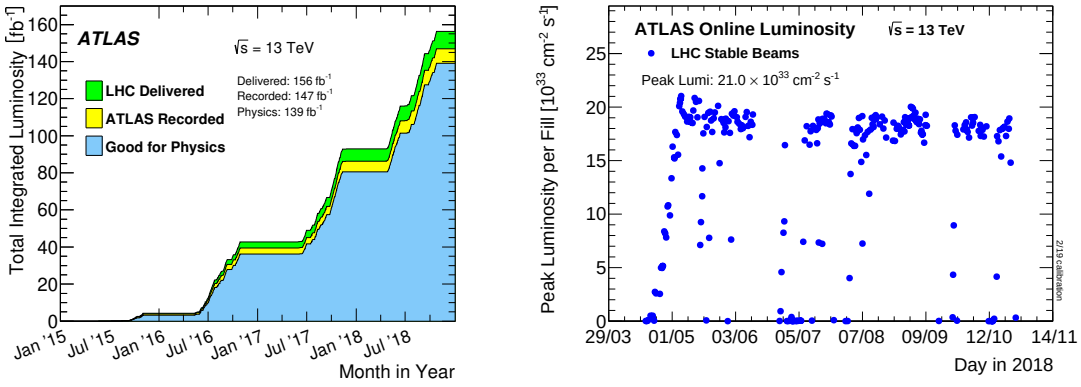

Figure 3.2.: Total integrated luminosity versus time delivered to ATLAS, recorded and certified to be good quality data [168] (left) and the peak instantaneous luminosity delivered to ATLAS in 2018 [169] (right).

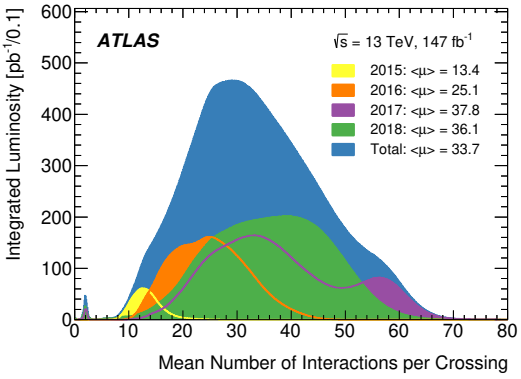

Figure 3.3.: Luminosity weighted distribution of the mean number of interactions per bunch crossing in the ATLAS detector during the data-taking periods of Run 2. [168]

During the 2015–2018 data-taking period called "Run 2" [167] each of the two beams consisted of up to 2 544 bunches containing about $1.1 \cdot 10^{11}$ protons each with a bunch spacing of 25 ns and a revolution frequency of $f_{\text{rev}} = 11\,246\,\text{Hz}$. The beta function varied between 0.25 m to 0.8 m.

The total integrated luminosity versus time delivered to ATLAS, recorded and certified to be good quality data and the peak instantaneous luminosity delivered to ATLAS in 2018 are shown in figure 3.2. 95.6% of the recorded proton-proton collision data collected at $\sqrt{s} = 13\,\text{TeV}$ was certified to be of good quality for physics analysis [168].

While a large number of protons per bunch and a high revolution frequency increase the luminosity and thus the event yield, they also increase the probability for multiple proton-proton interactions to occur within each bunch crossing (in-time pile-up) and additional proton-proton collisions occurring in bunch crossings just before or after the collision of interest (out-of-time pile-up) [170]. The average number of such simultaneous interactions (pile-up) was on average 33.7 in Run 2; their distribution in the years 2015–2018 are shown in figure 3.3.

3.2. The ATLAS experiment

The ATLAS [156] detector is a forward-backward symmetric general purpose detector facilitating precision measurements of the SM as well as searches for new physics beyond the SM. With a height of 25 m, a length of 44 m and a weight of roughly 7 000 tonnes it is the largest detector at CERN. Its cylindrical layout allows for a coverage of almost the entire solid angle around the interaction point. A schematic view of the ATLAS detector and the main detector components is shown in figure 3.4.

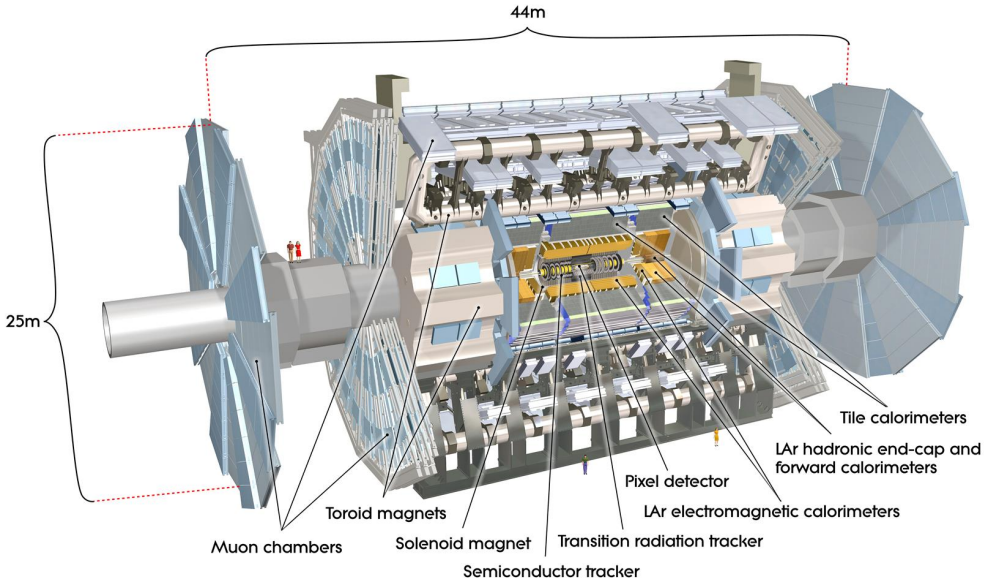

Figure 3.4.: Schematic view of the ATLAS detector showing the main detector components; Inner Detector (ID) immersed in a 2 Tesla solenoidal magnetic field consisting of the pixel detector, the Semi-Conductor (SCT) and the Transition Radiation Tracker (TRT); Electromagnetic (ECAL) and hadronic (HCAL) calorimeters; Muon chambers embedded in a toroidal magnetic field. [171]

The momenta of charged particles are obtained from the curvature of their tracks in the inner detector (ID), contained in a 2 Tesla solenoidal magnetic field. The surrounding electromagnetic (ECAL) and hadronic (HCAL) calorimeters measure the energy of electrons, photons and hadrons destructively. Muons are identified by their signature in the outer muon spectrometers, embedded in a toroidal magnetic field. Neutrinos traverse the detector without leaving any trace. The patterns of energy deposits in the ATLAS detector are shown in figure 3.5. This analyses selects electrons, muons and jets and thus utilises all parts of the detector in the central $|\eta|$ region; see chapter 5 for details on the the event selection.

The ATLAS coordinate system is explained in section 3.2.1. Sections 3.2.2 to 3.2.4 describe the inner detector, the calorimeters and the muon system. The trigger and data acquisition system is outlined in section 3.2.5.

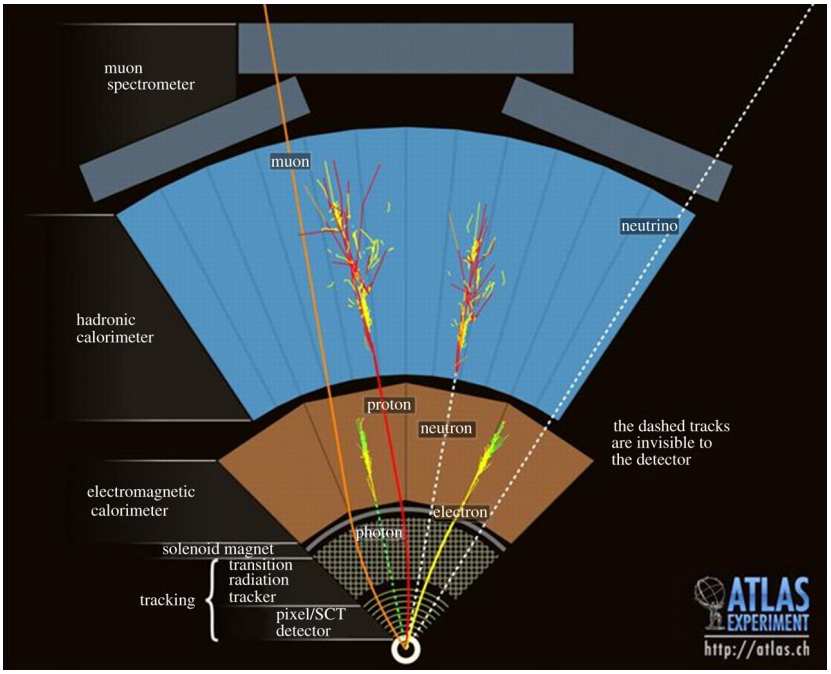

Figure 3.5.: Patterns of energy deposits of photons, electrons, protons, neutrinos and myons in the ATLAS detector. Neutrinos traverse the detector material without leaving any trace. [172]

3.2.1. ATLAS coordinate system

The trajectories of the particles emerging from the pp collisions are parametrised by spherical coordinates with the interaction point as origin [156] as illustrated in figure 3.6. The z-axis is aligned with the beam direction, the x-y-plane is transverse to the beam direction with the x-axis pointing towards the centre of the LHC ring and the y-axis pointing upwards. The azimuthal angle is defined as the angle in the x-y-plane and the polar angle θ as the angle with the beam axis.

The rapidity y is defined as:

$$y = \frac{1}{2} \ln \left(\frac{E + p_z}{E - p_z} \right) \tag{3.2}$$

As the difference of rapidities y_a and y_b is Lorentz invariant under boosts along the beam direction, a Lorentz invariant angular distance measure is given by $\Delta R_y = \sqrt{\Delta y^2 + \Delta \phi^2}$ with $\Delta y = y_a - y_b$ and $\Delta \phi = \phi_a - \phi_b$. The pseudorapidity η, defined as

$$\eta = -\ln \left(\tan \frac{\theta}{2} \right) \tag{3.3}$$

converges to the rapidity for $m \to 0$. Figure 3.7 illustrates the relationship between η and θ. The pseudorapidity is zero for $\theta = \pi/2$ and approaches $\pm\infty$ for $\theta \to 0$ and $\theta \to \pi$. The distance measure ΔR in the pseudorapidity-azimuthal angle space is defined as:

$$\Delta R = \sqrt{\Delta \eta^2 + \Delta \phi^2} \tag{3.4}$$

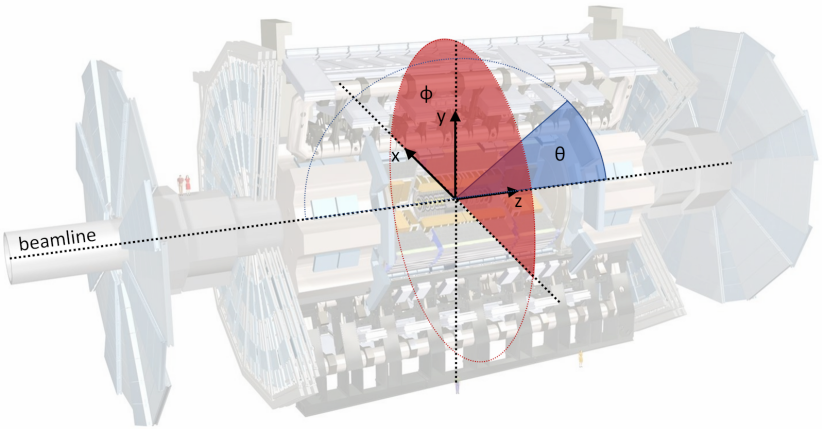

Figure 3.6.: Geometry of the ATLAS detector with Cartesian coordinates x, y and z. Particle tracks are parametrized by the spherical coordinates $\theta \in [0, \pi]$ defined in the R-z-plane and $\phi \in (-\pi, \pi]$ defined in the x-y-plane. Based on reference [171].

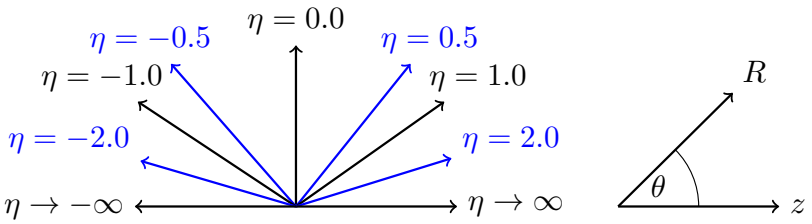

Figure 3.7.: Definition of the pseudorapidity η in the R-z-plane. The pseudorapidity is zero for $\theta = \pi/2$ and approaches $\pm\infty$ for $\theta \to 0$ and $\theta \to \pi$, respectively.

The transverse momentum p_T and the transverse energy E_T are defined in the $x-y$-plane transverse to the beam axis:

$$p_T = \sqrt{p_x^2 + p_y^2}, \quad E_T = \sqrt{E_x^2 + E_y^2} \tag{3.5}$$

3.2.2. Inner detector

Immersed in a 2 Tesla solenoidal magnetic field, the Inner Detector (ID) [156, 173], measures tracks of charged particles through their energy loss by ionization, aiming at excellent momentum resolution and primary and secondary vertex measurements important for electron and b-jet identification.

The Inner Detector (ID) consists of two precision tracking detectors, the pixel detector [174–176] and the Semiconductor Tracker (SCT) [156, 177], covering the region $|\eta| < 2.5$ at lower radii, and the Transition Radiation Tracker (TRT) [178, 179] covering the region up to $|\eta| < 2.0$ at higher radii as shown in figures 3.8 and 3.9. The pixel detector is mainly responsible for accurate vertex measurements and consists of 4 cylindrical barrel layers with a total of 79.2 million silicon pixel sensors and 3 forward and backward end-cap disk layers with a total of 13.2 million pixels. The SCT, focusing on precise momenta measurements, consists of 15 912 micro-strip sensors arranged in 4 cylindrical layers in the barrel and 2 x 9 disks in the end-caps. The TRT consists of 73

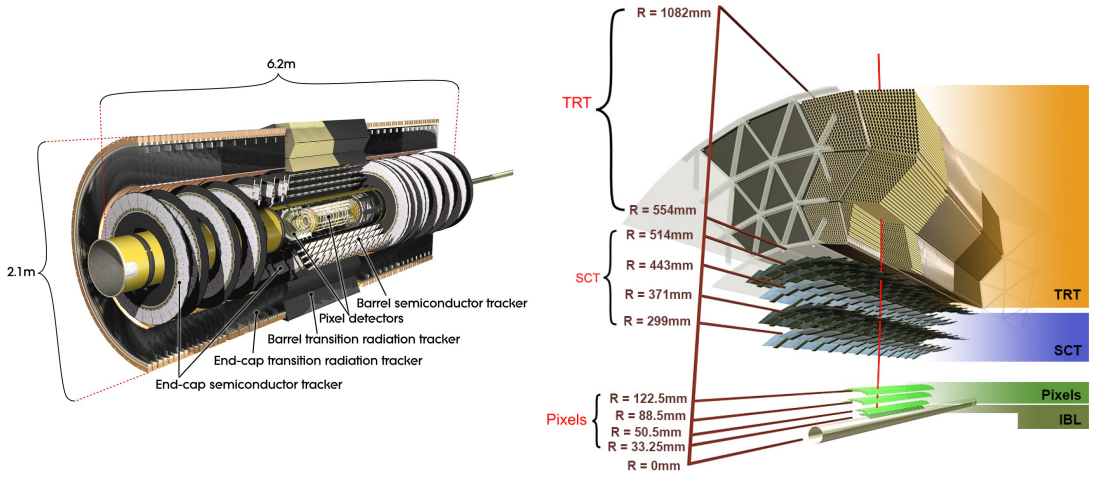

Figure 3.8.: Schematic view of the ATLAS inner detector (ID) in a cut-away view (left) [181] and sensors and structural elements of the inner detector in the central barrel region (right) [175], consisting of a 4-layer pixel detector, traversed by a charged track (red line) with a transverse momentum of 10 GeV.

layers of straws interleaved with fibres in the barrel and 160 straw planes interleaved with foils in the end-cap, filled with a $Xe/CO_2/O_2$ gas mixture. The TRT allows for continuous tracking with an average of 36 hits per track and discrimination between electrons and charged hadrons through the detection of transition radiation photons.

The intrinsic resolutions are limited by the finite resolution of the detector elements and positioning accuracy [180]. The IBL and pixel detectors have intrinsic resolutions of $8\,\mu\text{m} \times 40\,\mu\text{m}$ and $10\,\mu\text{m} \times 115\,\mu\text{m}$ along r-$\phi \times z$, respectively. The intrinsic resolutions of the SCT and TRT detectors along z are $40\,\mu\text{m}$ and $115\,\mu\text{m}$, respectively.

The relative momentum resolution of the tracking detector at ATLAS for transverse momenta p_T in units of GeV is given by [156]:

$$\frac{\sigma_{p_T}}{p_T} = 0.05\%\ p_T \oplus 1\% \tag{3.6}$$

where $\oplus$ denotes the sum in quadrature. The term proportional to p_T comes from uncertainties on the curvature measurement of charged particles in a magnetic field and the constant term arises from multiple scatterings of the charged particles within the detector material [99].

3.2.3. Calorimeter system

The ATLAS calorimeter system [156] shown in figure 3.10 utilises electromagnetic (ECAL) and hadronic (HCAL) sandwich calorimeters with alternating layers of passive material, in which showers form, and active material, in which the shower particles are counted via ionisation or scintillation light [182]. Ideally, high energy photons and electrons are stopped inside the ECAL, while hadrons leave only small energy depositions in the ECAL and are eventually stopped inside the HCAL.

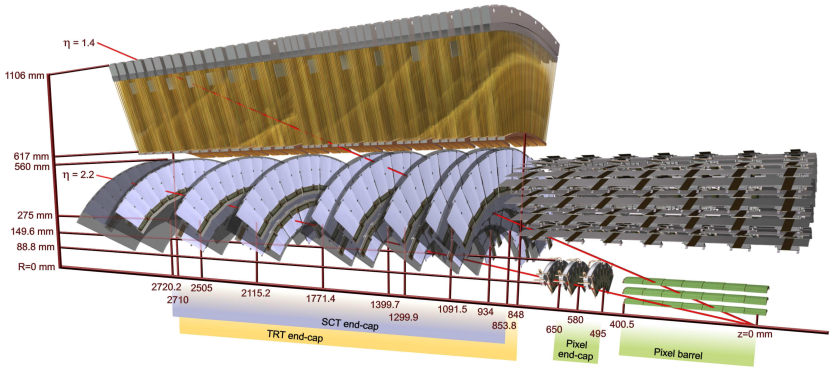

Figure 3.9.: Schematic view of the ATLAS end-cap inner detector consisting of three cylindrical silicon-pixel layers and nine SCT and TRT disks, traversed by two charged tracks (red lines) with a transverse momentum of 10 GeV at $\eta = 1.4$ and $\eta = 2.2$. [156]

The dominant processes by which photons and electrons loose their energy in the passive material are pair production and bremsstrahlung. The photons radiated by the electrons produce electron-positron pairs, which in turn radiate photons. The radiation length X_0 is defined as the length after which, on average, the energy of an electron has reduced to a fraction of $1/e$. Hadronic particles interact mainly strongly in the passive material via inelastic collisions with nuclei, spallation and evaporation. Photons from π^0 and η decays start electromagnetic showers. The interaction lengths λ defines the distance after which the probability of a hadron to survive has reduced to $1/e$.

The electromagnetic calorimeter uses liquid argon (LAr) as active and lead as passive material, providing full coverage in ϕ due to its accordion geometry. It consists of a barrel part ($|\eta| < 1.475$), two end-cap components (EMEC) ($1.375 < |\eta| < 3.2$) and a forward calorimter (FCal) covering the region $3.1 < |\eta| < 4.9$. The total thickness of the ECAL is larger then 22 and 24 radiation lengths (X_0) in the barrel and the end-caps, respectively.

The surrounding hadronic calorimeter utilises scintillator tiles as active and steel as passive material in the barrel region $0 < |\eta| < 1.7$. The Hadronic End-Cap (HEC) and Forward Calorimeters (FCal) extend the coverage up to $|\eta| < 4.9$ with liquid-argon as active and copper and tungsten as passive material. The HCAL has a total thickness of 11λ at $\eta = 0$.

The calorimeters are designed to yield energy resolutions for particles with an energy E in GeV of

$$\frac{\sigma_E}{E} = \frac{10\%}{\sqrt{E}} \oplus 0.7\%, \quad \frac{\sigma_E}{E} = \frac{50\%}{\sqrt{E}} \oplus 3\%, \quad \frac{\sigma_E}{E} = \frac{100\%}{\sqrt{E}} \oplus 10\% \tag{3.7}$$

in the ECAL, barrel/end-cap and the forward hadronic calorimeters, respectively [156]. The terms inversely proportional to $\sqrt{E}$ represent stochastic fluctuations in the shower and sampling fluctuations, while the constants correspond to detector non-uniformities and calibration uncertainties.

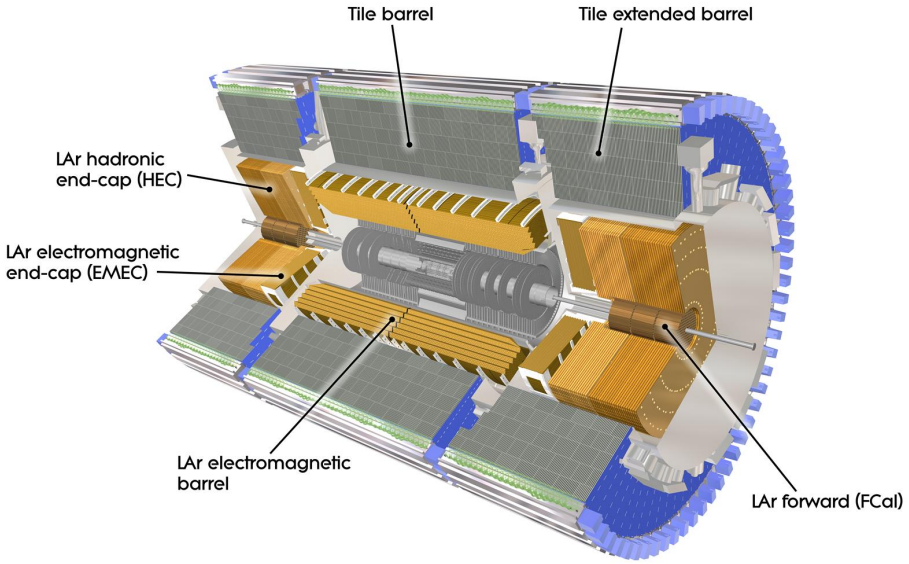

Figure 3.10.: Cut-away view of the ATLAS calorimeter system, consisting of electromagnetic caorimeters using liquid argon (LAr) as active and lead as absorber material and hadronic calorimeters using either steel/scintillator tiles or lead/LAr as absorber/instrumentation. [183]

3.2.4. Muon system

Muons lose their energy in matter predominantly through single collisions leading to ionisation and atomic or collective excitations. Bremsstrahlung, which is the dominant process for electrons, is proportional to the squared inverse mass and thus negligible for heavy charged particles below several hundred GeV of energy [182].

Since muons deposit only a small amount of energy inside the calorimeters, the Muon Spectrometer (MS) illustrated in figure 3.11 is the outermost part of the ATLAS detector such that electrons, photons and hadrons are contained within the calorimeters, but muons reach the MS. Monitored Drift Tubes (MDT) covering the range $|\eta| < 2.7$ and Cathode-Strip Chambers (CSC) within $2.0 < |\eta| < 2.7$ are mainly used for precision tracking, while Resistive Plate Chambers (RPC) and Thin Gap Chambers (TGC) ($1.05 < |\eta| < 2.7$) are mainly used for triggering.

The magnetic fields are generated by a large barrel toroid in the central region $|\eta| < 1.4$, two smaller end-cap magnets in the range $1.4 < |\eta| < 2.7$ and a combination of both in the transition region $1.4 < |\eta| < 1.6$.

The MS is designed to provide a momentum resolution better than 3% over a wide p_T range and of less than 10% for muons with $p_T \approx 1\,\text{TeV}$ [156, 184].

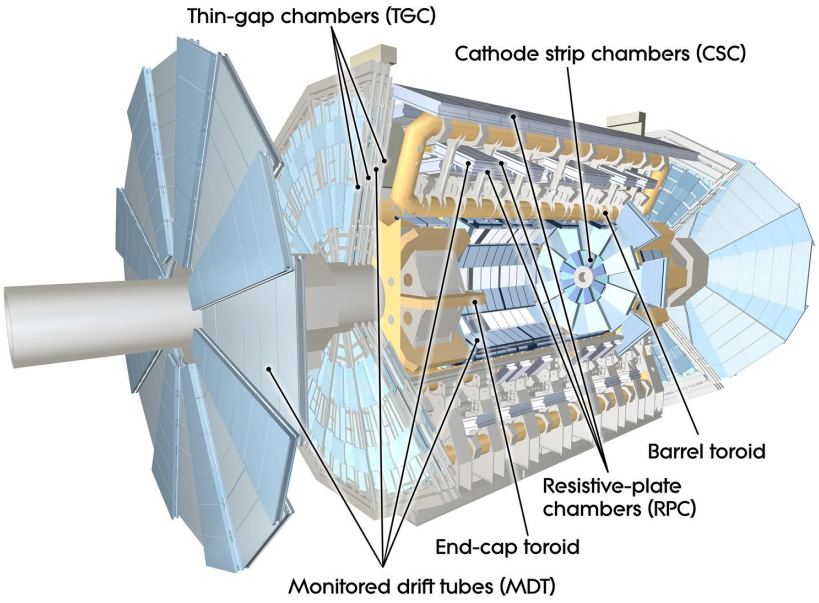

Figure 3.11.: Schematic view of the ATLAS Muon Spectrometer (MS) immersed in toroidal magnetic fields. Monitored Drift Tubes (MDT) and Cathode Strip Chambers (CSC) provide tracking information, Resistive Plate Chambers (RPC) and multi-wire Thin Gap Chambers (TGC) are used for bunch crossing identification. [185]

3.2.5. Trigger and data acquisition

With a storage requirement of about 1.6 MB per event and a collision rate of up to 40 MHz the amount of data generated is far too high for recording and offline processing and thus needs to be reduced, while maintaining a high selection efficiency for rare physics events.

The ATLAS Trigger and Data Acquisition system (TDAQ) [186, 187] shown in figure 3.12 reduces the output rate to about 100 kHz in the first-level hardware trigger (L1), limited by readout capabilities, and to $\approx 1\,000$ Hz, corresponding to 1.6 GB/s, in the high-Level software trigger (HLT), limited by offline processing capabilities. There are hundreds of trigger configurations tailored to physics analyses (primary triggers), efficiency and performance meausurements (support triggers), and detector calibrations (calibration triggers) considering physics objects like electrons, photons, taus, muons, jets, and missing transverse momentum. In this thesis, primary triggers for single electrons and muons are used.

The first-level trigger (L1), implemented in custom hardware, consists of the L1 calorimeter (L1Calo) and L1 muon (L1Muon) triggers as well as several other subsystems which send their output to the central trigger processor (CTP). Events accepted by the CTP are buffered in the read-out system (ROS) and processed by the high-Level software trigger (HLT).

The L1Calo trigger identifies regions of interest (RoI) which are defined for electrons as 2×2 clusters of trigger towers in the electromagnetic calorimeter, formed by summation of energy deposits within areas of 0.1×0.1 in $\Delta\eta \times \Delta\phi$, for which the sum of transverse energy in the neighbouring towers exceeds a predefined η-dependent

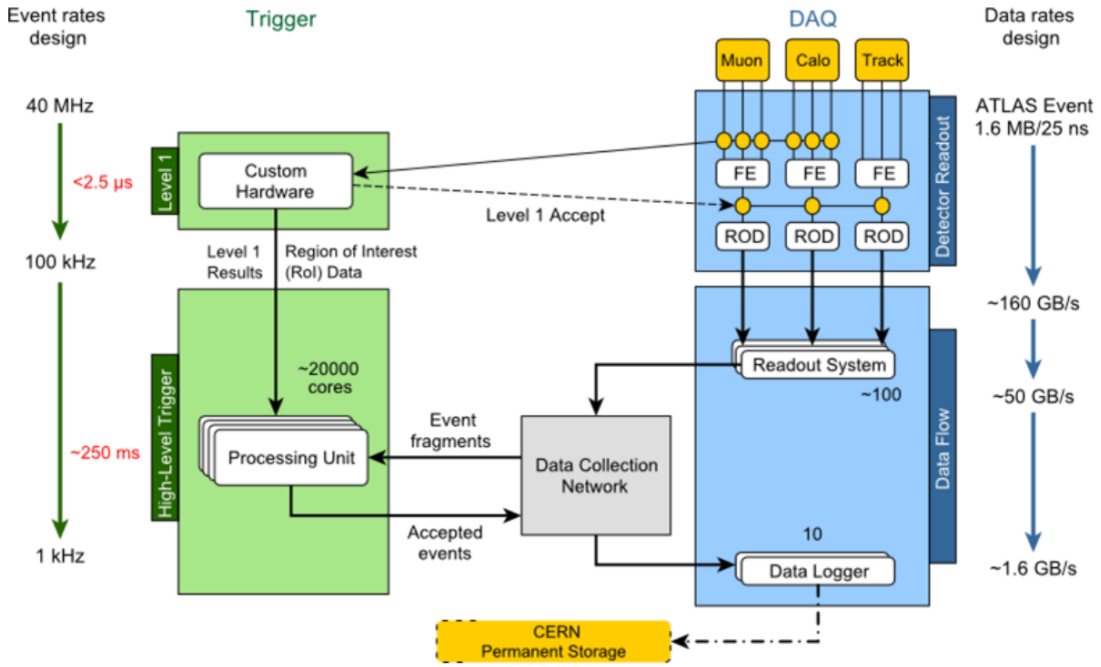

Figure 3.12.: The ATLAS Trigger and Data Acquisition (TDAQ) system, selecting events at a recording rate of $\approx 1\,\text{kHz}$ from up to 40 MHz of collisions in two steps by the first-level hardware trigger (L1) and the high-level software trigger (HLT). [187]

threshold. The L1Muon triggers use information from the RPC system in the barrel region ($|\eta| < 1.05$) and the TGC system in the end-cap regions ($1.05 < |\eta| < 2.4$) to identify muon candidates by spatial and temporal coincidences between the muon planes. The CTP forms the L1 trigger decision by applying the requirements specified in the trigger configuration and limits the minimum time between two accepted events to avoid overlapping readout windows to 100 ns, corresponding to four bunch crossings.

Events accepted by the L1 trigger are further processed by the HLT using finer-granularity calorimeter information, precision measurements from the MS and tracking information from the ID. Electron candidates are first identified from information on the energy deposits and shower shapes of clusters built from the calorimeter cells within the RoI identified by the L1Calo. Electrons are then reconstructed with clusters spatially matched to tracks extrapolated to the ECAL and classified by the likelihood-based (LH) method also used in the offline reconstruction described in section 4.1.2. Muon candidates from the L1Muon are refined with precise information from the MDT and CSC chambers.

The LHC Computing Grid (LCG) [188, 189] provides a data storage and analysis infrastructure for the recorded data. Events accepted by the HLT are stored at the local storage at the experimental site and transferred to the Tier-0 facility at CERN's computing centre for offline reconstruction. The raw data and reconstructed outputs are further distributed to Tier-1 centres performing large-scale reprocessing with round-the-clock operation in all continents and to Tier-2 sites, typically universities and other scientific institutes.

3.3. Monte Carlo simulation

The signal and background predictions needed to interpret the observed data were obtained from MC simulations performed by the ATLAS collaboration of the underlying physical processes described in chapter 6. These consist of the truth-level event generation described in section 3.3.1 and the detector simulation of reconstruction-level events outlined in section 3.3.2. Eventually, the simulated MC events are scaled to the integrated luminosity observed in data as explained in section 3.3.3.

3.3.1. Truth-level event generation

The event generation is typically divided into the following phases [190]: Hard process, parton shower, hadronisation, underlying event and unstable particle decays. Events simulated in the hard process are considered to be at the "parton level" and hereafter called "parton-level" events, while those events simulated with the full event generation chain including unstable particle decays are considered to be at the "particle level" and are called "particle-level" events.

Hard process

In the hard process, the probability distribution of a particular highest-momentum transfer process in the event is calculated from perturbation theory using the factorisation formula 2.33 involving matrix elements (MEs) and phase space integrations. The phase space integration is usually performed using Monte Carlo (MC) sampling methods due to the complexity of the processes, which assign a MC weight to each generated event.

Parton shower

The parton shower (PS) simulates the cascade of partons that is produced by gluon radiation from incoming and outgoing partons involved in the hard collision, referred to as initial-state radiation (ISR) and final-state radiation (FSR), respectively. The parton shower is simulated in a sequential step-by-step process starting from the hard process to lower momentum scales of the order of 1 GeV until perturbation theory breaks down. Typical choices of the momentum scale variable are the opening angle (Herwig 7 [191] and Sherpa 2.2.1 [192]), the relative transverse momentum of the gluon (Pythia 8.2 [193]) and the total invariant mass (Pythia 6.2 [194]).

While matrix elements allow for a systematic expansion in perturbation theory and are good for well-separated jets with tailored phase-space cuts and several partons in the final state, parton showers are well-suited to describe the internal structure of jets and the pattern of soft radiation between the jets [195]. There are three main options to combine MEs with PS avoiding double counting or gaps in the phase space coverage: Merging, vetoing parton showers (CKKW [196], CKKWL [197] and MLM [198]) and NLO matching (MC@NLO [199] and POWHEG [200]).

Hadronisation

Hadronisation describes how coloured partons form colourless hadrons. This process cannot be calculated from first principles and thus needs to be modelled [201]. The

two main models are the String Model [102], implemented in Pythia, and the Cluster Model [202, 203], implemented in Herwig and Sherpa.

The String Model describes a quark-antiquark pair emerging from the parton shower as a string of length l with tension $\kappa = 1\,\mathrm{GeV/fm}$ implying the potential $V(r) = \kappa r$. The String Model is based on the non-perturbative dynamics of the confinement of partons described in section 2.1.4. As the quark and antiquark move apart, the potential energy stored in the string increases linearly with the distance and it may break apart into two colour singlet systems by production of a new quark-antiquark or diquark-antidiquark pair. Gluons can be described as kinks on the string, carrying energy and momentum. The typical distance for a string break is 1–5 fm in the quark-antiquark rest frame. Further breaks may occur if the invariant mass of either of these string pieces is large enough. This process proceeds until only colour-singlet on-mass-shell hadrons remain. While the string model gives a very good description of data, it depends on many parameters that need to be tuned.

The Cluster Model, on the other hand, is based on the perturbative preconfinement property of parton showers: the mass spectrum of colour-singlet combinations of partons (clusters) depend only on the evolution scale Q_0 and the QCD scale Λ, but not on the scale Q or nature of the hard process initiating the shower for $Q \gg Q_0$. At the end of the shower evolution, all gluons are split into quark-antiquark or diquark-antidiquark pairs. Colour-singlet clusters are formed from adjacent colour-connected pairs, thus suppressing large masses. These clusters are treated as spectrum of excited mesons and decay further into hadrons. The Cluster Model performs slightly worse compared with the String Model, but uses fewer parameters.

Underlying event

In addition to the hard scatter process, also the evolution, hadronisation and interaction of the coloured proton remnants, not involved in the hard scatter process, are simulated as Underlying Event (UE). The Pythia and Sherpa implementations are based on the Multi Parton Interactions (MPI) model proposed by Sjöstrand and Zijl [204], while the Herwig implementation is based on an eikonal multiple scattering model [205].

Unstable particle decays

In the last step of event generation, unstable particles decay into particles that are stable on collider timescales ($\tau \gtrapprox 10^{-10}\,\mathrm{s}$) [201]. Many particle properties like decay modes and branching rates can be found in the Particle Data Group (PDG) [36] database. Different generators differ in the choice of included hadrons, decay modes and their simulation, including matrix elements and spin correlations. Special external packages such as EvtGen [206] for hadron decays and TAUOLA [207] for tau decays are used.

3.3.2. Detector simulation

The truth-level events, stored in a standard HepMC format [208], are further processed in a simulation of the ATLAS detector [209].

The passage of particles through the detector material is simulated in a GEANT4 [210] based simulation. Energy deposits in the sensitive parts of the detector are recorded as hits, containing the total energy deposition, position and time. At this stage, pile-up

contributions from additional pp collisions within a single bunch crossing (in-time pile-up) and due to signals from collisions in other bunch crossings (out-of-time pile-up) are overlaid using simulated soft *pp* collisions according to the measured distribution of the average number $< \mu >$ of *pp* interactions per bunch crossing [211].

In the ATLAS digitisation process these hits are converted into detector responses, i.e. into voltages and currents. These digits are propagated through an emulation of the Read Out Drivers (RODs) in the detector electronics and stored as Raw Data Objects (RDOs) in the same format as the recorded data.

For rare processes, systematic uncertainties and background effects in which a larger number of collisions but less precision is needed, the full Geant4 simulation time can be reduced by more than one order of magnitude with the ATLFAST-II fast simulation [212] which uses the parametrised calorimeter simulation FASTCALOSIM [213].

Events simulated with the detector simulation are considered to be at the "detector level" or "reconstruction level" and are hereafter considered as "detector-level" and "reconstruction-level" events.

3.3.3. Scale factors

The simulated events are further scaled to the integrated luminosity $\mathcal{L}_{\text{int}}$ according to the predicted cross section σ times branching ratio BR by a scale-factor ξ:

$$\xi = \frac{(\sigma \times \text{BR}) \cdot \mathcal{L}_{\text{int}} \cdot k}{\sum_i w_i'} \tag{3.8}$$

where the k-factor [121] corrects the sample specific cross sections included in the generators to the latest calculations and $\sum_i w_i'$ is the sum of unscaled MC weights of all simulated events.

Simulated detector-level events are further reweighted and scaled to mitigate differences between data and simulation. A pile-up weight is applied to correct the instantaneous luminosity distribution in MC to match the distribution measured in data [214]. Lepton scale factors are applied as described in sections 4.1.2 and 4.1.3. Furthermore, b-tagging, top-tagging and jet-vertex-tagging (JVT) weights are applied as described in section 4.1.4. These weights are derived from jet-by-jet efficiency and inefficiency scale factors that are defined as the ratio of the efficiencies measured in data and in simulation:

$$\text{SF}_{\text{eff}} = \frac{\epsilon_{\text{Data}}}{\epsilon_{\text{MC}}} \tag{3.9}$$

for tagged jets and by

$$\text{SF}_{\text{ineff}} = \frac{1 - \epsilon_{\text{Data}}}{1 - \epsilon_{\text{MC}}} = \frac{1 - \text{SF}_{\text{eff}}\epsilon_{\text{MC}}}{1 - \epsilon_{\text{MC}}} \tag{3.10}$$

for jets that are not tagged. The event weight is then multiplied by the product of the scale factors of all jets in that event.

The predicted number of events N and its statistical uncertainty ΔN are given by:

$$N = \sum_i w_i, \quad \Delta N = \sqrt{\sum_i w_i^2} \tag{3.11}$$

where w_i are the scaled MC weights and the sum runs over all generated events.

4. Physics object definition and reconstruction

Section 4.1 describes the definition and reconstruction of detector-level objects in data and simulated events using the various sub-detectors of the ATLAS experiment described in section 3.2. The definition of particle-level objects in truth-level events is given in section 4.2.

4.1. Detector-level objects

The following sections describe the detector-level physics objects used in this analysis: Tracks and primary vertices (4.1.1), electrons (4.1.2), muons (4.1.3), small-R and large-R jets (4.1.4) and missing transverse momentum (4.1.5). An overlap removal procedure to avoid double counting of energy depositions is explained in section 4.1.6. Table 4.1 gives an overview of the physics objects at the detector level.

Table 4.1.: Overview of detector-level physics objects used in this analysis.

Electrons	Tracks and calorimeter clusters (ID and ECAL) $p_T > 25\,\text{GeV}$, $\lvert\eta\rvert < 2.47$, $\lvert\eta\rvert \notin [1.37, 1.52]$ $\lvert z_0 \sin(\theta)\rvert < 0.5\,\text{mm}$, $\lvert d_0\rvert/\sigma(d_0) < 5$ Baseline: "LooseAndBLayer" identification Tight: "Tight" identification and "Fix (Tight)" isolation
Muons	Tracks and calorimeter clusters (ID, ECAL, HCAL and MS) $p_T > 25\,\text{GeV}$, $\lvert\eta\rvert < 2.5$ $\lvert z_0 \sin(\theta)\rvert < 0.5\,\text{mm}$, $\lvert d_0\rvert/\sigma(d_0) < 3$ Baseline: "Medium" identification Tight: "Medium" identification, "Tight" isolation
Small-R jets	Particle flow objects (ID, ECAL and HCAL) anti-k_t $R = 0.4$ $p_T > 25\,\text{GeV}$, $\lvert\eta\rvert < 2.5$ b-tagging: DNN (DL1r, 85% efficiency WP)
Large-R jets	Calorimeter clusters (ECAL and HCAL) anti-k_t $R = 1.0$, groomed $p_T > 200\,\text{GeV}$, $\lvert\eta\rvert < 2.0$ top-tagging: DNN (Contained top-tagger, 80% efficiency WP)
E_T^{miss}	Negative vector sum of the momenta of all hard objects and soft signals in the event

4.1.1. Tracks and primary vertices

Tracks [215–217] are reconstructed based on trajectory information from the pixel detector, including the IBL, SCT and TRT described in section 3.2.2. During clusterisation, pixels and strips in a given sensor with energy deposits above threshold are grouped into clusters, from which three-dimensional measurements referred to as space-points are created. Sets of three space-points form track seeds used in an iterative combinatorial track finding. A track score is assigned to the tracks according to the intrinsic resolutions and expected cluster multiplicities in the different subdetectors, holes, and the χ^2 of the track fit. An ambiguity-solving procedure is applied by removing clusters shared by more than two tracks, giving preference to tracks with a higher track score. Track candidates are required to have a transverse momentum of $p_T > 400\,\text{MeV}$ and a pseudorapidity of $|\eta| < 2.5$. Further requirements are applied on the transverse and longitudinal impact parameters, $|d_0| < 2.0\,\text{mm}$ and $|z_0 \sin\theta| < 3.0\,\text{mm}$, as well as on the number of clusters and holes in the detectors. Eventually, a track fit is performed using all available information for the remaining track candidates.

Primary vertices [218, 219] are defined as the points in space where proton-proton interactions took place. Starting from a collection of reconstructed tracks, primary vertices are reconstructed in two stages. First, the reconstructed tracks are associated to vertex candidates using pattern recognition techniques. Next, the actual vertex position and its covariance matrix are reconstructed in the vertex fitting. The hard-scatter primary vertex is identified as the primary vertex with the highest sum of the squared transverse momenta of contributing tracks, $\sum p_T^2$, since it is expected that the charged particles produced in hard-scatter interactions have on average larger transverse momenta than those produced in pile-up collisions. The longitudinal and transverse vertex position resolutions for events with a high jet multiplicity are about $30\,\mu\text{m}$ and 10-12 μm, respectively [220].

4.1.2. Electrons

Electrons are reconstructed based on information from the inner detector (ID) and the electromagnetic calorimeter (ECAL) [221]. They are required to have a transverse momentum larger than 25 GeV, an absolute rapidity of $|\eta| < 2.47$ and are excluded in the transition region between the barrel and the endcap of the calorimeter ($1.37 < |\eta| < 1.52$). The longitudinal impact parameter z_0 relative to the primary vertex and the transverse impact parameter d_0 relative to the beam axis must satisfy $|z_0 \sin(\theta)| < 0.5\,\text{mm}$ and $|d_0|/\sigma(d_0) < 5$, respectively.

The following sections describe the reconstruction, calibration, identification, isolation and charge identification as well as scale factors applied to simulated events.

Reconstruction

The reconstruction of electrons [221, 222] utilises clusters of energy deposits in the ECAL that are matched to a track in the ID.

First, proto-clusters are built from electromagnetic and hadronic calorimeter cells following a 4-2-0 topological cluster reconstruction. Cells are added to the proto-clusters depending on the significance $\zeta_{\text{cell}}^{\text{EM}}$ of the deposited cell energy with respect to the expected cell noise. Cells with $|\zeta_{\text{cell}}^{\text{EM}}| > 4$ are considered as seed cells. All neighbouring

cells with $|\zeta_{\text{cell}}^{\text{EM}}| \geq 2$ are added to the proto-cluster and become a seed cell in the next iteration. Eventually, the nearest-neighbor cells are added to the cluster irrespective of their energy significance. In case two proto-clusters share a cell with $|\zeta_{\text{cell}}^{\text{EM}}| \geq 2$ they are merged, if there are two or more local maxima within in proto-cluster, it is split into separate clusters. The EM energy of a cluster is defined as the energy from cells in the EM calorimeter; in the transition region ($1.37 < |\eta| < 1.63$) also the energy measured in the presampler and the scintillator between the cryostats is added. EM topological clusters are defined as clusters with an EM energy larger than 400 MeV and a fraction of EM energy to the total cluster energy larger than 0.5.

Track reconstruction is based on cluster creation, iterative track-finding, and additional measurements to recover non-prompt tracks [217]. Pixels and strips in a sensor with energy deposits above threshold are grouped into clusters. Space-points where the charged particle traverse the active material of the ID are obtained from individual clusters in the pixel detector and from clusters from both sides of a strip layer in the SCT. The track seeds, consisting of three space-points, are extended to full tracks of at least seven silicon hits per candidate track with a pattern-recognition algorithm using the pion hypothesis for the model of energy loss in the detector. Track candidates with $p_T > 400$ MeV are fitted using the ATLAS Global χ^2 Track Fitter [223]. An optimized Gaussian-sum filter (GSF) [224] is applied to tracks loosely matched to the EM cluster with at least four silicon hits to better account for the energy loss of charged particles in material.

Next, EM topological clusters with a minimum transverse energy E_T of 1 GeV matched to a track with at least four hits in the silicon tracking detectors are considered as seeds for superclusters, sorted by decreasing E_T. Clusters within a window of $\Delta\eta \times \Delta\phi = 0.075 \times 0.125$, or within $\Delta\eta \times \Delta\phi = 0.125 \times 0.300$ and matched to the same track, are added to the supercluster. The energy of the supercluster is given by the energy measured in the presampler and the first three LAr calorimeter layers, in the transition region $1.4 < |\eta| < 1.6$ also the energy measured in the scintillator between the cryostats is added. Finally, an initial energy calibration and position correction is applied to the electron superclusters, and track matching is performed in the same way as for the EM topological clusters.

Calibration

The electron energy is calculated from the energy deposited in the calorimeter and the presampler, the ratio of the energy deposits in the first and second layers of the EM calorimeter, the η value of the shower centre, and the η and ϕ differences between the shower center and the closest cell in the second calorimeter layer with a multivariate regression trained on simulated single particle samples as described in reference [225]. Residual differences between data and simulation are corrected for by intercalibration of the different calorimeter layers, corrections for energy shifts due to pile-up, and corrections for non-uniformities in the calorimeter response. Differences in the energy scale and resolution in dependence of η between data and simulation measured in $Z \to ee$ decays [221, 225] are corrected for in data and in simulation, respectively:

$$E^{\text{Data,corr}} = E^{\text{Data}}/(1+\alpha(\eta)), \quad \left(\frac{\sigma_E}{E}\right)^{\text{MC,corr}} = \left(\frac{\sigma_E}{E}\right)^{\text{MC}} \oplus c(\eta) \tag{4.1}$$

where $\alpha(\eta)$ and $c(\eta)$ are η-dependent correction factors.

Identification

A likelihood (LH) discriminant [222] constructed from quantities measured in the inner detector and the calorimeter is used to discriminate prompt isolated electrons from hadronic jets, converted photons and non-prompt electrons from heavy-flavour hadron decays.

The discriminating variables correspond to the primary electron track, including transition radiation in the TRT, the lateral and longitudinal development of the electromagnetic shower and the spatial compatibility of the primary electron track with the reconstructed cluster. The likelihood for a reconstructed electron to originate from signal, L_S, or background, L_B, is given by the product of the probability density functions (pdfs) for signal, $P_{S,i}(x_i)$, and background, $P_{B,i}(x_i)$, of the discriminating variables x_i:

$$L_{S(B)}(\mathbf{x}) = \prod_{i=1}^{n} P_{S(B),i}(x_i) \tag{4.2}$$

The pdfs were derived from $Z \to ee$ and $J/\Psi \to ee$ events using the tag-and-probe method [222] for $E_T < 15\,\text{GeV}$ and $E_T > 15\,\text{GeV}$, respectively. The likelihood discriminant is then given by

$$d_L = \frac{L_S}{L_S + L_B} \tag{4.3}$$

A set of four working points is defined in order of increasing background rejection and corresponds to increasing thresholds for the likelihood discriminant such that the selected samples are subsets of each other. The numerical values of the discriminant are obtained in simulation to reach target efficiencies of 93%, 88% and 80% for prompt electrons with $E_T = 40\,\text{GeV}$ for the "Loose", "Medium" and "Tight" operating points, respectively. The electron identification efficiency is typically increasing with the transverse energy and decreasing with the magnitude of the pseudorapidity $|\eta|$ of the electron; see e.g. figure 8 in reference [222].

From "Loose" to "Medium" and from "Loose" to "Tight", the background rejection improves by factors of approximately 2.0 and 3.5, respectively.

All operating points require at least two hits in the pixel detector and a total of seven hits in the pixel and SCT detectors. The "LooseAndBLayer", which uses the same threshold for the LH discriminant as the "Loose" working point, "Medium" and "Tight" operating points require one of these pixel hits to be in the innermost pixel layer to reduce the background from photon conversions.

In this analysis, "baseline" and "tight" electrons are required to satisfy the "LooseAndBLayer" and "Tight" working points, respectively.

Isolation

To further discriminate prompt electrons from background processes an isolation requirement is applied. Prompt electrons from signal processes typically exhibit little activity in the calorimeter and the inner detector around the candidate object in ΔR.

The calorimeter isolation E_T^{iso} is calculated as the sum of transverse energy of topological clusters within a cone of $\Delta R = 0.2$ centred around the electron, subtracting the energy deposited by the electron candidate, leakage, and pile-up corrections. The track isolation p_T^{iso} is computed as the sum of transverse momenta of selected tracks

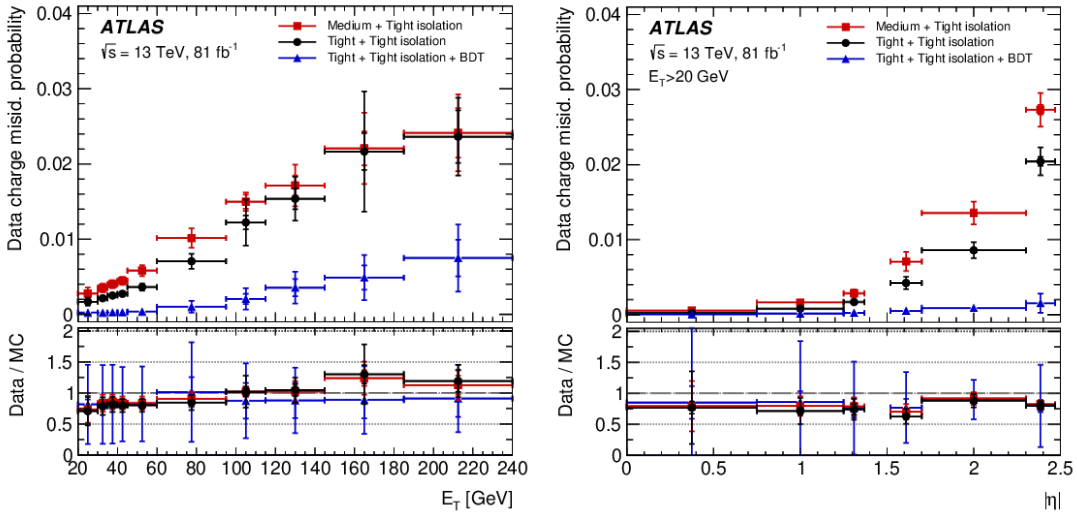

Figure 4.1.: Electron charge misidentification probabilities depending on E_T (left) and $|\eta|$ (right) measured in data. [221]

within a cone with variable size $\Delta R = \min\left(\frac{10\,\text{GeV}}{p_T[\text{GeV}]}, 0.2\right)$ centred around the electron track. The "Fix (Tight)" [221] working point sets upper thresholds for the calorimeter isolation $E_T^{\text{iso}}/p_T < 0.06$ and the track isolation $p_T^{\text{iso}}/p_T < 0.06$.

In this analysis, "tight" electrons are required to satisfy the "Fix (Tight)" isolation working point, while no isolation requirement is applied for "baseline" electrons.

Charge identification

The correct reconstruction of the sign of the lepton charge is an important aspect for the energy asymmetry measurement, as the top-quark charge is derived from the lepton charge. As the electric charge of an electron is obtained from the curvature of the associated track reconstructed in the inner detector, an incorrect track matching or a mismeasured curvature can result in electron charge misidentification.

As tracks become straighter for higher energies or large pseudorapidities, the misidentification rates increase with the electrons E_T and $|\eta|$ due to curvature mismeasurement. The main source of wrong track matching is bremsstrahlung followed by electron-positron pair production, resulting in three neighbouring tracks causing an ambiguity in the selection of the primary electron track. This effect is the largest in the pseudorapidity region $1.5 < |\eta| < 2.2$ as it depends on the amount of material traversed in the detector.

The charge identification probability ranges from 0.1% in the central region to about 3% at high $|\eta|$ as shown in figure 4.1.

Efficiency scale factors

The detector simulation accuracy is improved by application of a multiplicative scale factor to the event weight in simulation. This scale factor is defined as the ratio of the p_T- and η-dependent efficiency measured in data and in simulation as described in section 3.3.3. The total electron efficiency consists of the reconstruction, identification,

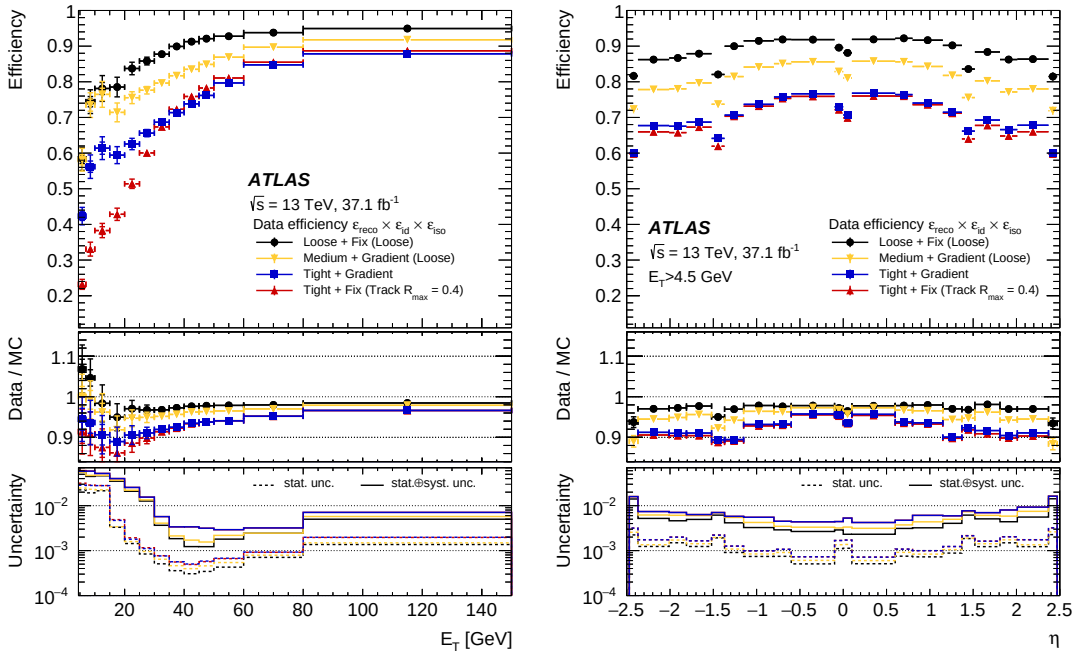

Figure 4.2.: Product of the electron reconstruction, identification and isolation efficiencies in dependence of E_T (left) and η (right) as measured in $Z \Rightarrow ee$ data events for various identification and isolation requirements. [222]

isolation, and trigger efficiencies, which were measured in $Z \to ee$ and $J/\Psi \to ee$ events [222]. Figure 4.2 shows the product of the reconstruction, identification and isolation efficiencies in dependence of p_T and η as measured in $Z \Rightarrow ee$ data events.

4.1.3. Muons

Muons are reconstructed based on information from the inner detector (ID), the electromagnetic (ECAL) and hadronic (HCAL) calorimeters and the Muon Spectrometer (MS) [226]. They are required to have $p_T > 25\,\text{GeV}$ and $|\eta| < 2.5$. The longitudinal and transverse impact parameters of the track associated with the muon candidate must satisfy $|z_0 \sin(\theta)| < 0.5\,\text{mm}$ and $|d_0|/\sigma(d_0) < 3$, respectively. The following sections describe the reconstruction, calibration, identification, isolation, charge identification and scale factors applied to simulated events.

Reconstruction

The reconstruction of muons [226, 227] is primarily based on information from the ID and MS tracking detectors; information from the ECAL and HCAL is used in the determination of track parameters and to account for energy loss in the calorimeters. Depending on which parts of the detectors are used, the following four muon types are defined:

- Combined (CB) muons: Combination of ID and MS
- Segment-tagged (ST) muons: Combination of ID and muon drift tube chambers (MDT) or cathode strip chambers (CSC)
- Calorimeter-tagged (CT) muons: Track in the ID matched to energy deposits in the calorimeter
- Extrapolated (ME) muons: MS track compatible with the interaction point (IP)

The reconstruction of tracks is performed independently in the ID and the MS. Tracks in the ID are reconstructed as described in section 4.1.1. Tracks in the MS are reconstructed by fitting hit patterns inside each muon chamber to form straight-line segments. These individual segments are combined into preliminary track candidates taking into account directional constrains from the position of the interaction point and the muon bending in the magnetic field. For each track candidate, a χ^2 fit of the muon trajectory through the magnetic field is performed, taking into account interactions with the detector material and possible misalignments between the detector chambers. The fit is repeated after removing outliers and adding hits matching the trajectory that were not assigned to the original track candidate. For the combined (CB) muons used in this analysis, a combined track is formed in a global fit using the hits from both the ID and MS subdetectors based on the "Chain 3" algorithms defined in [228], taking into account the energy loss in the calorimeters, and extrapolated to the beam line.

Muons can be detected within pseudorapidities of up to $|\eta| < 2.7$ over a wide p_T range from 3 GeV to 1 TeV [229]. The limiting factors for the momentum resolution are fluctuations in the energy loss of the muons traversing the material in front of the spectrometer at low momentum $p_T < 20\,\text{GeV}$, multiple scattering in the spectrometer in the intermediate momentum range and the single-hit resolution limited by detector characteristics for $p_T > 300\,\text{GeV}$.

Calibration

Several corrections derived in J/Ψ and $Z \to \mu\mu$ events are applied to the simulated muon momentum to increase the agreement between data and simulation [226]. The momentum scale is corrected for inaccuracies in the description of the magnetic field, detector dimensions and the simulation of the energy loss in the calorimeter and detector material. The muon momentum is smeared by the momentum resolution that can be parametrised as:

$$\frac{\sigma(p_T)}{p_T} = r_0/p_T \oplus r_1 \oplus r_2 p_T \tag{4.4}$$

where the first term corresponds to fluctuations in the energy loss, the second term to multiple scattering, magnetic field inhomogeneities and radial hit displacements, and the last term to the spatial resolution and residual misalignments of the muon spectrometer. These corrections are applied individually to the ID and MS transverse momenta; the CB muon momentum is then obtained from a weighted average of these.

Identification

Muon identification [226, 227] is performed to select prompt muons with a high efficiency while suppressing background from pion and kaon decays and ensuring a robust

Table 4.2.: Muon reconstruction efficiencies for prompt muons with a transverse momentum between 20 and 100 GeV from W-boson decays and for hadrons with four identification selection criteria. [226]

Selection	ϵ_μ [%]	$\epsilon_{\text{Hadrons}}$ [%]
Loose	98.1	0.76
Medium	96.1	0.17
Tight	91.8	0.11
High-p_T	80.4	0.13

momentum measurement. The "Loose", "Medium" and "Tight" identification selections are defined as inclusive categories such that the tighter categories are subsets of the looser ones. While the "Loose" and "Tight" criteria are aimed at maximal reconstruction efficiency and purity, respectively, the "Medium" criteria minimise the systematic uncertainties associated with reconstruction and calibration.

A comparison of the prompt and fake reconstruction efficiencies for the four identification criteria is given in table 4.2. This analysis uses the Medium identification criteria for both "baseline" and "tight" muons. In the pseudorapidity range $|\eta| < 2.5$ the "Medium" identification uses combined (CB) muon tracks. The CB tracks are required to have at least 3 hits in at least two MDT layers, except for the $|\eta| < 0.1$ region, where tracks with at least one MDT layer are allowed. Additionally, the significance of the absolute value of the difference in the ratio of the charge and momentum of the muons measured in the ID and MS with respect to the corresponding uncertainties must be less than seven.

Isolation

Muon isolation variables [226] are defined to discriminate prompt muons originating from W-, Z- or Higgs-boson decays from nearby hadronic activity. The particle flow isolation is based on track and calorimeter isolation variables calculated from charged particle and neutral particle flow objects described in section 4.1.4.

The track isolation variable $p_T^{\text{varcone}x}$ is calculated by summing up the transverse momentum of selected tracks within a cone of size $\Delta R = \min\left(\frac{10\,\text{GeV}}{p_T}, x/100\right)$ centred around the muon track direction. The calorimeter isolation variable newflowisol20 is calculated as the sum of positive energy of the neutral energy flow objects within a cone of $\Delta R = 0.2$ centred around the muon direction.

The "FixedCutPflowTight_FixedRad" [230] working point applies a cut on a combination of $p_T^{\text{varcone}x}$ and newflowisol20 depending on the muon p_T:

- $p_T^{\text{varcone30}} + 0.4$ newflowisol20 $< 0.045\ p_T$ for $p_T < 50\,\text{GeV}$
- $p_T^{\text{varcone20}} + 0.4$ newflowisol20 $< 0.045\ p_T$ for $p_T > 50\,\text{GeV}$

The "FixedCutPflowTight_FixedRad" isolation is required for "tight" muons, while no isolation is required for "baseline" muons.

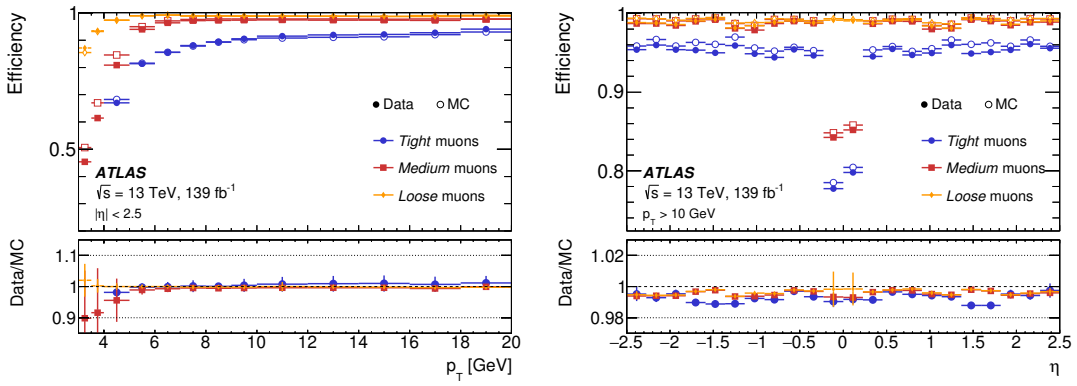

Figure 4.3.: Muon reconstruction and identification efficiency as a function of p_T (left) and $|\eta|$ (right) derived in $J/\Psi \to \mu\mu$ and $Z \to \mu\mu$ events. [227]

Charge identification

As the muon charge is measured in both the inner detector and the muon spectrometer and due to the long lever arm to the muon system, the charge misidentification rates are much smaller for muons than for electrons. The charge misidentification rate for muons satisfying the Medium selection criteria was found to be about $4.7 \cdot 10^{-6}$ in simulated $Z \to \mu\mu$ events [231].

Efficiency scale factors

The reconstruction, identification, isolation, and vertex association efficiencies were measured with the tag-and-probe method in $J/\Psi \to \mu\mu$ and $Z \to \mu\mu$ events [226, 227]. Differences between data and simulation in the p_T and η dependent efficiencies are corrected for in simulation as described in section 3.3.3. The reconstruction and identification efficiency as a function of p_T and $|\eta|$ is shown in figure 4.3.

4.1.4. Jets

Small-R and large-R jets are reconstructed based on information from the inner detector (ID) and the electromagnetic (ECAL) and hadronic (HCAL) calorimeters. Small-R jets are reconstructed from particle flow objects clustered with the anti-k_T algorithm with radius parameter $R = 0.4$ and required to have $p_T > 25\,\text{GeV}$ and $|\eta| < 2.5$. Large-R jets are reconstructed from topological clusters formed with the anti-k_T algorithm with radius parameter $R = 1.0$ and required to have $p_T > 200\,\text{GeV}$ and $|\eta| < 2.0$.

The following sections introduce topological clusters and particle flow objects, explain the jet clustering algorithms and describe the reconstruction and calibration of small-R and large-R jets. Eventually, the identification of jets originating from b-hadron and top-quark decays as well as the suppression of pile-up jets is explained.

Topological clusters

Calorimeter cells are combined into three-dimensional topological clusters [232] using a nearest-neighbour algorithm based on the significance of the energy deposits compared to the expected noise from electronics and pile-up.

The calorimeter cells are initially calibrated to the electromagnetic (EM) scale that correctly accounts for energy deposits from electromagnetic showers. The Local Hadronic Cell Weighting (LCW) [233] scheme applies energy corrections determined in simulated single pion events depending on the likelihood for a cluster to be generated by electromagnetic energy deposits.

To account for the position of the hard-scatter primary vertex an origin correction [234] is applied to the topological clusters on an event-by-event basis.

Particle flow objects

The particle flow algorithm [234, 235] combines the better energy and angular resolution as well as pile-up resilience of the tracking detectors over the calorimeter at low p_T for charged particles with the ability of the calorimeter to reconstruct both the charged and neutral particles. To avoid double counting, the corresponding energy of the particle needs to be subtracted from the calorimeter if the energy measurement of the ID is used.

First, well-measured tracks within $|\eta| < 2.5$ and $p_T > 0.5\,\text{GeV}$ are selected if they have at least nine hits in the silicon detectors and no missing hits in the pixel detector. High-energetic tracks with a p_T above 100 GeV or with a very high calorimeter activity in a cone of $\Delta R < 0.15$ around the extrapolated particle are removed as they are better reconstructed in the calorimeter and the accurate removal of the associated track energy becomes difficult. Also tracks matched to electrons and muons satisfying medium quality criteria are excluded, as the algorithm is optimized for the subtraction of hadronic showers from charged pions. Next the selected tracks are extrapolated to the calorimeter and matched to topological clusters calibrated at the EM scale based on the angular topological cluster widths and the ratio of cluster energy and track momentum. To correctly subtract the energy from the calorimeter, the expected deposited particle energy for a particle with measured momentum p^{trk} is estimated as $\langle E_{\text{dep}} \rangle = p^{\text{trk}} \langle E^{\text{clu}}_{\text{ref}} / p^{\text{clu}}_{\text{ref}} \rangle$ with the expectation $\langle E^{\text{clu}}_{\text{ref}} / p^{\text{clu}}_{\text{ref}} \rangle$ obtained from simulated single-pion events. In the next stage of the algorithm, additional clusters are added if the shower seems to be split across several clusters, based on the significance of the difference between the expected energy and that of the matched topological cluster. Eventually, the expected energy deposits of the tracks in the corresponding topological clusters are subtracted cell-by-cell based on a parametrised shower shape. Finally, topological cluster remnants consistent with the expected shower fluctuation are removed under the assumption that the topological cluster system was produced by a single particle.

The selected tracks, charged particle flow objects, and remaining clusters, neutral particle flow objets, represent the reconstructed event without double counting of energy depositions.

Jet clustering

As quarks and gluons hadronise as described in section 3.3.1, they are reconstructed as cone-shaped jets e.g. from four-vectors of stable simulated particles ("truth jets"), reconstructed tracks in the inner detector ("track jets") or energy deposits in the calorimeter ("calorimeter jets"). Sequential recombination algorithms combine these objects

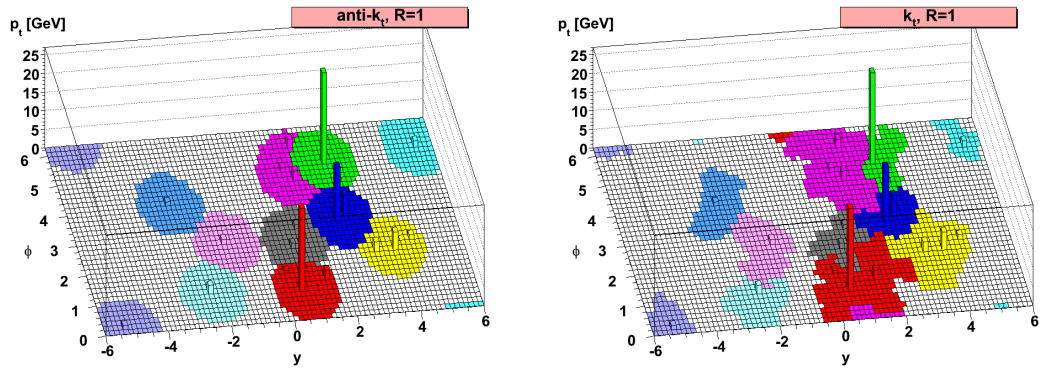

Figure 4.4.: Behaviour of the anti-k_t (left) and k_t (right) jet clustering algorithms in a parton-level event together with 10^4 random infinitely soft "ghost" particles. The coloured regions show which ghosts are clustered into the jets. The anti-k_T algorithm produces perfectly conical jets with radius R for well-separated high transverse momentum objects, while the k_t algorithm results in more complex jet shapes depending on the specific set of ghosts. [236]

based on the following distance measure [236]:

$$d_{ij} = \min(k_{t_i}^{2p}, k_{t_j}^{2p}) \frac{\Delta_{ij}^2}{R^2}, \quad d_{iB} = k_{ti}^{2p} \tag{4.5}$$

with transverse momentum k_{t_i}, rapidity y_i and azimuth angle ϕ_i of object i and separation in y-ϕ-space $\Delta_{ij}^2 = (y_i - y_j)^2 + (\phi_i - \phi_j)^2$. The radius parameter R determines the minimal distance between two clustered jets and the parameter p determines the relative importance of the energy with respect to geometrical scales. The clustering process proceeds as follows: First, the smallest distance d is identified. If it is a distance d_{ij} between two objects, those are combined, if it is a distance d_{iB} between an object and the beam axis, this object is called a jet and removed from the list of objects. Next, the distances are recalculated and the procedure is repeated until no objects are left.

The inclusive k_t algorithm [237] sets $p = 1$ and thus follows the idea to reverse the parton shower to reconstruct the parent parton by combining low k_T objects first [238]. The Cambridge/Aachen algorithm [239] simply combines the nearest objects in y-ϕ-space with $p = 0$. Setting $p = -1$ results in the anti-k_t jet-clustering algorithm [236], which adds all soft, i.e. low p_T, objects within a circle of radius R to a hard, i.e. high p_T, object if there are no other hard objects within a distance of $2R$, resulting in a perfectly conical jet. Two hard objects within a distance of Δ_{12} will be combined to a single jet with a more complex shape. Two hard objects within a distance of $R < \Delta < 2R$ will be clipped, depending on the transverse momenta and separation. The different behaviours of the k_t and anti-k_t jet clustering algorithms are depicted in figure 4.4.

In this thesis the anti-k_t algorithm is used to reconstruct small-R jets with $R = 0.4$ and large-R jets with $R = 1.0$. The k_t algorithm is used to cluster subjets in large-R jets in the process of trimming and for boosted hadronic top identification described below.

Small-R jets

Small-R jets are reconstructed with the anti-k_t algorithm with radius parameter $R = 0.4$ from neutral particle flow objects and tracks matched to the hard-scatter primary vertex as described in reference [234]. They are required to have a transverse momentum above 25 GeV and an absolute pseudorapidity of $|\eta| < 2.5$.

Jet calibration techniques [234] are applied to account for an inaccurate reconstruction in the detector as well as imperfect simulations of the detector material and the involved physics processes. In the jet energy scale (JES) calibration [234], the four-momentum at the detector level is corrected to the particle-level energy scale by scaling the jet p_T, energy and mass. The JES calibration consists of simulation-based jet calibrations in dijet events applied to both simulation and data and of in-situ jet calibrations in dijet, Z+jets γ+jets, and multijet events applied only to data. The full chain of calibration steps is visualised in figure 4.5.

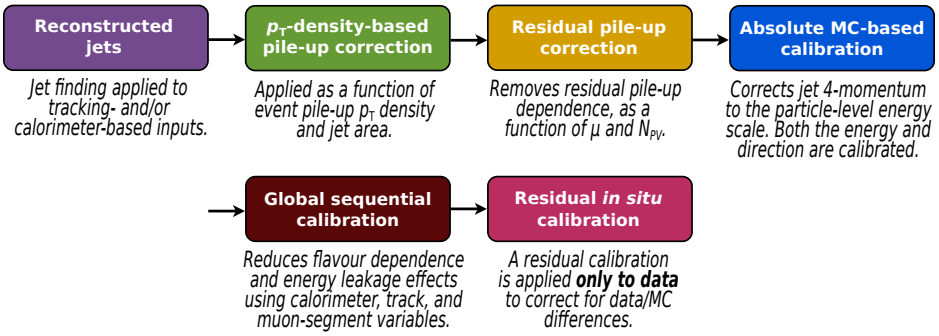

Figure 4.5.: Small-R jet reconstruction and calibration procedure. [234]

First, contributions to the jet energy from pile-up are removed in a correction based on the jet area and transverse momentum density and a residual correction. Energy losses in passive material, out-of cone effects, and non-compensating calorimeter responses are corrected for in the absolute JES calibration derived from the average jet energy response $R_E = \langle E_{\text{reco}}/E_{\text{truth}} \rangle$ in dependence of the jet energy and η. Biases in the η reconstruction from changes in the calorimeter technology and granularity are taken into account with a correction based on the difference between the reconstructed and truth-level η. Dependencies on the flavour and energy distribution of the constituent particles, their transverse distributions and shower shape fluctuations, as well as the initiating particles, are reduced using calorimeter, track and muon-segment variables in the global sequential calibration (GSC).

In-situ calibrations derived in dijet, Z+jets, γ+jets, and multijet events are applied to data to correct the jet for differences between the jet response in data and simulation due to an imperfect simulation of the detector material, the hard scattering and underlying event, jet development, pile-up conditions, and particle interactions. The jet response is calculated as the average ratio of the jet p_T to the transverse momentum of a well-calibrated reference object, p_T^{ref}, $R = \langle p_T/p_T^{\text{ref}} \rangle$. Differences in the jet energy scale between data and simulation are expressed by the double ratio from the response observed in data and in simulation, $c = R^{\text{Data}}/R^{\text{MC}}$. In the η-intercalibration, the energy scale of forward jets with $0.8 \leq |\eta| < 4.5$ is corrected to match that of central jets

with $|\eta| < 0.8$ using the p_T balance in dijet events. In Z+jets and γ+jets events, the p_T of the jet is balanced against the p_T of the Z boson or photon. In multijet events, a single high-p_T jet is balanced against a system of well-calibrated low-p_T jets. The final calibration factor is derived from a weighted combination of the dijet, Z+jets, γ+jets and multijet calibrations.

The relative jet energy resolution (JER) can be parametrised as:

$$\frac{\sigma(p_T)}{p_T} = \frac{N}{p_T} \oplus \frac{S}{\sqrt{p_T}} \oplus C \tag{4.6}$$

where N is the noise term due to electronic noise in the front-end electronics and pile-up, S the stochastic term due to statistical fluctuations in the amount of energy deposited and C the constant term corresponding to energy depositions in passive material, the starting point of the hadron showers and non-uniform calorimeter response. The dominating terms for transverse momenta below 30 GeV, between 30 and 400 GeV and above 400 GeV are the noise term, the stochastic term, and the constant term, respectively. The JER is derived from a combination of measurements in dijet events using the scalar balance between the transverse momenta of the two leading jets and direct estimates of the noise term obtained from data samples recorded from unbiased random triggers. The JER ranges from 25% for low $p_T \approx 20$ GeV jets to 4% at very high $p_T > 2.5$ TeV [234]. Jets in simulated samples are smeared to ensure that the jet energy resolution in simulation matches the resolution observed in data.

Large-R jets

Large-R jets are reconstructed with the anti-k_t algorithm with radius parameter $R = 1.0$ from topological clusters calibrated according to the LCW scheme and required to have $p_T > 200$ GeV and $|\eta| < 2.0$. The reconstruction and calibration procedure of large-R jets is illustrated in figure 4.6.

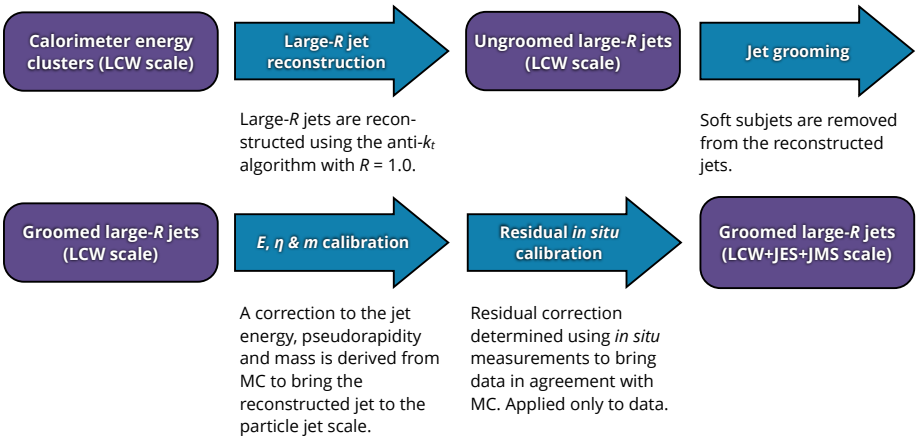

Figure 4.6.: Large-R jet reconstruction and calibration procedure. [233]

After reconstruction, a grooming procedure is applied to large-R jets to reduce the effects of pile-up, soft emissions and the underlying event by reclustering the jet constituents with the k_t algorithm with radius parameter $R = 0.2$, removing all subjets

with $p_T^{\text{subjet}}/p_T^{\text{jet}} < 0.05$ and recalculating the jet four-momentum from the remaining constituents.

The jet energy scale (JES) calibration restores the reconstructed calorimeter energy scale to that of particle-level jets in a simulation-based calibration and corrects for residual differences between data and simulation in in-situ calibrations. The simulation-based JES calibration factor c_{JES} is applied as a multiplicative scale factor to the jet four-momentum and the pseudorapidity correction $\Delta\eta$ changes the direction. Both corrections are derived from simulated dijet events. The in-situ calibrations are derived in dijet, Z+jets, γ+jets and multijet events with the same methods as for the small-R jets described above.

The jet mass scale (JMS) calibration corrects for effects on the jet mass response due to the splitting of topological clusters, multiple particles in a single topological cluster or particles that did not form topological clusters in a simulation-based calibration, and for residual differences between data and simulation in in-situ calibrations. The simulation-based JMS calibration c_{JMS} is derived from the average jet mass response $R_m = \langle m_{\text{reco}}/m_{\text{truth}} \rangle$ in simulated dijet events and is applied as a scale factor to the jet mass after the simulation-based JES calibration. The in-situ JMS calibration is derived from the forward folding method [233, 240, 241] that includes fits to the W-boson and top-quark peaks in the jet mass distribution in top-quark pair production events and from the calorimeter-to-tracker response double-ratio method [233, 242] using dijet events.

The jet energy resolution (JER) and jet mass resolution (JMR) are used to smear jets in MC simulation to match the resolution in data. The relative jet energy resolution (JER) is measured in dijet events and ranges from 7% at $p_T = 300\,\text{GeV}$ to 4% at $p_T = 1\,\text{TeV}$ [233]. The jet mass resolution (JMR) obtained from the forward folding method is about 10% [243].

The large-R jet mass resolution is further improved by adding information from the measurement of the charged component of the jet within the ID, taking advantage of independent systematic effects between the ID and the calorimeter. A track jet is reconstructed from ID tracks which are ghost-associated [244] to the topological cluster large-R jet. The track-assisted mass m^{TA} is then defined as $m^{\text{TA}} = m^{\text{track}} p_T^{\text{calo}}/p_T^{\text{track}}$, where m^{track} is the uncalibrated mass of the track jet and p_T^{calo} and p_T^{track} are the transverse momenta of the calorimeter and track jet, respectively. The combined jet mass is then given by [233]:

$$m^{\text{comb}} = w_{\text{calo}} m^{\text{calo}} + w_{\text{TA}} m^{\text{TA}} \tag{4.7}$$

where the weights w_{calo} and w_{TA} are obtained by minimising the JMR in multijet events.

B-jet identification

The identification of small-R jets containing b-hadrons ("b-jets") and discrimination against the large jet background containing c- but no b-hadrons ("c-jets") or neither b- nor c-hadrons ("light-flavour jets") is of major importance in a large number of SM precision measurements and searches for new phenomena. Specifically for top quarks, which decay almost exclusively into a W boson and a bottom quark, an efficient b-tagging algorithm is vital for a good signal efficiency and background rejection.

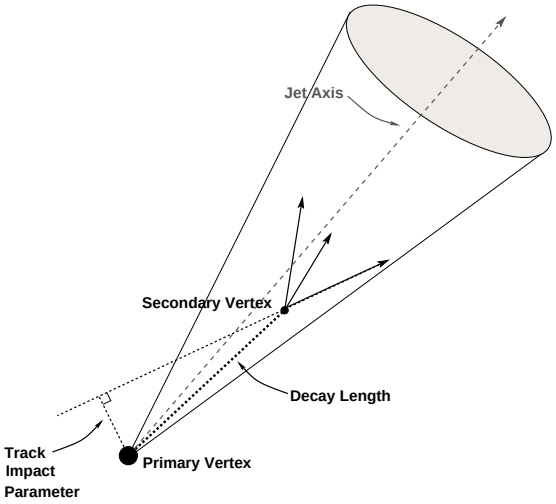

Figure 4.7.: B-jet identification: the secondary vertex, reconstructed from tracks with a large impact parameter, hints at a long-lived particle in the jet. [245]

Various b-tagging algorithms used to identify b-jets exploit the long lifetime of about 1.5 ps, the high mass and high decay multiplicity of b-hadrons as well as the properties of the b-quark fragmentation into b-hadrons [220]. Figure 4.7 illustrates how the long lifetime of b-hadrons yields at least one vertex displaced from the hard-scatter interaction point.

The DL1 b-tagging algorithm [220] is based on a deep feed-forward neural network (NN) with a multidimensional output corresponding to the probabilities for a jet to be a b-jet, a c-jet, or a light-flavour jet. The outputs of the low-level tagging algorithms based on impact parameters (IP2D and IP3D [246]), secondary vertex finding (SV1 [247]) and topological multi-vertex finding (JetFitter [248]) are used as inputs.

The DL1r b-tagging algorithm [220, 249] extends the DL1 algorithm by adding discriminating variables constructed by a recurrent neural network (RNNIP) [246], which exploits correlations between tracks within the jet. The DL1r b-tagging discriminant is defined as:

$$D_{\mathrm{DL1r}} = \ln\left(\frac{p_{\mathrm{b}}}{f_{\mathrm{c}}p_{\mathrm{c}} + (1-f_{\mathrm{c}})p_{\mathrm{light}}}\right) \tag{4.8}$$

where p_{b}, p_{c} and p_{light} are the b-jet, c-jet and light-flavour jet probabilities and $f_{\mathrm{c}} = 0.018$ controls the importance of the c-jet rejection. All jets with a discriminant value above a specific cut value are considered to be b-identified or b-tagged.

In this analysis the DL1r b-tagging algorithm is used to identify small-R b-jets at the 85% b-jet efficiency working point, corresponding to a cut value of 0.41. This working point provides rejection factors of ≈ 30 for light-flavour jets and ≈ 3 for c-jets, determined on anti-k_T R=0.4 particle flow jets with $20 < p_T < 250\,\mathrm{GeV}$ and $|\eta| < 2.5$ in simulated $t\bar{t}$ events [220]. Large-R jets are considered to be b-identified if they are within a cone of $\Delta R < 1.0$ of at least one b-identified small-R jet.

Differences between data and simulation due to an imperfect description of the detector response and physics modelling effects are mitigated by application of b-tagging weights in simulation as described in section 3.3.3 with p_T dependent jet-by-jet scale factors derived in di-leptonic $t\bar{t}$ events [220].

Boosted hadronic top identification

High transverse momentum hadronically decaying top quarks are identified with deep neural networks (DNN) using large-R jets built from locally calibrated topological clusters as defined in section 4.1.4 and jet substructure variables as inputs [250]. The top taggers are valid for jets with $p_T \in [350, 4000]$ GeV for contained and inclusive top definitions with signal efficiencies of 50% and 80%. Both definitions require signal jets to be matched to a particle-level jet, which is in turn matched to a parton-level top quark. Additionally, the contained top tagger requires the particle-level jet to have a mass above 140 GeV and to have at least one ghost-associated [244] b-hadron.

The inputs used for the DNN [250] are calibrated jet kinematics p_T, m^{comb} [251], energy correlation ratios e_3, C_2, D_2 [252, 253], N-subjettiness τ_1, τ_2, τ_{21}, τ_3, τ_{32} [254, 255] and splitting measures $\sqrt{d_{12}}$, $\sqrt{d_{23}}$ [256].

N-subjettiness τ_N [254] is a measure of how well a jet can be considered to consist of N subjets. Given N subjets of a jet, τ_N is defined as:

$$\tau_N = \frac{1}{d_0} \sum_k p_{T,k} \min(\Delta R_{1,k}, \Delta R_{2,k}, ..., \Delta R_{N,k}) \tag{4.9}$$

where k runs over all constituent particles with transverse momenta $p_{T,k}$ and distance $\Delta R_{i,k}$ in the rapidity-azimuth plane to subjet i. The normalisation factor is $d_0 = \sum_k p_{T,k} R_0$ where R_0 is the characteristic jet radius used in the jet clustering algorithm. Ideally, the N subjets are chosen to minimize τ_N over all possible candidate subjet directions, resulting in a strictly decreasing function τ_N of N. In practice, however, due to computational constraints, the N subjets are obtained using an exclusive-k_T clustering algorithm which returns exactly N jets [237, 257, 258].

Jets with a small value of $\tau_N \approx 0$ have their constituents aligned with the direction of the subjets indicating that they are well described by N or fewer subjets. For jets with larger $\tau_N \gg 0$, however, large fractions of the energy are pointing into directions not covered by the subjets hint towards at least $N + 1$ subjets. The ratios $\tau_{32} = \tau_3/\tau_2$ and $\tau_{21} = \tau_2/\tau_1$ thus allow for discrimination between jets containing a three-prong, two-prong, and one-prong structure. For top quarks decaying into a hadronically decaying W boson and a b-jet, a three-prong structure is expected. The distribution of τ_{32} exhibits small values with a maximum around 0.3 for top jets and around 0.75 for multijet and W-jet background. For τ_{21} the separation of signal and background is less pronounced, but still provides some discrimination [259].

Figure 4.8 shows the signal efficiency in dependence of the leading large-R jet p_T measured in $t\bar{t}$ events in data and a comparison of the light-quark and gluon jet background rejection with a tagger based on the two variables m^{comb} and τ_{32} evaluated in simulated dijet and γ+jet events. The chosen top-tagger has an efficiency of 80% for large-R jets satisfying the contained definition and a rejection factor for light-quark and gluon jet background ranging from ≈ 10 to ≈ 50 for large-R jets with transverse momenta of 2 000 GeV and 350 GeV, respectively.

Similar as for b-tagging, p_T and m^{comb} dependent top-tagging jet-by-jet scale factors, derived in semi-leptonic $t\bar{t}$ and multijet/γ+jets events [260], are applied in simulation as explained in section 3.3.3.

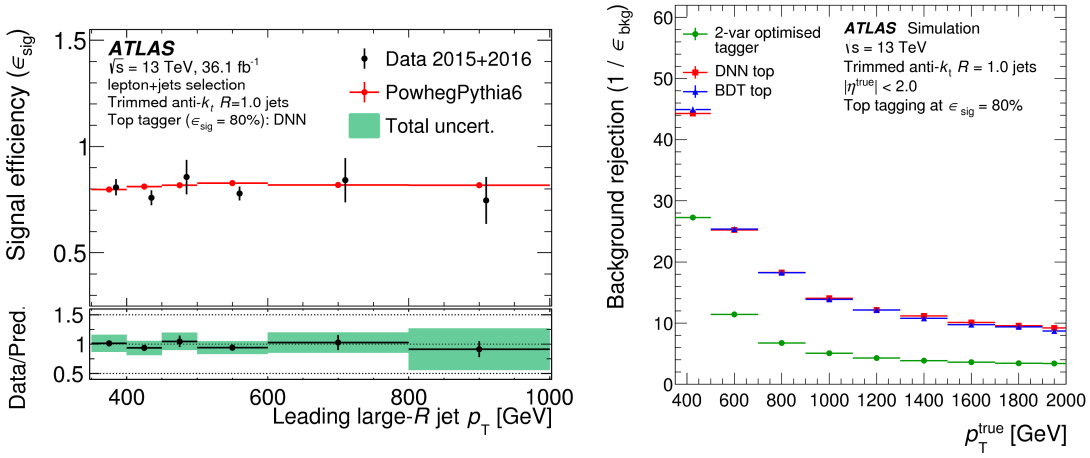

Figure 4.8.: The signal efficiency for the DNN top-quark tagger as a function of the leading large-R jet p_T (left) and a comparison of the light-quark and gluon jet background rejection with a multivariate BDT tagger and a tagger based on the two variables m^{comb} and τ_{32} (right). [250]

Pile-up suppression

Jets not originating from the hard-scatter vertex, defined as the primary vertex with the highest sum of squared track momenta, can be suppressed by application of the jet-vertex-tagger (JVT) [261, 262], a multivariate combination of the corrected jet vertex fraction (corrJVF) and R_{pT} defined below. The jet vertex fraction (JVF) is defined as the ratio of the scalar sum of the p_T of tracks matched to the jet originating from a given primary vertex to the scalar sum of the p_T of all tracks matched to the jet. The corrected jet vertex fraction (JVF) takes into account the pile-up dependence and is defined as:

$$\text{corrJVF} = \frac{p_T^{\text{HS}}}{p_T^{\text{HS}} + \frac{p_T^{\text{PU}}}{0.01 \cdot n_{\text{track}}^{\text{PU}}}} \tag{4.10}$$

where p_T^{HS} is the scalar sum of the p_T of the tracks matched to the jet and originating from the hard-scatter vertex, p_T^{PU} the scalar sum of the p_T of all tracks matched to the jet not originating from the primary vertex and $n_{\text{track}}^{\text{PU}}$ the number of pile-up tracks per event.

The variable R_{pT} is defined as the ratio of the scalar sum of the p_T of the tracks matched to the jet that originate from the hard-scatter vertex to the fully calibrated jet p_T:

$$R_{pT} = \frac{\sum_k p_{T,k}^{\text{track}}(\text{HS})}{p_T^{\text{jet}}} \tag{4.11}$$

Both corrJVF and R_{pT} are expected to be larger for HS than for PU jets as shown in figures 12 and 13 in reference [261]. The multivariate JVT discriminant is defined as the relative probability of a jet to originate from the hard-scatter vertex at each point of the two-dimensional corrJVF–R_{pT} plane, derived in simulated dijet events and based on a k-nearest neighbour (kNN) algorithm. Small-R jets with JVT < 0.7, $p_T < 60\,\text{GeV}$ and $|\eta| < 2.4$ are rejected in this analysis. This so called "Tight" working point provides an efficiency for signal jets to pass the JVT selection of 90% for jets with $20 < p_T < 50\,\text{GeV}$ and a pile-up jet rejection factor of ≈ 100, as estimated in

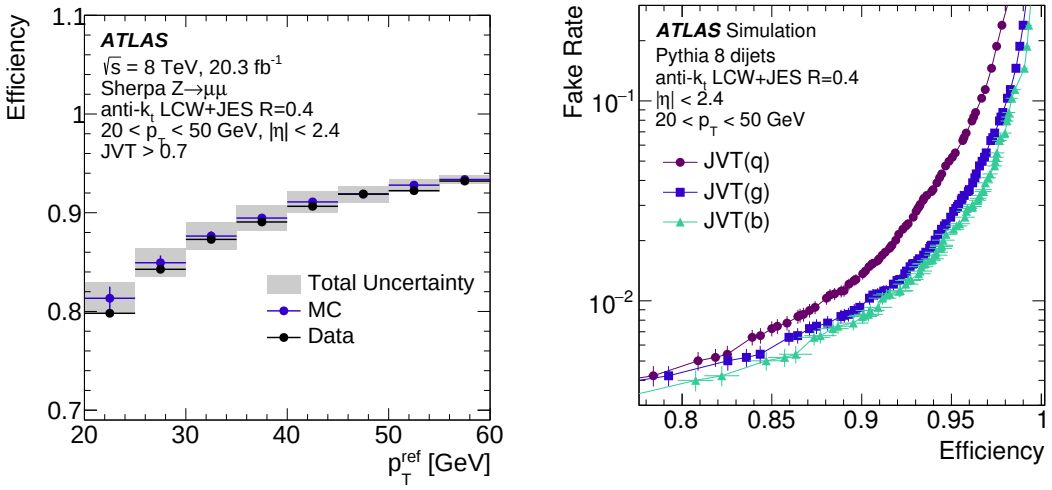

Figure 4.9.: JVT tagging efficiency for hard-scatter jets versus $p_T(Z)$ in $Z(\rightarrow \mu\mu)$+jets events in data and simulation (left) and the fake rate from pile-up jets versus the JVT tagging efficiency for hard-scatter jets for jets originating from quarks, gluons and b-quarks in simulated dijet events (right). [261]

$(Z \rightarrow \mu\mu)$+jets and simulated dijet events [262]. Figure 4.9 shows the JVT tagging efficiency for hard-scatter jets in dependence of the transverse momentum and versus the fake rate from pile-up jets.

A JVT weight derived in $Z \rightarrow \mu\mu$ events is applied to each simulated event as explained in section 3.3.3 to account for differences in the p_T-dependent JVT efficiencies between data and simulation.

4.1.5. Missing transverse momentum

The missing transverse momentum allows for the partial reconstruction of undetected particles produced in proton-proton collisions. Momentum conservation requires zero momentum in the plane transverse to the beam axis, but not longitudinal to the beam axis, as the longitudinal momentum components of the interacting particles are unknown. Any imbalance in the transverse plane may thus indicate the presence of weakly interacting particles like SM neutrinos or BSM particles.

The missing transverse momentum vector $\vec{E}_T^{\text{miss}}$ is defined as the momentum imbalance in the plane transverse to the beam axis and is obtained from the negative vector sum of the momenta of all hard objects and soft signals in the event [263]:

$$\vec{E}_T^{\text{miss}} = \vec{E}_T^{\text{miss,hard}} + \vec{E}_T^{\text{miss,soft}} = -\sum_{i\in[\text{hard objects}]} \vec{p}_{T,i} - \sum_{j\in[\text{soft signals}]} \vec{p}_{T,j} \qquad (4.12)$$

The hard objects are fully calibrated electrons, muons, photons, hadronically decaying τ-leptons and jets reconstructed from calorimeter energy deposits. Charged-particle tracks not associated with the hard objects form the soft signals which may contain contributions from the hard scatter as well as the underlying event and pile-up interactions [264]. To avoid double counting of reconstructed charged-particle tracks from the inner detector, energy deposits in the calorimeter and reconstructed muons, a signal

ambiguity resolution procedure which rejects already used signals when combining the various contributions is applied; see reference [263] for further details.

The magnitude E_T^{miss} and the azimuth coordinate ϕ^{miss} are given by:

$$E_T^{\text{miss}} = |\vec{E}_T^{\text{miss}}| = \sqrt{(E_x^{\text{miss}})^2 + (E_y^{\text{miss}})^2}, \quad \phi^{\text{miss}} = \tan^{-1}(E_y^{\text{miss}}/E_x^{\text{miss}}) \tag{4.13}$$

4.1.6. Overlap removal

An overlap removal procedure [265, 266] is applied to avoid double counting of energy depositions and biases on position and energy reconstruction from close-by objects.

In the lepton-lepton overlap removal, any electron found to share a track with a muon is removed, assuming that the muon has radiated a hard photon.

The electron-jet overlap removal aims to remove reconstructed jets that are identical with reconstructed prompt electrons, but to keep semi-leptonically decaying heavy-flavour jets as well as light-flavour jets that can fake a loose lepton. All jets within $\Delta R < 0.2$ of an electron are removed, while any subsequently found electron within $\Delta R < 0.4$ of a jet is removed.

The muon-jet overlap removal aims at the separation of prompt muons from hadron decays within a jet and to remove jets originating from FSR or bremsstrahlung photons. All jets with less than 3 associated tracks within $\Delta R < 0.2$ of a muon or with a ghost-associated [244] muon inner-detector track are removed. Any subsequently found muons within $\Delta R < 0.4$ of a jet are removed.

4.2. Particle-level objects

Particle level objects are defined similarly to the reconstructed objects to minimise model-dependent corrections for detector efficiency and resolution effects.

According to the ATLAS proposal for truth-level particle definitions [267], particles with a mean lifetime satisfying $c\tau > 10\,\text{mm}$ ($\tau \gtrapprox 10^{-10}\,\text{s}$) are considered to be stable. Leptons, jets and missing transverse momentum are defined as described in sections 4.2.1, 4.2.2 and 4.2.3, respectively. Table 4.3 summarises the particle-level physics objects used in this analysis.

4.2.1. Leptons

Prompt leptons are generated final-state electrons, muons, taus or neutrinos not originating from hadron decays. Electrons and muons from τ decays are considered as prompt leptons.

Born and bare leptons are defined as leptons prior and after QED Final State Radiation (FSR), respectively. Charged bare leptons are dressed using close-by photons by adding the photon four-momenta within a cone for $\Delta R < 0.1$ around the lepton. Prompt leptons are required to have $p_T > 25\,\text{GeV}$ and $|\eta| < 2.5$.

4.2.2. Jets

Particle-level jets are created by clustering all stable particles originating from the hard-scatter interaction in the simulation event record except for dressed prompt electrons and muons as well as neutrinos.

Table 4.3.: Overview of particle-level physics objects used in this analysis.

Electrons & muons	Final-state leptons not originating from hadrons dressed with nearby photons ($\Delta R < 0.1$) $p_T > 25\,\text{GeV}$, $\lvert\eta\rvert < 2.5$
Jets	Stable particles from the HS interaction except for dressed prompt electrons, muons and neutrinos
small-R jets	anti-k_t $R = 0.4$ $p_T > 25\,\text{GeV}, \lvert\eta\rvert < 2.5$ b-identification via ghost-association
large-R jets	anti-k_t $R = 1.0$ $p_T > 200\,\text{GeV}, \lvert\eta\rvert < 2.0$ b-identification via small-R jets within $\Delta R < 1.0$
E_T^{miss}	Transverse momentum sum of all neutrinos not from hadron decays

Small-R jets are clustered with the anti-k_T algorithm with $R = 0.4$ and are required to have $p_T > 25\,\text{GeV}$ and $|\eta| < 2.5$.

Large-R jets are clustered with the anti-k_T algorithm with $R = 1.0$ and the same grooming procedure as at the detector level. Only large-R jets with $p_T > 200\,\text{GeV}$ and $|\eta| < 2.0$ are considered in this analysis.

Since heavy-flavour (HF) hadrons have a shorter lifetime than the stable particle definition requires, they are not included in the construction of truth-level jets. The jet flavour is assigned via ghost-association [244] by including HF hadrons with an infinitesimal transverse momentum in the jet clustering algorithm without modifying the properties of the hard jets. Small-R jets are considered to be b-flavoured (b-identified) if they contain at least one b-hadron with $p_T > 5\,\text{GeV}$ and c-flavoured if they contain at least one c-hadron with $p_T > 5\,\text{GeV}$, but no b-hadron. Large-R jets are considered to be b-flavoured (b-identified) if there is at least one b-flavoured small-R jet within a cone of $\Delta R < 1.0$.

4.2.3. Missing transverse momentum

The missing transverse momentum is defined as the sum of all neutrinos not originating from hadron decays.

4.2.4. Overlap removal

Particle-level objects are subject to an overlap removal procedure similar to that applied for the detector-level objects as described in reference [266] in which all electrons and muons within $\Delta R < 0.4$ of a truth-level jet are removed.

5. Event selection and reconstruction

To measure the energy asymmetry in jet-associated top-quark pair production, $t\bar{t}j$ signal events need to be selected and reconstructed in data and simulation. As described in section 2.2.3 there are three decay channels for $t\bar{t}$ events; the all-hadronic, semi-leptonic and di-leptonic channels. This analysis focuses on semi-leptonic $t\bar{t}$ events with an additional jet in which one of the top quarks decays hadronically and the other one leptonically as illustrated in figure 5.1. This channel is characterised by exactly one lepton, missing transverse energy from the neutrino and at least five jets in the final state. The all-hadronic channel provides similar statistics, but complicates the reconstruction due to the many combinatorial possibilities of at least seven jets in the final state. The di-leptonic channel has the cleanest signature, but suffers from low statistics and ambiguities in the neutrino reconstruction with two neutrinos accounting for the missing transverse momentum.

Within the semi-leptonic channel there are two topologies; the boosted topology in which the hadronically decaying top quark has a high transverse momentum such that its decay products are typically collimated in a single large-R jet, and the resolved topology, in which the individual decay products are well separated. This analysis focuses on the boosted topology for two reasons; first, the energy asymmetry is enhanced with respect to the resolved phase space as shown in figure 2.22 in section 2.3.4 and discussed in reference [75], second, the correct assignment of jets is much more complicated in the resolved topology due to the many combinatorial possibilities, which lead to large uncertainties in the energy asymmetry from migrations in ΔE and θ_j as studied in a master thesis [268].

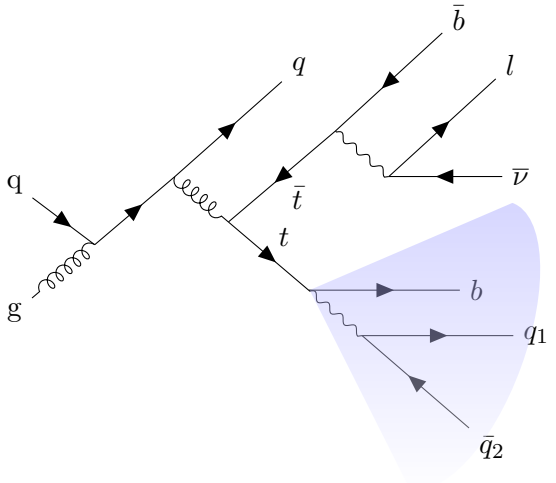

Figure 5.1.: Exemplary Feynman diagram for $t\bar{t}j$ production in the semi-leptonic decay channel. In the boosted topology, the decay products of the hadronically decaying top quark are typically collimated in a single large-R jet.

Table 5.1.: Single-electron and single-muon trigger configuration for the 2015 and 2016–2018 data-taking periods. The identification and isolation criteria as well as their efficiencies for electrons and muons are described in sections 4.1.2 and 4.1.3, respectively. The exact trigger configuration names are listed in table A.2 in appendix A

Year	Electrons			Muons		
	p_T	Identification	Isolation	p_T	Identification	Isolation
2015	24	Medium	-	20	-	Loose
	60	Medium	-	50	-	-
	120	Loose	-			
2016–2018	26	Tight	Loose	26	-	Medium
	60	Medium	-	50	-	-
	140	Loose	-			

The event selection and reconstruction described in sections 5.1 and 5.2 are based on typical analyses such as cross section [266] and rapidity asymmetry [65] measurements in semi-leptonic $t\bar{t}$ events in the boosted topology, adapted for the inclusion of an associated jet and primarily optimised to yield the highest expected sensitivity to the energy asymmetry for jet emission perpendicular to the beam axis. The optimisation is described in more detail in section 9.2. If not stated otherwise, the same selection and reconstruction is applied at both detector and particle level to minimise model-dependent corrections for detector efficiency and resolution effects. The technical implementation at the particle level was made public in reference [269]. Simulated $t\bar{t}$ events passing the event selection and reconstruction criteria at the detector level that do pass or fail the particle-level criteria are referred to as "fiducial" $t\bar{t}$ or "non-fiducial" $t\bar{t}$ events, respectively.

5.1. Event selection

This analysis targets $t\bar{t}j$ events produced in the partonic process $qg \to t\bar{t}q$ that generates the energy asymmetry as described in section 2.3.4 with one hadronically and one leptonically decaying top quark in the boosted topology. The signature for these events consists of one high p_T top-tagged large-R jet from the hadronically decaying top quark, a charged lepton (electron or muon), missing transverse momentum and a small-R b-identified jet from the leptonically decaying top quark and an additional small-R jet.

Single-electron and single-muon triggers [270, 271] were used to reduce the event rate as described in section 3.2.5. Table 5.1 summarises the p_T, identification and isolation requirements for the applied trigger configurations. The transverse energy thresholds range from 24 to 140 GeV and from 20 to 50 GeV for electrons and muons, respectively, where some triggers with the lowest thresholds incorporate isolation requirements. The exact trigger configuration names are listed in table A.2 in appendix A.

The selected events are required to contain exactly one tight charged lepton l (electron or muon) with a transverse momentum above 27 GeV. Events containing additional baseline leptons with $p_T > 25$ GeV are vetoed. At particle level, there is no distinction between tight and baseline leptons.

To suppress events containing fake or non-prompt leptons at the detector level, the missing transverse energy is required to be larger than 20 GeV and the sum of E_T^{miss} and the reconstructed transverse W-boson mass m_T^W [1] is required to be larger than 60 GeV. These cuts are not applied at the particle level.

At least one top-tagged large-R jet with $p_T > 350$ GeV and a separation of $\Delta\phi(j_h, l) > 1.0$ to the lepton is required. The hadronic top-quark candidate j_h is defined as the highest p_T large-R jet satisfying these conditions. At the detector level, the contained top-tagger is used as described in section 4.1.4, while particle level large-R jets are considered to be top-tagged if they have a mass larger than 140 GeV and are b-flavoured as described in section 4.2.2.

Next, at least one small-R jet is required to be close to the lepton candidate l within $\Delta R(j_l, l) < 2.0$ and separated from the hadronic top-quark candidate with $\Delta R(j_l, j_h) > 1.5$. The leptonic top b-jet candidate j_l is defined as the highest p_T identified b-jet satisfying these conditions; in case no identified b-jet satisfies these conditions, the highest-p_T small-R jet is taken.

The associated jet candidate j_a is identified with the remaining highest-p_T small-R jet with $p_T > 100$ GeV that is separated from the hadronic top-quark candidate j_h, $\Delta R(j_a, j_h) > 1.5$, and the lepton, $\Delta R(j_a, l) > 0.4$. The cut value of 100 GeV was chosen to provide a trade-off between increasing asymmetries [74] and a decreasing statistical precision for increasing transverse momenta.

Furthermore, at least one small-R jet is required to be identified as a b-jet to suppress events originating from background processes. The probability to reject a $t\bar{t}$ signal event with two b-jets both of which are not identified is around 2% at the 85% b-tagging working point, while requiring two b-identified jets would increase this probability to about 28%. If exactly one small-R jet is identified as a b-jet, either the leptonic top b-jet candidate j_l or the hadronic top candidate j_h must be b-identified. The second condition is always fulfilled at the particle level due to the boosted hadronic top identification criteria. If two or more small-R jets are identified as b-jets, both candidates j_l and j_h must be identified as b-jets.

The event selection is summarised in table 5.2.

[1] The transverse W-boson mass is defined as $m_T^W = \sqrt{p_T^l E_T^{\text{miss}}(1 - \cos\Delta\phi)}$, where $\Delta\phi$ is the angle between the lepton candidate l and the missing transverse momentum vector $\vec{E}_T^{\text{miss}}$ in the plane transverse to the beam axis.

Table 5.2.: Selection of events with semi-leptonically decaying top quarks in the boosted topology. The selection criteria are identical at the detector and particle level, except for the E_T^{miss} and m_T^W requirements, which are applied only at the detector level, and the heavy flavour identification. The leptonically decaying top-quark candidate t_l is built from the four-vector sum of the lepton l, the neutrino ν and the small-R jet j_l. The neutrino ν is reconstructed from the missing transverse momentum and a constraint on the four-momenta of the W boson as described in section 5.2.1.

Object	Detector level	Particle level
1 lepton (e, μ) ℓ	$p_T > 27\,\text{GeV}$ no other leptons with $p_T > 25\,\text{GeV}$	
1 neutrino ν	$E_T^{\text{miss}} > 20\,\text{GeV}$ $E_T^{\text{miss}} + m_T^W > 30\,\text{GeV}$	-
1 large-R jet j_h	$p_T > 350\,\text{GeV}$ $\Delta\Phi(j_h, \ell) > 1.0$ top-tagged (DNN) $m(j_h) > 140\,\text{GeV}$, b-identified	
1 small-R jet j_l	$p_T > 25\,\text{GeV}$ $\Delta R(j_l, \ell) < 2.0$, $\Delta R(j_l, j_h) > 1.5$ prefer highest p_T b-identified jet	
1 small-R jet j_a	$p_T > 100\,\text{GeV}$ prefer highest p_T jet $\Delta R(j_a, j_h) > 1.5$	
≥ 1 identified b-jet	$= 1$: either j_l or j_h must be b-identified ≥ 2: both j_l and j_h must be b-identified	

5.2. Event reconstruction

5.2.1. Neutrino reconstruction

Neutrinos do not leave any trace in the detector and can thus not be directly reconstructed. The neutrino four-momentum is obtained from the missing transverse momentum described in section 4.1.5 and a constraint on the four-momenta of the W boson and its decay products [272]:

$$p_W = p_l + p_\nu \tag{5.1}$$

Squaring this equation and neglecting the invariant masses $p_l^2 = m_l^2$ and $p_\nu^2 = m_\nu^2$ leads to the following constraint on the z component of the neutrino four-momentum:

$$p_{z,\nu}^2 - 2\frac{\mu p_{z,l}}{E_l^2 - p_{z,l}^2} p_{z,\nu} + \frac{E_l^2 p_{T,\nu}^2 - \mu^2}{E_l^2 - p_{z,l}^2} = 0 \tag{5.2}$$

with $\mu = m_W^2/2 + p_{T,l} p_{T,\nu} \cos\Delta\phi$ where m_W is the W boson pole mass of 80.4 GeV [36] and $\Delta\phi$ the angle between the transverse momenta of the lepton and the neutrino.

This equation has two solutions:

$$p_{z,\nu}^{\pm} = \frac{\mu p_{z,l}}{p_{T,l}^2} \pm \sqrt{\frac{\mu^2 p_{z,l}^2}{p_{T,l}^4} - \frac{E_l^2 p_{l,\nu}^2 - \mu^2}{p_{T,l}^2}}, \tag{5.3}$$

If both solutions are real, the one with the smallest $|p_{z,\nu}|$ is chosen and the neutrino four-momentum is given by:

$$(E, p_{x,\nu}, p_{y,\nu}, p_{z,\nu}) = (|\vec{p}_\nu|, E_T^{\text{miss}} \cos\phi, E_T^{\text{miss}} \sin\phi, \min(|p_{z,\nu}^{\pm}|)) \tag{5.4}$$

In case the reconstructed transverse mass of the W boson is larger than the W-boson pole mass both solutions are complex. Assuming that the deviations arise from an imperfect E_T^{miss} reconstruction and that the charged lepton momentum is measured precisely, $p_{x,\nu}$ and $p_{y,\nu}$ are varied minimally from $E_T^{\text{miss}} \cos\phi$ and $E_T^{\text{miss}} \sin\phi$ in a kinematic fit, requiring $m_T^W = m_W$ to obtain a single real solution for $p_{z,\nu}$ [272].

5.2.2. $t\bar{t}j$ system

The hadronic top-quark candidate t_h is given by the large-R jet j_h satisfying the p_T, lepton separation, and top-identification requirements described in section 5.1. The leptonic top-quark candidate t_l is reconstructed from the sum of the four-momenta of the lepton candidate l, the reconstructed neutrino ν, and the leptonic top b-jet candidate j_l. The charge of the leptonic top candidate is given by the charge of the lepton, and the opposite charge is assigned to the hadronic top candidate. The associated jet j_a is given by the remaining highest-p_T small-R jet that is separated from j_h and l as described in section 5.1.

The $t\bar{t}j$ system is built from the sum of the four-momenta of t_h, t_l and j_a. To calculate ΔE, θ_j and θ_j^{opt} in equations 2.36, 2.38 and 2.39, respectively, these four-momenta are boosted into the $t\bar{t}j$ reference frame. The rapidity of the $t\bar{t}j$ system in the laboratory frame is denoted by $y_{t\bar{t}j}$.

6. Data and Monte Carlo samples

The following sections describe the data, signal, and background samples used in this thesis. All signal and background processes were modelled using MC simulations performed by the ATLAS collaboration as described in section 3.3, except for non-prompt and fake lepton backgrounds, which were estimated from data as explained in section 6.3.2. The decay of heavy hadrons was simulated with EvtGen [206] in all simulated samples except for those background samples generated with Sherpa [192]. The truth-level events (TRUTH) were further processed with a simulation of the detector response using either a full simulation with the GEANT4 [210] toolkit (FS) or a fast simulation with the ATLFAST-II [212] software (AF) as described in section 3.3.2. The simulation was performed independently for the data-taking periods 2015–2016, 2017 and 2018 to account for the different detector conditions and pile-up profiles.

Tables A.1 to A.12 in appendix A list all samples used in this analysis with the corresponding cross sections and event numbers. To ease data replication and to reduce computing time, these samples were further processed with the AnalysisBase [273, 274] framework to create smaller subsamples containing only the variables and events relevant for this analysis. These subsamples were stored at local disks and further analysed using private code [275].

6.1. Data samples

This analysis used the full Run 2 dataset at $\sqrt{s} = 13\,\text{TeV}$ collected with the ATLAS detector in the 2015–2018 data-taking period corresponding to a total integrated luminosity of $139\,\text{fb}^{-1}$ with an uncertainty of 1.7% [167]. Only those events certified to be of good quality for physics analysis [168] with all the ATLAS detector components being operational and stable LHC beam conditions were considered.

6.2. Signal modelling

Standard model top-quark pair production ($pp \to t\bar{t}$) samples were used to build the response matrix in the unfolding as explained in chapter 7, for the evaluation of modelling uncertainties described in chapter 8 and for data/MC comparisons presented in section 9.4.1. The SM and SMEFT predictions used for the evaluation of the measurement results in chapter 9 and for the SMEFT interpretation in chapter 10 were obtained from dedicated samples with jet-associated top-quark pair production ($pp \to t\bar{t}j$) events. An overview of all signal modelling samples used in this analysis is given in table 6.1.

6.2.1. Standard Model top-quark pair production

Standard Model top-quark pair production ($pp \to t\bar{t}$) events were generated with the POWHEG BOX V2 [200] generator, which provides matrix elements (MEs) at next-to-

Table 6.1.: Overview of $t\bar{t}$ and $t\bar{t}j$ samples used in this analysis. Shown are the dataset identifier (DSID), generator name, simulation type and purpose. More information on the cross sections and simulated number of events are listed in tables A.3 and A.12 in appendix A. The $t\bar{t}$ samples contain only the semi- and di-leptonic decay channels. To evaluate systematic uncertainties due to final state radiation, sliced samples filtered by the scalar sum of transverse momenta of all particle-level jets (H_T) were used. The mass variation, ME/PS matching and PS samples are subdivided into semi-leptonic and di-leptonic $t\bar{t}$ decay channels. The $t\bar{t}j$ samples contain only the semi-leptonic decay channel.

Sample	DSID	Generator	Type	Purpose
$t\bar{t}$	410470	Powheg+Pythia 8.2	FS	Nominal, FSR, ISR, PDF
	407342–44		FS	FSR (H_T slices)
	4010470		AF	Nominal
	411046, 411054		AF	$m_t = 172\,\text{GeV}$
	411049, 411057		AF	$m_t = 173\,\text{GeV}$
	410480, 410482		AF	$h_{\text{damp}} = 3\,m_t$
	411288		AF	ME/PS matching
	410464–65	Madgraph 5+Pythia 8.2	AF	ME/PS matching
	410557–58	Powheg+Herwig 7.04	AF	PS
$t\bar{t}j$	500336	Madgraph 5+Pythia 8.2	TRUTH	SM prediction (NLO)
	500934		TRUTH/AF	SM prediction (LO)
	500935–61		TRUTH/AF	SMEFT contributions

leading order (NLO) in the strong coupling constant α_S, using the NNPDF3.0nlo [118] PDF set. The renormalisation and factorisation scales were set to $\mu_R = \mu_F = \sqrt{m_t^2 + p_{T,t}^2}$ [276], and the h_{damp} parameter [277], which controls the transverse momentum of the first additional emission beyond the LO Feynman diagram in the parton shower (PS), was set to $1.5\,m_t$. For PS and hadronisation, these events were interfaced with Pythia 8.2 [193] using the A14 tuned parameter set [278] and the NNPDF2.3lo [118] PDF set.

The baseline or nominal $t\bar{t}$ samples were simulated with both the full and the fast detector simulation software. Various alternative samples used to estimate the $t\bar{t}$ modelling uncertainties were either obtained by reweighting the events in the nominal sample or simulated with the fast simulation software Atlfast-II [212]. Reweighted samples were generated by varying μ_R and μ_F independently by factors of 0.5 and 2.0, the strong coupling constant in the initial state ("Var3c"), in the final state, as well as the PDF set using the PDF4LHC [279] prescription. A variation of the PS and hadronisation model is provided by the Powheg Box v2 generator interfaced with Herwig 7.04 [191, 205] instead of Pythia 8.2, using the H7UE [191] tune and the MMHT2014lo [280] PDF set. The matching between the ME and PS was varied using the MadGraph5_aMC@NLO 2.6 [281] generator with the NNPDF3.0nlo PDF set interfaced with Pythia 8.2 using the A14 tune and the NNPDF2.3lo PDF set, as well as a variation of the h_{damp} parameter from $1.5\,m_t$ to $3\,m_t$ with the nominal generator. The impact of mass variations was studied with samples using the same settings

as for the nominal signal sample but a top-quark mass of 172 GeV and 173 GeV.

Except for the mass variation samples, all $t\bar{t}$ samples assume a top-quark mass of $m_t = 172.5\,\text{GeV}$ and were normalised to the inclusive production cross section of $\sigma(t\bar{t}) = 832 \pm 51\,\text{pb}$, calculated by Top++ 2.0 [282] at next-to-next-to-leading order (NNLO) in QCD including the resummation of next-to-next-to-leading logarithm (NNLL) soft-gluon terms [283–288]. The renormalisation and factorisation scale choice for all $t\bar{t}$ samples is identical to that of the nominal signal sample.

6.2.2. SM and SMEFT jet-associated top-quark pair production

Jet-associated top-quark pair production ($pp \to t\bar{t}j$) events were generated with MadGraph5_aMC@NLO 2.7 using the NNPDF3.0nlo PDF set with $\mu_R = \mu_F = m_t$. These events were further interfaced with Pythia 8.2 using the A14 tune and the NNPDF2.3lo PDF set. The SM prediction was obtained from matrix elements at NLO in α_S, while the SM-EFT interference and EFT-EFT contributions were generated at LO in α_S using the SMEFTatNLO [152] package. For robustness checks, the SM prediction was also obtained with the same settings as the SM-EFT and EFT-EFT contributions. To evaluate scale uncertainties, samples with nine different scale variations were generated by varying μ_R and μ_F independently by factors of 0.5 and 2.0.

The $t\bar{t}j$ samples were produced specifically for this analysis and contain only semi-leptonic $t\bar{t}$ events with at least one jet with $p_T > 70\,\text{GeV}$ at parton level and at least one top (or antitop) quark with $p_T > 300\,\text{GeV}$. Since the $t\bar{t}j$ events were mainly used for the interpretation of the energy asymmetry at particle level, most of these events were not processed with a detector-level simulation. For robustness studies of the unfolding procedure described in section 9.3.2, a subset of $t\bar{t}j$ events was processed with the Atlfast-II simulation software.

6.3. Background modelling

There are two classes of background events: Events with "prompt" or "real" leptons, i.e. electrons and muons produced in W- or Z-boson decays as described in section 6.3.1, and events with "fake" or "non-prompt" leptons arising from another source as described in section 6.3.2. Tables 6.2 and 6.3 summarise the background samples used in this analysis. Except for systematic variations of the single-top samples, all simulated background samples were processed with the full detector simulation software.

6.3.1. Backgrounds with prompt leptons

V+jets (W+jets and Z+jets)

The main background in this analysis originates from jet-assocated W-boson production, in which a leptonically decaying W boson might fake a leptonically decaying top quark, while the other jets can have a signature similar to that of a hadronically decaying top quark. Another background source are Z+jets events with a leptonically decaying Z boson, where one of the leptons is mis-identified or produced outside the detector acceptance. Figures 6.1 and 6.2 show exemplary leading order Feynman diagrams for W+jets and Z+jets production, respectively.

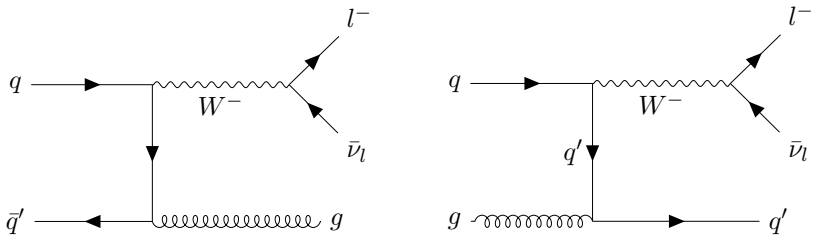

(a) W+jets ($q\bar{q}$) (b) W+jets (qg)

Figure 6.1.: Exemplary leading order Feynman diagrams for W+jets production with a subsequent W-boson decay in quark-antiquark annihilation (a) and quark-gluon fusion (b). Additional jets may arise from higher order corrections such as initial- and final-state radiation.

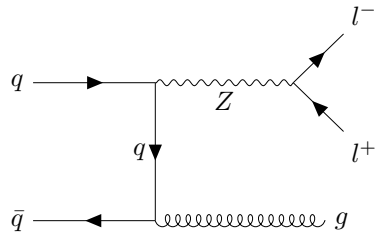

Figure 6.2.: Exemplary leading order Feynman diagram for Z+jets production with a leptonically decaying Z boson. Additional jets may arise from higher order corrections such as initial- and final-state radiation.

V+jets (W+jets and Z+jets) events with leptonically decaying W/Z bosons were simulated with Sherpa 2.2.1 [192] based on the NNPDF3.0nnlo [118] PDF set, containing up to 2 additional jets at NLO and 3-4 additional jets at LO. For W+jets events, reweighted samples were obtained by varying μ_R and μ_F up and down by a factor of 2, the ME to PS matching scale (CKKW) up and down by factors of 1.5 and 1.33, respectively, and the resummation scale for the parton shower (QSF) up and down by a factor of 4. Further reweighted samples were obtained by using a set of 100 PDF variations following the NNPDF3.0nlo description.

Single-top

Exemplary Feynman diagrams for single-top production in the s-, t-, and Wt-channels at leading order in the strong coupling constant α_S are shown in figure 6.3. In the dominating Wt-channel with a cross section of 71.7 ± 3.8 pb [289, 290], a virtual down-type quark produces a top-quark and a W boson, resulting in a final state very similar to that of $t\bar{t}$ production. For instance, a Wt-channel event with a hadronically decaying top quark and a leptonically decaying W boson and an additional bottom quark mimicking a leptonically decaying top quark cannot be distinguished from a semi-leptonically decaying $t\bar{t}$ event. The second most important single-top background is t-channel production with the highest single-top cross section of 216.99 ± 9.04 pb [289, 290]. A virtual W boson is exchanged between incoming up- and down-type quarks (antiquarks) from

Table 6.2.: Overview of V+jets (W+jets and Z+jets), $t\bar{t}H$, $t\bar{t}V$ and VV samples used in this analysis. Shown are the dataset identifier, generator name and simulation type. More information on the cross sections and simulated number of events can be found in tables A.4 to A.11 in appendix A. The V+jets samples are further subdivided by the maximum of the sum of the transverse momenta of all particle-level jets and the transverse momentum of the W/Z boson as well as the appearance of b-jets and c-jets. The $t\bar{t}H$, $t\bar{t}V$ and VV samples are further split by the decay channel.

Sample	DSID	Generator	Type
W+jets ($W \to e\nu$)	364170–83	Sherpa 2.2.1	FS
W+jets ($W \to \mu\nu$)	364156–69		
W+jets ($W \to \tau\nu$)	364184–97		
Z+jets ($Z \to ee$)	364114–27	Sherpa 2.2.1	FS
Z+jets ($Z \to \mu\mu$)	364100–13		
Z+jets ($Z \to \tau\tau$)	364128–41		
$t\bar{t}H$	346343–45	Powheg+Pythia 8.2	FS
$t\bar{t}V$ ($t\bar{t}W$)	410155	Powheg+Pythia 8.2	FS
$t\bar{t}V$ ($t\bar{t}Z$)	410156–57, 410218–20		
VV (WW)	363359–60	Powheg+Pythia 8.2	FS
VV (WZ)	363357–58, 363489		
VV (ZZ)	363355–56, 364250, 364253–55		

the proton. In the s-channel, which constitutes the smallest single top background contribution due to its small cross section of $10.32 \pm 0.40\,\text{pb}$ [289, 290], a virtual W boson is produced in $q\bar{q}'$-scattering that decays into a top and a bottom quark.

Single-top Wt-, s- and t-channel events were generated at NLO in α_S with Powheg-Box v2 using the NNPDF3.0nlo PDF set interfaced with Pythia 8.2 using the A14 tune and the NNPFD23lo PDF set. At NLO, final states like $tW\bar{b}$ appear that have Feynman diagrams identical to $t\bar{t}$ production as shown in figure 6.4 with a subsequent decay of the $\bar{t}$ into a $\bar{b}W$ pair. The interference between Wt and $t\bar{t}$ production was taken into account by application of the diagram removal scheme [291]. The renormalisation and factorisation scales were set to $\mu_R = \mu_F = \sqrt{m_t^2 + p_{T,t}^2}$ for Wt production and to $\mu_R = \mu_F = \sqrt{m_b^2 + p_{T,b}^2}$ for s- and t-channel production. All nominal single-top samples were simulated with both the full and fast detector simulation software.

The nominal single-top samples were reweighted by varying μ_R and μ_F independently by factors of 0.5 and 2.0 as well as the strong coupling constant in the initial-state shower (Var3c) to evaluate FSR and ISR systematic uncertainties. To evaluate PDF uncertainties, reweighted samples were obtained using the PDF4LHC prescription. Samples produced with the nominal generator interfaced with Herwig 7.04 using the H7UE tune and the MMHT2014lo PDF set instead of Pythia 8.2 were used to

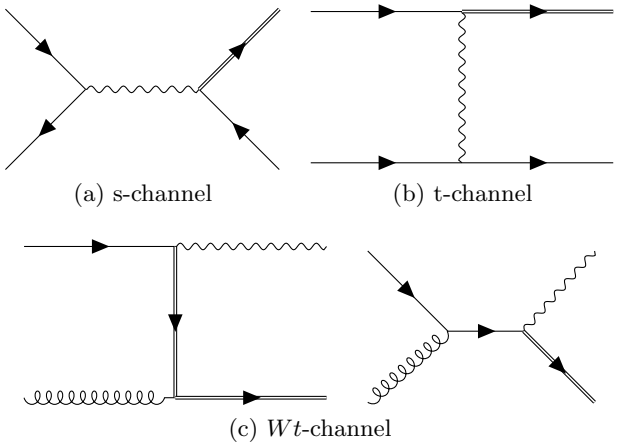

(a) s-channel (b) t-channel

(c) Wt-channel

Figure 6.3.: Leading order Feynman diagrams for single-top production. Double fermion lines indicate top quarks.

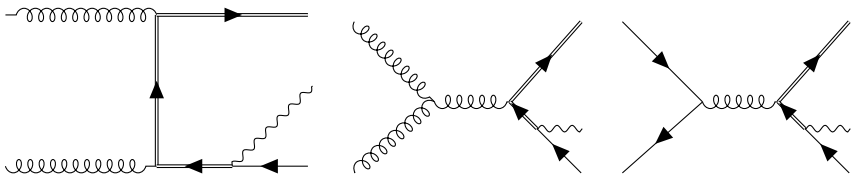

Figure 6.4.: Exemplary next-to-leading order Feynman diagrams for single-top Wt production that can be interpreted as $t\bar{t}$ production at leading order with a subsequent antitop-quark decay. Double fermion lines indicate top quarks.

estimate the impact of the PS and hadronisation model. Uncertainties from the PS/ME matching were estimated with a sample generated with MADGRAPH5_aMC@NLO 2.6 using the NNPDF3.0NLO PDF set interfaced with PYTHIA 8.2 using the A14 tune and the NNPDF2.3LO PDF set. Single-top Wt samples produced with the diagram subtraction (DS) scheme [291] instead of the DR scheme were used the evaluate the uncertainty due to this treatment of the interference.

$t\bar{t}X$

Top-antitop quark pairs can also be produced in association with a vector or a Higgs boson as shown in figure 6.5. Although the signature of $t\bar{t}X$ events is identical to top-quark pair production with an associated jet, these backgrounds are of minor importance due to much smaller cross sections.

The $t\bar{t}V$ and $t\bar{t}H$ events were simulated with MADGRAPH5_aMC@NLO 2.6 and POWHEGBOX, respectively, using the NNPDF3.0NLO PDF set, interfaced with PYTHIA 8.2 using the A14 tune and the NNPDF2.3LO PDF set.

Table 6.3.: Overview of single-top Wt-, s- and t-channel samples used in this analysis. Shown are the dataset identifier (DSID), generator name, simulation type and purpose. More information on the cross sections and simulated number of events can be found in tables A.8 and A.9 in appendix A. The POWHEG+PYTHIA samples are subdivided into events with top and antitop quarks.

Sample	DSID	Generator	Type	Purpose
Wt	410646, 410647	POWHEG+PYTHIA 8.2	FS	Nominal, FSR, ISR, PDF
	410654, 410655	POWHEG+PYTHIA 8.2	FS	DR/DS
	410646, 410647	POWHEG+PYTHIA 8.2	AF	Nominal
	412002	MADGRAPH5+PYTHIA 8.2	AF	ME/PS matching
	411036, 411037	POWHEG+HERWIG 7.04	AF	PS
s-channel	410644, 410645	POWHEG+PYTHIA 8.2	FS	Nominal, FSR, ISR, PDF
	410644, 410645	POWHEG+PYTHIA 8.2	AF	Nominal
	412005	MADGRAPH 5+PYTHIA 8.2	AF	ME/PS matching
	411034, 411035	POWHEG+HERWIG 7.04	AF	PS
t-channel	410658, 410659	POWHEG+PYTHIA 8.2	FS	Nominal, FSR, ISR, PDF
	410658, 410659	POWHEG+PYTHIA 8.2	AF	Nominal
	412006	MADGRAPH 5+PYTHIA 8.2	AF	ME/PS matching
	411033, 411032	POWHEG+HERWIG 7.04	AF	PS/hadronisation

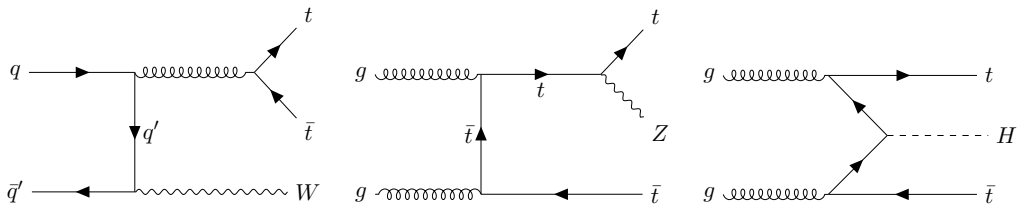

(a) $t\bar{t} + W$ (b) $t\bar{t} + Z$ (c) $t\bar{t} + H$

Figure 6.5.: Exemplary leading order Feynman diagrams for $t\bar{t} + W$ (a), $t\bar{t} + Z$ (b) and $t\bar{t} + H$ (c) production. Additional jets may result from higher order corrections such as initial- and final-state radiation.

Diboson

The production of two massive gauge bosons, WW, WZ and ZZ, constitutes another background channel similar to W+jets and Z+jets production. Figure 6.6 shows exemplary leading order Feynman diagrams for diboson production in the s-, t- and u-channel. Diboson events with at least one of the massive gauge bosons decaying leptonically were simulated with SHERPA 2.2.1 based on the NNPDF3.0NNLO PDF set, containing up to 1 additional jet at NLO and up to 3 additional jets at LO.

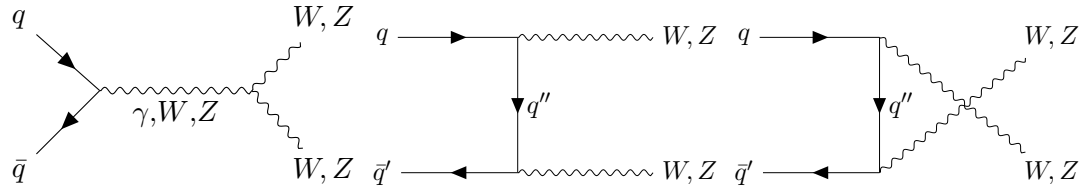

(a) s-channel (b) t-channel (c) u-channel

Figure 6.6.: Exemplary leading order Feynman diagrams for diboson production. Additional jets may result from higher order corrections such as initial- and final-state radiation.

6.3.2. Backgrounds with fake or non-prompt leptons

Events with non-leptonic objects that satisfy the lepton selection criteria ("fake" leptons) and non-prompt leptons constitute the so called "fake/non-prompt" lepton backgrounds. As the dominant source of these events is QCD multijet production with a cross section several orders of magnitude larger than for W-boson and top-quark production this background is hereafter referred to as "Multijet".

Non-prompt and fake electrons can originate from semi-leptonic decays of b- and c-hadrons, photon conversion and jets with large electromagnetic energy depositions [292]. The main contributions to non-prompt and fake muons come from semi-leptonic decays of b- and c-hadrons, charged hadron decays in the tracking volume or in hadronic showers and punch-through particles emerging from high-energy hadronic showers and reaching the MS.

The total contribution of events with fake or non-prompt leptons was estimated with the data-driven "matrix-method" [292]. This method relies on two tiers of lepton selection criteria, the "baseline" and "tight" criteria described in sections 4.1.2 and 4.1.3 for electrons and muons, respectively. The fractions of true prompt leptons and fake/non-prompt leptons passing the baseline criteria that do also pass the tight criteria are called the "real efficiency" (ϵ_r) and "fake efficiency" (ϵ_f), respectively. Baseline leptons that fail to satisfy the tight criteria are called "loose" leptons.

The relation between the measured numbers of tight and loose leptons, N^t and N^l, and the unknown numbers of prompt and fake leptons in the baseline sample, N_r^b and N_f^b, is given by:

$$\begin{pmatrix} N^t \\ N^l \end{pmatrix} = \begin{pmatrix} \epsilon_r & \epsilon_f \\ 1-\epsilon_r & 1-\epsilon_f \end{pmatrix} \begin{pmatrix} N_r^b \\ N_f^b \end{pmatrix} \tag{6.1}$$

Inversion of this matrix and using that $N_f^t = f N_f^b$ yields the number of fake leptons in the baseline sample:

$$N_f^b = \frac{1}{\epsilon_r - \epsilon_f} \left[(\epsilon_r - 1) N^t + \epsilon_r N^l \right] \tag{6.2}$$

from which the number of fake leptons in the tight sample can be determined as:

$$N_f^t = \epsilon_f N_f^b = \frac{\epsilon_f}{\epsilon_r - \epsilon_f} \left[(\epsilon_r - 1) N^t + \epsilon_r N^l \right] \tag{6.3}$$

Table 6.4.: Definition of signal and control regions used to determine the real (ϵ_r) and fake efficiencies (ϵ_f).

Selection	SR	CR ϵ_r	CR ϵ_f
N baseline leptons	$== 1$	$== 1$	$== 1$
N tight leptons	$== 1$	≥ 0	≥ 0
E_T^{miss}	$\geq 20\,\text{GeV}$	$\geq 20\,\text{GeV}$	$\leq 20\,\text{GeV}$
b-tagged jets	≥ 1	$== 0$	≥ 1

To determine the total number of fake leptons in the tight sample a "fake weight" w_i is defined for each single baseline-lepton event corresponding to eq. 6.3:

$$w_i = \begin{cases} \frac{\epsilon_f}{\epsilon_r - \epsilon_f}(\epsilon_r - 1) & \text{if the lepton in event } i \text{ is tight} \\ \frac{\epsilon_f \epsilon_r}{\epsilon_r - \epsilon_f} & \text{if the lepton in event } i \text{ is loose} \end{cases} \tag{6.4}$$

The total number of fake/non-prompt leptons in the tight sample is estimated by the sum of weights over all single baseline-lepton events observed in data:

$$N_f^t = \sum_{\text{events}} w_i \tag{6.5}$$

with a statistical uncertainty of

$$\sigma_{N_f^t} = \sqrt{\sum_i w_i^2} \tag{6.6}$$

The real and fake efficiencies are parametrised with respected to the p_T and $|\eta|$ of the lepton and measured separately for electrons and muons in the data-taking periods 2015/2016, 2017 and 2018. The efficiencies were extracted from control regions that are orthogonal to the signal region as shown in table 6.4.

The real efficiencies were obtained from simulated $t\bar{t}$ events, corrected for differences between data and simulation with scale factors measured in data [222, 293]. The control region consists of single baseline-lepton events with $E_T^{\text{miss}} > 20\,\text{GeV}$ and 0 b-tagged jets. The efficiency from real electrons (muons) ranges from 83% (77%) to 95% (95%), depending on the lepton p_T, $|\eta|$ and data-taking period. Figure 6.7 shows the real efficiencies for electrons and muons ranging from 83% to 95% and 77% to 95%, respectively.

The fake efficiencies were estimated using single baseline-lepton events in data, with a reversed requirement on the missing transverse momentum, $E_T^{\text{miss}} < 20\,\text{GeV}$, to suppress the real lepton contributions from W-boson and $t\bar{t}$ events. To calculate the efficiency, the estimated number of real prompt-lepton events from MC simulation was subtracted from the number of events with tight and baseline leptons in data before the ratio of these numbers was taken. The typical contribution of these real events is in the order of 20–30% and 40–60% for baseline and tight leptons, respectively. The efficiencies for fake/non-prompt electrons (muons) shown in figure 6.8 range from 23% (13%) to 59% (23%), depending on the lepton p_T, $|\eta|$ and data-taking period.

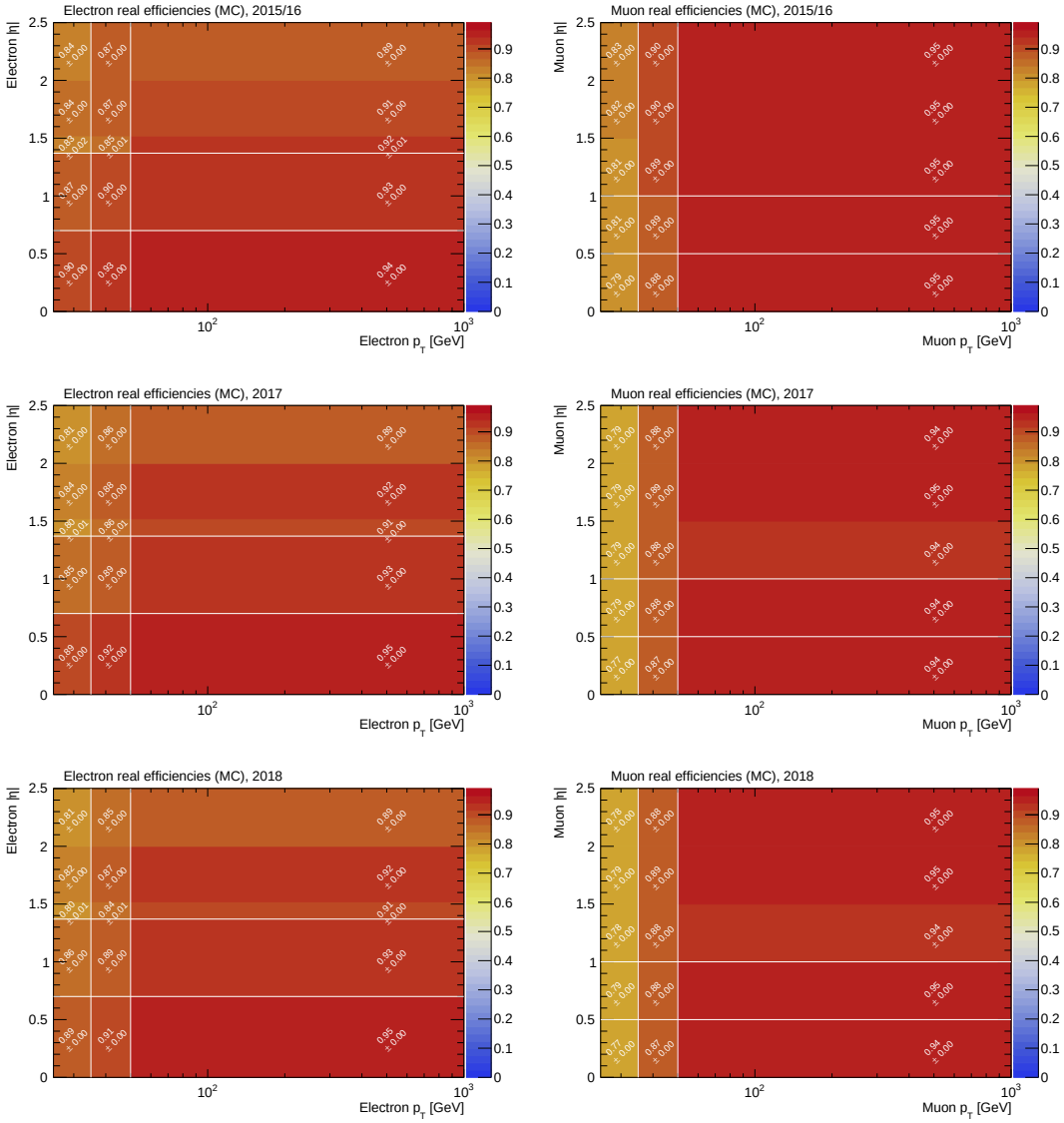

Figure 6.7.: Real efficiency, defined as the fraction of true prompt leptons passing the baseline criteria that do also pass the tight criteria, for electrons (left) and muons (right) for the 2015/16 (top), 2017 (middle) and 2018 (bottom) data-taking periods.

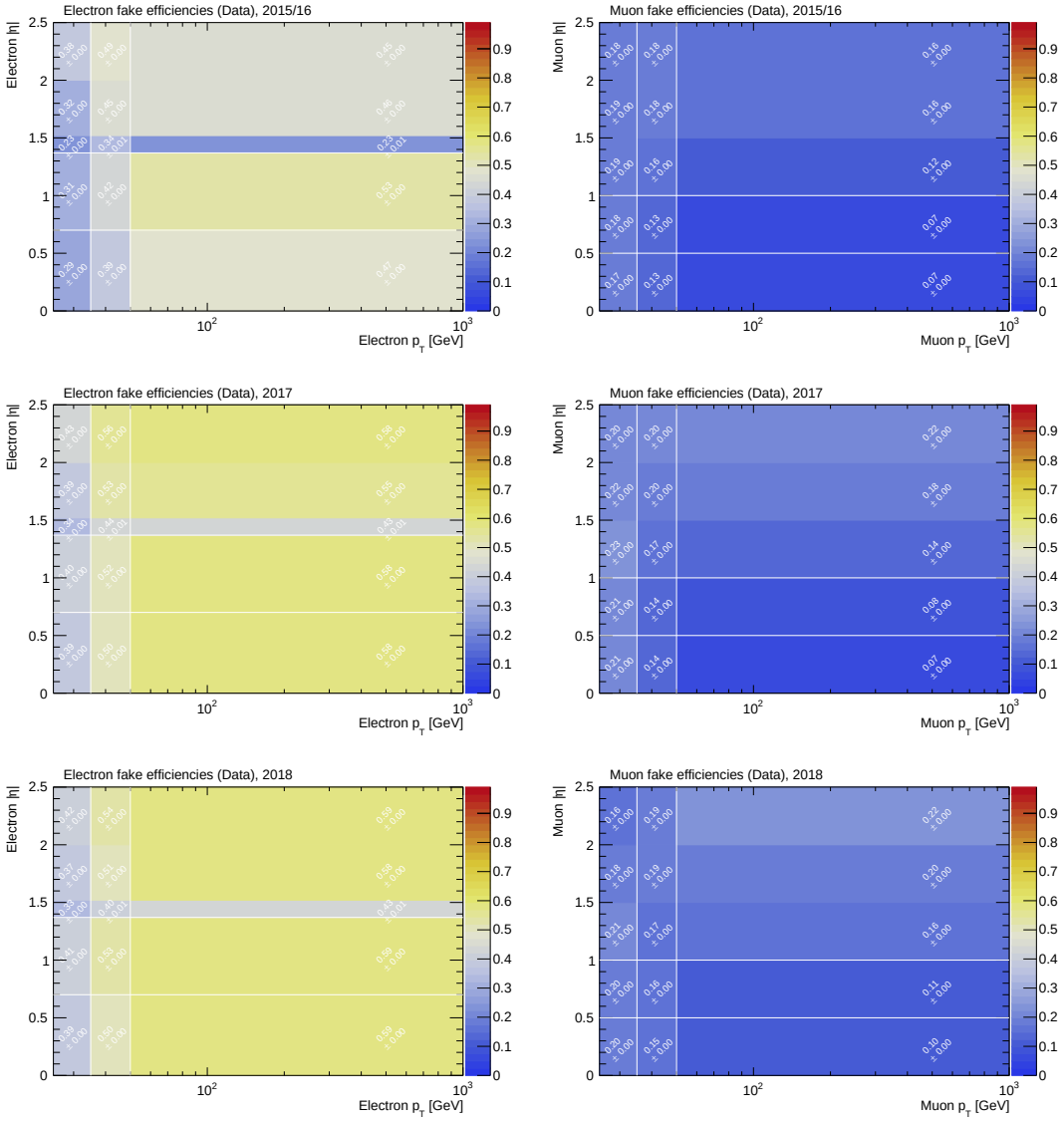

Figure 6.8.: Fake efficiency, defined as the fraction of fake/non-prompt leptons passing the baseline criteria that do also pass the tight criteria, for electrons (left) and muons (right) for the 2015/16 (top), 2017 (middle) and 2018 (bottom) data-taking periods.

7. Unfolding

The energy asymmetry is measured at the particle level, in the following also referred to as truth level, to facilitate the comparison with SM and BSM theory predictions as performed in chapters 9 and 10 without the need to simulate the detector response as well as with other experiments which exhibit different detector responses.

The process of correcting measured detector-level distributions for experimental effects like a finite reconstruction resolution, limited acceptance and efficiency, non-linear responses and mis-reconstructed events to bring them to the truth level is called "unfolding". The Fully Bayesian Unfolding (FBU) [61, 294] method provides the full posterior probability density for the truth-level distribution by application of Bayesian inference, taking into account experimental and modelling uncertainties. In this measurement, the ΔE vs. θ_j distribution is observed at the detector level and unfolded to the particle level, from which the posterior density of the energy asymmetry is calculated.

Section 7.1 introduces the key idea of the FBU method; the inclusion of systematic and statistical uncertainties are explained in sections 7.2 and 7.3, respectively. Sections 7.4 and 7.5 describe the sampling of the posterior density of the truth-level distribution and the calculation of the posterior density of the energy asymmetry, respectively.

7.1. Introduction

Given an observed detector-level spectrum $D \in \mathbb{N}^{N_r}$ with N_r bins, a background prediction $B \in \mathbb{N}^{N_r}$ and a response matrix $\mathcal{M} \in \mathbb{R}^{N_r} \times \mathbb{R}^{N_t}$, the posterior probability of the truth-level spectrum $T \in \mathbb{R}^{N_t}$ with N_t particle-level bins is given by application of Bayes' theorem:

$$P(T|D, \mathcal{M}, B) \propto \mathcal{L}(D|T, \mathcal{M}, B)\pi(T) \tag{7.1}$$

where $\mathcal{L}(D|T, \mathcal{M}, B)$ is the likelihood function of D conditional on T, $\mathcal{M}$ and B, and $\pi(T)$ is the prior probability density for the truth-level spectrum T, which reflects the experimentalist's knowledge about the truth-level distribution T before the measurement is performed. In this analysis a so-called "uninformative" prior with a uniform probability density is used as a conservative choice. With this flat prior equal probabilities are assigned to all T spectra within a wide range between zero and twice the SM prediction $\tilde{T}$:

$$\pi(T) \propto \begin{cases} 1 & \text{if } \mathrm{T}_i \in [0, 2\tilde{T}_i], \forall i \in [1, N_t] \\ 0 & \text{otherwise} \end{cases} \tag{7.2}$$

Let $R = (r_i) \in \mathbb{R}^{N_\mathrm{r}}$ and $B = (b_i) \in \mathbb{R}^{N_\mathrm{r}}$ denote the signal and background predictions, respectively, at the detector-level. Assuming that the number of observed data events d_i in bin i is Poisson distributed with mean $r_i + b_i$, the likelihood of observing the spectrum $D = (d_i)$ is given by the product of the Poisson probabilities for each bin:

$$\mathcal{L}(D|T, \mathcal{M}, B) = \prod_{i=1}^{N_\mathrm{r}} \mathrm{Pois}(d_i | r_i(T, \mathcal{M}) + b_i) \tag{7.3a}$$

$$\mathrm{Pois}(x|\lambda) = \frac{\lambda^x}{x!} e^{-\lambda} \tag{7.3b}$$

The signal distribution at the detector level R is related to the truth-level distribution T via the response matrix $\mathcal{M} = (m_{ij})$ that models the detector response:

$$r_i(T, \mathcal{M}) = \sum_{j=1}^{N_\mathrm{t}} m_{ij} t_j, \qquad m_{ij} = \frac{\epsilon_j p_{ij}}{f_{\mathrm{acc},i}} \tag{7.4}$$

with efficiency, migration matrix and acceptance fraction defined as follows:

- Efficiency $\epsilon = (\epsilon_j) \in \mathbb{R}^{N_t}$: ϵ_j is the efficiency for an event produced in truth-level bin j to be observed in any detector-level bin, i.e. the combined detector acceptance, reconstruction efficiency and selection efficiency
- Migration matrix $P = (p_{ij}) \in \mathbb{R}^{N_r} \times \mathbb{R}^{N_t}$: The element p_{ij} denotes the conditional probability for an event produced in truth-level bin j to be observed in detector-level bin i given that it is observed in any detector-level bin
- Acceptance fraction $f_\mathrm{acc} = (f_{\mathrm{acc},i}) \in \mathbb{R}^{N_r}$: $f_{\mathrm{acc},i}$ is the fraction of events passing the detector-level selection in bin i that satisfy the fiducial phase-space selection at particle level

Figure 7.1 depicts the concatenation of the three bins in θ_j, $[0, \pi/4, 3\pi/5, \pi]$, and the four bins in ΔE, $[-\infty, -100, 0, 100, \infty]$ GeV, to the twelve bins used for the detector- and particle-level distributions in the unfolding. This binning choice is discussed in section 9.3.3. The migration matrix, efficiencies and acceptances used in this analysis are shown in figures 7.2 and 7.3. The migration matrix is largely diagonal, indicating a well performing reconstruction; the mean efficiency and acceptance are $\epsilon = 34.4\,\%$ and $f_\mathrm{acc} = 69.6\,\%$, respectively. The resulting response matrix is shown in figure 7.4.

Figure 7.5 depicts the individual migration matrices for ΔE, $y_{t\bar{t}j}$ and θ_j for the non-optimised and optimised (see eq. 2.41) event yields. The largest migrations between bins appear for the energy difference between same-sign bins. The sign of ΔE is correctly reconstructed at the detector level in 94% of all cases. The sign of the rapidity of the $t\bar{t}j$ system, $y_{t\bar{t}j}$, is correctly reconstructed in 98% of all events. For the non-optimised event yield, the detector-level event is reconstructed in the correct θ_j bin in 95% of all cases, taking into account migrations in $y_{t\bar{t}j}$, this number reduces to 93%.

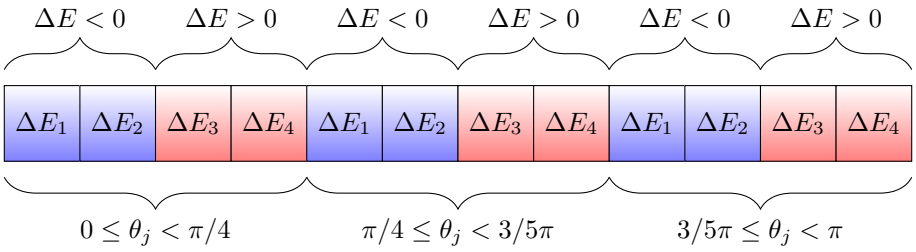

Figure 7.1.: Concatenation of the three bins in θ_j, $[0, \pi/4, 3\pi/5, \pi]$, and the four bins in ΔE, $[-\infty, -100, 0, 100, \infty]$ GeV, to the 12 ΔE vs. θ_j bins used both at the detector and the truth level.

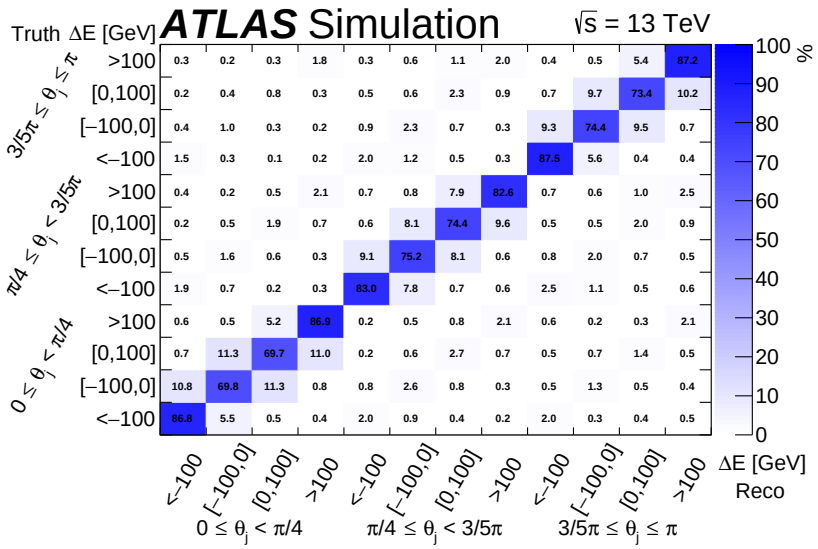

Figure 7.2.: Migration matrix $P = (p_{ij})$ as estimated with the SM $t\bar{t}$ sample. The elements p_{ij} denote the probability of a reconstructed event produced in truth-level bin j to be reconstructed in detector-level bin i. This figure was published as figure 4 in reference [83].

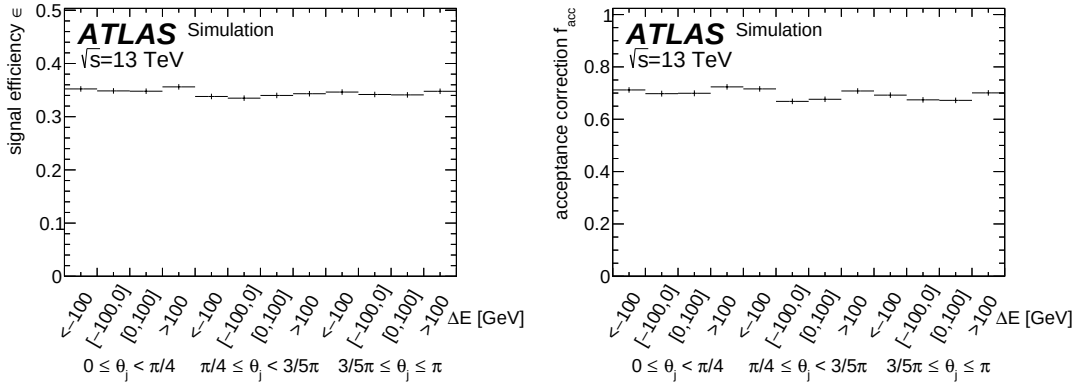

Figure 7.3.: Signal efficiency ϵ (left) and acceptance correction f_{acc} (right) in the particle- and detector-level bins, respectively, as estimated with the SM $t\bar{t}$ sample. MC statistical uncertainties are denoted by error bars. [83]

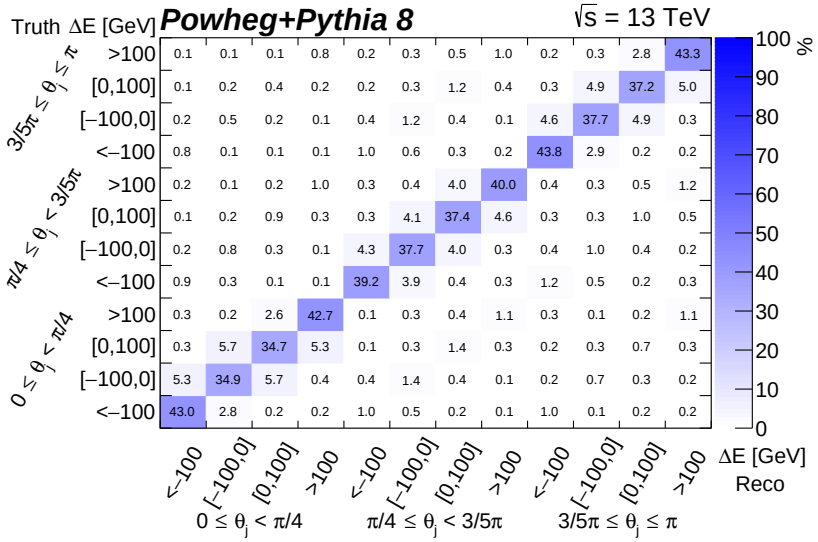

Figure 7.4.: Response matrix $\mathcal{M} = (m_{ij})$ as estimated with the SM $t\bar{t}$ sample. The elements m_{ij} are defined in eq. 7.4 as the product of the migration p_{ij}, the efficiency ϵ_j, and the inverse acceptance fraction $f_{\text{acc},i}$.

7.2. Systematic uncertainties

Systematic uncertainties are included by introducing nuisance parameters (NPs) $\theta = (\theta^k) \in \mathbb{R}^{N_\theta}$ with prior probability distribution $\pi(\theta)$ into the likelihood from eq. 7.3a:

$$\mathcal{L}(D|T, \mathcal{M}, B, \theta) = \prod_{i=1}^{N_\text{r}} \text{Pois}(d_i | r_i(T, \mathcal{M}, \theta) + b_i(\theta))) \tag{7.5}$$

Let $\theta = (\theta_s, \theta_b) \in \mathbb{R}^{N_{\theta_s}+N_{\theta_b}}$ be the vector of nuisance parameters $\theta_s = (\theta_s^i) \in N_\theta^s$ for uncertainties in the modelling, object identification, reconstruction and calibration and $\theta_b = (\theta_b^i) \in N_{\theta_b}$ the vector for background normalisation uncertainties; one for each of the $N_b = N_{\theta_b}$ background process. The detector-level signal prediction can then be written as:

$$r_i(T, \mathcal{M}, \theta) = r_i(T, \mathcal{M}, 0) \left(1 + \sum_{k=1}^{N_{\theta_s}} \theta_s^k \Delta r_i^k\right) \tag{7.6}$$

where $r_i(\text{T}, \mathcal{M}, 0)$ is defined as in eq. 7.4 and Δr_i^k is the relative systematic uncertainty on the number of signal events in bin i corresponding to the k-th nuisance parameter θ_s^k. Similarly, the detector-level background prediction in bin i is given by the sum over all background processes j:

$$b_i(\theta) = \sum_{j=1}^{N_b} b_i^j(\theta) \tag{7.7a}$$

$$b_i^j(\theta) = b_i^j(1 + \theta_b^j \Delta b^j) \left(1 + \sum_{k=1}^{N_{\theta_s}} \theta_s^k \Delta b_i^{j,k}\right) \tag{7.7b}$$

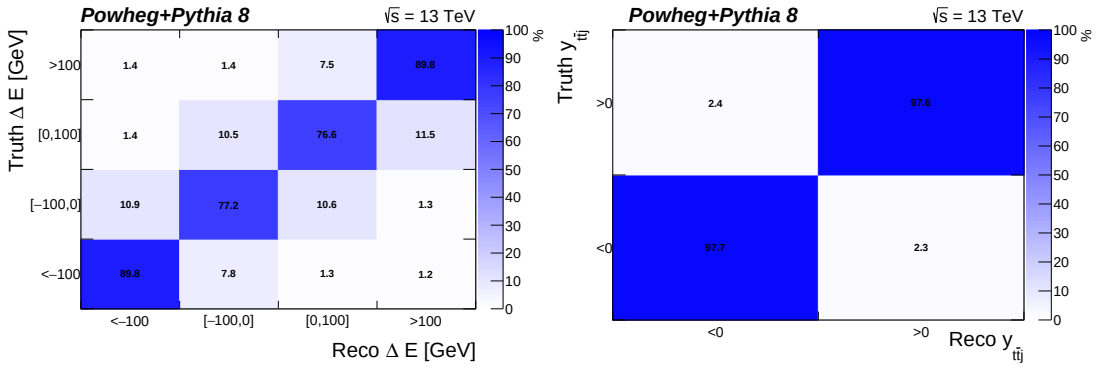

(a)

(b)

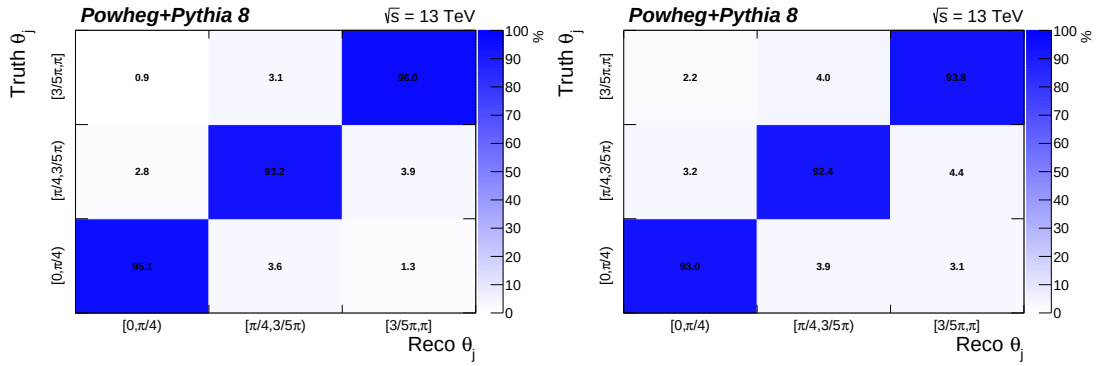

(c) Non-optimised event yield

(d) Optimised event yield

Figure 7.5.: Migration matrices for ΔE (a), the rapidity of the $t\bar{t}j$ system $y_{t\bar{t}j}$ (b), the jet scattering angle θ_j for the non-optimised (c) and the optimised (d) event yields; see eq. 2.41. The elements denote the probability of a reconstructed event produced in truth-level bin j to be reconstructed in detector-level bin i given that it is reconstructed in any detector-level bin.

where b_i^j is the nominal background prediction in bin i, Δb^j the relative uncertainty on the background normalisation corresponding to the nuisance parameter θ_b^j, and $\Delta b_i^{j,k}$ the relative systematic uncertainty in bin i corresponding to the k-th nuisance parameter θ_s^k. The nuisance parameters are not observed and thus integrated out to obtain the marginal likelihood; this process is also referred to as "marginalisation":

$$\mathcal{L}(D|T,\mathcal{M},B) = \int \mathcal{L}(D|T,\mathcal{M},B,\theta)\pi(\theta)\mathrm{d}\theta \tag{7.8}$$

A standard normal prior $\mathcal{N}(\mu = 0, \sigma = 1)$ is assumed for the nuisance parameters for all systematic uncertainties except for the background normalisation uncertainties, for which a truncated Gaussian distribution is used to avoid unphysical negative event yields for the background predictions which have normalisation uncertainties of up to 50%.

7.3. Statistical uncertainties on background predictions

The likelihood introduced in equations 7.3 and 7.5 does not reflect the fact that the background predictions suffer from statistical fluctuations due to limited sample sizes used in their estimation. These statistical uncertainties are taken into account with an approach similar to that outlined in references [295, 296] by introducing additional nuisance parameters $\gamma = (\gamma_i) \in \mathbb{R}^{N_\gamma \equiv N_r}$, one NP for each detector-level bin. The total background prediction in each bin i of the detector-level distribution in eq. 7.7 is multiplied by γ_i:

$$b_i(\theta, \gamma) = \gamma_i b_i(\theta) \tag{7.9}$$

The background estimation b_i with a statistical uncertainty of Δb_i corresponds to an auxiliary measurement of $\tau_i = (b_i/\Delta b_i)^2$ background events following a Poisson distribution with the same relative uncertainty $\Delta\tau_i/\tau_i = \Delta b_i/b_i$. The probability to obtain b_i in the background estimation from a population with mean $\gamma_i b_i$ can thus be written as $\mathrm{Pois}(\tau_i|\gamma\tau_i)$. This Poisson constraint is added to the likelihood in eq. 7.5:

$$\mathcal{L}(D|T, \mathcal{M}, B, \theta, \gamma) = \prod_{i=1}^{N_\mathrm{r}} \mathrm{Pois}(d_i|r_i(T, \mathcal{M}, \theta) + b_i(\theta, \gamma)))\mathrm{Pois}(\tau_i|\gamma\tau_i) \tag{7.10}$$

Since the nuisance parameters γ are not observed, they need to be integrated out of the likelihood like the other NPs:

$$\mathcal{L}(D|T, \mathcal{M}, B) = \int \mathcal{L}(D|T, \mathcal{M}, B, \theta, \gamma)\pi(\theta)\pi(\gamma)\mathrm{d}\theta\mathrm{d}\gamma \tag{7.11}$$

where $\pi(\gamma)$ is conservatively chosen as a flat prior similar to that of eq. 7.2 ranging from zero to two:

$$\pi(\gamma) \propto \begin{cases} 1 & \text{if } \gamma_i \in [0, 2], \forall i \in [1, N_r] \\ 0 & \text{otherwise} \end{cases} \tag{7.12}$$

7.4. Sampling

The posterior probability distribution of the truth-level spectrum, $P(T|D, \mathcal{M}, B)$, is determined from equations 7.1 and 7.10 by sampling the $N_q := N_t + N_\theta + N_\gamma$ dimensional parameter space with joint probability density

$$P(T, \theta, \gamma|D, \mathcal{M}, B) \propto \mathcal{L}(\mathcal{D}|\mathcal{T}, \mathcal{M}, \mathcal{B}, \theta, \gamma)\pi(T)\pi(\theta)\pi(\gamma) \tag{7.13}$$

and integrating out the nuisance parameters θ and γ:

$$P(T|D, \mathcal{M}, B) = \int P(T, \theta, \gamma|D, \mathcal{M}, B)\mathrm{d}\theta\mathrm{d}\gamma \tag{7.14}$$

Setting $q = (T, \theta, \gamma)$ and suppressing $\mathcal{M}$ and B in the notation, eq. 7.13 reads:

$$P(q|D) \propto \mathcal{L}(D|q)\pi(q) =: f(q) \tag{7.15}$$

The simplest possible sampling algorithms are grid sampling and uniform sampling, where $f(q)$ is evaluated at equally spaced positions and uniformly distributed random

points along each dimension, respectively. Markov Chain Monte Carlo (MCMC) methods [297] improve the efficiency by sampling relatively more points in regions with large likelihoods. The key idea of MCMC methods is to construct a Markov chain X whose distribution converges to the distribution one wants to sample from. A Markov chain is a sequence $(X_n)_{n\in\mathbb{N}}$ of random variables that depend only on their direct predecessor:

$$P(X_{n+1} = x_{n+1}|X_n = x_n, ..., X_0 = x_0) = P(X_{n+1} = x_{x+1}|X_n = x_n) \tag{7.16}$$

For homogenous Markov chains, the transition probability $P(X_{n+1} = x_{x+1}|X_n = x_n)$ is independent of n and can be interpreted as a Markov matrix K that defines a random walk where the probability to arrive at y after one step starting from x is given by $K(x, y) \equiv P(X_{n+1} = y|X_n = x)$. The Metropolis algorithm [298, 299] starts from a Markov matrix $J(x, y)$ to define the Metropolis matrix $K(x, y)$

$$K(x,y) = \begin{cases} J(x,y)\ \min\left(1, \frac{\pi(y)J(y,x)}{\pi(x)J(x,y)}\right) & \text{if } x \neq y, J(x,y) > 0 \\ 0 & \text{if } x \neq y, J(x,y) = 0 \\ 1 - \sum_{z\neq x} K(x,z), & \text{if } x = y \end{cases} \tag{7.17}$$

The fundamental theorem of Markov chains guarantees that the Markov chain defined by the matrix $K(x, y)$ converges to the distribution π, i.e. that the probability to observe $X_n = y$ is given by $\pi(y)$ as $n \to \infty$, independent of the starting state X_0. The problem of sampling from the posterior distribution π thus translates into the problem of sampling states from the Markov chain X, which can be performed with following algorithm [300]:

1. Start from an initial value $x_t = x$
2. Sample a new parameter value y from $J(x, y)$
3. Calculate the probability to accept the new parameter value y:

$$p_a(y, x) = \min\left(1, \frac{\pi(y)J(y,x)}{\pi(x)J(x,y)}\right) \tag{7.18}$$

4. Draw u from a uniform distribution on the interval $[0, 1]$ and set

$$x_{t+1} = \begin{cases} y \text{ if } p_a > u \\ x \text{ if } p_a \leq u \end{cases} \tag{7.19}$$

5. Repeat the sampling until the desired number of sampling steps is reached

The output of the sampling algorithm is a list of parameter values (x_i) that approximates the target distribution π. In the case of Fully Bayesian Unfolding, $x = q$ and the target distribution $\pi(x)$ is given by $P(q|D)$ which is defined in eq. 7.15 up to a normalisation factor that cancels out in the acceptance probability p_a.

The Hamiltonian Monte Carlo (HMC) [301, 302] method improves the sampling efficiency by transforming the random walk behaviour in the Metropolis algorithm to a simulation of Hamiltonian dynamics to increase the acceptance probability. In statistical mechanics, the probability to observe a system in a state with position q

and momentum p is proportional to $\exp(-H(q,p)/T)$, where the Hamiltonian H is the energy function and T the temperature of the system. Interpreting the parameters of interest q as particle positions, their negative logarithm corresponds to a potential energy function $U(q) = -\ln(P(q|D))$. To simulate Hamiltonian dynamics, auxiliary momentum variables $p \in \mathbb{R}^{N_q}$ are introduced together with a kinetic energy function $K(p) = \sum_i p_i^2/m_i$, where m_i denotes the variance of p_i. Setting $H(q,p) = U(q) + K(p)$ and $T = 1$ results in the following joint density of q and p:

$$P(q,p) \propto \exp(-H(q,p)) \tag{7.20}$$

Setting $x = (q,p)$ and $\pi(x) = P(q,p)$, the HMC method uses the Metropolis algorithm, with the random sampling of the proposed new parameter value being replaced by Hamiltonian dynamics: In the first step of an iteration, the momentum variable p is replaced by a random draw from a multivariate Gaussian distribution. In step 2, a new state $y = (q^\star, p^\star)$ is proposed based on a discrete time approximation of Hamilton's equations using L steps with stepsize ϵ. Since this proposal is symmetric, $J(x,y)$ and $J(y,x)$ cancel in step 3. Steps 4 and 5 are identical to the Metropolis algorithm. The parameters L and ϵ need to be chosen carefully; too large values of L result in trajectories that loop back, while too small values of L results in a random walk behaviour. Similarly, too large or small values of ϵ lead to low acceptance rates and wasted computation time due to too many simulation steps, respectively.

The No-U-Turn Sampler (NUTS) [303] used in this analysis avoids the need to hand-tune the number of steps L and the stepsize ϵ in the HMC method. To determine L, NUTS builds a binary tree $\mathcal{B}$ of position-momentum states until the trajectory makes a "U-turn", i.e. starts to loop back towards another position in the trajectory, or leads to states with a very low probability. At each sampling step t, $\mathcal{B}_t$ starts from a single node $x = (p,q)$ and doubles its number of points in each iteration j by choosing a random direction v_j drawn from a uniform distribution $U(\{-1,1\})$ and taking 2^j discrete Hamiltonian simulation steps of size $v_j\epsilon$. The binary tree is expanded until a continuation of the simulation would reduce the distance between the leftmost and rightmost states of any subtree. The proposed state $y = (q^\star, p^\star)$ is then randomly taken from the set of simulated points $\mathcal{B}_t$. The stepsize ϵ is adaptively tuned using the dual averaging scheme of Nesterov [304]. In this scheme, ϵ is updated after each sampling step t in the tuning phase such that the average acceptance probability of all the states in $\mathcal{B}_t$ converges to the target acceptance rate.

This analysis uses four Markov chains with each 10 000 sampling steps and 2 500 tuning steps, the latter of which are discarded in the final sample, resulting in 40 000 sampling points that approximate the posterior distribution defined in eq. 7.13. The target acceptance was set to 80%. Multiple chains were used to test convergence with the Gelman-Rubin statistic [305, 306] and to reveal possible multiple modes in the posterior. The technical implementation is based on the PyFBU code [307] that utilises the PyMC3 package [308].

Due to the limited number of sampling steps and the inherent randomness of sampling, the unfolded asymmetries and their uncertainties will slightly differ each time the unfolding is performed. In 200 repetitions of the unfolding procedure in data with identical settings, the relative numerical uncertainties on the unfolded results were found to be of the order of at most 0.5% and are thus negligble.

7.5. Asymmetry extraction

The output of the unfolding is a list of truth-level spectrum and nuisance parameter values, (T, θ, γ), with a sampling distribution approximating the joint probability distribution $P(T, \theta, \gamma | D, \mathcal{M}, B)$ defined in equation 7.13. The posterior probability distribution of the truth-level spectrum $P(T|D, \mathcal{M}, B)$ is obtained by integrating out the nuisance parameters as in eq. 7.14. The posterior probability distribution of the energy asymmetry can then be calculated as:

$$P(A_E(\theta_j)|D, \mathcal{M}, B) = \int \delta(A_E(\theta_j) - A_E(\theta_j, T)) P(T|D, \mathcal{M}, B)\, \mathrm{d}T$$

where $A_E(\theta_j, T)$ is defined as in eq. 2.38. In practice, the posterior distribution is obtained by calculating the energy asymmetry from the truth-level spectrum at each sampling point. The estimate and variance of the energy asymmetry A_E are given by the mean and variance of the posterior distribution. The marginalised posterior distributions of the nuisance parameters are given by projections on the corresponding one-dimensional nuisance parameter space.

8. Systematic uncertainties

Various theoretical and experimental uncertainties affect the signal and background predictions as described in sections 8.1 and 8.2, respectively. Section 8.3 explains the assignment of nuisance parameters to these uncertainties. Unless stated otherwise, all nuisance parameters have a Gaussian prior with mean 0 and standard deviation 1. The treatment of MC statistical uncertainties on the response matrix is explained in section 8.4; the inclusion of statistical uncertainties on the background predictions was discussed in section 7.3.

8.1. Theoretical uncertainties

The theoretical uncertainties considered in this analysis are uncertainties on the inclusive cross sections of the background predictions obtained from simulation as well as $t\bar{t}$, single-top and W+jets modelling uncertainties.

8.1.1. Inclusive cross sections

Nuisance parameters are assigned to the uncertainties in the inclusive cross sections of the background predictions obtained from simulation. The relative uncertainties for the two most important backgrounds, W+jets and single-top, are 5% [309] and 5.3% [289, 290], respectively. A conservative uncertainty of 50% [266] is applied to the remaining Z+jets, diboson, $t\bar{t}V$ and $t\bar{t}H$ samples, which contribute by only 3% to the total expected event yield. Since the predicted number of $t\bar{t}$ events does not enter the unfolding procedure, no nuisance parameter is assigned to the relative $t\bar{t}$ cross section uncertainty of 6.1% [282] which is applied in data/MC comparison plots in section 9.4.1.

8.1.2. $t\bar{t}$ signal modelling uncertainties

Signal modelling uncertainties affect the response matrix m_{ij} defined in eq. 7.4 that is used in the unfolding process. Due to the large number $N_r \times N_t$ of bins in this matrix, it is not feasible to estimate the systematic uncertainty in each of these bins in a statistically significant way. Instead, the impact of the systematic uncertainty on the signal distribution R is considered in the unfolding using eq. 7.6 as described in section 7.2. To decorrelate the impact on R due to the uncertainty in the response matrix and due to the uncertainty in the truth-level prediction, the nominal response matrix in eq. 7.4 is replaced by its systematic variation to obtain an estimate of the systematic variation of R due to the variation in m_{ij}:

$$r_i^{\text{syst.}}(\mathrm{T}, \mathcal{M}) = \sum_{j=0}^{N_r} m_{ij}^{\text{syst.}} t_j^{\text{nominal}} \tag{8.1}$$

Since the energy asymmetry is not affected by the total number of $t\bar{t}$ events, only the shape differences between the nominal and systematic variation of r_i are considered in the following. Thus, the systematic variations $r_i^{\text{syst.}}$ are normalised such that their sum over all detector level bins agrees with the total signal prediction in the nominal sample. Following $t\bar{t}$ signal modelling uncertainties were considered in this analysis, where the codes in brackets denote the dataset identifier (DSID) and the detector simulation method:

***$t\bar{t}$* parton shower and hadronisation modelling:** Uncertainties on the parton shower (PS) and hadronisation modelling were obtained from the shape-only difference of the Powheg+Pythia 8 (410470AF) and Powheg+Herwig 7.04 (411033AF, 411032AF) predictions.

***$t\bar{t}$* ME/PS matching:** Uncertainties on the NLO ME/PS matching procedure were estimated from a comparison between the Powheg and Madgraph 5 generators as well as a variation of the h_{damp} parameter from $1.5\,m_t$ to $3.0\,m_t$. Since the nominal Powheg+Pythia 8 (410470AF) sample was produced with different Pythia settings for top-quark decay matrix element corrections and global recoil in the showering than the Madgraph 5+Pythia 8 (410464AF and 410465AF) samples, the first comparison was performed with the dedicated Powheg+Pythia 8 (411288AF) sample. The systematic uncertainty from the h_{damp} variation is obtained from the shape-only difference between the dedicated Powheg+Pythia 8 (410480AF and 410482AF) predictions and the nominal Powheg+Pythia 8 (410470AF) prediction.

***$t\bar{t}$* FSR modelling:** Uncertainties on final-state radiation were obtained using alternative MC generator weights stored within the nominal Powheg+Pythia 8 (410470FS) $t\bar{t}$ sample which correspond to a variation of the renormalisation scale μ_R in the final-state shower by factors of 0.5 and 2.0. Since the FSR variations suffer from large statistical uncertainties, dedicated Powheg+Pythia 8 (407354FS, 407355FS, 407356FS) samples filtered by the scalar sum of transverse momenta of all particle-level jets (H_T) were used to increase the MC statistic.

***$t\bar{t}$* ISR modelling:** Three sources of uncertainty were considered for the modelling of initial-state radiation: variations of the strong coupling constant in the initial state shower up and down by 10%, represented by variations of the Var3c parameter set in Pythia 8.2, as well as independent variations of μ_R and μ_F up and down by a factor of 2. All these variations were obtained from internal weights of the nominal Powheg+Pythia 8 (410470FS) sample.

***$t\bar{t}$* parton distribution functions:** The uncertainties on parton distribution functions were evaluated with a set of 30 PDF variations using the PDF4LHC15 prescription. The PDF variations were obtained using alternative MC generator weights stored within the nominal Powheg+Pythia 8 (410470FS) sample. The systematic shift for each nuisance parameter is given by the symmetrised shape-only difference of the nominal and the varied predictions.

Top-quark mass: Uncertainties on the top-quark mass were considered by varying m_t up and down by 0.5 GeV [44] in dedicated Atlfast-II Powheg+Pythia 8 samples (411049AF, 411057AF and 411046AF, 411054AF) and comparing these predictions to the nominal Powheg+Pythia 8 (410470AF) prediction.

Table 8.1 summarises the $t\bar{t}$ signal modelling uncertainties used in this analysis.

Table 8.1.: Summary of $t\bar{t}$ signal modelling uncertainties. The ME/PS matching, PS & hadronisation and top-quark mass uncertainties were obtained by comparing dedicated samples simulated with ATLFAST-II. The FSR, ISR and PDF uncertainties were evaluated using alternative MC weights stored in the nominal POWHEG+PYTHIA 8 sample passed through the full detector simulation. The one- and two-sided systematic uncertainties were symmetrised as explained in section 8.3.2.

Uncertainty	Description	Type
ME/PS matching	POWHEG+PYTHIA 8 vs. MADGRAPH 5+PYTHIA 8	one-sided
	Variation of h_{damp} from $1.5\,m_t$ to $3.0\,m_t$	one-sided
PS & hadronisation	POWHEG+PYTHIA 8 vs. POWHEG+HERWIG 7.04	one-sided
FSR	Variation of μ_R up and down by a factor of 2	two-sided
ISR	Variation of α_S up and down by 10%	two-sided
	Variation of μ_R up and down by a factor of 2	two-sided
	Variation of μ_F up and down by a factor of 2	two-sided
PDF	30 PDF variations (PDF4LHC)	one-sided
Top-quark mass	Variation of m_t up and down by 0.5 GeV	two-sided

8.1.3. Single-top modelling uncertainties

The following single-top modelling uncertainties were obtained from the samples described in section 6.3.1:

Single-top parton shower and hadronisation modelling: The uncertainty in the PS and hadronisation modelling was estimated by the difference of the POWHEG+PYTHIA 8 (410644–47AF, 410658–59AF) and POWHEG+HERWIG 7.04 (411032–411037AF) predictions.

Single-top ME/PS matching: Uncertainties on the NLO ME/PS matching procedure were estimated by the difference of the POWHEG+PYTHIA 8 (410644–47AF, 410658–59AF) and MADGRAPH 5+PYTHIA 8 (412002–412005AF) predictions.

Single-top FSR modelling Uncertainties in the modelling of FSR were obtained using alternative MC generator weights stored within the nominal POWHEG+PYTHIA 8 (410644–47FS, 410658–59FS) samples which correspond to up and down variations of the renormalisation scale μ_R in the final-state shower by a factor of 2.

Single-top ISR modelling: Uncertainties in the ISR modelling were estimated from alternative MC generator weights stored within the nominal POWHEG+PYTHIA 8 (410644–47FS, 410658–59FS) samples which correspond to three sources of uncertainty: variations of the PYTHIA 8.2 Var3c eigentune, corresponding to up and down variations of the strong coupling constant in the initial-state shower by 10%, as well as independent variations of μ_R and μ_F up and down by a factor of 2.

Single-top parton distribution functions: The uncertainties on parton distribution functions were evaluated using a set of 30 PDF variations in the PDF4LHC15 prescription obtained using alternative MC generator weights stored within the nominal POWHEG+PYTHIA 8 (410644–47FS, 410658–59FS) samples. The PDF uncertainties

Table 8.2.: Summary of single-top modelling uncertainties. The ME/PS matching, PS & hadronisation and Wt diagram removal (DR/DS) uncertainties were evaluated by comparing dedicated samples. The FSR, ISR and PDF uncertainties were obtained using alternative MC weights stored in the nominal Powheg+Pythia 8 sample. Single-top PDF uncertainties are fully correlated with the $t\bar{t}$ PDF uncertainties. All one- and two-sided systematic uncertainties were symmetrised as explained in section 8.3.2.

Uncertainty	Description	Type
PS & hadronisation	Powheg+Pythia 8 vs. Powheg+Herwig 7.04	one-sided
ME/PS matching	Powheg+Pythia 8 vs. Madgraph 5+Pythia 8	one-sided
FSR	Variation of μ_R up and down by a factor of 2	two-sided
ISR	Variation of α_S up and down by 10%	two-sided
	Variation of μ_R up and down by a factor of 2	two-sided
	Variation of μ_F up and down by a factor of 2	two-sided
PDF	30 PDF variations (PDF4LHC)	one-sided
Wt DR/DS	Powheg+Pythia 8 DR vs. DS	one-sided

were treated as fully correlated between the s-, t- and Wt-channels as well as with $t\bar{t}$ production. Since their effect is already included in the cross-section uncertainty, only the shape differences between the varied and nominal predictions were considered.

Single-top Wt-channel overlap removal The MC samples used for $t\bar{t}$ and single top Wt-channel production contain an overlap in the final state described in section 6.3.1 which is accounted for by the diagram removal (DR) [291] approach. An alternative approach, the diagram subtraction (DS) [291], leads to a different prediction of the single-top contribution. An uncertainty due to this treatment of the interference was estimated by the difference between Powheg+Pythia 8 predictions using the DR (410646–47FS) and the DS (410654–55FS) approaches.

Except for the PDF uncertainties, all of the above uncertainties were considered to be uncorrelated across the different production channels. Table 8.2 summarises the single-top modelling uncertainties.

8.1.4. W+jets modelling uncertainties

The following W+jets modelling uncertainties were obtained from reweighting the nominal Sherpa 2.2.1 samples described in section 6.3.1:

***W*+jets parton shower:** The uncertainty in the QSF scale used for resummation of soft gluon emissions [310] was estimated by varying the scale parameter up and down by a factor of 2.

***W*+jets ME/PS matching:** The uncertainty in the ME/PS matching was evaluated by varying the matrix element matching scale (CKKW) [310] up and down by factors of 1.5 and 1.33, respectively.

Table 8.3.: Summary of W+jets modelling uncertainties. All W+jets modelling uncertainties were obtained using alternative MC weights stored in the nominal Sherpa 2.2.1 sample and were symmetrised as described in section 8.3.2.

Uncertainty	Description	Type
Parton shower	Variation of the QSF scale up and down by a factor of 2	two-sided
ME/PS matching	Variation of the CKKW scale up and down by factors of 1.5 and 1.33	two-sided
ME scale	Variation of μ_R up and down by a factor of 2	two-sided
	Variation of μ_F up and down by a factor of 2	two-sided
HF composition	30% norm. uncertainty on W+b and W+c events	one-sided
PDF	100 PDF variations (NNPDF3.0)	one-sided

***W*+jets ME scale uncertainties:** Both the renormalisation μ_R and factorisation μ_F scales were varied independently up and down by a factor of 2 [310].

***W*+jets heavy-flavour (HF) composition:** The uncertainty in the fraction of W+jets events containing jets originating from b- or c-quarks was taken into account by filtering the W+jet events into separate W+b, W+c and W+light samples and varying the individual normalisation of the HF samples up and down by 30% [311]. The filtering was performed based on the number of particle-level b- and c-jets in the event: W+b events contain at least one particle-level b-jet, W+c events at least one c- but no b-jet, and W+light events only light-flavour jets. The relative fraction of events in the signal region is 33.4%, 45.3% and 21.3%, respectively.

***W*+jets parton distribution functions:** The uncertainties on parton distribution functions were evaluated using a set of 100 PDF variations following the NNPDF3.0 [118] description, obtained using alternative MC generator weights stored within the nominal Sherpa 2.2.1 samples. Since their effect is already included in the cross-section uncertainty, only the shape differences between the varied and nominal predictions were considered.

Table 8.3 summarises the W+jets modelling uncertainties.

8.2. Experimental uncertainties

The following sections describe the experimental uncertainties on the integrated luminosity, the pile-up estimation, and the reconstruction of the lepton, jets, and missing transverse energy.

8.2.1. Luminosity

One nuisance parameter was assigned to the uncertainty in the combined 2015–2018 integrated luminosity of 1.7% [167], obtained using the LUCID-2 detector [312]. This uncertainty affects only the background prediction estimated from simulation which was scaled by the luminosity as described in section 3.3.3.

8.2.2. Pile-up

One nuisance parameter was assigned to the up and down variations of the pile-up weight used to correct the instantaneous luminosity distribution in MC as described in section 3.3.3.

8.2.3. Leptons

Efficiencies: Lepton identification, reconstruction, isolation, and trigger scale factors [222, 226] were applied to detector-level events as described in sections 3.3.3, 4.1.2 and 4.1.3. Twelve nuisance parameters were assigned to these uncertainties; one nuisance parameter for each scale factor for electrons and two nuisance parameters for each scale factor for muons, reflecting statistical and systematic uncertainties.

Energy and momentum scale and resolution: Systematic uncertainties in the energy and momentum scale and resolution corrections [225, 226] described in sections 4.1.2 and 4.1.3 were taken into account with two nuisance parameters for electrons and five nuisance parameters for muons.

The electron energy scale and resolution uncertainties are related to pile-up, the calibration of the calorimeter layers, the material in front of the calorimeter, non-linearity of the cell energy measurement, and modelling of the shower shape on the electron energy scale and resolution corrections. The systematic uncertainty in the energy scale ranges from 0.03% to 0.2% and increases with $|\eta|$. The relative uncertainty in the energy resolution ranges from 5% for electrons with $30\,\text{GeV} < E_T < 60\,\text{GeV}$ to 50% for high-energetic electrons.

The muon momentum scale and resolution uncertainties correspond to the variation of several fit parameters as well as misalignments of the MS chambers. The uncertainties in the momentum scale varies from 0.05% for $|\eta| < 1$ to 0.3% for $|\eta| \approx 2.5$; the momentum resolution uncertainty ranges from 1.7% to 2.9%.

8.2.4. Jets

Jet energy scale and resolution: Small-R and large-R jets were calibrated as described in section 4.1.4. Uncertainties on the jet energy scale from the in-situ measurements like analysis selection cuts, event topology dependence, simulation mis-modelling, statistical limitations and uncertainties in the calibration of the electrons, muons and photons were taken into account by 15 (16) effective nuisance parameters for small-R (large-R) jets [233, 234]. These effective nuisance parameters were obtained from an eigenvector decomposition of the combined covariance matrix and are grouped into detector, statistical, modelling and mixed uncertainty sources. 18 nuisance parameters cover the uncertainties on pile-up, flavour dependence, and additional effects. The systematic uncertainty on the jet energy scale ranges from 1% to 5% for small-R jets [234] and from 1% to 2% for large-R jets [233].

Jet mass scale and resolution: The relative uncertainty on the jet mass scale (JMS) and jet mass resolution (JMR) range from 1%–5% [233] and 10%–20% [240], respectively. There are 18 NPs for uncertainties on the JMS, seven related to the forward folding method, nine to the R_{trk} method and one to the event topology. 11 NPs were considered for the JMR uncertainties. The dominating uncertainties originate from parton shower and hadronisation modelling.

Jet-vertex-tagging: One nuisance parameter was assigned to variations of the JVT weight described in sections 3.3.3 and 4.1.4, reflecting a 2% systematic uncertainty on the hard-scatter jet efficiency due to potential mis-modelling of the JVT distribution in simulation.

B-tagging: Uncertainties affecting the b-, c- and light-jet b-tagging efficiencies from statistical sources and systematic uncertainties related to the detector calibration and physics modelling were taken into account by an eigenvector decomposition of the full covariance matrix in bins of jet p_T [220]. These eigenvector variations were applied to the b-tagging scale factors described in section 4.1.4, together with the uncertainty from the extrapolation to higher p_T regions above 400 GeV. There are nine, four and four nuisance parameters on the b-, c- and light-jet b-tagging efficiencies, respectively, as well as two nuisance parameters on the extrapolation.

Top-tagging: Uncertainties on the $t\bar{t}$, multijet and γ+jet modelling, large-R jet energy scale and jet energy resolution, flavour-tagging uncertainties and other detector experimental uncertainties on the top-tagging scale factors described in section 4.1.4 were taken into account by up and down variations of the scale factors according to the uncertainty sources. There are 18 nuisance parameters covering these variations.

8.2.5. Missing transverse energy

Two nuisance parameters are assigned to the total uncertainty on the scale and resolution of the soft track components of E_T^{miss} [263]. All remaining components are associated with reconstructed objects and affected by the corresponding uncertainties.

8.3. Smoothing, symmetrisation and pruning

The following sections describe the smoothing procedure applied to mitigate effects due to statistical fluctuations in the modelling uncertainty estimates, the symmetrisation of systematic uncertainties and the assignment of nuisance parameters, as well as a pruning method to reduce the number of nuisance parameters to save computing time in robustness studies.

8.3.1. Smoothing

In order to mitigate effects due to statistical fluctuations in the MC samples used to estimate modelling systematic uncertainties a "smoothing" procedure was applied. To assess the statistical significance of the systematic variation in a given bin of the detector-level ΔE vs. θ_j distribution, defined as the relative difference between nominal and systematically varied event yields, a bootstrapping method similar to that outlined in reference [313] was used. For each event, n weights were drawn from a Poisson distribution with mean 1 and the event was reweighted by each of these weights, resulting in n replicas of the nominal and systematically varied distributions. The random number generator was seeded with the event number and dataset identifier such that identical events received identical reweightings to account for correlations between samples simulated with the same generator.

The smoothing procedure was applied independently in each of the three θ_j bins, starting with four ΔE bins. The uncertainty in a ΔE bin is considered to be statistically significant if it is more than two standard deviations away from 0. This $2\,\sigma$ criterion

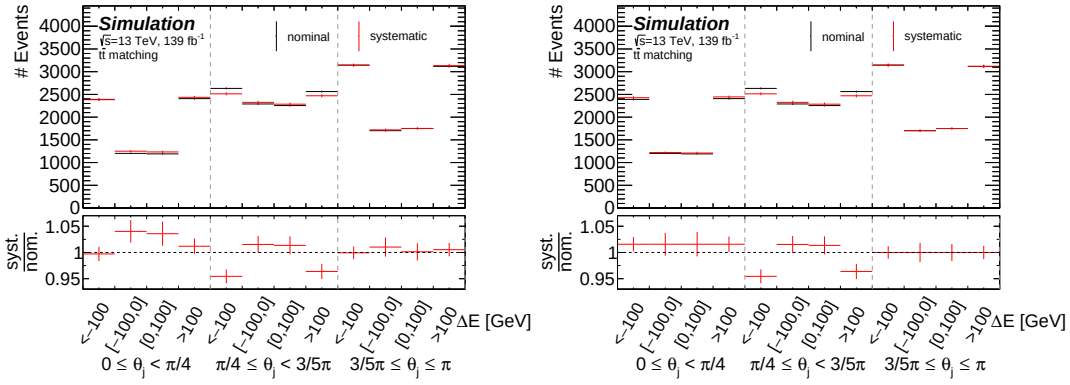

(a) before smoothing (b) after smoothing

Figure 8.1.: $t\bar{t}$ matching uncertainty before (left) and after (right) smoothing. The error bars correspond to the MC statistical uncertainty estimated as the standard deviation of the corresponding replicas.

gives a probability of $1 - 0.95^4 = 19\%$ that an uncertainty caused by a statistical fluctuation passes the significance criterion; a 1σ criterion would give a probability of 80%.

If the uncertainty in at least one of the four ΔE bins in a θ_j bin is significant, the uncertainty in all four bins is left unchanged. Otherwise, the same-sign ΔE bins are merged, resulting in two ΔE bins. If any of these have a statistically significant uncertainty, the uncertainties of these two bins are applied to the corresponding unmerged bins. Otherwise, all four ΔE bins are merged. If the uncertainty on the combined bin is significant, the uncertainty in all four bins is set to this value, effectively removing the shape of the systematic uncertainty, but keeping its normalisation.

The application of the smoothing procedure for the $t\bar{t}$ matching uncertainty is illustrated in figure 8.1. From the four ΔE bins in the central θ_j bin, the uncertainty in at least one of the four ΔE bins is statistically significant by more than two standard deviations, such that the uncertainties were kept unchanged. In the first θ_j bin, only the uncertainty on the combination of the four ΔE bins was found to be statistically significant, thus the same relative uncertainty was applied to all four bins. In the last θ_j bin, neither the individual bins nor the merged combinations were found to be statistically significant; thus the uncertainty was set to zero in all four ΔE bins.

Figure 8.2 shows the application of the smoothing procedure on the $t\bar{t}$, W+jets and single-top modelling uncertainties. In most cases, systematic uncertainties obtained from reweighted events tend to be statistically significant due to the high correlation between the systematically-shifted and the nominal distributions resulting in a small statistical uncertainty. For $t\bar{t}$ modelling, the parton shower "AFPH7", matching "h_{damp}" and mass variation systematic uncertainties were found to be statistically insignificant and were thus removed. The systematic uncertainties based on reweighting were mostly kept, while the FSR uncertainty was smoothed away in all but the central θ_j bin due to a large spread of FSR weights resulting in a non-negligible statistical uncertainty despite the correlation with the nominal distribution. For W+jets, all of the systematic variations are statistically significant, except for the up variations of the factorisation and renormalisation scales in the central θ_j bin.

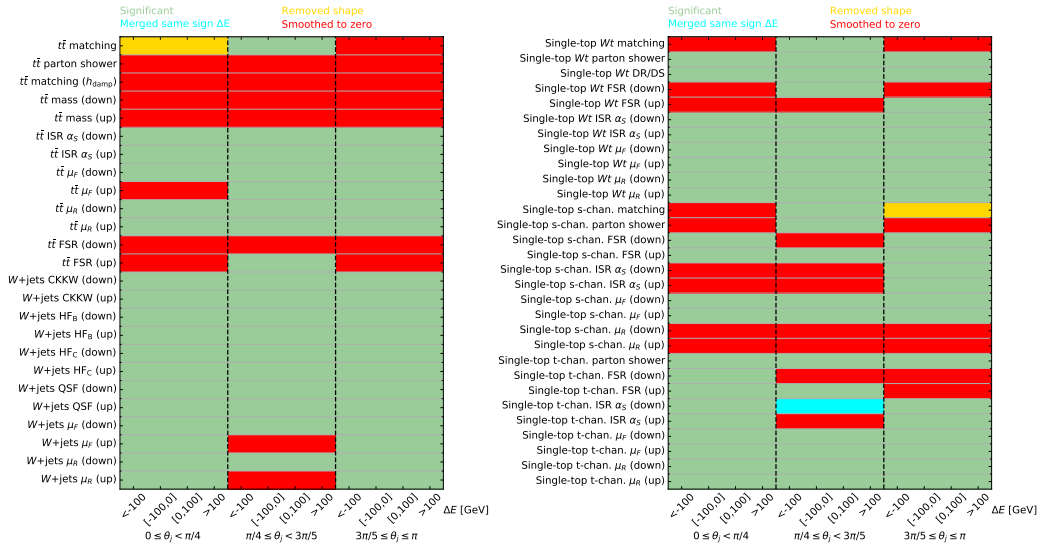

Figure 8.2.: Smoothing for the $t\bar{t}$, W+jets (left) and single-top (right) modelling uncertainties. The smoothing procedure is applied independently in the three θ_j bins. Systematic variations in green are found to be statistically significant and are thus kept unaltered, while those in red are set to zero. Same-sign ΔE bins are merged for blue variations. For systematic variations in yellow, the shape information is removed by merging all four ΔE bins

8.3.2. Symmetrisation

Systematic uncertainties are included in the FBU via nuisance parameters as described in section 7.2. For each nuisance parameter and sample, a relative systematic uncertainty Δr_i or Δb_i is assigned in each bin i of the ΔE vs. θ_j detector-level distributions in equations 7.6 and 7.7. For one-sided systematics, this uncertainty in bin i is given by the relative difference of the systematically-shifted $r_i^{\text{syst.}}$ and nominal $r_i^{\text{nom.}}$ detector-level event yields:

$$\Delta r_i = \frac{r_i^{\text{syst.}} - r_i^{\text{nom.}}}{r_i^{\text{nom.}}} \tag{8.2}$$

For two-sided variations, the average absolute difference between the up- and down-sided variation with respect to nominal is taken as magnitude of the uncertainty,

$$|\Delta r_i| = \frac{|r_i^{\text{up}} - r_i^{\text{nominal}}| + |r_i^{\text{down}} - r_i^{\text{nominal}}|}{2} \tag{8.3}$$

where the sign of Δr_i is given by the sign of the difference of the up and down variations:

$$\text{sign}(\Delta r_i) = \text{sign}(r_i^{\text{up}} - r_i^{\text{down}}) = \frac{r_i^{\text{up}} - r_i^{\text{down}}}{|r_i^{\text{up}} - r_i^{\text{down}}|} \tag{8.4}$$

Similar equations hold for the background prediction b_i and its uncertainty Δb_i.

The information on the sign of the relative uncertainty in all bins of the reconstruction level distribution ensures the preservation of the correlation structure between the bins. Figure 8.3 illustrates the symmetrisation of the $t\bar{t}$ FSR uncertainty before and after smoothing. All $t\bar{t}$ modelling uncertainties after smoothing and symmetrisation are shown in figure 8.4.

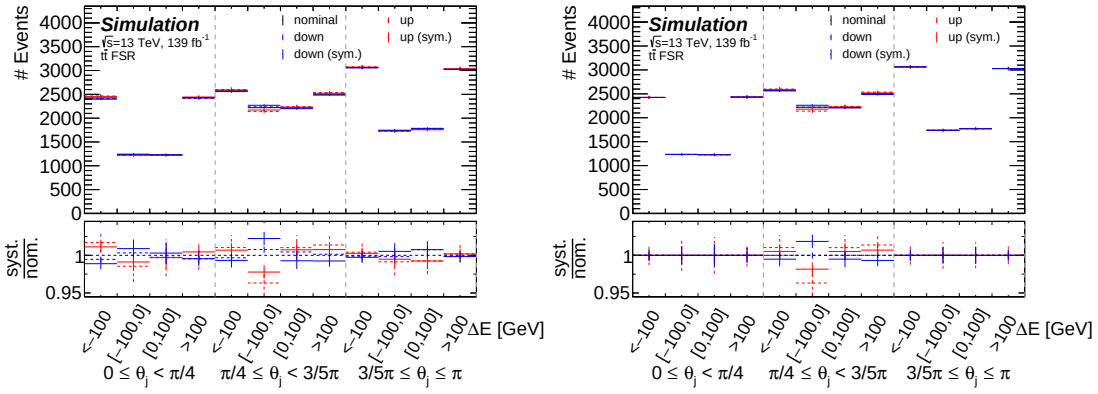

(a) $t\bar{t}$ FSR before smoothing

(b) $t\bar{t}$ FSR after smoothing

Figure 8.3.: Symmetrisation of the $t\bar{t}$ FSR uncertainty before (left) and after (right) smoothing. The error bars correspond to the MC statistical uncertainty estimated as the standard deviation of the corresponding replicas.

8.3.3. Pruning

A pruning procedure was applied in some optimisation and robustness studies described in sections 9.2 and 9.3 to reduce the number of nuisance parameters used in the unfolding to save computing time and disk space requirements. A systematic uncertainty is discarded if the maximum absolute value of the relative uncertainties in all ΔE vs. θ_j bins is below a threshold p for $t\bar{t}$ signal and below $4p$ for all background samples. Figure 8.5 illustrates the pruning procedure in case of the $t\bar{t}$ modelling uncertainties. The $t\bar{t}$ mass, parton shower, and h_{damp} uncertainties were smoothed away as described in section 8.3.1 and were thus discarded for all possible pruning thresholds. The $t\bar{t}$ matching and FSR uncertainties on the other hand will be kept for all illustrated pruning thresholds. In this analysis, a pruning threshold of $p = 0.005$ was applied, reducing the number of nuisance parameters from 339 to 154. The impact on the uncertainty after unfolding was found to be less than 3% across all θ_j bins.

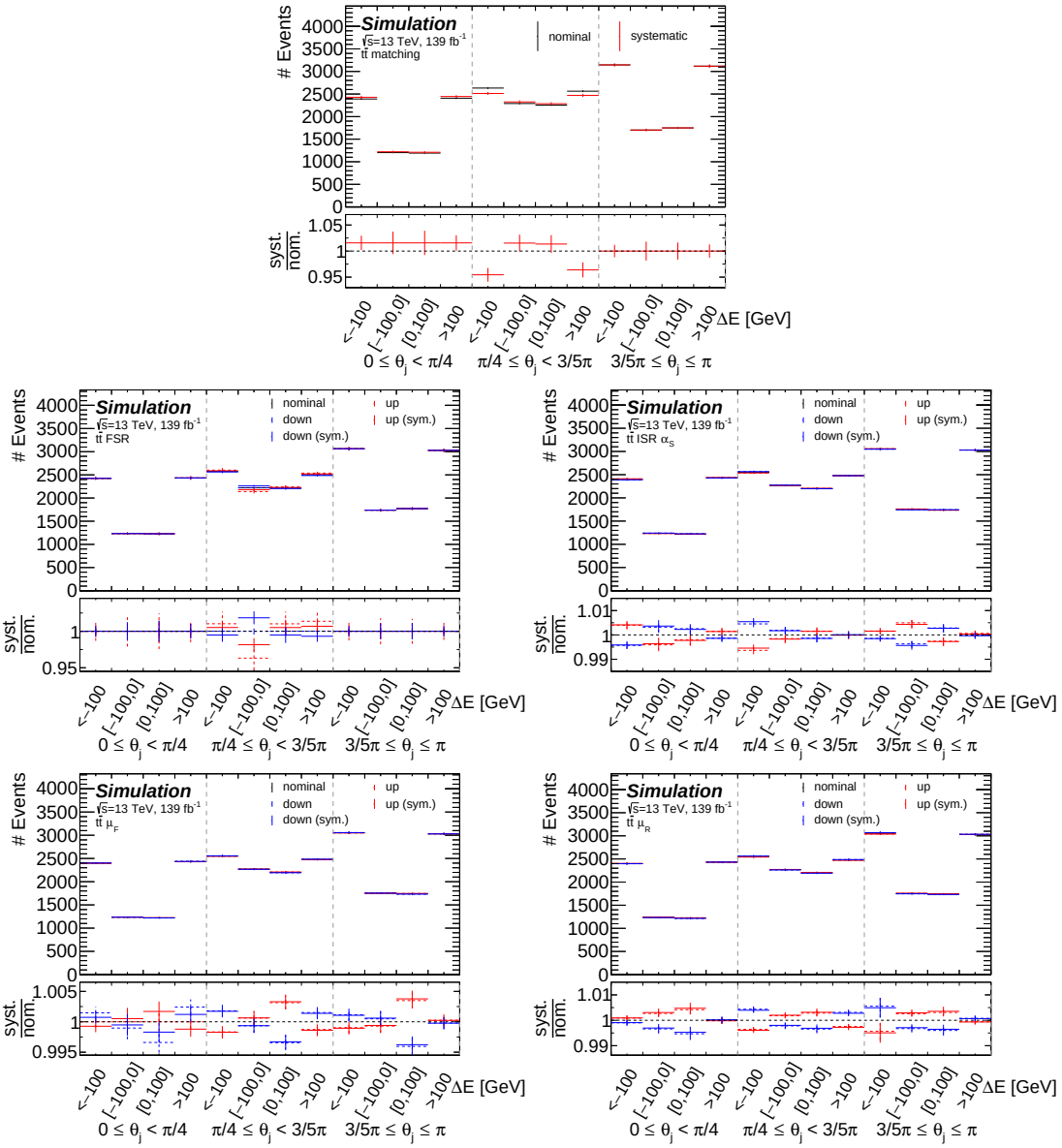

Figure 8.4.: Modelling uncertainties on the ΔE vs. θ_j $t\bar{t}$ signal distribution after smoothing and symmetrisation. The error bars correspond to the MC statistical uncertainty estimated as the standard deviation of the corresponding replicas. The $t\bar{t}$ mass, parton shower, and h_{damp} uncertainties were found to be statistically insignificant in all bins and are thus not shown.

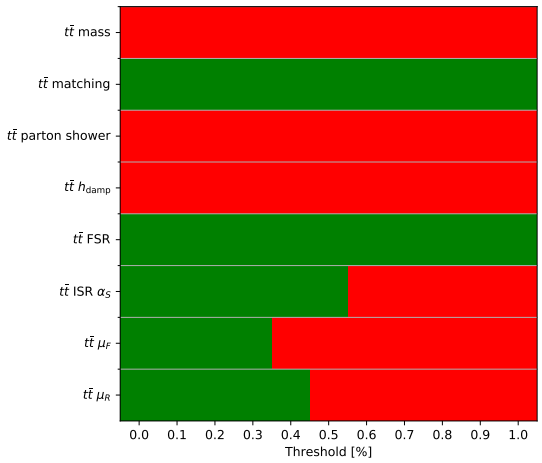

Figure 8.5.: Pruning of the $t\bar{t}$ modelling uncertainties. For a given threshold, systematic uncertainties in green are kept while those in red are discarded. The $t\bar{t}$ matching, FSR and ISR uncertainties are kept for a pruning threshold of 0.005.

8.4. MC statistical uncertainties on the response matrix

The uncertainty from the limited size of the MC sample used to estimate the response matrix was evaluated by repeating the unfolding procedure for $n = 200$ replicas of the response matrix defined in eq. 7.4, keeping all other inputs fixed. The replicas were obtained with the bootstrapping method described in section 8.3.1 taking into account correlations between identical events at the particle and the detector level.

Figure 8.6 shows the unfolded inclusive and differential asymmetries and their uncertainties in data, considering only data statistical uncertainties. The covariance matrix of the mean values of the asymmetries yields an estimate of the uncertainties and their correlations from limited MC statistics in the signal sample. The evolution of these uncertainties with the number of replicas is shown in figure 8.7. They are found to converge for $n \gtrapprox 100$ and decrease with the number of events in the corresponding bin; see table 9.16 in section 9.4.1.

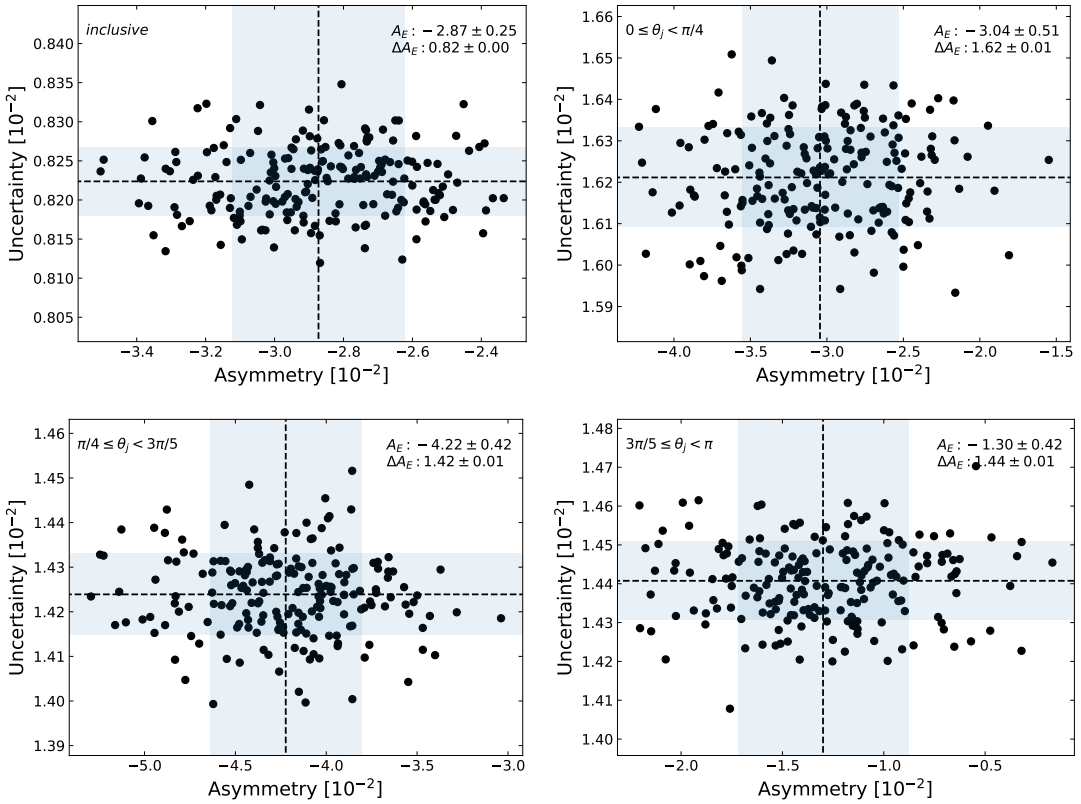

Figure 8.6.: Asymmetries and uncertainties after unfolding with data statistical uncertainties only for each of the 200 replicas. The numbers denote the mean values and standard deviations of the asymmetries A_E and their uncertainties ΔA_E.

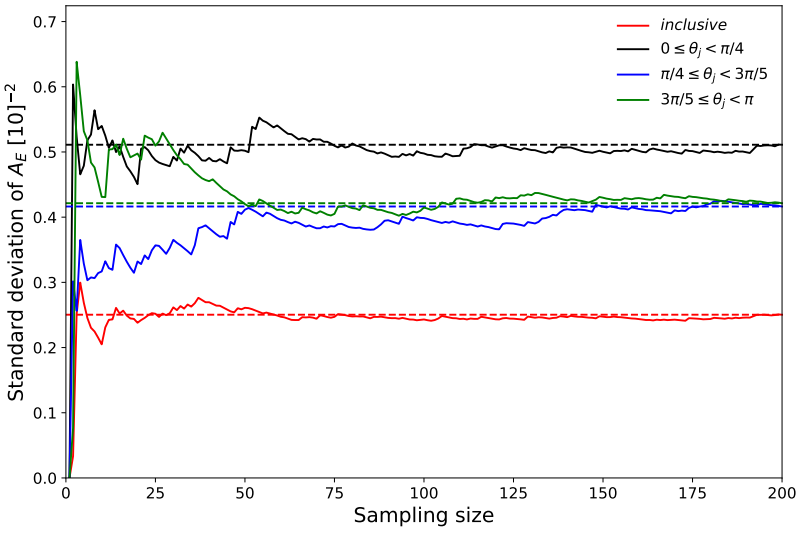

Figure 8.7.: Evolution of the standard deviation of the unfolded energy asymmetry with the number of replicas of the response matrix. The dashed lines correspond to the standard deviations obtained with the full number of replicas.

9. Measurement

This chapter presents the energy asymmetry measurement using $139\,\text{fb}^{-1}$ of proton-proton collision data collected by the ATLAS experiment during the 2015–2018 data-taking period. The results of this measurement were published in reference [83].

The full analysis chain from event selection, reconstruction and unfolding was set up and optimised using pseudo-data, effectively blinding the recorded data to avoid any biases. The expected results of the energy asymmetry measurement are presented in section 9.1. Section 9.2 discusses the main alternatives considered in the optimisation; various robustness tests are illustrated in section 9.3. The results measured in data are presented in section 9.4. Section 9.5 gives an outlook for the energy asymmetry measurement in future data-taking periods.

9.1. Expectation

This section describes the expectation of the energy asymmetry measurement using pseudo-data obtained from the sum of the nominal $t\bar{t}$ signal and background predictions described in chapter 6. The events were selected and reconstructed as described in chapter 5. Section 9.1.1 shows the results of the unfolding procedure described in chapter 7; the impact of systematic uncertainties is discussed in section 9.1.2.

9.1.1. Expected unfolding results

The Fully Bayesian Unfolding method provides a full posterior distribution of the particle-level ΔE vs. θ_j distribution from which the posterior distribution of the energy asymmetry is calculated as described in section 7.5. Figure 9.1 illustrates the marginalised posterior distributions of the inclusive and differential energy asymmetry obtained from the unfolding procedure before adding MC statistical uncertainties on the response matrix. These distributions are found to be Gaussian shaped as can be seen by the overlay of a χ^2 fit with a standard normal distribution; the quoted standard deviations can thus be easily interpreted as 68% confidence levels. The true particle-level asymmetries and the unfolded asymmetries are compared in table 9.1. The full covariance matrix of the energy asymmetry obtained from the sum of the covariance matrix of the posterior distribution after unfolding and the covariance matrix corresponding to the MC statistical uncertainty as described in section 8.4 is shown in table 9.2.

The expected sensitivity of the energy asymmetry is evaluated with a goodness-of-fit test [314]. Assuming that the energy asymmetry A_E is Gaussian distributed with mean μ and covariance matrix C, the χ^2 value defined as:

$$\chi^2 = (A_E - \mu)^T C^{-1} (A_E - \mu) \tag{9.1}$$

follows a chi-square distribution with ν degrees of freedom, χ^2_ν, where $\nu = 3$ is the number of θ_j bins for the differential energy asymmetry and $\nu = 1$ for the inclusive

Table 9.1.: True particle-level asymmetries and unfolding results for pseudo-data. "Truth" denotes the true particle-level asymmetry in pseudo-data with MC statistical uncertainties. The unfolding was performed with expected data statistical uncertainties only ("Stat. only") and with both expected data statistical and systematic uncertainties ("Stat.+Syst."). The MC statistical uncertainties on the response matrix "MC stat." were evaluated as described in section 8.4. The total uncertainties were obtained by adding the "Stat.+Syst." and "MC Stat." uncertainties in quadrature.

Scenario	$A_E \pm \Delta A_E [10^{-2}]$			
	Inclusive	$0 \leq \theta_j \leq \frac{\pi}{4}$	$\frac{\pi}{4} \leq \theta_j \leq \frac{3\pi}{5}$	$\frac{3\pi}{5} \leq \theta_j \leq \pi$
Truth	(-0.64 ± 0.16)	(0.65 ± 0.31)	(-2.30 ± 0.27)	(0.05 ± 0.27)
Stat. only	(-0.65 ± 0.77)	(0.56 ± 1.53)	(-2.31 ± 1.34)	(0.10 ± 1.32)
Stat.+Syst.	(-0.67 ± 1.02)	(0.55 ± 1.99)	(-2.33 ± 1.90)	(0.10 ± 1.56)
MC stat.	0.25	0.52	0.42	0.42
Total	(-0.67 ± 1.05)	(0.55 ± 2.05)	(-2.33 ± 1.95)	(0.10 ± 1.61)

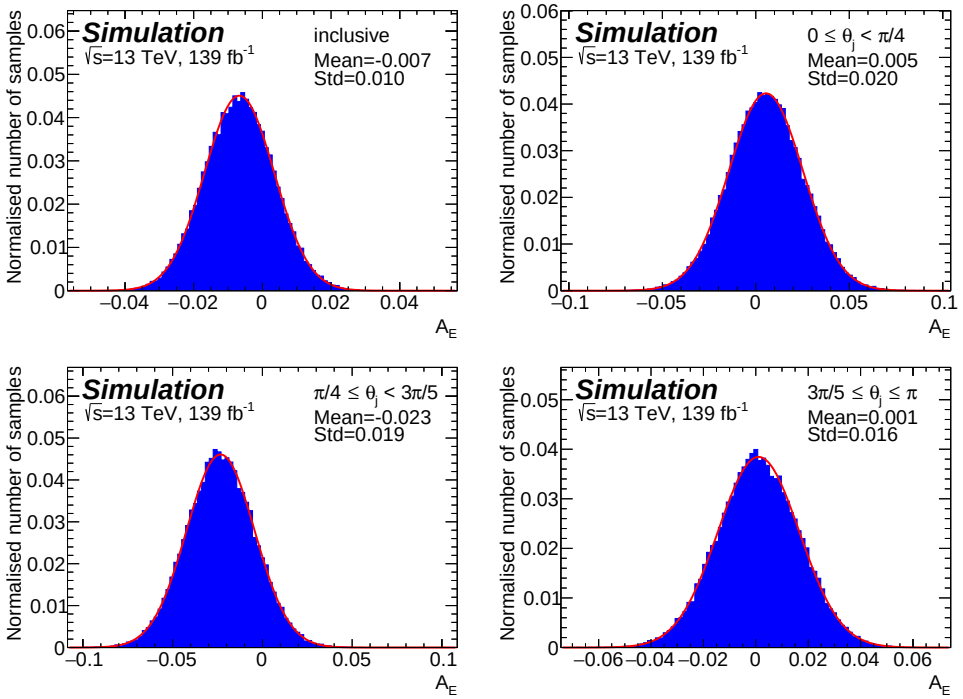

Figure 9.1.: Marginal posterior distributions of the inclusive and differential energy asymmetry in pseudo-data without MC statistical uncertainties on the response matrix. A Gaussian fit to the data was overlaid in red.

Table 9.2.: Expected covariance matrix of the energy asymmetry obtained from pseudo-data in $[10^{-4}]$. The covariance between the pairs of θ_j bins was obtained by the sum of the covariance of the posterior distribution after unfolding and the covariance corresponding to the MC statistical uncertainties as described in section 8.4.

	$0 \leq \theta_j < \frac{\pi}{4}$	$\frac{\pi}{4} \leq \theta_j < \frac{3\pi}{5}$	$\frac{3\pi}{5} \leq \theta_j \leq \pi$
$0 \leq \theta_j < \frac{\pi}{4}$	4.2205	-0.1066	-0.1289
$\frac{\pi}{4} \leq \theta_j < \frac{3\pi}{5}$	-0.1066	3.7853	-0.0894
$\frac{3\pi}{5} \leq \theta_j \leq \pi$	-0.1289	-0.0894	2.6063

energy asymmetry. Since the χ^2_ν distribution has a mean of ν, the reduced χ^2, defined as χ^2_ν/ν, serves as a measure of goodness-of-fit. Reduced χ^2 values below one indicate that the data fits the hypothesis better than expected on average given the size of the measurement uncertainties, while values much larger than one give reason to doubt the hypothesis. A quantitative measure is the p-value, defined as the probability under the null hypothesis to observe an asymmetry that has an equal or larger discrepancy from the prediction than the measured one:

$$p = 1.0 - \mathrm{CDF}_{\chi^2_\nu}(\chi^2) \tag{9.2}$$

where $\mathrm{CDF}_{\chi^2,\nu}$ is the cumulative distribution function of the χ^2 distribution with ν degrees of freedom. In physics analyses, the p-value is typically expressed in terms of the significance level Z defined as the number of standard deviations σ corresponding to an area equal to $1 - p$ under the normal distribution $\mathcal{N}(\mu, \sigma)$ [315, 316]:

$$P(\mu - Z\sigma \leq X \leq \mu + Z\sigma) = 1 - p \tag{9.3}$$

The significance level Z is then given by:

$$Z = \mathrm{CDF}^{-1}_{\mathcal{N}}(1 - p/2) \tag{9.4}$$

where $\mathrm{CDF}_{\mathcal{N}}$ is the cumulative distribution function of the standard normal distribution $\mathcal{N}(0, 1)$. The expected significances of the energy asymmetry obtained in pseudo-data with the covariance matrix shown in table 9.2 with respect to the null hypothesis that the energy asymmetry is zero in all θ_j bins ($\mu = 0$) are listed in table 9.3.

9.1.2. Expected systematic uncertainties

The Fully Bayesian Unfolding method provides a full posterior distribution of the energy asymmetry from which the marginalised posterior distributions in the individual bins shown in figure 9.1 were obtained. These distributions provide estimates for the mean value and total uncertainty of the energy asymmetry, but not for the contributions of the individual systematic uncertainties. A typical approach to assess the impact of the individual uncertainties is to repeat the unfolding for each uncertainty by fixing the corresponding nuisance parameter to its best-fit value $\hat{\theta}$ shifted by its uncertainties $\pm\sigma$ and to compare the unfolding results [66]. This approach, however, requires much

Table 9.3.: Expected significance of the energy asymmetry with respect to the null hypothesis that the asymmetry is exactly zero ($\mu = 0$) evaluated with a χ^2 goodness-of-fit test for the inclusive and differential asymmetries as well as the individual bins. The χ^2, χ^2/ν, p and Z values were calculated as described in equations 9.1 to 9.4.

	χ^2	χ^2/ν	p	Z
Inclusive	0.41	0.41	0.5225	0.64
Differential	1.49	0.50	0.6841	0.41
$0 \leq \theta_j < \frac{\pi}{4}$	0.07	0.07	0.7903	0.27
$\frac{\pi}{4} \leq \theta_j < \frac{3\pi}{5}$	1.44	1.44	0.2308	1.20
$\frac{3\pi}{5} \leq \theta_j \leq \pi$	< 0.01	< 0.01	0.9482	0.06

computing time due to the many nuisance parameters for which the unfolding needs to be repeated. Therefore, an alternative approach based on the idea of linear regression is used in this analysis. Approximating a function $y = f(x)$ to linear order in x, it can be written as [316]:

$$y = \alpha + \beta x, \quad \alpha = \langle y \rangle - \beta \langle x \rangle, \quad \beta = \frac{\mathrm{Cov}(y, x)}{\mathrm{Cov}(x, x)} \tag{9.5}$$

where α and β are the estimates of a χ^2 minimisation, assuming that y follows a normal distribution for a given value of x. The change in y, Δy, due to a change in x, Δx, is thus given by:

$$\Delta y = \frac{\mathrm{Cov}(y, x)}{\mathrm{Cov}(x, x)} \Delta x \tag{9.6}$$

and the effect of a one σ variation in x, $\Delta x = \sigma_x$, on y reads:

$$\Delta y = \frac{\mathrm{Cov}(y, x)}{\mathrm{Cov}(x, x)} \sigma_x = \frac{\mathrm{Cov}(y, x)}{\sigma_x} \tag{9.7}$$

The post-marginalisation impact on the energy asymmetry in bin i due to a one σ shift of the nuisance parameter θ_k is thus given by:

$$\Delta A_E^i = \frac{\mathrm{Cov}(A_E^i, \theta_k)}{\sqrt{\mathrm{Cov}(\theta_k, \theta_k)}} \tag{9.8}$$

The covariances were estimated by the sample covariances of the joint posterior distributions of A_E^i and θ_k. The pre-marginalisation impact of a systematic uncertainty was obtained by multiplying the post-marginalisation impact ΔA_E^i with the ratio of the pre- to post-marginalisation standard deviation of its nuisance parameter. Figure 9.2 shows a ranking of the expected systematic uncertainties by their impact on the inclusive and differential energy asymmetry. For comparison, the expected data statistical uncertainty was obtained as the standard deviation of the posterior energy asymmetry distribution in the unfolding of pseudo-data with all nuisance parameters fixed to their post-marginalised central values. The impact of the MC statistical uncertainty on the $t\bar{t}$ response matrix was evaluated with the bootstrapping method described in section 8.4.

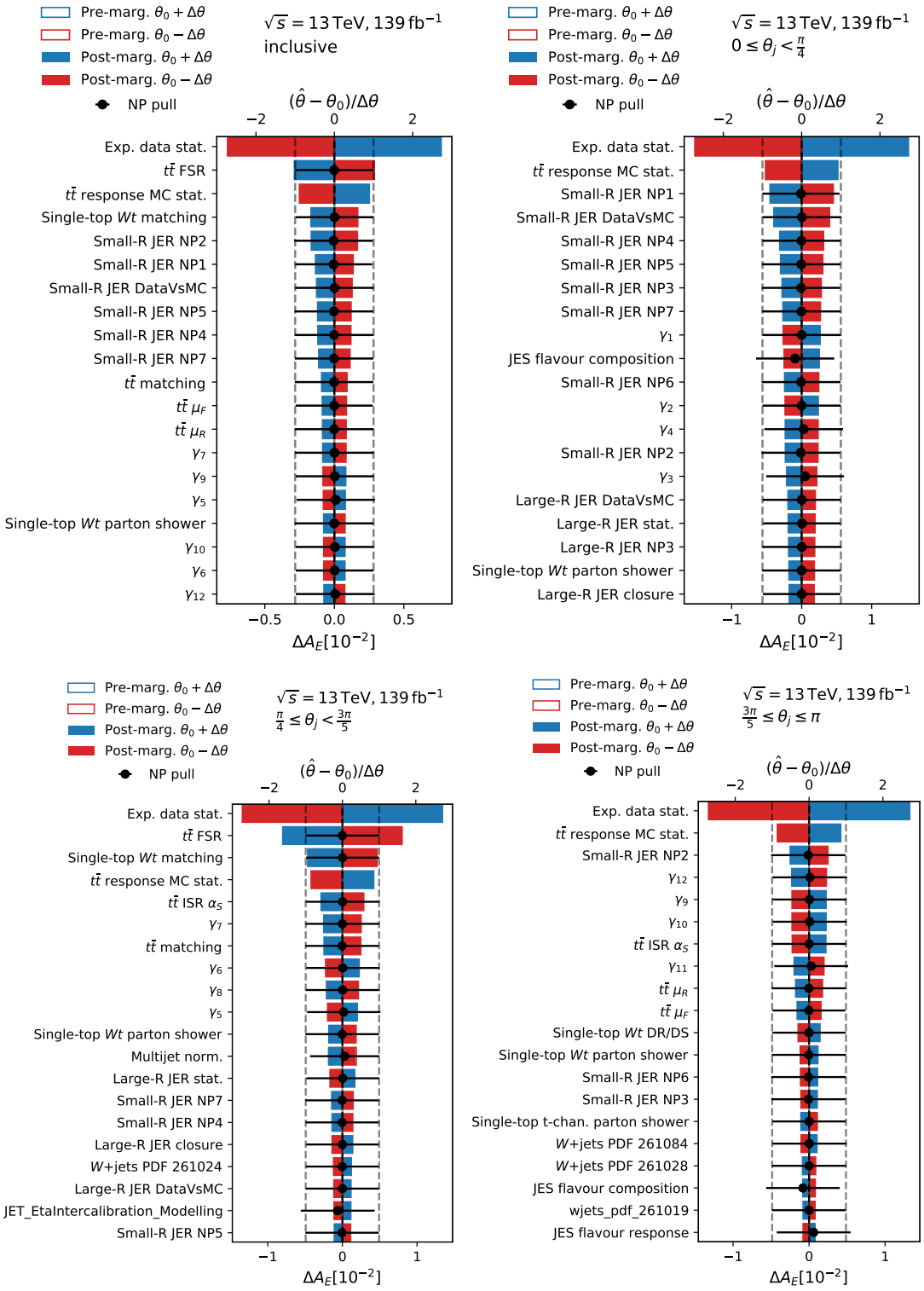

Figure 9.2.: Ranking of expected systematic uncertainties on the inclusive and differential energy asymmetry. Blue and red areas show the impact on the energy asymmetry from a one σ variation of the corresponding nuisance parameter as defined in eq. 9.8. The means and standard deviations of the posterior distributions of the nuisance parameters, normalised to their pre-marginalisation standard deviations, are illustrated by black dots and error bars, respectively.

With the same number of parameters of interest as observables and a uniform prior for the truth-level ΔE vs. θ_j distribution, the post-marginalisation distributions of the nuisance parameters are not expected to deviate from their pre-marginalisation distributions. The joint probability of the parameters of interest and the nuisance parameters given in eq. 7.13 does not impose a penalty on nuisance parameter values deviating from their pre-marginalisation central values except for the decreasing prior probability. For each value of the nuisance parameters drawn randomly from their prior distribution, there exists a parameter of interest value such that the prediction matches the data in all bins, leaving the likelihood in eq. 7.5 unchanged. With a different number of observables than parameters of interest, or a non-uniform truth-level prior distribution, this would no longer be the case, and the post-marginalisation distributions of the nuisance parameters would be expected to be constrained compared to their pre-marginalisation distribution as studied in section 9.3.4.

Indeed, the post-marginalisation distributions of the standardised nuisance parameters have a mean around zero and a standard deviation around one. Small correlations between the systematic uncertainties, especially with the background normalisation uncertainties with truncated prior distributions, can lead to small deviations in the mean value. Figure 9.3 shows the correlations of the 20 highest ranked systematic uncertainties with each other and with the inclusive and differential energy asymmetries. It has been checked, however, that the mode of the joint probability in eq. 7.10 is obtained for nuisance parameter values corresponding to the mode of their pre-marginalisation systematic uncertainties using the maximum a posteriori (MAP) estimation in PyMC3 [308].

The data statistical uncertainty is expected to be by far the largest uncertainty in all bins of the inclusive and differential energy asymmetry; it is the largest in the first θ_j bin with the highest number of events, and of similar size in the central and last θ_j bins; see table 9.16 for the event numbers in the individual bins. The MC statistical uncertainty on the response matrix is among the highest ranked systematic uncertainties in all bins. In the central θ_j bin, the uncertainty on the $t\bar{t}$ final-state radiation is dominating, while it does not appear in the first and last bin, as it was found to be not statistically significant as shown in figure 8.3 and discussed in section 8.3.1.

To assess the impact of the systematic uncertainties by category, Gaussian error propagation is applied. The covariance matrix of a function $f(x)$ is given by [317]:

$$\mathrm{Cov}_f = G\mathrm{Cov}_x G^T \tag{9.9}$$

where Cov_x is the covariance matrix of x and G the matrix given by the derivatives of f with respect to x: $G_{ij} = \frac{\partial f_i}{\partial x_j}$. For the energy asymmetry, this equation reads:

$$\mathrm{Cov}(A_E^i, A_E^j) = \frac{\partial A_E^i}{\partial \theta_k}\mathrm{Cov}(\theta_k, \theta_l)\frac{\partial A_E^j}{\partial \theta_l} \tag{9.10}$$

where the derivatives of A_E^i with respect to nuisance parameter θ_k are approximated by $\partial A_E^i/\partial\theta_k = \Delta A_E^i/\Delta\theta_k = \mathrm{Cov}(A_E^i, \theta_k)/\mathrm{Cov}(\theta_k, \theta_k)$ as in eq. 9.6. Table 9.4 shows the expected impact of the systematic uncertainties on the inclusive and differential energy asymmetry by category.

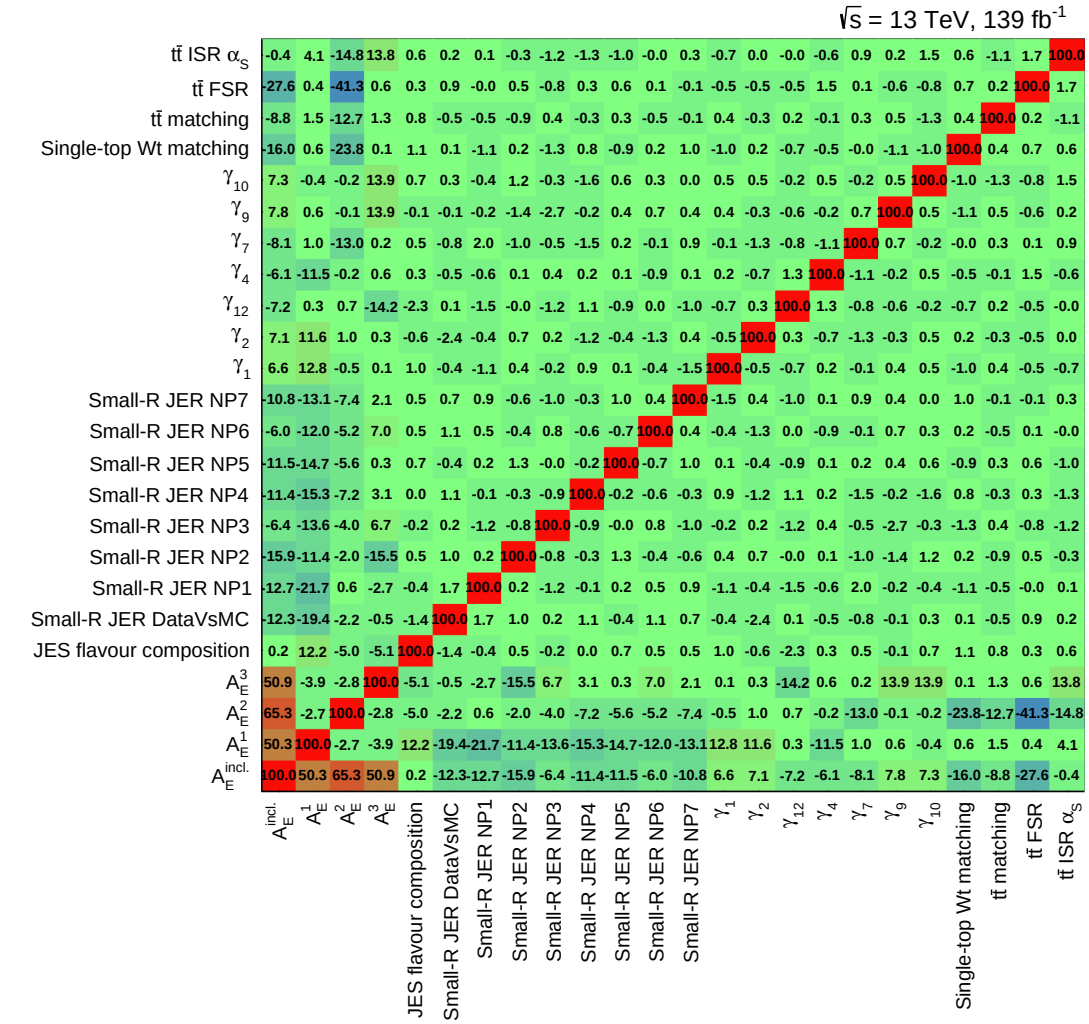

Figure 9.3.: Correlation matrix for the highest ranked expected systematic uncertainties in pseudo-data with each other and with the inclusive and differential energy asymmetry. For better visibility, the correlations are scaled by a factor of 100.

The jet energy resolution uncertainty is by far the largest systematic uncertainty in the first θ_j bin and much smaller in the central and last θ_j bins. This is explained by the distribution of the pseudorapidity of the associated jet in the three θ_j bins shown on the left in figure 9.4. The kinematic selection of a small jet scattering angle with respect to the incoming parton in the $t\bar{t}j$ system corresponds to jets close to the beamline, i.e. with large absolute values of the pseudorapidity. The JER uncertainty increases with the absolute value of $|\eta|$ within the considered fiducial volume [234] as shown on the right in figure 9.4 due to the increasing detector material in front of the calorimeters [318] and the discontinuities created by the transition region between the barrel and endcap region around $|\eta| \approx 1.4$ described in section 3.2.3. In the central θ_j bin, the $t\bar{t}$ modelling uncertainties are the dominating systematic uncertainties, mostly

Table 9.4.: Expected energy asymmetry uncertainties by category. The uncertainty of each category is calculated with Gaussian error propagation using eq. 9.10. Uncertainties in the luminosity and cross sections of the Z+jets, VV, $t\bar{t}V$ and $t\bar{t}H$ backgrounds are found to be negligible and are thus not listed.

Scenario	ΔA_E $[10^{-2}]$			
	inclusive	$0 \leq \theta_j < \frac{\pi}{4}$	$\frac{\pi}{4} \leq \theta_j < \frac{3\pi}{5}$	$\frac{3\pi}{5} \leq \theta_j \leq \pi$
Data stat. uncertainty (exp.)	0.77	1.50	1.30	1.30
$t\bar{t}$ modelling	0.33	0.09	0.90	0.33
$t\bar{t}$ response MC statistics	0.25	0.52	0.42	0.42
W+jets modelling and PDF	0.28	0.29	0.47	0.36
Single-top modelling	0.20	0.25	0.52	0.24
$t\bar{t}$ and single-top PDF	0.04	0.07	0.09	0.06
Multijet	0.25	0.49	0.48	0.44
Jet energy resolution	0.34	1.00	0.41	0.33
Other detector uncertainties	0.17	0.45	0.42	0.26
Total	1.10	2.10	2.00	1.60

driven by FSR, ISR and matching uncertainties. Additional radiation can change the energies of the reconstructed top-quark candidates, and additional jets can disturb the correct assignment of jets to these candidates. Different radiation and matching assumptions will thus move events between different energy bins in the ΔE vs. θ_j distribution as illustrated in figure 8.4; this effect is more relevant in the central θ_j bin, where the different energy bins have closer populations than in the other angular bins. Migrations in the energy bins have thus a larger relative impact in the central θ_j region.

In the last θ_j bin, the absence of these effects leads to much smaller JER and $t\bar{t}$ modelling uncertainties. Thus the uncertainty in the multijet estimation becomes the dominating systematic uncertainty, which itself is mostly driven by the statistical uncertainties in the data-driven estimate described in section 6.3.2 as can be seen in the high ranking of the $\gamma's$ in figure 9.2. In each θ_j bin, the effect of the $\gamma's$ corresponding to the positive (negative) ΔE bins decrease (increase) the energy asymmetry.

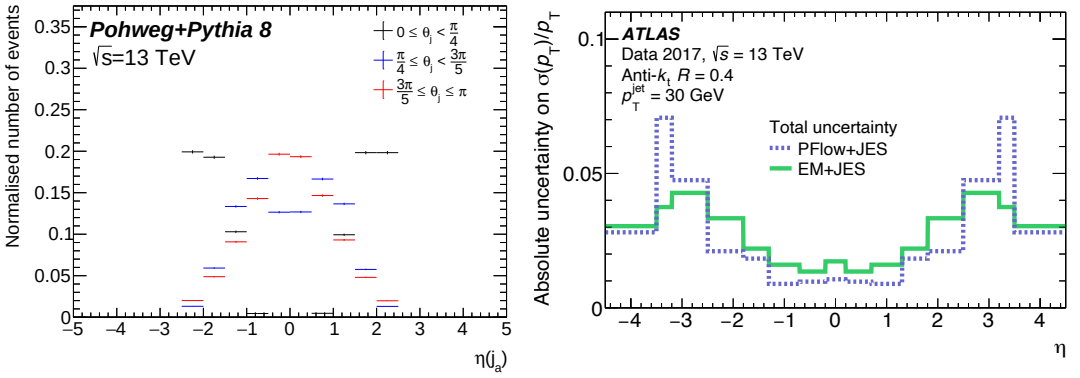

Figure 9.4.: Pseudorapidity η of the associated jet in the three θ_j bins in simulated fiducial $t\bar{t}$ events at the detector level with MC statistical uncertainties (left) and jet energy resolution systematic uncertainty as a function of η [234] (right). This analysis uses PFlow+JES jets as described in section 4.1.4.

9.2. Optimisation studies

This section describes the optimisation of the binning in the jet scattering angle θ_j and discusses the main alternatives in the event selection and reconstruction to the chosen setup described in chapter 5.

9.2.1. Binning of the jet scattering angle

The SM prediction of the energy asymmetry at the parton level exhibits a minimum at $\theta_j \approx 2\pi/5$, which increases in absolute value for the boosted compared to the loose phase space; see figures 2.21 and 2.22 in section 2.3.4. The goal of this analysis is to measure the energy asymmetry at the particle level in the θ_j region with the highest possible significance. Thus the θ_j range is divided into three bins, where the central bin covers the minimum of the energy asymmetry. The bin boundaries were chosen to maximise the expected statistical significance of the energy asymmetry at the particle level in the central bin. Figure 9.5 shows the SM prediction of the differential energy asymmetry in the boosted phase space at particle level, obtained from simulated $t\bar{t}$ events with the nominal Powheg+Pythia 8 generator as described in section 6.2.1 with the event selection and reconstruction described in section 5. The energy asymmetry is clearly negative in the central θ_j region. Table 9.5 shows the expected energy asymmetries and their statistical uncertainties, assuming that the event numbers are Poisson distributed, for a selection of tested bin boundaries. The highest expected statistical significance for the energy asymmetry in the central bin, A_E^2, is obtained in the range $\pi/4 \leq \theta_j \leq 3\pi/5$.

Differing response matrices and systematic uncertainties between the binning choices may give rise to a different optimal binning choice when taking into account the unfolding procedure from the detector to the particle level. The unfolding procedure was thus repeated for the various binning choices, including all systematic uncertainties without smoothing except for MC statistical uncertainties on the response matrix. As can be seen in table 9.6, the optimal binning choice remains unaltered when unfolding effects and systematic uncertainties are taken into account.

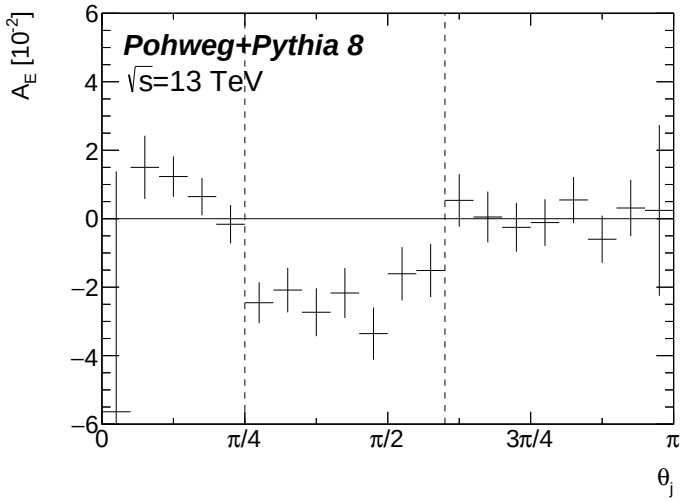

Figure 9.5.: SM prediction of the energy asymmetry at the particle level in $t\bar{t}$ events obtained with POWHEG+PYTHIA 8 as described in section 6.2.1. Error bars denote the MC statistical uncertainties. Dashed lines indicate the optimal binning that yields the highest statistical significance of the energy asymmetry in the central bin, assuming that the event numbers follow a Poisson distribution as in data.

Table 9.5.: Expected asymmetries and statistical uncertainties for various binning choices of the jet scattering angle θ_j. The energy asymmetry in the central bin, A_E^2, is expected to have the highest statistical significance $Z = |A_E^2|/\Delta A_E^2$ within the range $\pi/4 \leq \theta_j \leq 3\pi/5$ indicated by bold numbers.

$\theta_j^{\min}\,[\pi/20]$	$\theta_j^{\max}\,[\pi/20]$	$A_E^2\,[10^{-2}]$	$\Delta A_E^2\,[10^{-2}]$	Z
4	11	-1.94	1.23	1.58
4	12	-1.90	1.17	1.62
4	13	-1.68	1.12	1.51
5	11	-2.40	1.38	1.74
5	**12**	**−2.30**	**1.30**	**1.77**
5	13	-1.99	1.23	1.62
6	11	-2.38	1.57	1.52
6	12	-2.26	1.45	1.56
6	13	-1.89	1.35	1.40

Table 9.6.: Expected unfolding results for various binning choices in the jet scattering angle θ_j. The unfolding was performed taking into account all systematic uncertainties without smoothing excluding MC statistical uncertainties on the response matrix. The energy asymmetry in the central bin, A_E^2, is expected to have the highest significance $Z = A_E^2/\Delta A_E^2$ within the range $\pi/4 \leq \theta_j \leq 3\pi/5$ indicated by bold numbers.

$\theta_j^{\min}\,[\pi/20]$	$\theta_j^{\max}\,[\pi/20]$	$A_E^2\,[10^{-2}]$	$\Delta A_E^2\,[10^{-2}]$	Z
4	11	−2.03	2.02	1.01
4	12	−1.96	1.90	1.03
4	13	−1.73	1.68	1.03
5	11	−2.43	2.13	1.14
5	**12**	**−2.33**	**2.03**	**1.15**
5	13	−1.99	1.85	1.08
6	11	−2.45	2.44	1.00
6	12	−2.32	2.11	1.10
6	13	−1.94	2.01	0.97

9.2.2. Selection and reconstruction optimisation

The event selection and reconstruction criteria described in chapter 5 were based on typical analyses in the boosted lepton+jets channel such as differential cross section [266] and rapidity asymmetry [65] measurements. These criteria were optimised to yield the highest expected sensitivity to the energy asymmetry in the central θ_j region, while maintaining a high signal purity, efficiency and acceptance, as well as a good reconstruction of the top-quark candidates. This section first introduces a subset of alternative selections centred around the baseline selection and then explains the metrics used to choose the optimal selection. Eventually, the chosen trade-off between those metrics is motivated.

The first two alternative selections affect the choice of the top-tagger and the b-tagging working point at the detector level. As described in section 4.1.4, there exist inclusive and contained top-tagging definitions at the 50% and 80% working points. As this analysis is dominated by statistical uncertainties, only the looser 80% working points were considered. The first alternative selection, labelled as "Inclusive top-tagger" uses the inclusive instead of the contained definition. The second alternative selection "b-tagging 77% WP" uses the tighter 77% working point for the b-tagging algorithm described in section 4.1.4 instead of the 85% working point.

The next two selection variations affect the p_T and hadronic top identification requirements at the particle level. The baseline particle-level selection was chosen as close as possible to the detector-level selection to minimise bin-to-bin migrations and to ensure a balanced relationship between efficiency and acceptance defined in eq. 7.4 in section 7.1. Loosening particle-level selection requirements will increase the acceptance while decreasing the efficiency, keeping the number of detector-level events unaltered. In the baseline selection, the transverse momenta of the hadronic top and the associated jet candidates are required to be above 350 and 100 GeV, respectively. The first alternative selection, labelled as "reduced p_T", lowers these requirements to 330 GeV and 90 GeV,

respectively, at the particle level. The b-flavour and mass, $m(j_h) > 140\,\text{GeV}$, requirements on the particle-level hadronic top-quark candidate agree with the requirements applied during the training of the top-tagging algorithm described in section 4.1.4. In two alternative selections, the b-flavour requirement is removed ("no b-flavour (j_h)") and the mass requirement is loosened to 120 GeV ("$m(j_h) > 120\,\text{GeV}$").

The following variations affect the selection and reconstruction at both the particle and the detector level. The absolute value of the energy asymmetry increases with the transverse momentum of the associated jet as can be seen from eq. 2.37 in section 2.3.4. The associated jet p_T itself has a steeply falling distribution as shown in figure 9.20. Any cut value thus provides a trade-off between an increased asymmetry and an increased statistical precision. The baseline cut value of 100 GeV was inspired by phenomenological studies [74, 268], two alternative values of 50 GeV and 200 GeV were tested in the selections "$p_T(j_a) = 50\,\text{GeV}$" and "$p_T(j_a) = 200\,\text{GeV}$", respectively. The reconstruction quality of the leptonic top b-jet candidate can be improved by requiring it to be b-identified ("j_l b-identified") and by narrowing the cone around the lepton within which it has to be found to 1.0 instead of 2.0 ("$\Delta R(j_l, l) < 1.0$"). In inclusive $t\bar{t}$ events, the top-quark candidates are mostly back-to-back, resulting in a large angular separation in $\Delta\Phi(j_h, l)$ as required in the rapidity asymmetry measurement [65]. With three particles in the final states this does not need to be the case such that the baseline selection requires an angular separation of $\Delta\Phi(j_h, l) > 1.0$ as in the differential cross section measurement [266]. The alternative of $\Delta\Phi(j_h, l) > 2.0$ is considered in the last selection variation.

The predicted $t\bar{t}$ signal and background event numbers for the various selection and reconstruction criteria are shown in table 9.7. The variations affecting only the particle-level criteria do not affect the detector-level event yields and are thus not shown. The total event number in the baseline selection is around 30 000 and reduces only slightly to about 29 000 for the tighter b-tagging WP, while it nearly doubles to 57 000 for the inclusive top-tagger. The signal purity increases slightly from 87% to 90% when tightening the b-tagging WP, but decreases a lot to 80% when switching to the inclusive top-tagging definition, corresponding to an increase in the W+jets background fraction from 5% to 9%. The effect on the signal purity from the other variations is somewhere in between, while the increased p_T requirement of the associated jet to 200 GeV and the reduced cone size around the lepton to $\Delta R(j_l, l) < 1.0$ decrease the total event number by roughly 50% to about 15 000 and 17 000, respectively.

Table 9.8 shows the event yields for the $t\bar{t}$ signal and the fiducial $t\bar{t}$ signal at the detector level, the particle-level $t\bar{t}$ event yield as well as the efficiency and the acceptance fraction. The inclusive top-tagging definition increases the $t\bar{t}$ event yield significantly by more than 70% from 26 000 to 46 000 compared to the baseline selection, but has a much smaller impact on the fiducial $t\bar{t}$ event yield of less than 20%. Correspondingly, the efficiency increases from 34% to 40%, while the acceptance fraction decreases strongly from 70% to only 47%, meaning that 53% of the events reconstructed at the detector level do not pass the particle-level selection. The effect of all other variations is limited to the range of 30%–36% on the efficiency and of 69%–74% on the acceptance fraction.

The reconstruction quality is evaluated in terms of matching rates and differences between the detector-, particle- and parton-level top-quark candidate masses. The hadronic top-quark candidate j_h, the leptonic top b-jet candidate j_l and the associated jet j_a at the detector level are considered to be matched to the particle level if they

Table 9.7.: Detector-level event numbers for the $t\bar{t}$ signal and background predictions for various selection/reconstruction scenarios. The numbers in brackets denote the fraction of events with respect to the total event number in percent. Selection variations affecting only the particle-level selection do not change the detector-level event yields and are thus not shown.

Variation	Total	$t\bar{t}$	W+jets	Single-top Wt	Multijet	Other
Baseline	30234	26367 (87.2)	1599 (5.3)	675 (2.2)	578 (1.9)	1015 (3.4)
Inclusive top-tagger	57109	45766 (80.1)	5106 (8.9)	2130 (3.7)	1551 (2.7)	2555 (4.5)
b-tagging 77% WP	28874	25963 (89.9)	936 (3.2)	666 (2.3)	475 (1.6)	835 (2.9)
$p_T(j_a) = 50\,\text{GeV}$	47887	42110 (87.9)	2360 (4.9)	1087 (2.3)	876 (1.8)	1454 (3.0)
$p_T(j_a) = 200\,\text{GeV}$	14868	12872 (86.6)	894 (6.0)	330 (2.2)	241 (1.6)	531 (3.6)
j_l b-identified	25526	22959 (89.9)	880 (3.4)	508 (2.0)	388 (1.5)	792 (3.1)
$\Delta R(j_l, l) < 1.0$	16996	15234 (89.6)	648 (3.8)	242 (1.4)	352 (2.1)	520 (3.1)
$\Delta\Phi(j_h, l) > 2.0$	24716	21564 (87.2)	1244 (5.0)	527 (2.1)	569 (2.3)	812 (3.3)

Table 9.8.: Total, $t\bar{t}$ and fiducial $t\bar{t}$ event yields at the detector level, $t\bar{t}$ event yield at the particle level (PL) and efficiencies and acceptance fractions for the selection/reconstruction variations.

Variation	Total	$t\bar{t}$	$t\bar{t}$ fid.	$t\bar{t}$ PL	ϵ	f_{acc}
Baseline	30234	26367	18360	53239	0.34	0.70
Inclusive top-tagger	57109	45766	21534	53239	0.40	0.47
b-tagging 77% WP	28874	25963	18003	53239	0.34	0.69
reduced p_T (j_h, j_l)	30234	26367	19611	65873	0.30	0.74
no b-flavour (j_h)	30234	26367	18802	57426	0.33	0.71
$m(j_h) > 120$ GeV	30234	26367	19561	63814	0.31	0.74
$p_T(j_a) = 50\,\text{GeV}$	47887	42110	29378	81882	0.36	0.70
$p_T(j_a) = 200\,\text{GeV}$	14868	12872	8969	27273	0.33	0.70
j_l b-identified	25526	22959	16050	49101	0.33	0.70
$\Delta R(j_l, l) < 1.0$	16996	15234	10516	29397	0.36	0.69
$\Delta\Phi(j_h, l) > 2.0$	24716	21564	15025	43260	0.35	0.70

lie within cones of 1.0, 0.4 and 0.4, respectively, to the corresponding particle-level objects. Both j_h and j_l at the detector and particle levels are considered to be matched to the parton level if they lie within cones of 1.0 to the hadronically decaying top quark and of 0.4 to the b-quark from the leptonically decaying top-quark decay. Since the parton corresponding to the associated jet j_a is not available at the parton level, it is considered to be matched if it is neither matched to the hadronically decaying top quark nor to the b-quark from the leptonically decaying top-quark decay. Tables 9.9 and 9.10 show the matching rates between detector- and parton-level objects and between the detector- and particle- and particle- and parton-level objects, respectively. In 78% of $t\bar{t}$ events all detector-level jets are matched to the corresponding parton-level objects

Table 9.9.: Matching rates for various selection/reconstruction criteria between detector- and parton-level objects for fiducial $t\bar{t}$ and all $t\bar{t}$ signal events.

Variation	Matching rate [%]							
	$t\bar{t}$				fiducial $t\bar{t}$			
	all	j_h	j_l	j_a	all	j_h	j_l	j_a
Baseline	77.6	93.7	81.6	92.4	84.9	97.8	86.4	95.6
Inclusive top-tagger	74.0	88.8	80.7	89.2	83.9	96.8	85.9	95.0
b-tagging 77% WP	76.5	93.4	80.7	91.9	84.1	97.8	85.6	95.4
reduced p_T (j_h, j_a)	77.6	93.7	81.6	92.4	84.9	97.8	86.4	95.6
no b-flavour j_h	77.6	93.7	81.6	92.4	83.7	96.3	86.1	94.7
$m(j_h) > 120$ GeV	77.6	93.7	81.6	92.4	84.8	97.7	86.3	95.6
$p_T(j_a) = 50\,\text{GeV}$	78.2	94.6	82.4	92.0	84.3	98.1	86.0	94.7
$p_T(j_a) = 200\,\text{GeV}$	78.4	94.3	81.8	94.9	86.6	98.1	87.7	98.0
j_l b-identified	84.3	93.1	88.9	92.7	91.6	97.8	93.2	96.5
$\Delta R(j_l, l) < 1.0$	82.0	94.2	86.7	93.4	90.6	98.0	92.4	97.3
$\Delta\Phi(j_h, l) > 2.0$	79.0	93.5	83.3	91.7	85.9	98.1	87.5	95.4

in the baseline selection. For fiducial $t\bar{t}$ signal, this number increases to 85%. The hadronic top candidate is correctly identified in 94% and 98% of all cases for the $t\bar{t}$ and fiducial $t\bar{t}$ events, respectively, signalling a very good reconstruction with the contained top-tagging definition. The associated jet is correctly identified in 92% and 96% of all cases, respectively. Note that by the matching definition there might be more than one associated jet with $p_T > 100\,\text{GeV}$; any associated jet will be considered to be matched if it is neither matched to the hadronically decaying top quark nor to the b-quark from the leptonically decaying top quark. It has been checked, however, that in more than 80% of the events there is only one additional jet with a transverse momentum above 100 GeV. Furthermore, the fraction of quark- to gluon-initiated jets was found to be 74% for the highest compared to 45% for the second-highest p_T additional jet, indicating that the selection of the associated jet performs well in selecting quark-initiated jets.

The leptonic top b-jet candidate, on the other hand, is matched to the corresponding parton-level b-quark in only 82% and 86% of the $t\bar{t}$ and fiducial $t\bar{t}$ events, respectively, leaving room for future improvements in the event reconstruction. The agreement between detector- and particle-level jets is very good with matching rates of more than 99%, 94% and 95% for the hadronic top-quark, leptonic top b-jet and the associated jet candidates, respectively. The matching rates between the particle- and parton-level objects are similar to those between the detector- and parton-level objects, with a somewhat smaller matching rate to the hadronically decaying top quark of 94% compared to 98%, explainable by the less sophisticated hadronic top identification at the particle level.

The mass reconstruction of the top-quark candidates is evaluated in terms of the mean ("bias") and the standard deviation ("resolution") of the differences between the top-quark candidate masses for fiducial $t\bar{t}$ signal events at the detector, particle and parton levels shown in table 9.11. In the baseline selection, the bias on the hadronic and

Table 9.10.: Matching rates for various selection/reconstruction criteria between detector- and particle-level objects and between particle- and parton-level objects for fiducial $t\bar{t}$ signal events.

Variation	Matching rate [%]							
	Detector/particle level				Particle/parton level			
	all	j_h	j_l	j_a	all	j_h	j_l	j_a
Baseline	92.3	99.5	93.7	94.6	82.7	94.1	86.2	95.0
Inclusive top-tagger	91.9	99.1	93.5	94.2	82.7	94.1	86.2	95.0
b-tagging 77% WP	91.8	99.5	93.3	94.1	82.7	94.1	86.2	95.0
reduced p_T (j_h, j_l)	92.3	99.5	93.8	94.6	82.9	94.4	86.3	95.0
no b-flavour (j_h)	92.3	99.5	93.8	94.6	77.9	88.3	85.2	91.1
$m(j_h) > 120$ GeV	92.2	99.4	93.7	94.5	82.1	93.4	85.9	94.6
$p_T(j_a) = 50\,\text{GeV}$	90.7	99.6	93.2	92.4	83.3	94.9	86.8	95.1
$p_T(j_a) = 200\,\text{GeV}$	94.6	99.3	95.4	97.6	83.3	94.8	85.8	96.7
j_l b-identified	95.1	99.5	96.6	96.3	89.1	94.0	92.9	94.9
$\Delta R(j_l, l) < 1.0$	97.0	99.8	98.5	97.7	84.6	94.3	88.9	95.2
$\Delta\Phi(j_h, l) > 2.0$	92.5	100.0	93.8	94.7	84.5	94.3	88.3	94.9

leptonic top-quark candidates at the detector level compared to the parton level are $-0.7\,\text{GeV}$ and $15\,\text{GeV}$, respectively, with mass resolutions of $30\,\text{GeV}$ and $72\,\text{GeV}$. The bias of the leptonic top-quark candidate is driven by the preference of the highest p_T b-jet candidate in the selection process. The particle- to parton-level bias and resolution of the hadronic top candidate are slightly larger with $1.6\,\text{GeV}$ and $33\,\text{GeV}$ due to the less sophisticated particle-level top-identification, while the resolution of the leptonic top candidate mass is slightly better with $66\,\text{GeV}$. Across the tested configurations, the detector- to parton-level hadronic top-quark mass resolution varies between $28\,\text{GeV}$ and $33\,\text{GeV}$; the inclusive top-tagger has the largest bias of $-3.6\,\text{GeV}$ and one of the worst resolutions of $33\,\text{GeV}$. The resolution of the leptonic top-quark candidate ranges from $44\,\text{GeV}$ to $73\,\text{GeV}$; the best reconstruction of the leptonic top-quark candidate is obtained when requiring the leptonic top b-jet candidate to be close to the lepton within a cone of $\Delta R(j_l, l) < 1.0$, providing a bias of $-0.9\,\text{GeV}$ and a resolution of $44\,\text{GeV}$. Requiring the leptonic top b-jet candidate to be b-identified reduces the resolution from $72\,\text{GeV}$ in the baseline selection to $56\,\text{GeV}$.

The expected central values and uncertainties of the energy asymmetry in pseudo-data, unfolded with expected data statistical uncertainties only and with all systematic uncertainties without smoothing are presented in table 9.12. The true particle-level asymmetries agree with the "Stat. only" central values within the last digit and are thus not listed. The significances of the asymmetry in the central θ_j bin in the "Stat. only" scenario range from 1.0 for the "$\Delta R(j_l, l < 1.0)$" selection to 2.2 with the inclusive top-tagging definition; the baseline scenario provides the second highest statistical significance of 1.7. The selections with looser particle-level requirements show a smaller absolute value of the energy asymmetry in the central bin, but no reduction in the expected uncertainty. The variations of the associated jet p_T requirement show the strongest

Table 9.11.: Mass resolution of the top-quark candidates for various selection/reconstruction scenarios. Shown are the means and standard deviations of the mass differences between the detector-, parton- and particle-level hadronic (t_h) and leptonic (t_l) top-quark candidates.

	$\mu \pm \sigma$ [GeV] of Δm					
	detector-parton		detector-particle		particle-parton	
	t_h	t_l	t_h	t_l	t_h	t_l
Baseline	-0.7 ± 29.6	14.6 ± 72.0	-1.5 ± 17.2	1.7 ± 51.9	1.6 ± 33.2	15.4 ± 66.4
Inclusive top-tagger	-3.6 ± 33.3	14.8 ± 72.1	-3.9 ± 20.6	1.6 ± 52.6	1.6 ± 33.2	15.4 ± 66.4
b-tagging 77% WP	-0.7 ± 29.7	15.8 ± 73.4	-1.5 ± 17.1	2.7 ± 53.7	1.6 ± 33.2	15.4 ± 66.4
reduced p_T (j_h, j_l)	-0.8 ± 29.1	14.2 ± 71.2	-1.0 ± 17.1	1.4 ± 51.4	-0.1 ± 31.3	14.7 ± 65.1
no b-flavour (j_h)	-0.5 ± 29.9	14.5 ± 71.5	-1.7 ± 17.3	1.6 ± 51.2	3.2 ± 35.7	16.3 ± 66.9
$m(j_h) > 120$ GeV	-2.4 ± 29.8	14.6 ± 71.9	-0.8 ± 17.4	1.7 ± 52.0	-5.6 ± 34.5	15.2 ± 65.9
$p_T(j_a) = 50\,\text{GeV}$	-1.6 ± 27.9	16.6 ± 73.6	-1.4 ± 16.6	2.0 ± 52.9	0.3 ± 31.1	17.5 ± 68.1
$p_T(j_a) = 200\,\text{GeV}$	1.3 ± 33.4	10.0 ± 66.1	-1.8 ± 18.2	0.1 ± 45.3	4.3 ± 37.5	11.7 ± 62.3
j_l b-tagged	-0.8 ± 29.6	6.8 ± 56.0	-1.5 ± 17.1	-1.1 ± 41.3	1.4 ± 33.2	9.8 ± 52.9
$\Delta R(j_l, l) < 1.0$	-0.2 ± 30.7	-0.9 ± 44.1	-1.6 ± 17.0	-4.2 ± 24.9	2.5 ± 35.1	3.7 ± 45.4
$\Delta\Phi(j_h, l) > 2.0$	-1.0 ± 29.3	13.7 ± 69.8	-1.5 ± 16.4	2.1 ± 51.1	1.3 ± 32.9	13.9 ± 62.9

impact on the expected energy asymmetry, ranging from -1.6% for "$p_T(j_a) = 50\,\text{GeV}$" to -2.6% for "$p_T(j_a) = 200\,\text{GeV}$". In both cases, the expected significance of the energy asymmetry in the central bin is smaller than in the baseline selection. Taking into account systematic uncertainties in the unfolding process, the significance in the central bin ranges from 0.8 to 1.2; the baseline scenario provides an expected sensitivity of 1.2. The smallest expected sensitivity is obtained for the best reconstruction of the leptonic b-jet candidate, "$\Delta R(j_l, l) < 1.0$", while the inclusive top-tagger yields the best expected sensitivity. In the central bin, the uncertainty decreases by about 4% with the inclusive compared to the contained top-tagging definition, while the central value is biased by $\approx 5\%$. The largest effect is seen in the last θ_j bin, where the uncertainty decreases from $1.8 \cdot 10^{-2}$ to $1.5 \cdot 10^{-2}$, while the uncertainty in the first bin increases slightly.

Considering all of the figures of merit discussed above, the baseline selection provides the most balanced trade-off between the expected significance of the energy asymmetry in the central θ_j region, reconstruction quality and signal purity. The loosened requirements at the particle level move events from non-fiducial to fiducial $t\bar{t}$ signal and thus deteriorate the top-quark candidate reconstruction quality; the expected sensitivity does not significantly benefit from the increased acceptance fraction. The alternative p_T requirements of the associated jet do increase statistical precision at the cost of a smaller absolute value of the energy asymmetry or vice versa; both variations, however, lead to much smaller expected sensitivities of the asymmetry. Tighter requirements on the leptonic top b-jet candidate and on the hadronic top-quark candidate do increase the reconstruction quality, but decrease the already limited event numbers, resulting in higher expected uncertainties. The tighter b-tagging WP has only a small effect on the reconstruction and expected statistical significance, but suffers from larger systematic uncertainties. The inclusive top-tagging definition provides the highest expected significances and nearly doubles the number of selected events at the detector level. At the

Table 9.12.: Expected unfolding results for various selections in pseudo-data with expected data statistical uncertainties only ("Stat. only") and with all systematic uncertainties except for MC statistical uncertainties on the response matrix without smoothing ("Stat.+Syst."). Shown are the central values and standard deviations of the unfolded pseudo-data, as well as the significance $Z = |A_E|/\Delta A_E$ of the asymmetry.

	Scenario	$A_E \pm \Delta A_E\,[10^{-2}]\,(Z = |A_E|/\Delta A_E)$ inclusive	$0 \le \theta_j \le \frac{\pi}{4}$	$\frac{\pi}{4} \le \theta_j \le \frac{3\pi}{5}$	$\frac{3\pi}{5} \le \theta_j \le \pi$
Stat. only	Baseline	-0.65 ± 0.77 (0.84)	0.65 ± 1.54 (0.42)	-2.31 ± 1.34 (1.72)	0.05 ± 1.32 (0.04)
	Inclusive top-tagger	-0.65 ± 0.61 (1.06)	0.65 ± 1.20 (0.54)	-2.30 ± 1.06 (2.17)	0.05 ± 1.06 (0.05)
	b-tagging 77% WP	-0.64 ± 0.77 (0.83)	0.65 ± 1.55 (0.42)	-2.29 ± 1.34 (1.71)	0.06 ± 1.31 (0.05)
	reduced p_T (j_h, j_l)	-0.49 ± 0.78 (0.62)	0.50 ± 1.57 (0.32)	-2.04 ± 1.37 (1.49)	0.29 ± 1.35 (0.21)
	no b-flavour (j_h)	-0.71 ± 0.76 (0.92)	0.51 ± 1.52 (0.33)	-2.20 ± 1.34 (1.64)	-0.10 ± 1.32 (0.07)
	$m(j_h) > 120$ GeV	-0.64 ± 0.78 (0.82)	0.47 ± 1.54 (0.30)	-2.08 ± 1.34 (1.55)	-0.01 ± 1.34 (0.01)
	$p_T(j_a) = 50\,\text{GeV}$	-0.37 ± 0.62 (0.60)	0.16 ± 1.25 (0.13)	-1.56 ± 1.16 (1.35)	0.28 ± 0.99 (0.28)
	$p_T(j_a) = 200\,\text{GeV}$	-0.76 ± 1.10 (0.69)	1.25 ± 2.22 (0.57)	-2.56 ± 1.75 (1.46)	-0.18 ± 2.07 (0.09)
	j_l b-tagged	-0.58 ± 0.79 (0.74)	0.74 ± 1.60 (0.46)	-2.27 ± 1.36 (1.67)	0.17 ± 1.38 (0.12)
	$\Delta R(j_l, l) < 1.0$	-0.29 ± 0.96 (0.31)	0.75 ± 1.94 (0.38)	-1.82 ± 1.68 (1.08)	0.40 ± 1.62 (0.25)
	$\Delta\Phi(j_h, l) > 2.0$	-0.47 ± 0.85 (0.55)	0.60 ± 1.67 (0.36)	-2.20 ± 1.52 (1.44)	0.33 ± 1.44 (0.23)
Stat.+Syst.	Baseline	-0.65 ± 1.13 (0.58)	0.59 ± 2.19 (0.27)	-2.34 ± 2.03 (1.16)	0.12 ± 1.81 (0.07)
	Inclusive top-tagger	-0.64 ± 1.02 (0.63)	0.70 ± 2.22 (0.31)	-2.41 ± 1.95 (1.24)	0.09 ± 1.49 (0.06)
	b-tagging 77% WP	-0.68 ± 1.25 (0.54)	0.48 ± 2.25 (0.21)	-2.30 ± 2.14 (1.07)	0.09 ± 1.97 (0.05)
	reduced p_T (j_h, j_l)	-0.50 ± 1.07 (0.47)	0.39 ± 2.21 (0.18)	-2.05 ± 1.95 (1.05)	0.35 ± 1.83 (0.19)
	no b-flavour (j_h)	-0.72 ± 1.06 (0.68)	0.43 ± 2.21 (0.19)	-2.25 ± 1.89 (1.19)	-0.02 ± 1.75 (0.01)
	$m(j_h) > 120$ GeV	-0.64 ± 1.13 (0.57)	0.39 ± 2.31 (0.17)	-2.14 ± 2.03 (1.05)	0.07 ± 1.89 (0.04)
	$p_T(j_a) = 50\,\text{GeV}$	-0.37 ± 1.00 (0.37)	0.15 ± 1.86 (0.08)	-1.54 ± 1.81 (0.85)	0.25 ± 1.66 (0.15)
	$p_T(j_a) = 200\,\text{GeV}$	-0.72 ± 1.53 (0.47)	1.20 ± 3.11 (0.39)	-2.51 ± 2.97 (0.84)	-0.08 ± 2.72 (0.03)
	j_l b-tagged	-0.59 ± 1.26 (0.47)	0.64 ± 2.27 (0.28)	-2.33 ± 2.03 (1.15)	0.28 ± 1.98 (0.14)
	$\Delta R(j_l, l) < 1.0$	-0.30 ± 1.34 (0.22)	0.63 ± 2.71 (0.23)	-1.81 ± 2.38 (0.76)	0.48 ± 2.04 (0.23)
	$\Delta\Phi(j_h, l) > 2.0$	-0.45 ± 1.25 (0.36)	0.56 ± 2.51 (0.22)	-2.21 ± 2.35 (0.94)	0.41 ± 1.86 (0.22)

same time, however, the acceptance fraction drops from 70% to 47%, the fraction of hadronic top-quark candidates not matched to the parton-level object nearly doubles from 6% to 11%, and the background contamination increases from about 13% to 20%. While the impact of the larger background is already partially reflected in the unfolding procedure, especially the increasing W+jets contribution from 5% to 9% would require a more thorough investigation of the background modelling and its uncertainty. These drawbacks outweigh the small decrease in uncertainty of the energy asymmetry in the central θ_j bin.

9.3. Robustness checks

The energy asymmetry measurement was optimised under the assumption that the response matrix defined in eq. 7.4 is given by its SM prediction, taking into account the $t\bar{t}$ modelling uncertainties described in section 8.1. The possible impact of physics beyond the SM on the unfolding results is evaluated in the stress tests described in sections 9.3.1 and 9.3.2 performed in pseudo-data. Furthermore, the binning in ΔE used in the unfolding procedure is a tunable parameter, whose impact on the asymmetry is analysed in sections 9.3.3 and 9.3.4.

9.3.1. Linearity stress tests

Linearity stress tests were performed to ensure that the unfolding procedure yields the correct truth-level asymmetry for a wide range of possible particle-level asymmetries. In these tests, the signal events of the nominal prediction were reweighted at both the detector and the particle level based on the particle-level energy difference ΔE. The unfolding was then repeated with the modified pseudo-data, obtained from the sum of the reweighted signal and nominal background predictions, keeping the nominal response matrix fixed. Fiducial $t\bar{t}$ signal events with weight w were reweighted by a reweighting factor $(1 + k\Delta E)$, resulting in the new weight w':

$$w' = w(1 + k\Delta E), \quad k \in [-0.06, 0.06] \tag{9.11}$$

where k was chosen such as to yield particle-level asymmetries in a wide range between -0.15 and $+0.15$. Since these weights depend on particle-level observables and can thus not be assigned to non-fiducial signal events at the detector level, the non-fiducial signal events were scaled such that the acceptance fraction in each of the ΔE vs. θ_j bins remains constant. Figure 9.6 shows the unfolded versus true particle-level asymmetries with the expected data statistical uncertainties only and with both expected statistical and systematic uncertainties. To reduce computing time, the pruning procedure described in section 8.3.3 was applied without smoothing of the systematic uncertainties. The slopes, offsets, and their uncertainties were obtained from linear least-squared fits of the unfolded to the true particle-level asymmetries:

$$A_E^{\text{unf.}} = \text{offset} + \text{slope}\ A_e^{\text{truth}} \tag{9.12}$$

The bias in the measurement was calculated from the slope and offset:

$$\text{Bias} = A_E^{\text{unf.}} - A_E^{\text{truth}} = A_E^{\text{unf.}} - (A_E^{\text{unf.}} - \text{offset})/\text{slope} \tag{9.13}$$

evaluated at the SM prediction. Its uncertainty is given by Gaussian error propagation of the uncertainties from the slope and offset. The slopes and offsets are found to be very close to one and zero, respectively. Consequently, the bias is found to be negligible in all bins with and without systematic uncertainties. The unfolding procedure is thus found to be stable with respect to linear reweightings of the signal distribution and expected to give correct results over a wide range of asymmetry values.

9.3.2. SMEFT robustness

The robustness of the unfolding method with respect to SMEFT contributions is evaluated similarly to the linearity stress test described in section 9.3.1. The SM-EFT and EFT-EFT contributions to the ΔE vs. θ_j distribution of the operator with the largest impact on the energy asymmetry, C_{Qq}^{11}, simulated as described in section 6.2.2, were added to the SM pseudo-data. To isolate the effects from SMEFT contributions from the generator dependent effects from the differences between the samples generated with Powheg+Pythia 8 and MadGraph5_aMC@NLO 2.7 in this robustness check, the SM pseudo-data and response matrix was obtained from the MadGraph5_aMC@NLO 2.7 simulation using exactly the same settings as for the SMEFT contributions. The robustness checks were performed for various C_{Qq}^{11} coefficient values

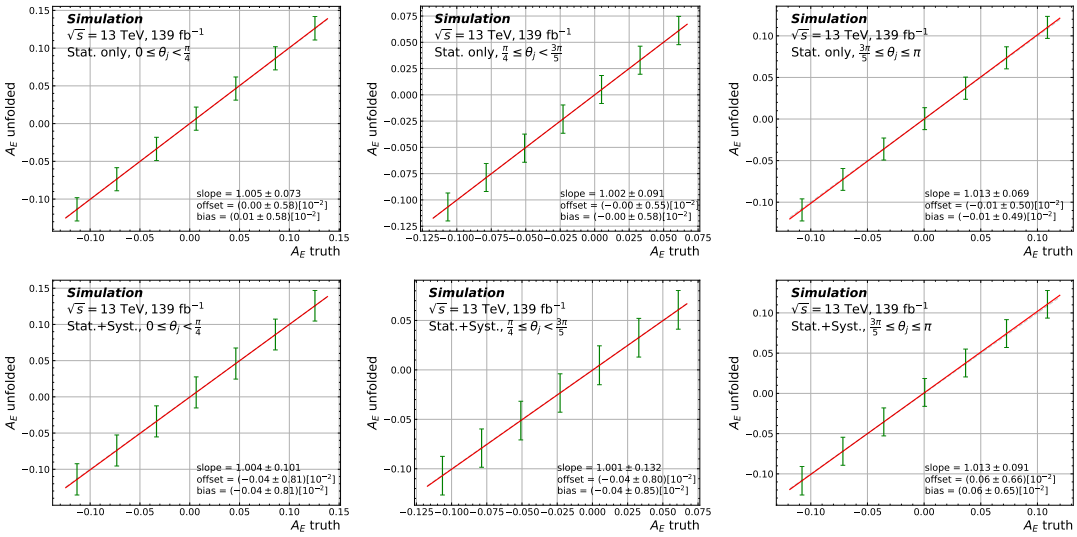

Figure 9.6.: Unfolded versus true particle-level ("truth") asymmetries for various linear reweightings of the $t\bar{t}$ signal distribution with expected data statistical uncertainties only (top) and with expected data statistical uncertainties and all systematic uncertainties except for MC statistical uncertainties on the response matrix after pruning and without smoothing (bottom). The red lines show the results of linear least squares fits.

ranging from -1.0 to 1.0 with a stepsize of 0.25, roughly covering the $1\,\sigma$–$3\,\sigma$ limits of the bounds [-0.38,0.42] from current global fits [53].

In a first closure test, both the ΔE vs. θ_j distribution and the response matrix used as inputs to the unfolding contain the SMEFT contributions. To evaluate the quality of the closure, the pseudo-data was scaled according to its MC statistical power, such that its relative uncertainty $\Delta N/N$ equals the relative uncertainty $\sqrt{N}/N$ of a Poisson distribution, and the unfolding was performed without any systematic uncertainties. Table 9.13 shows the true particle-level asymmetries and unfolded values for C_{Qq}^{11} values of -0.75, 0.0 and 0.75, roughly corresponding to the $2\,\sigma$ bounds from current global fits and to the SM prediction; the scenarios "MC stat.*" correspond to the described first closure test. The unfolded asymmetries match the true particle-level asymmetries perfectly with deviations of less than 1% well within the MC statistical uncertainties.

The robustness of the unfolding procedure with respect to variations in the response matrix due to SMEFT contributions was evaluated by varying only the ΔE vs. θ_j pseudo-data distribution, while the response matrix was kept fixed at its SM value corresponding to $C_{Qq}^{11} = 0$. The unfolding was performed with MC statistical uncertainties only as described above ("MC stat.") and with expected data statistical uncertainties including all systematic uncertainties ("Full syst.") without smoothing after pruning and without MC statistical uncertainties on the response matrix. The $t\bar{t}$ modelling systematic uncertainties were evaluated as described in section 9.1.2. As can be seen from table 9.13, the unfolded asymmetries deviate from the true asymmetries by up to 15% in outer θ_j bins and up to 7% in the central θ_j bin. These deviations are found to be well covered by the $t\bar{t}$ modelling uncertainties, in fact, already the MC statistical uncertainties on the response matrix shown in table 9.1 are large enough to cover these.

Table 9.13.: True particle-level asymmetries ("Truth") with MC statistical uncertainties and unfolded asymmetries for various values of the EFT coefficient C_{Qq}^{11}. The unfolding was performed with the SM response matrix, corresponding to $C_{Qq}^{11} = 0.0$, except for scenarios labelled with a "*", in which the response matrix incorporates the SMEFT operator contributions. Scenarios labelled as "MC stat." have the pseudo-data inputs scaled according to the MC statistical power. The "Full syst." scenarios represent the unfolding with all systematics after pruning without smoothing, except for MC statistical uncertainties on the response matrix, with the expected data statistical uncertainties. The $t\bar{t}$ modelling uncertainties were calculated from the "Full Syst." scenarios as described in section 9.1.2.

C_{Qq}^{11}	Scenario	$A_E \pm \Delta A_E [10^{-2}]$			
		inclusive	$0 \leq \theta_j \leq \frac{\pi}{4}$	$\frac{\pi}{4} \leq \theta_j \leq \frac{3\pi}{5}$	$\frac{3\pi}{5} \leq \theta_j \leq \pi$
-0.75	Truth	(-0.03 ± 0.11)	(-2.43 ± 0.21)	(-1.53 ± 0.17)	(3.27 ± 0.18)
	MC stat.*	(-0.03 ± 0.24)	(-2.43 ± 0.50)	(-1.52 ± 0.41)	(3.26 ± 0.42)
	MC stat.	(0.01 ± 0.24)	(-2.76 ± 0.50)	(-1.55 ± 0.42)	(3.64 ± 0.42)
	Full syst.	(0.00 ± 0.98)	(-2.86 ± 1.98)	(-1.59 ± 1.70)	(3.71 ± 1.54)
	$t\bar{t}$ modelling	(0.00 ± 0.62)	(-2.86 ± 0.96)	(-1.59 ± 1.10)	(3.71 ± 0.94)
+0.0	Truth	(-1.45 ± 0.12)	(-1.05 ± 0.22)	(-2.33 ± 0.20)	(-0.89 ± 0.20)
	MC stat.*	(-1.45 ± 0.28)	(-1.05 ± 0.57)	(-2.33 ± 0.50)	(-0.89 ± 0.49)
	MC stat.	(-1.45 ± 0.28)	(-1.05 ± 0.56)	(-2.33 ± 0.50)	(-0.89 ± 0.49)
	Full syst.	(-1.46 ± 1.05)	(-1.12 ± 2.03)	(-2.37 ± 1.88)	(-0.83 ± 1.65)
	$t\bar{t}$ modelling	(-1.46 ± 0.61)	(-1.12 ± 0.93)	(-2.37 ± 1.13)	(-0.83 ± 0.96)
+0.75	Truth	(-0.45 ± 0.11)	(-2.96 ± 0.21)	(-2.29 ± 0.17)	(3.27 ± 0.18)
	MC stat.*	(-0.45 ± 0.25)	(-2.97 ± 0.50)	(-2.29 ± 0.42)	(3.27 ± 0.42)
	MC stat.	(-0.44 ± 0.24)	(-3.28 ± 0.51)	(-2.44 ± 0.42)	(3.67 ± 0.42)
	Full syst.	(-0.45 ± 0.99)	(-3.36 ± 1.99)	(-2.46 ± 1.70)	(3.72 ± 1.55)
	$t\bar{t}$ modelling	(-0.45 ± 0.62)	(-3.36 ± 0.98)	(-2.46 ± 1.08)	(3.72 ± 0.94)

Figure 9.7 visualises the unfolded versus true particle-level asymmetries with MC statistical uncertainties and with the expected data statistical uncertainties including all systematic uncertainties. The slopes and offsets between these two scenarios are very similar, the slopes deviate by less than 5% from 1 in the central θ_j bin and by up to 19% in the outer θ_j bins. The biases calculated at the SM value, however, are found to be negligible in all bins and scenarios with a maximum value of 0.0015 and well within the MC statistical uncertainty, assuming that the individual measurements were performed independently.

Overall, the unfolding procedure is found to be robust with respect to SMEFT coefficient variations within the $2\,\sigma$ limits of current global fits, and uncertainties on the response matrix due to SMEFT contributions are assumed to be covered by the $t\bar{t}$ modelling uncertainties.

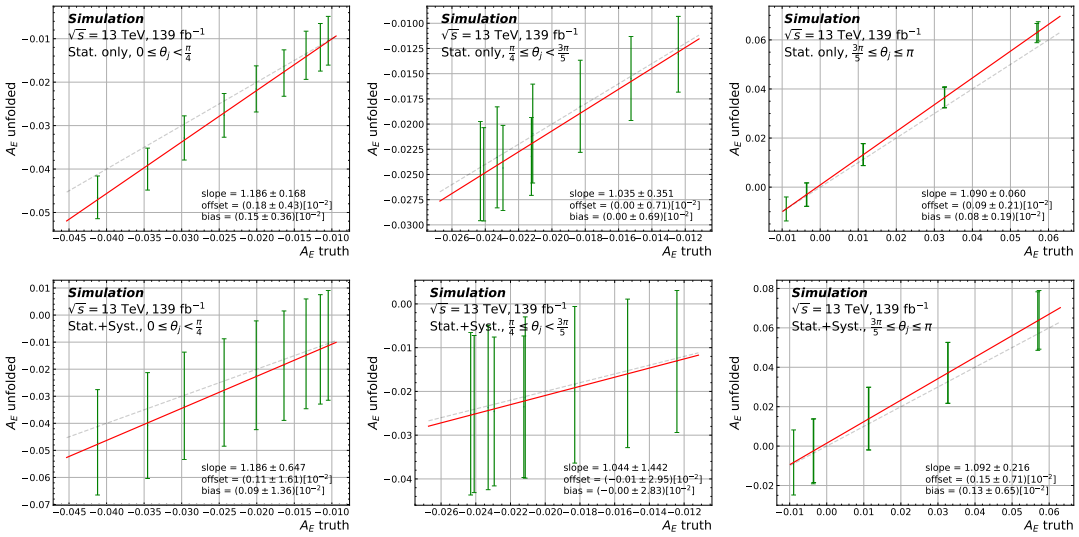

Figure 9.7.: Unfolded versus true particle-level ("truth") asymmetries for variations of C_{Qq}^{11} within the range of $[-1.0, 1.0]$ with MC statistical uncertainties only (top) and with MC statistical uncertainties and all systematic uncertainties except for MC statistical uncertainties on the response matrix after pruning and without smoothing (bottom). The red lines show the results of linear least squares fits. Dashed lines (45°) represent an idealised scenario where the unfolded values equal the truth asymmetries.

9.3.3. Binning in ΔE

Four bins in ΔE were chosen to account for the different migration behaviour for small and large energy differences, as well as a high number of events in each bin to reduce statistical uncertainties. The bin boundaries, $[-\infty, -100, 0, 100, \infty]$, where chosen such as to ensure a largely diagonal migration matrix and to yield similar event numbers in all four ΔE bins; see figures 7.2 and 9.17, respectively. This section evaluates the impact of the binning choice on the energy asymmetry measurement.

Table 9.14 shows the expected unfolding results for different binning choices with statistical uncertainties and with both statistical and systematic uncertainties, except for MC statistical uncertainties on the response matrix. The systematic uncertainties were pruned as described in section 8.3.3 and no smoothing was applied to save computing time. The unfolded energy asymmetry is found to be robust with respect to the binning choice with variations of the expected uncertainty less than 10% among all binning choices and θ_j bins, except for the smallest binning choice of 50 GeV, where the systematic uncertainties suffer from statistical fluctuations due to the limited number of events in the central ΔE regions.

Figures 9.8 and 9.9 show the slopes, offsets, and biases obtained in the robustness checks with respect to linearity stress tests and SMEFT robustness checks described in sections 9.3.1 and 9.3.2, respectively, for the various binning choices. The chosen binning in ΔE exhibits the slopes closest to one in the linearity checks and the smallest biases in the SMEFT robustness test in the central θ_j bin. The bias evaluated at the SM prediction is found to be negligible in all θ_j bins. Overall, however, the slopes, offsets, and biases are found to be robust with respect to the binning choice.

Table 9.14.: Expected asymmetries and uncertainties with different binning choices $[-\infty, -x, 0, x, \infty]$ GeV in ΔE. Shown are the true particle-level predictions ("Truth") with MC statistical uncertainties and the unfolding results based on expected data statistical uncertainties only ("Stat. only") and with all systematics except for MC statistical uncertainties on the response matrix after pruning without smoothing ("Stat.+Syst."). Bold numbers indicate the chosen binning.

	x	$A_E \pm \Delta A_E$ $[10^{-2}]$			
		inclusive	$0 \leq \theta_j \leq \frac{\pi}{4}$	$\frac{\pi}{4} \leq \theta_j \leq \frac{3\pi}{5}$	$\frac{3\pi}{5} \leq \theta_j \leq \pi$
Truth		-0.64 ± 0.16	0.65 ± 0.31	-2.30 ± 0.27	0.05 ± 0.27
Stat. only	50	-0.66 ± 0.81	0.66 ± 1.66	-2.30 ± 1.40	0.01 ± 1.38
	75	-0.64 ± 0.78	0.65 ± 1.58	-2.30 ± 1.34	0.06 ± 1.34
	100	$\mathbf{-0.65 \pm 0.77}$	$\mathbf{0.66 \pm 1.53}$	$\mathbf{-2.31 \pm 1.35}$	$\mathbf{0.04 \pm 1.32}$
	125	-0.64 ± 0.76	0.66 ± 1.51	-2.29 ± 1.33	0.05 ± 1.32
	150	-0.64 ± 0.76	0.64 ± 1.51	-2.28 ± 1.33	0.05 ± 1.30
Stat.+Syst.	50	-0.65 ± 1.23	0.53 ± 2.54	-2.26 ± 2.20	0.09 ± 1.78
	75	-0.60 ± 1.19	0.76 ± 2.31	-2.30 ± 2.08	0.09 ± 1.91
	100	$\mathbf{-0.64 \pm 1.09}$	$\mathbf{0.61 \pm 2.14}$	$\mathbf{-2.34 \pm 1.94}$	$\mathbf{0.12 \pm 1.73}$
	125	-0.64 ± 1.05	0.60 ± 2.16	-2.31 ± 1.84	0.12 ± 1.71
	150	-0.62 ± 1.08	0.56 ± 2.12	-2.27 ± 1.89	0.15 ± 1.71

9.3.4. Number of truth-level bins

Only two ΔE bins are necessary to calculate the energy asymmetry in each bin of the jet scattering angle. The same-sign ΔE bins could thus be merged at the particle level, resulting in a total of six particle-level bins (parameters of interest, POIs), while the number of detector-level bins (observables) is kept at twelve. With more observables than POIs, the unfolding is expected to put constraints on the systematic uncertainties that are stronger than their pre-marginalisation standard deviations. Figures 9.10 and 9.11 show the migration matrix, efficiencies and acceptances for this setup. The resulting response matrix is shown in figure 9.12. In contrast to the default setup with twelve parameters of interest shown in figure 7.2, the non-diagonal migration matrix reflects the expected fraction of detector-level events in the small ($|\Delta E| < 100$) and large ($|\Delta E| > 100$) ΔE bins. The signal efficiencies are given by event-weighted averages of the efficiencies in same-sign ΔE bins for twelve POIs in figure 7.3, and the acceptances are identical to the twelve POIs case.

Table 9.15 compares the unfolding results for pseudo-data with twelve and six parameters of interest. The expected data statistical uncertainties decrease slightly in the inclusive asymmetry as well as in all differential θ_j bins. The total uncertainties decrease by about 4% in the first and central θ_j bins, but do not change significantly in the last θ_j bin.

Figure 9.13 shows the ranking of the systematic uncertainties, obtained with the same methods as described in section 9.1.2. As with twelve POIs in figure 9.2, the data statistical uncertainty is expected to be by far the dominating uncertainty, followed

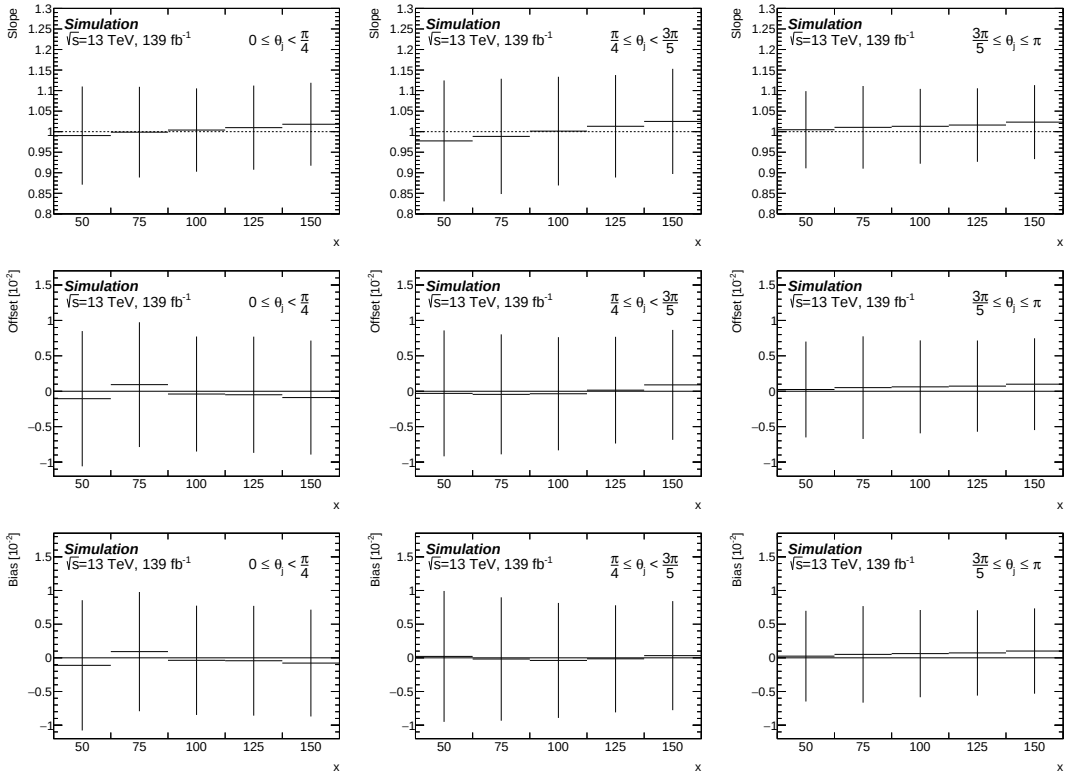

Figure 9.8.: Slopes, offsets, and biases in the linearity tests in dependence of the binning in ΔE, $[-\infty, -x, 0, x, \infty]$ GeV, with expected data statistical and all systematic uncertainties except for MC statistical uncertainties on the response matrix after pruning and without smoothing.

by JER uncertainties in the first θ_j bin and $t\bar{t}$ and single-top modelling uncertainties in the central bin. In contrast to the twelve parameter case, however, there are clear differences between the pre- and post-marginalisation uncertainties for the $t\bar{t}$ modelling uncertainties. The argument discussed in section 9.1.2 that for each configuration of the nuisance parameters there exist a truth-level ΔE vs. θ_j distribution with the same prior probability as all other truth-level distributions such that the prediction matches the observed data is not valid in this case. With six POIs, it is no longer possible to find a configuration that fits all twelve observables simultaneously; thus nuisance parameter values deviating from zero will reduce the likelihood in eq. 7.5 through both its own prior as well as the Poisson probability to observe the data given the prediction. This leads to constraints on the posterior distribution of the nuisance parameters stronger than in their prior distribution. Furthermore, the reduction in the likelihood through the Poisson probability can offset the reduction through the nuisance parameter's prior when it deviates from the central value of it's prior distribution in data, allowing the unfolding method to not only assign an uncertainty to the unfolded distribution, but also to correct its central value.

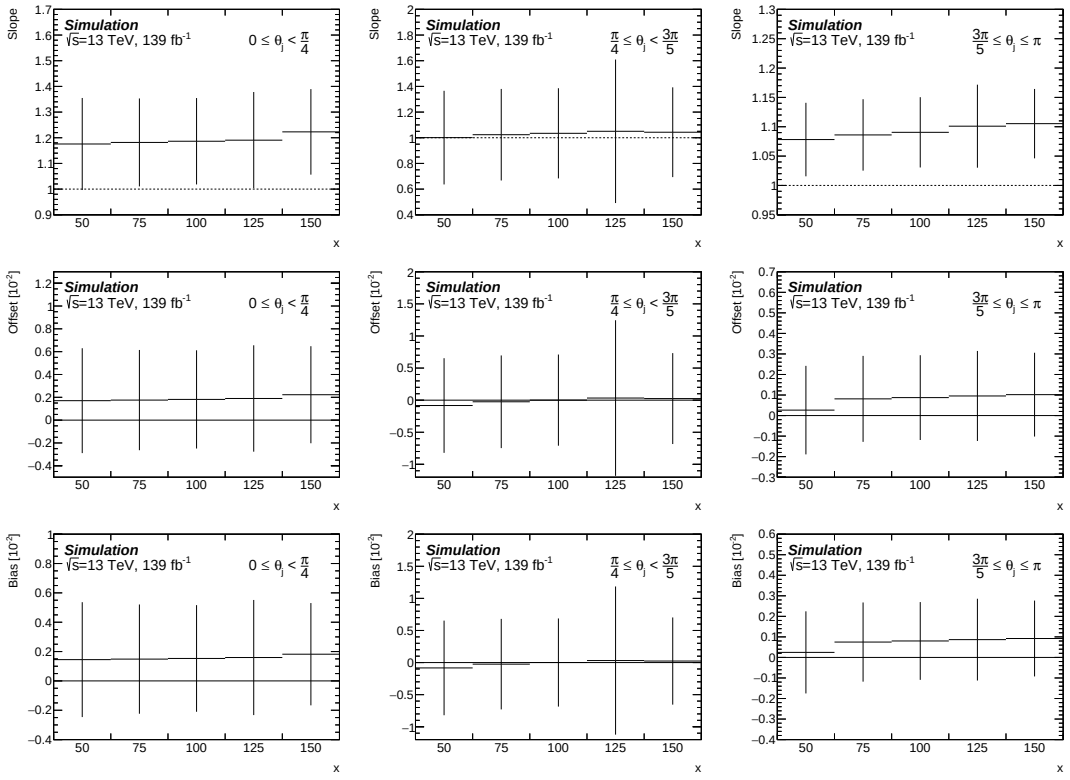

Figure 9.9.: Slopes, offsets, and biases in the SMEFT closure tests in dependence of the binning in ΔE, $[-\infty, -x, 0, x, \infty]$ GeV, with MC statistical uncertainties.

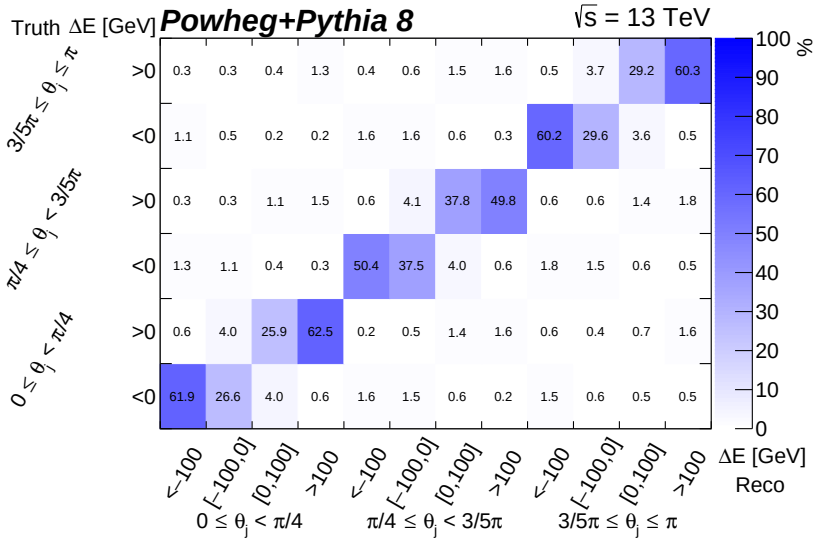

Figure 9.10.: Migration matrix $P = (p_{ij})$ as estimated with the SM $t\bar{t}$ sample for six parameters of interest. The elements p_{ij} denote the probability of a reconstructed event produced in truth-level bin j to be reconstructed in detector-level bin i.

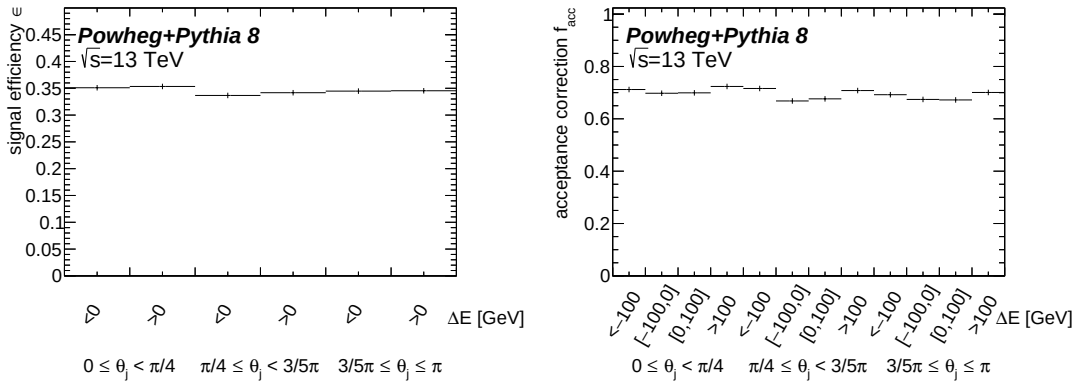

Figure 9.11.: Signal efficiency ϵ (left) and acceptance correction f_{acc} (right) in the particle- and detector-level bins, respectively, as estimated with the SM $t\bar{t}$ sample for six parameters of interest. MC statistical uncertainties are denoted by error bars.

While pulls in nuisance parameters can not any more be fully offset by a change in the true particle-level ΔE vs. θ_j distribution, they can be partially offset by pulls in other nuisance parameters, introducing correlations between the systematic uncertainties. Figure 9.14 shows the correlations between the highest ranked systematic uncertainties as well as the inclusive and differential energy asymmetries. In contrast to the small correlations of at most 3% between the systematic uncertainties observed in the twelve POIs case shown in figure 9.3, the $t\bar{t}$ modelling uncertainties show positive correlations at the order of 20%.

The $t\bar{t}$ matching, FSR and parton shower uncertainties for twelve and six POIs are compared in figure 9.15. The positive correlation between the $t\bar{t}$ matching and parton shower systematic uncertainties in case of six POIs is clearly driven by the opposite shapes in the first and last θ_j bins, such that a positive change in one NP is partially offset by a positive change in the other. A similar offsetting shape can be seen in the central bin between the $t\bar{t}$ matching and FSR uncertainties. The matching uncertainty shown in the top of figure 9.15 becomes much larger in the six POIs case, with deviations of up to 10% compared to less than 5% in the twelve POIs case; also the effects in the outer angular bins become statistically significant and are no longer smoothed away. Similarly, the parton shower uncertainty becomes statistically significant in the outer θ_j bins, while the FSR uncertainty remains similar to the twelve POIs case. Note that any difference in the twelve vs. six POIs case comes solely from the changed shape of the response matrix with six particle-level and twelve detector-level bins, i.e. one particle-level bin for two detector-level bins, reflecting the relative number of events with large ($|\Delta E| > 100\,\text{GeV}$) and small ($|\Delta E| < 100\,\text{GeV}$) energy differences. With six POIs, this relative number becomes an input of the unfolding procedure, such that its uncertainty does also enter the unfolding process. While the systematic uncertainties put into the unfolding increase, the total uncertainty after unfolding decreases as shown in table 9.15 due to the constraints discussed above.

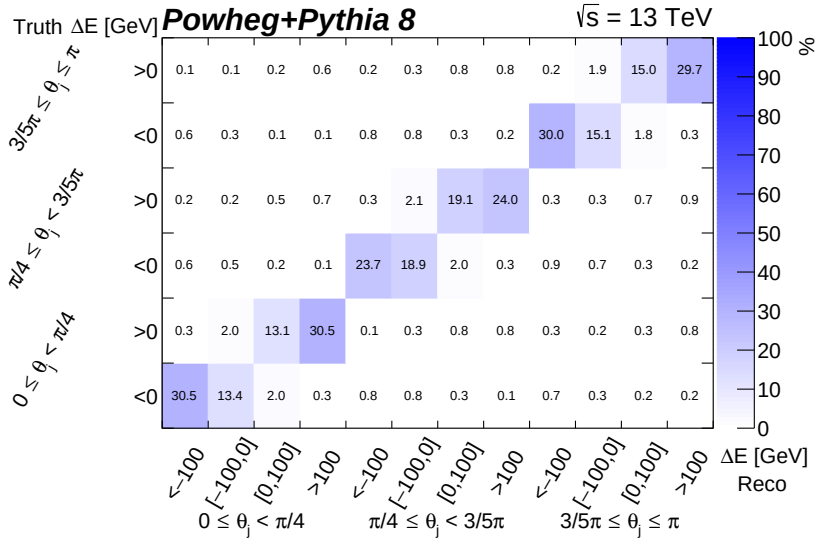

Figure 9.12.: Response matrix $\mathcal{M} = (m_{ij})$ as estimated with the SM $t\bar{t}$ sample for six parameters of interest. The elements m_{ij} are defined in eq. 7.4 as the product of the migration p_{ij}, the efficiency ϵ_j, and the inverse of the acceptance fraction $f_{\text{acc},i}$.

Table 9.15.: True particle-level asymmetries ("Truth") with MC statistical uncertainties and unfolding results for pseudo-data with twelve and six parameters of interest. The unfolding was performed with expected data statistical uncertainties only ("Stat. only") and with both expected data statistical and systematic uncertainties ("Stat.+Syst."). The MC statistical uncertainties on the response matrix "MC stat." were evaluated as described in section 8.4. The total uncertainties were obtained by adding the "Stat.+Syst." and "MC Stat." uncertainties in quadrature.

	Scenario	$A_E \pm \Delta A_E[10^{-2}]$ Inclusive	$0 \leq \theta_j < \frac{\pi}{4}$	$\frac{\pi}{4} \leq \theta_j < \frac{3\pi}{5}$	$\frac{3\pi}{5} \leq \theta_j \leq \pi$
	Truth	(-0.64 ± 0.16)	(0.65 ± 0.31)	(-2.30 ± 0.27)	(0.05 ± 0.27)
12 POIs	Stat. only	(-0.65 ± 0.77)	(0.56 ± 1.53)	(-2.31 ± 1.34)	(0.10 ± 1.32)
	Stat.+Syst.	(-0.67 ± 1.02)	(0.55 ± 1.99)	(-2.33 ± 1.90)	(0.10 ± 1.56)
	MC stat.	0.25	0.52	0.42	0.42
	Total	(-0.67 ± 1.05)	(0.55 ± 2.05)	(-2.33 ± 1.95)	(0.10 ± 1.61)
6 POIs	Stat. only	(-0.65 ± 0.74)	(0.62 ± 1.46)	(-2.29 ± 1.33)	(0.04 ± 1.29)
	Stat.+Syst.	(-0.66 ± 1.01)	(0.61 ± 1.91)	(-2.29 ± 1.84)	(0.03 ± 1.56)
	MC stat.	0.24	0.48	0.41	0.41
	Total	(-0.66 ± 1.04)	(0.61 ± 1.97)	(-2.29 ± 1.88)	(0.03 ± 1.61)

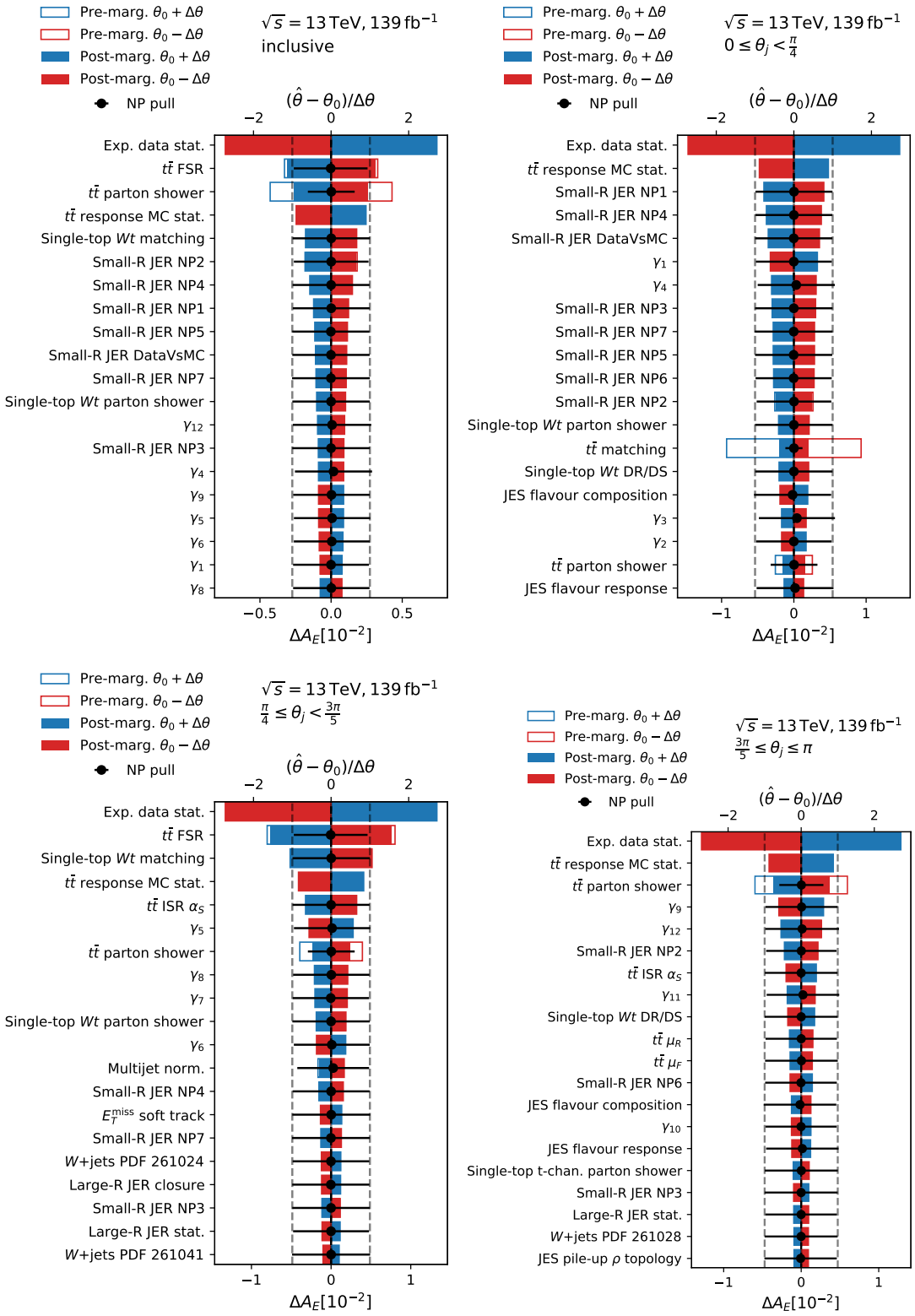

Figure 9.13.: Ranking of expected uncertainties on the inclusive and differential energy asymmetry in pseudo-data with six parameters of interest. Blue and red areas show the impact on the energy asymmetry from a one σ variation of the corresponding nuisance parameter as defined in eq. 9.8. The means and standard deviations of the posterior distributions of the nuisance parameters, normalised to their pre-marginalisation standard deviations, are illustrated by black dots and error bars.

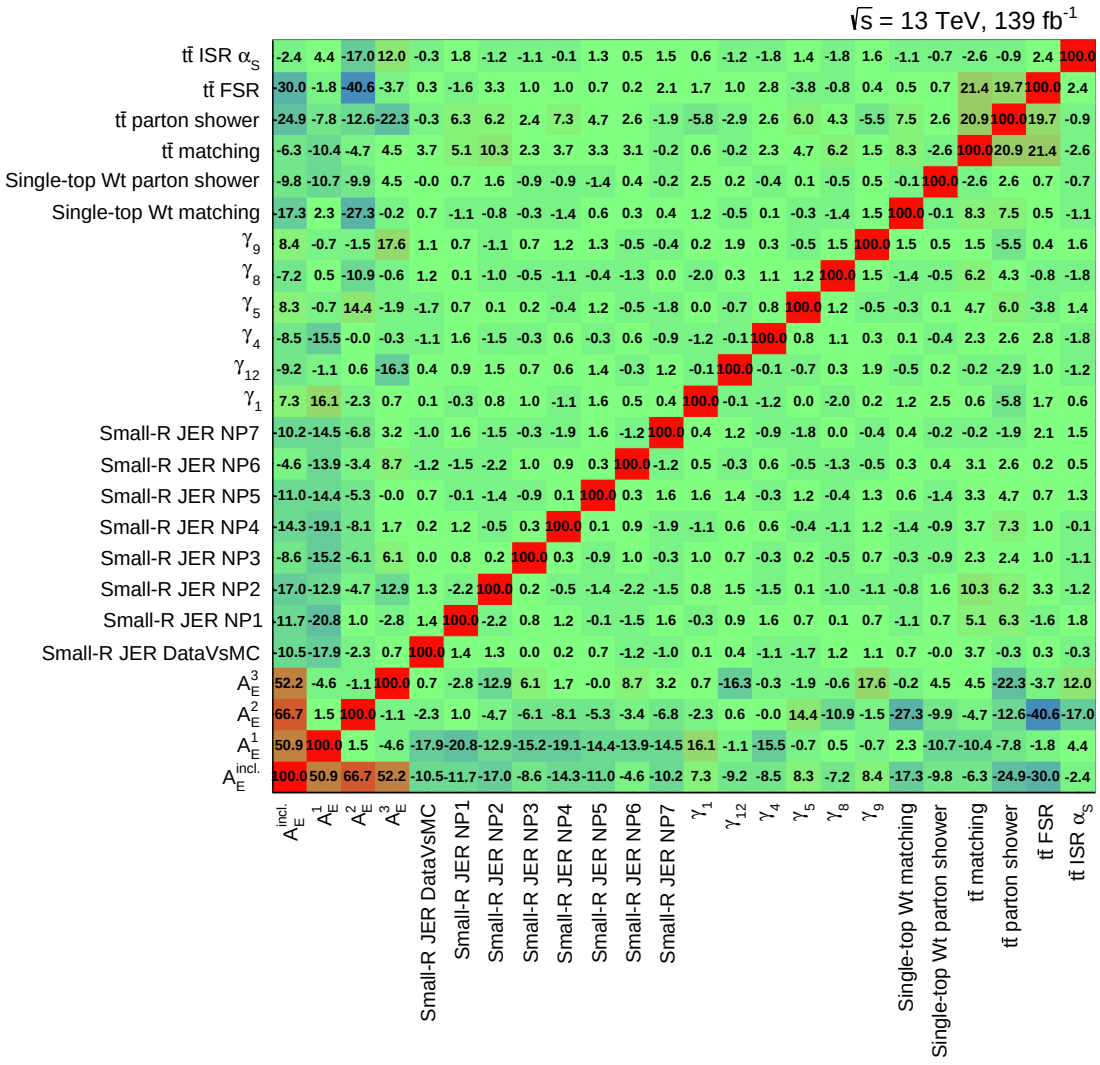

Figure 9.14.: Correlation matrix for the highest ranked expected systematic uncertainties in pseudo-data with each other and with the inclusive and differential energy asymmetry using six POIs. For better visibility, the correlations are scaled by a factor of 100.

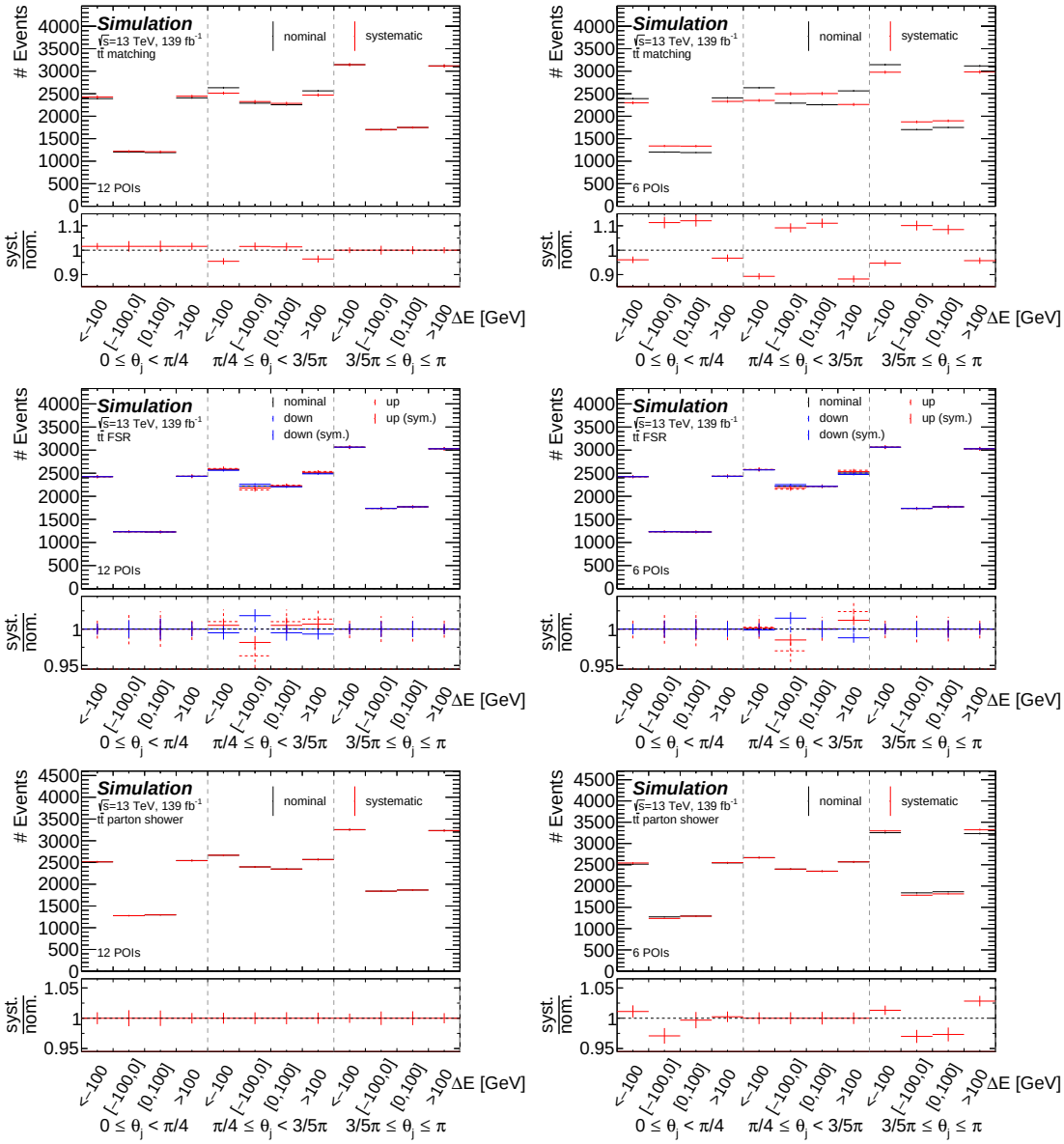

Figure 9.15.: Comparison of $t\bar{t}$ matching (top), FSR (middle) and parton shower (bottom) modelling uncertainties with twelve (left) and six (right) parameters of interest after smoothing. The error bars correspond to the MC statistical uncertainty estimated as the standard deviation of the corresponding replicas.

The linearity stress tests discussed in section 9.3.1 were also performed with six POIs. Figure 9.16 shows the unfolded versus true particle-level asymmetries for expected data statistical uncertainties only and with all systematic uncertainties except for MC statistical uncertainties on the response matrix after pruning and without smoothing. The slopes deviate by up to 25% from 1, compared to deviations of at most 1% in the twelve POIs case shown in figure 9.6. This feature is a combination of the linear reweighting procedure and of the larger population in the outer than the inner ΔE bins in each θ_j bin. Reweighting the truth-level distribution with a weight proportional to ΔE according to eq. 9.11 increases (decreases) the event yield for the outer bin for positive (negative) energy differences compared to the inner bin, effectively changing the migration for a given truth-level ΔE bin in each θ_j bin. Assuming that the correct true particle-level distribution is drawn in the sampling, after folding it with the nominal response matrix, the first ΔE will have too many events with respect to the pseudo-data distribution, the second too few, the third too many and the fourth too few. The sampling will give preference to the bins with the smallest uncertainty, i.e. the highest statistics, which are the outer ΔE bins. The sampled event yield in the negative true particle-level ΔE bin will thus be reduced and the positive true particle-level ΔE bin will be increased during the sampling, leading to an increased energy asymmetry compared to the correct one.

The results listed in table 9.15 show that the reduction in the number of parameters of interests from twelve to six reduces both the expected data statistical and the total uncertainty after unfolding by about 5% in the first two θ_j bins. Furthermore,

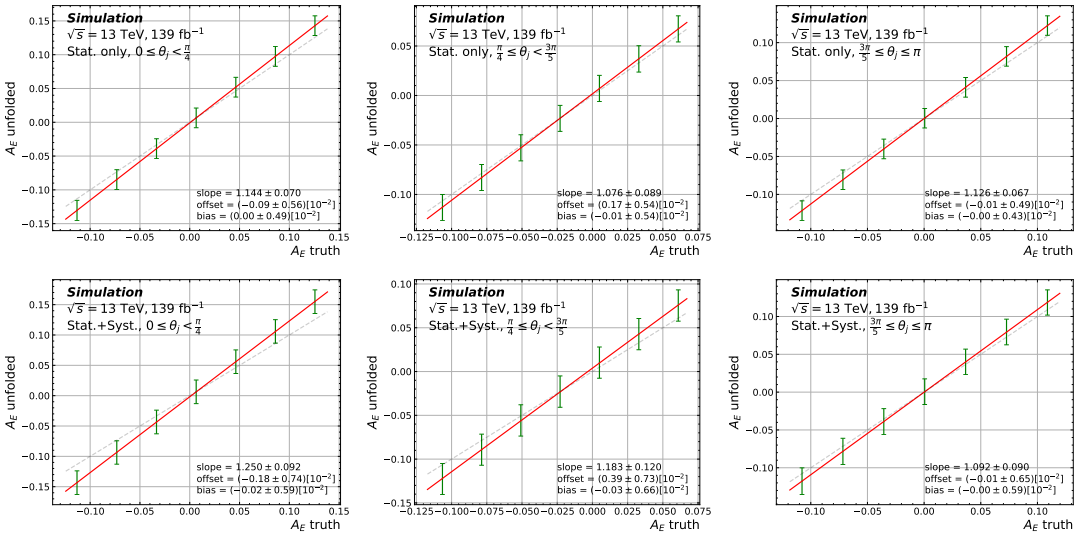

Figure 9.16.: Expected unfolded versus true particle-level ("truth") asymmetries for various linear reweightings of the particle-level distribution with expected data statistical uncertainties (top) and with expected data statistical uncertainties and all systematic uncertainties except for MC statistical uncertainties on the response matrix after pruning and without smoothing (bottom) using six POIs. The red lines show the results of linear least squares fits. Dashed lines (45°) represent an idealised scenario where the unfolded values equal the truth asymmetries.

the systematic uncertainties can be constrained with respect to their prior distributions and pulled to accommodate differences between data and simulation as seen in figure 9.13 and discussed above. These benefits, however, are accompanied with drawbacks. First, the most significant constraints concern the $t\bar{t}$ modelling uncertainties, especially the $t\bar{t}$ matching uncertainty and parton shower uncertainties. In contrast to most of the other uncertainties, these were not derived as Gaussian uncertainties, but are single-sided uncertainties, for which a prior distribution must be assumed. While a Gaussian distribution itself is per se a common assumption, putting large constraints on this distribution requires a more thorough understanding and justification of this uncertainty. Second, the linearity stress tests shown in figure 9.16 exhibit a weakness in the assumption of a fixed ratio between the event numbers in large and small $|\Delta E|$ bins. Especially in light of the following SMEFT interpretation of the unfolding results, it is appropriate to put as little assumptions on the underlying true particle-level distributions as possible into the unfolding process to ensure a high stability with respect to various models. The usage of twelve parameters of interest is thus well justified despite the small decrease in expected sensitivity, and the comparison with six parameters of interest shows that expected sensitivity is quite robust also with respect to a change of this important parameter.

9.4. Data measurement

Section 9.4.1 provides a comparison of various detector-level distributions observed in data and the corresponding predictions obtained in simulation and data-driven estimates. The unfolding results in data are presented in section 9.4.2; the corresponding systematic uncertainties are discussed in section 9.4.3.

9.4.1. Comparisons of data to the predictions

The FBU procedure described in chapter 7 provides a posterior detector-level distribution of the ΔE vs. θ_j observable used in the unfolding process based on the signal response matrix and background predictions. The expected signal distribution is not used as an input to the unfolding, such that systematic uncertainties affecting the signal normalisation do not need to be taken into account, leading to reduced uncertainties of the detector-level distribution. In general, the FBU procedure can furthermore constrain the effect of individual systematic uncertainties and improve the agreement between data and prediction also for other than the unfolded distributions by pulling the nuisance parameters. With a flat prior for the particle-level distribution and the same number of observables (detector-level bins) and parameters of interest (particle-level bins), however, the systematic uncertainties are largely unconstrained and not significantly shifted from zero. The main effect in the decrease of systematic uncertainties on the detector-level distribution is thus given by the removal of systematic uncertainties on the signal normalisation.

The post-marginalisation detector level distribution of ΔE vs. θ_j is given by the mean and standard deviation of the posterior detector-level distribution sampled during the unfolding process, and thus reflects all uncertainties with their correct correlations. All pre-marginalisation and the post-marginalisation distributions for observables that are not used in the unfolding procedure are approximated as follows.

The signal and background predictions in detector-level bin i can be written as:

$$r_i(T, \mathcal{M}, \theta) = r_i(T, \mathcal{M}, 0)(1 + \theta_s \Delta r) \left(1 + \sum_{k=1}^{N_{\theta_s}} \theta_s^k \Delta r_i^k \right) \tag{9.14}$$

$$b_i^j(\theta) = b_i^j(1 + \theta_b^j \Delta b^j) \left(1 + \sum_{k=1}^{N_{\theta_s}} \theta_s^k \Delta b_i^{j,k} \right) \tag{9.15}$$

with the same notation as in equations 7.6 and 7.7 in section 7.2, with an additional nuisance parameter θ_s for the signal normalisation and the corresponding relative uncertainty Δr. The central values in the figures were obtained by setting all nuisance parameters to zero (pre-marginalisation) or the the mean value of their posterior distribution after unfolding (post-marginalisation). The uncertainties were obtained via Gaussian error propagation with uncertainties on the nuisance parameters of one (pre-marginalisation) and of the standard deviation of the posterior distribution (post-marginalisation). Two-sided systematics were symmetrised as described in section 8.3.2 and no smoothing procedure was applied. Since the $t\bar{t}$ signal distribution is not used in the unfolding there is no corresponding nuisance parameter θ_s for the normalisation and the mean and standard deviation of the ratio of the unfolded to the predicted truth-level yield serve as proxies for the mean and standard deviation, respectively, of the multiplicative factor $(1 + \theta_s \Delta r)$.

Table 9.16 compares the event yields for the signal and background predictions before unfolding (pre-marginalisation) to the event yield observed in data. The fiducial $t\bar{t}$ signal events correspond to $t\bar{t}$ events passing the detector-level selection that do also pass the particle-level requirements, while the non-fiducial $t\bar{t}$ signal events pass only the detector-level selection as described in section 5. The predicted event yield is roughly 10% larger than the observed data due to an overestimation of the $t\bar{t}$ yield in the boosted phase space at NLO; see references [266, 319] and figure B.1 in appendix B.1 for further details.

The signal purity, i.e. the fraction of simulated $t\bar{t}$ events to the total predictions, is 87%. 70% of the $t\bar{t}$ signal constitute the fiducial $t\bar{t}$ signal. The remaining 30% are mostly events in which the hadronic top-quark candidate does not pass the p_T, mass and b-flavour requirements at the particle level. The uncertainty of $\approx 21\%$ on the $t\bar{t}$ event yield is mostly driven by normalisation uncertainties from signal modelling effects which do not affect the energy asymmetry observable. The dominating background process is W-boson production with a contribution of about 5% due to a final state similar to that of $t\bar{t}$ events as described in section 6.3.1. The validity of the modeling of this background was checked in a W+jets control region close to the signal region described in appendix B.2 and the observed discrepancies to data are covered within its systematic uncertainties. The single-top Wt and multijet backgrounds each contribute by about 2%.

Figure 9.17 shows a comparison of data to the pre- and post-marginalisation prediction for the ΔE vs. θ_j distribution used in the unfolding. The agreement between the data and the prediction after marginalisation is perfect, with identical uncertainties. This is an expected feature of the unfolding being performed with the same number of observables and parameters of interest; the particle-level distribution will be drawn in

Table 9.16.: Event yields for the simulated signal and background predictions with pre-marginalisation uncertainties as described in chapter 8, compared with the event yield observed in data. Predictions were rounded to two significant digits. The inclusive event numbers were published in table 1 in reference [83].

	Events			
	inclusive	$0 \leq \theta_j < \frac{\pi}{4}$	$\frac{\pi}{4} \leq \theta_j < \frac{3\pi}{5}$	$\frac{3\pi}{5} \leq \theta_j \leq \pi$
$t\bar{t}$ fiducial	$18\,000 \pm 3700$	5200 ± 1100	6600 ± 1300	6600 ± 1300
$t\bar{t}$ non-fiducial	8000 ± 1700	2100 ± 410	2900 ± 720	3000 ± 610
W+jets	1600 ± 860	350 ± 190	610 ± 330	650 ± 350
Single-top Wt	680 ± 340	180 ± 70	270 ± 150	230 ± 120
Multijet	580 ± 300	160 ± 80	190 ± 100	230 ± 120
$t\bar{t}V$	400 ± 200	72 ± 36	187 ± 94	140 ± 70
Z+jets	210 ± 110	45 ± 23	84 ± 43	82 ± 41
VV	168 ± 85	34 ± 17	67 ± 34	67 ± 34
$t\bar{t}H$	147 ± 74	27 ± 14	70 ± 35	49 ± 25
Single-top t-channel	82 ± 40	25 ± 11	25 ± 16	33 ± 12
Single-top s-channel	8 ± 3	1 ± 1	4 ± 2	2 ± 1
Total	$30\,000 \pm 5300$	8200 ± 1500	$11\,000 \pm 2100$	$11\,000 \pm 1900$
Data	27 265	7446	9995	9824

such a way that the corresponding detector level distribution fits the data distribution within its uncertainty.

Figure 9.18 shows the data/prediction comparisons for the jet scattering angle θ_j with non-optimised and optimised event numbers as well as the top- and antitop-quark energies in the $t\bar{t}j$ rest frame. The non-optimised event yield for the jet scattering angle θ_j is symmetric around $\pi/2$ as expected for a symmetric pp beam and has maxima slightly below $\pi/4$ and above $3/4\pi$. The optimised event yield for θ_j exhibits a skewed distribution with a more pronounced maximum slightly below $\pi/4$. The top- and antitop-quark energies in the $t\bar{t}j$ rest frame exhibit very similar distributions peaking between 400 and 500 GeV. The transverse momenta of the top-quark candidates, separated by decay channel and charge, are shown in figure 9.19. The transverse momentum of the hadronically decaying top quark is characterised by a steeply falling distribution with a maximum between 350 GeV and 400 GeV; the cut at 350 GeV is determined by the p_T requirement of the large-R jet described in section 5.1. The leptonically decaying top-quark candidate, on the other hand, has a more symmetric distribution peaking around 300 GeV, since there is no explicit p_T requirement in the event selection. The top- and antitop-quark momenta, given by superposition of these two distributions, are very similar. Figure 9.20 illustrates the transverse momentum of the associated jet and the mass of the $t\bar{t}$ system. Similarly to the hadronically top-quark candidates transverse momentum, the associated jet p_T is a steeply falling distribution characterised by the p_T in the event selection. The $m_{t\bar{t}}$ distribution is mostly concentrated in the range of 600 GeV $\lessapprox m_{t\bar{t}} \lessapprox$ 1200 GeV well above the $t\bar{t}$ production threshold. For all of these

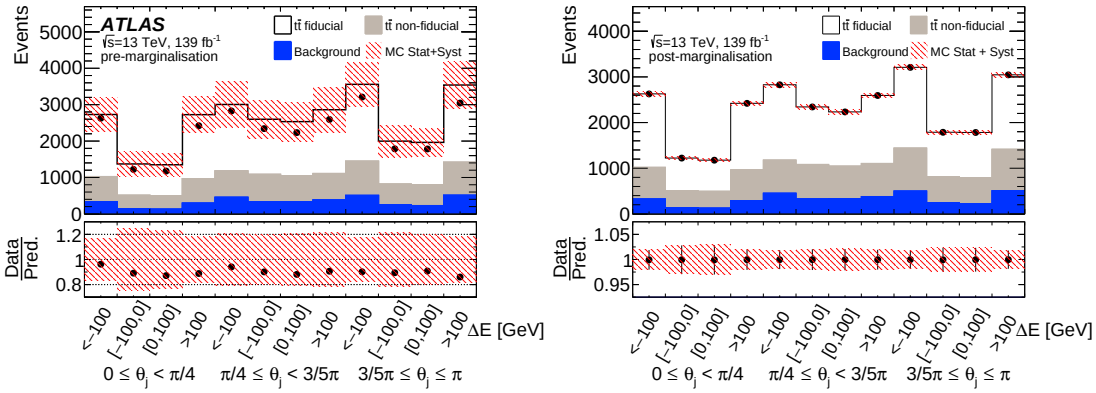

Figure 9.17.: Comparison of ATLAS data (black markers) to the pre- (left) and post-marginalisation (right) distribution for the ΔE vs. θ_j observable used in the unfolding. The event numbers correspond to the optimised cross section as defined in eq. 2.39. The left plot was published as figure 5 in reference [83].

distributions, the main discrepancies between data and prediction are observed in the normalisation, which is clearly improved in the post-marginalisation distribution. For the top-quark candidates transverse momenta, the predictions seem to overestimate high-p_T events, resulting in somewhat downward sloping data over prediction ratios, well within the uncertainties.

The agreement of the prediction with the observed data was evaluated with a goodness-of-fit test as described in section 9.1.1 for all of these distributions, taking into account the full covariance matrix between the systematic uncertainties. The reduced χ^2 values range from 0.20 to 1.13 before and from 0.13 to 1.11 after marginalisation; the significances of the deviations are always below one σ and do mostly decrease after marginalisation. This strengthens the interpretation that the prediction agrees well with the data for various observables, with deviations largely caused by normalisation uncertainties that do not affect the energy asymmetry, as well as that the systematic uncertainties are of reasonable size.

Table 9.17 shows the detector-level asymmetries for the signal and background predictions, ordered by event number. The most important backgrounds are the W+jets, single-top Wt and multijet (fake and non-prompt leptons) events. The multijet events, which are not expected to show any asymmetry, exhibit the largest asymmetry in the central θ_j bin, but also the largest statistical uncertainty, and are thus found to be compatible with zero in all three bins. The W+jets events are found to have a large and statistically significant negative asymmetry in all bins, which is due to the asymmetric transverse momenta requirements on the hadronically and leptonically decaying top-quark candidates in the boosted phase space. The selected events are required to have exactly one lepton, thus the W boson does typically decay leptonically and will be reconstructed as part of the leptonically decaying top-quark candidate. Due to the parton distribution function of the proton, there are more events with W^+ than W^- bosons, such that the leptonically decaying top-quark candidate is more often positively than negatively charged. The hadronically decaying top-quark candidate, which has, on average, a larger energy than the leptonically decaying one, is more often negative than positive, resulting in a negative energy asymmetry.

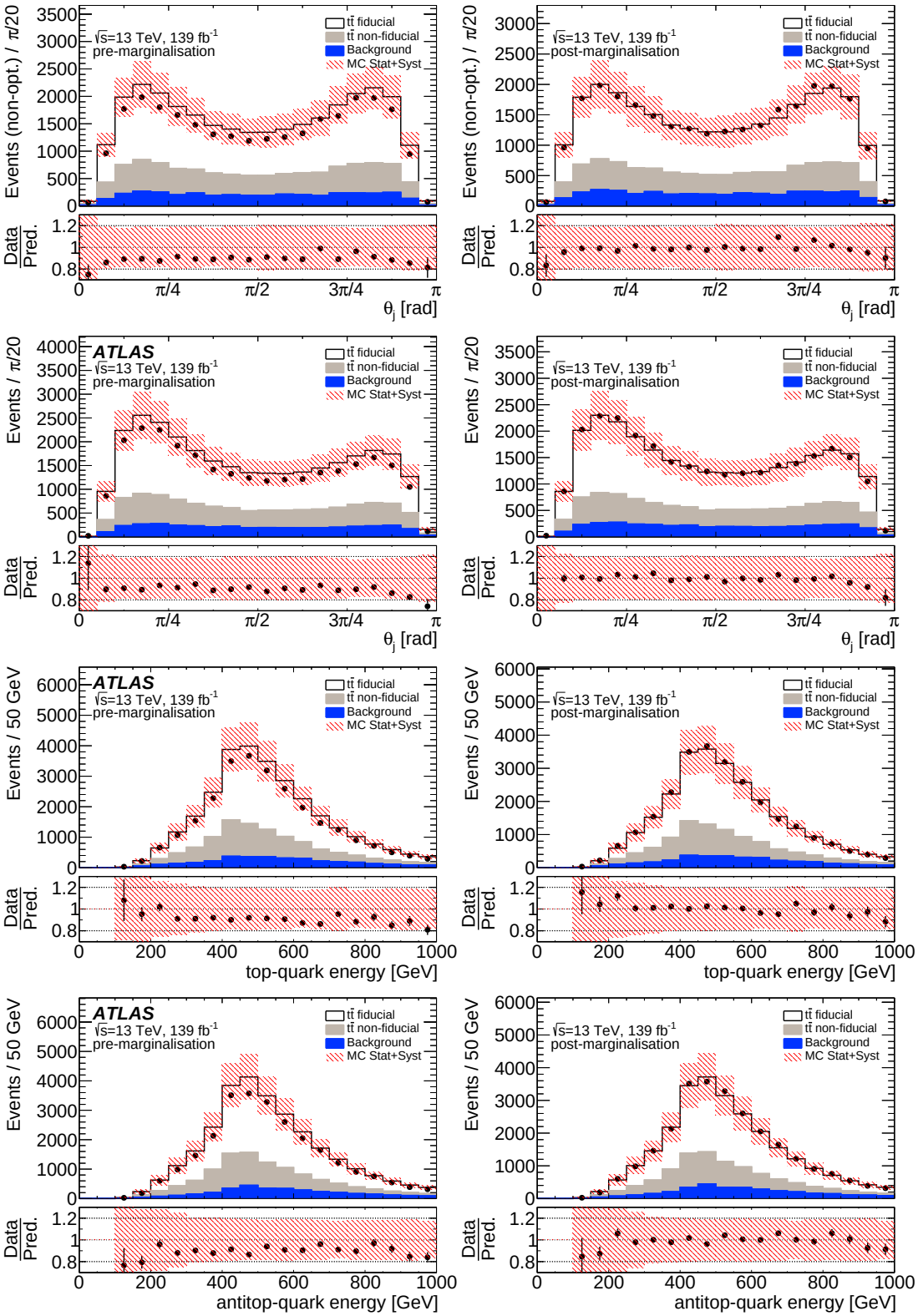

Figure 9.18.: Comparison of ATLAS data (black markers) to the pre- (left) and post-marginalisation (right) distributions for the jet scattering angle θ_j with non-optimised and optimised event numbers, the top- and antitop-quark energies in the $t\bar{t}j$ rest frame. The plots labelled with "ATLAS" were published in figure 2 in reference [83].

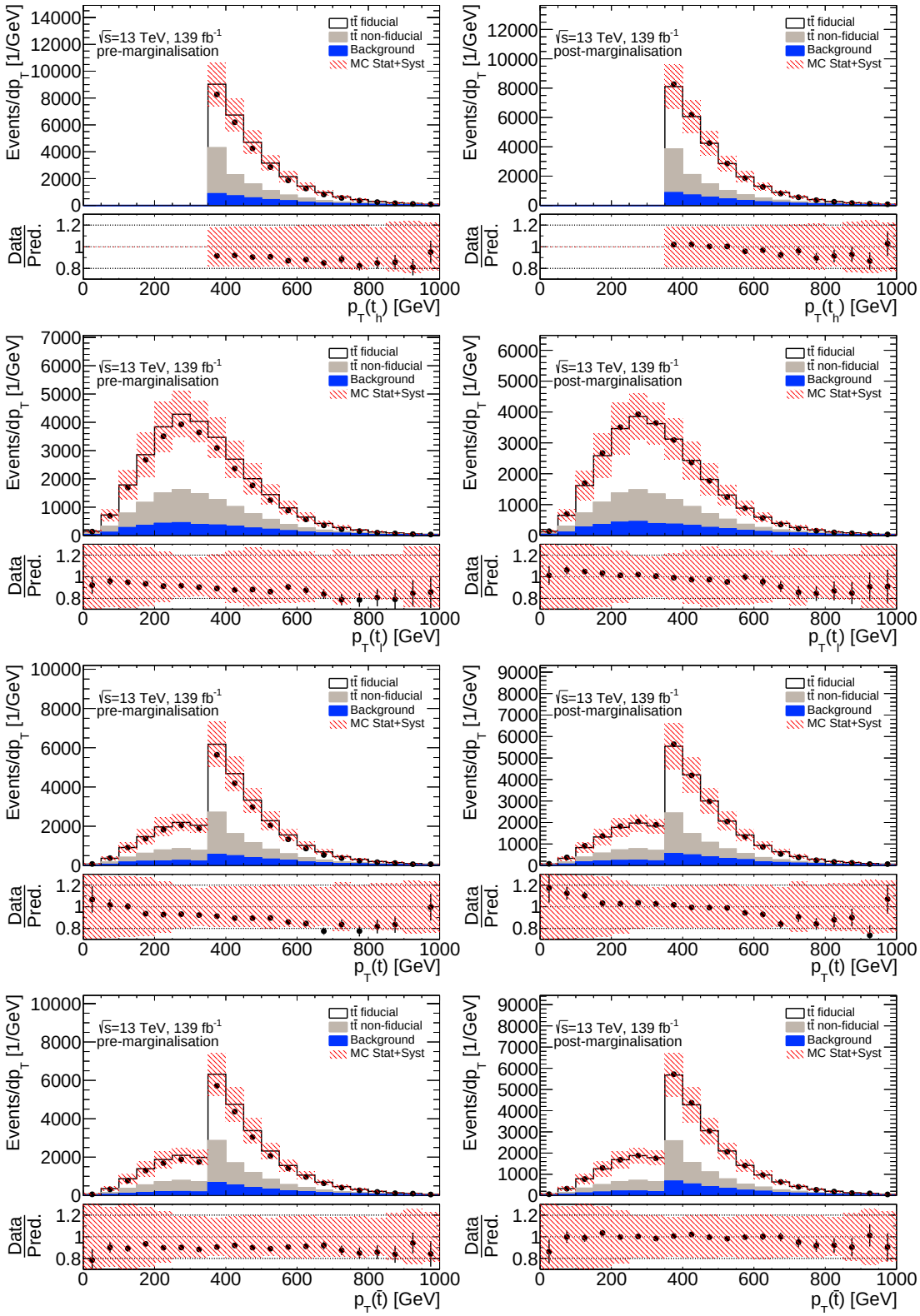

Figure 9.19.: Comparison of ATLAS data (black markers) to the pre- (left) and post-marginalisation (right) distributions for the transverse momenta of the top, antitop, hadronically and leptonically decaying top-quark candidates.

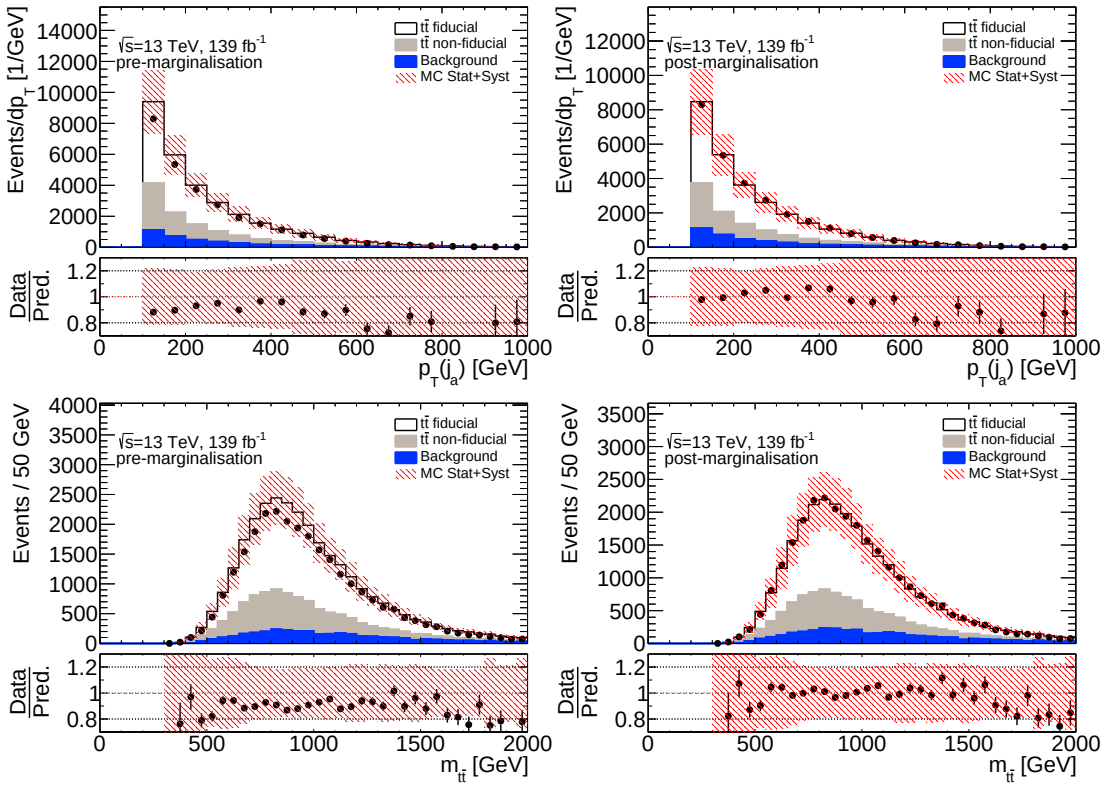

Figure 9.20.: Comparison of ATLAS data (black markers) to the pre- (left) and post-marginalisation (right) distributions for the associated jet p_T and the mass of the $t\bar{t}$ system.

Table 9.17.: Predicted detector-level asymmetries in units of $[10^{-2}]$ for signal and background with statistical uncertainties and statistical significance $Z = |A_E|/\Delta A_E$.

Sample	inclusive $A_E \pm \Delta A_E$	Z	$0 \le \theta_j < \frac{\pi}{4}$ $A_E \pm \Delta A_E$	Z	$\frac{\pi}{4} \le \theta_j < \frac{3\pi}{5}$ $A_E \pm \Delta A_E$	Z	$\frac{3\pi}{5} \le \theta_j \le \pi$ $A_E \pm \Delta A_E$	Z
$t\bar{t}$ fiducial	-0.32 ± 1.33	0.24	0.83 ± 2.51	0.33	-1.52 ± 2.23	0.68	-0.03 ± 2.23	0.01
$t\bar{t}$ non-fiducial	-1.26 ± 2.02	0.62	-1.21 ± 3.94	0.31	-1.42 ± 3.35	0.42	-1.13 ± 3.31	0.34
W+jets	-7.55 ± 4.53	1.67	-8.40 ± 9.71	0.87	-10.39 ± 7.34	1.42	-4.42 ± 7.12	0.62
Single-top Wt	0.40 ± 6.96	0.06	-0.20 ± 13.61	0.01	-3.88 ± 11.08	0.35	5.76 ± 11.86	0.49
Multijet	3.49 ± 7.52	0.46	-7.03 ± 14.39	0.49	13.48 ± 13.16	1.02	2.54 ± 11.86	0.21
$t\bar{t}V$	-3.33 ± 9.05	0.37	-1.49 ± 21.28	0.07	-5.85 ± 13.21	0.44	-0.93 ± 15.27	0.06
Z+jets	0.01 ± 12.43	0.00	0.73 ± 26.90	0.03	-0.19 ± 19.71	0.01	-0.19 ± 19.95	0.01
VV	-2.36 ± 13.95	0.17	4.53 ± 30.93	0.15	-6.37 ± 22.04	0.29	-1.85 ± 22.15	0.08
$t\bar{t}H$	0.21 ± 14.91	0.01	-0.74 ± 34.55	0.02	-0.12 ± 21.54	0.01	1.19 ± 25.78	0.05
Single-top s-channel	-16.21 ± 19.85	0.82	-14.65 ± 36.24	0.40	-17.11 ± 36.19	0.47	-16.70 ± 31.39	0.53
Single-top t-channel	-18.94 ± 65.46	0.29	-18.05 ± 153.69	0.12	-24.15 ± 92.63	0.26	-11.47 ± 115.60	0.10

9.4.2. Data measurement results

The energy asymmetry measured in data is compared to the SM prediction in table 9.18 and figure 9.21. The SM prediction contains MC statistical and scale uncertainties, the latter were calculated from the envelope of nine different scale variations, obtained by independent up and down variations of the renormalisation and factorisation scales by a factor of 2. The uncertainties of the prediction are generally much smaller than for the measurement except for the last θ_j bin, which is dominated by scale uncertainties. The marginal posterior distributions of the inclusive and differential energy asymmetry observed in data, without MC statistical uncertainties on the response matrix, are shown in figure 9.22 and found to have a Gaussian shape, simplifying the interpretation of the uncertainties as 68% confidence levels. The covariance matrix of the measured energy asymmetry is shown in table 9.20. The correlations between the energy asymmetry values in different θ_j bins are found to be smaller than 5% in magnitude.

Table 9.18.: The inclusive and differential energy asymmetry as measured in data compared to the SM prediction obtained from simulated $t\bar{t}j$ events with MadGraph5_aMC@NLO+ Pythia 8 at NLO including MC statistical and scale uncertainties as described in section 6.2.2 and to the expected asymmetry, assuming that the SM prediction would be measured with the uncertainties obtained in simulated $t\bar{t}$ events. The results for the differential energy asymmetry were published in table 3 in reference [83].

Scenario	$A_E \pm \Delta A_E\,[10^{-2}]$			
	inclusive	$0 \leq \theta_j \leq \frac{\pi}{4}$	$\frac{\pi}{4} \leq \theta_j \leq \frac{3\pi}{5}$	$\frac{3\pi}{5} \leq \theta_j \leq \pi$
Data	-2.9 ± 1.1	-3.2 ± 2.1	-4.3 ± 2.0	-1.3 ± 1.8
SM prediction	-1.9 ± 0.4	-1.3 ± 0.3	-3.7 ± 0.3	-0.6 ± 1.3
SM expectation	-1.9 ± 1.1	-1.3 ± 2.1	-3.7 ± 2.0	-0.6 ± 1.6

The significance of the measured energy asymmetry and its agreement with the SM prediction were evaluated with a χ^2 goodness-of-fit test [314] as described in section 9.1.1. Table 9.19 shows the goodness-of-fit results for the inclusive and combined differential energy asymmetries as well as for the individual bins. The null hypotheses are $\mu = 0$ and $\mu = A_E^{\mathrm{SM}}$ for the evaluation of the significance and the agreement with the SM prediction, respectively. The covariance matrix contains the covariance of the measurement in table 9.20, as well as the uncertainties on the prediction in table 9.18 for $\mu = A_E^{\mathrm{SM}}$, which are assumed to be uncorrelated between the bins. The measured asymmetry is in very good agreement with the SM prediction in the inclusive and differential measurements as well as in all individual bins, with no deviation larger than $1\,\sigma$. The p-value for the differential measurement is 0.80. The probability to observe an asymmetry that has an equal or larger discrepancy from zero in the central θ_j bin is below 4%, corresponding to a significance of $2.1\,\sigma$.

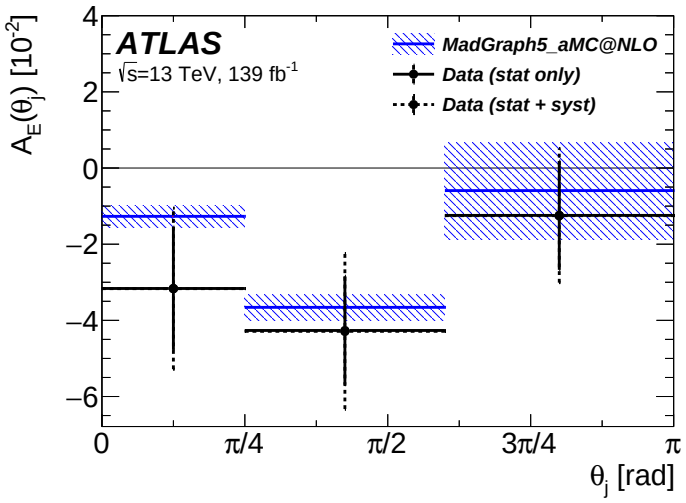

Figure 9.21.: Data measurement and SM prediction of the energy asymmetry differential in θ_j. Solid and dashed black error bars denote the statistical and total uncertainties of the measurement in data. The SM prediction was obtained from simulated $t\bar{t}j$ events with MadGraph5_aMC@NLO+ Pythia 8 at NLO including MC statistical and scale uncertainties (blue shaded bands) as described in section 6.2.2. This figure was published as figure 7 in reference [83].

Table 9.19.: Significance of the energy asymmetry measured in data with respect to the null hypothesis that the asymmetry is exactly zero ($\mu = 0$) and agreement between the measurement and SM prediction ($\mu = A_E^{\mathrm{SM}}$), both evaluated with a χ^2 goodness-of-fit test for the inclusive and differential asymmetries as well as for the individual bins. The χ^2, χ^2/ν, p and Z values were calculated as described in equations 9.1 to 9.4.

	$\mu = 0$				$\mu = A_E^{\mathrm{SM}}$			
	χ^2	χ^2/ν	p	Z	χ^2	χ^2/ν	p	Z
Inclusive	6.96	6.96	0.0083	2.64	0.76	0.76	0.3832	0.87
Differential	7.53	2.51	0.0567	1.91	1.02	0.34	0.7970	0.26
$0 \leq \theta_j < \frac{\pi}{4}$	2.24	2.24	0.1342	1.50	0.79	0.79	0.3734	0.89
$\frac{\pi}{4} \leq \theta_j < \frac{3\pi}{5}$	4.42	4.42	0.0356	2.10	0.09	0.09	0.7608	0.30
$\frac{3\pi}{5} \leq \theta_j \leq \pi$	0.51	0.51	0.4771	0.71	0.09	0.09	0.7620	0.30

Table 9.20.: Covariance matrix of the measured energy asymmetry in $[10^{-4}]$. The covariance between the pairs of θ_j bins was obtained by the sum of the covariance of the posterior distribution after unfolding and the covariance of the MC statistical uncertainties as described in section 8.4.

	$0 \leq \theta_j < \frac{\pi}{4}$	$\frac{\pi}{4} \leq \theta_j < \frac{3\pi}{5}$	$\frac{3\pi}{5} \leq \theta_j \leq \pi$
$0 \leq \theta_j < \frac{\pi}{4}$	4.473	-0.118	-0.170
$\frac{\pi}{4} \leq \theta_j < \frac{3\pi}{5}$	-0.118	4.165	-0.087
$\frac{3\pi}{5} \leq \theta_j \leq \pi$	-0.170	-0.087	3.096

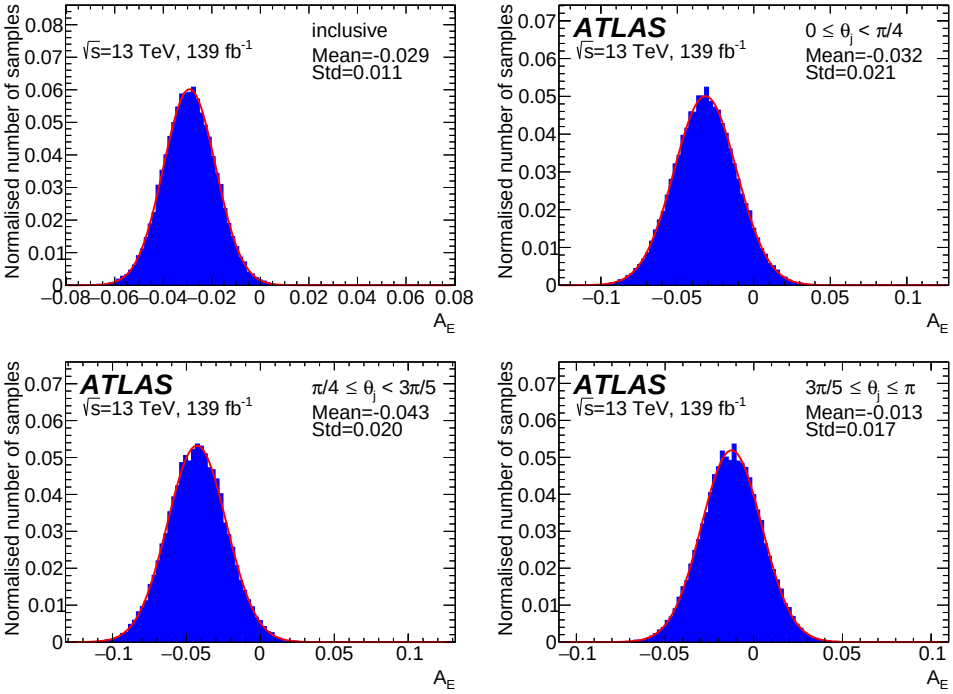

Figure 9.22.: Marginal posterior distributions of the inclusive and differential energy asymmetry in data without MC statistical uncertainties on the response matrix. A Gaussian fit to the data was overlaid in red. The distributions for the differential energy asymmetry were published as auxiliary material in reference [83].

9.4.3. Systematic uncertainties

Table 9.21 shows a breakdown of the systematic uncertainties on the energy asymmetry by category, derived from the posterior distributions of the energy asymmetry, the nuisance parameters, and their correlations as described in section 9.1.2. The data statistical uncertainties are slightly larger in data than in pseudo-data in table 9.1 due to the overestimation of the $t\bar{t}$ event yield in simulation as discussed in section 9.4.1. The relative importance and size of the systematic uncertainties is similar to that observed in pseudo-data; the jet energy resolution, $t\bar{t}$ modelling, and multijet estimation are the dominating systematic uncertainties in the first, second and third θ_j bin, respectively. The ranking of the individual uncertainties is shown in figure 9.23 and agrees well with the ranking seen in pseudo-data in figure 9.2. The correlations between the individual uncertainties, the inclusive and the differential energy asymmetry are depicted in figure 9.24. As expected for an equal number of parameters of interest and observables and a uniform truth prior, the correlations between the nuisance parameters are very small at the order of at most 2%.

Table 9.21.: Uncertainties on the inclusive and differential energy asymmetries by category. The uncertainty of each category is calculated with Gaussian error propagation using eq. 9.10. Uncertainties in the luminosity and cross sections of the Z+jets, VV, $t\bar{t}V$ and $t\bar{t}H$ backgrounds are found to be negligible and are thus not listed. The differential uncertainties were published in table 2 in reference [83].

Scenario	ΔA_E $[10^{-2}]$			
	inclusive	$0 \leq \theta_j < \frac{\pi}{4}$	$\frac{\pi}{4} \leq \theta_j < \frac{3\pi}{5}$	$\frac{3\pi}{5} \leq \theta_j \leq \pi$
Data statistical uncertainty	0.82	1.60	1.40	1.40
$t\bar{t}$ modeling	0.32	0.08	0.87	0.34
$t\bar{t}$ response MC statistics	0.25	0.51	0.42	0.42
W+jets modeling and PDF	0.31	0.29	0.49	0.42
Single-top modelling	0.24	0.28	0.60	0.29
$t\bar{t}$ and single-top PDF	0.05	0.08	0.10	0.07
Multijet	0.28	0.53	0.54	0.51
Jet energy resolution	0.35	0.98	0.40	0.36
Other detector uncertainties	0.18	0.42	0.43	0.30
Total	1.10	2.10	2.00	1.80

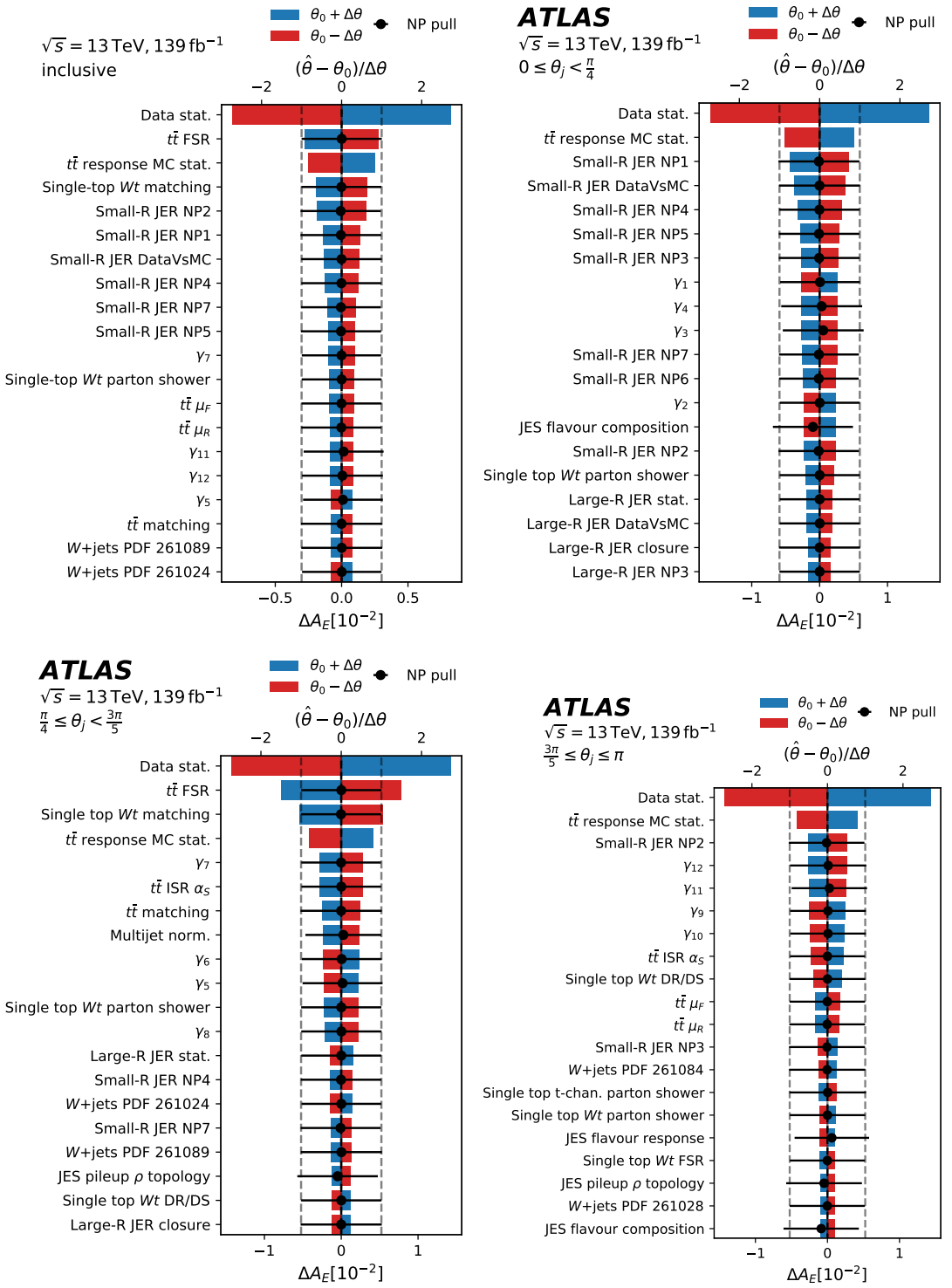

Figure 9.23.: Ranking of systematic uncertainties on the inclusive and differential energy asymmetry. Blue and red areas show the impact on the energy asymmetry from a one σ variation of the corresponding nuisance parameter as defined in eq. 9.8. The means and standard deviations of the posterior distributions of the nuisance parameters, normalised to their pre-marginalisation standard deviations, are illustrated by black dots and error bars. The ranking for the differential asymmetry was published in figure 6 in reference [83].

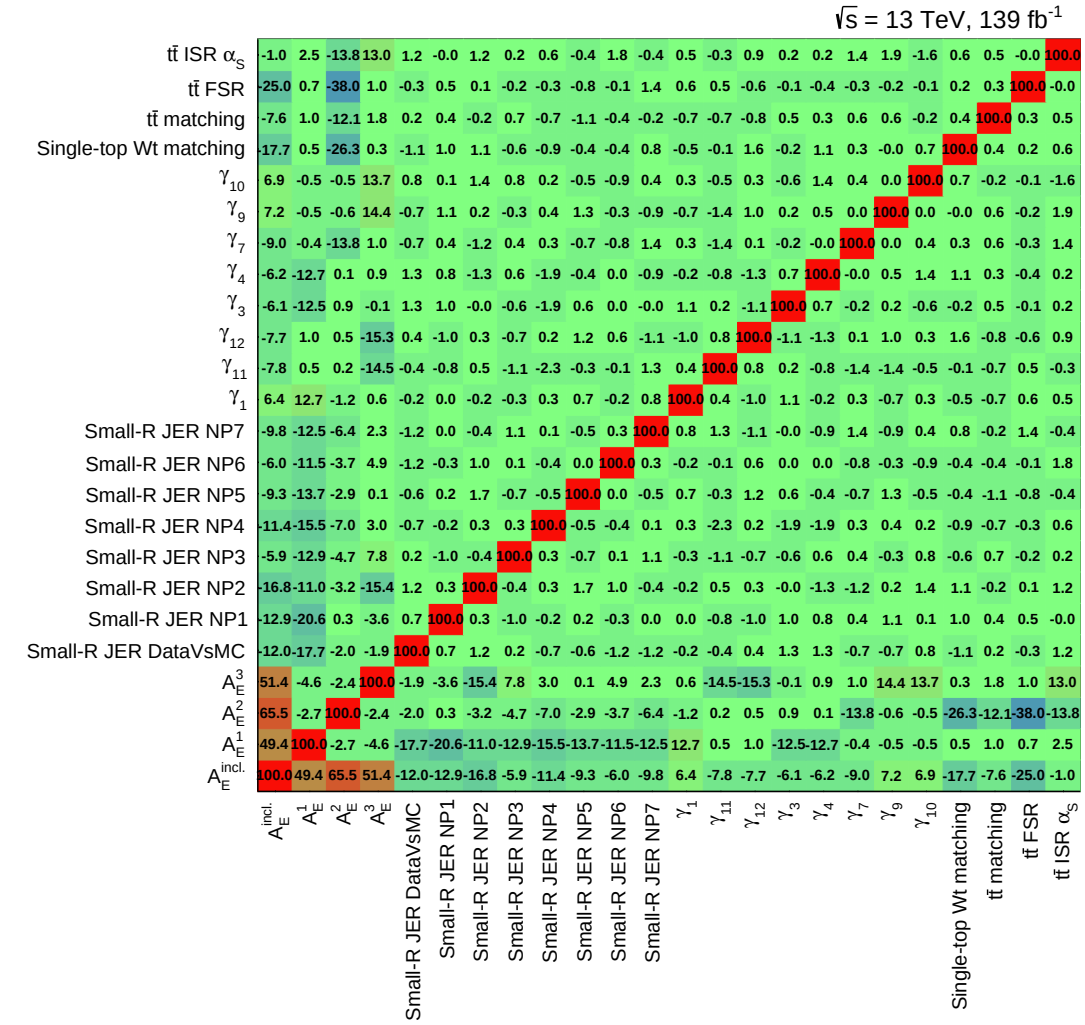

Figure 9.24.: Correlation matrix for the highest ranked systematic uncertainties in data between each other and the inclusive and differential energy asymmetry. For better visibility, the correlations are scaled by a factor of 100.

9.5. Expectations for Run 3 and beyond

The energy asymmetry was measured to be different from zero in the central θ_j bin with a significance of $2.1\,\sigma$; the combined significance of the asymmetry was found to be $1.9\,\sigma$; see table 9.19 in section 9.4.2.

In searches, significances above $3\,\sigma$ and $5\,\sigma$ are considered as "evidence" and "discovery", respectively. Significances of $1\,\sigma$, $2\,\sigma$, $3\,\sigma$ and $5\,\sigma$ correspond to p-values of $31.73 \cdot 10^{-2}$, $45.50 \cdot 10^{-3}$, $27.00 \cdot 10^{-4}$ and $57.33 \cdot 10^{-8}$, respectively. This section explores the expected significances with respect to the null hypothesis of a vanishing energy asymmetry for Run 3 and beyond.

The High-Luminosity Large Hadron Collider (HL-LHC) [320] is a planned major upgrade for the LHC and expected to increase the event rate by a factor of five and

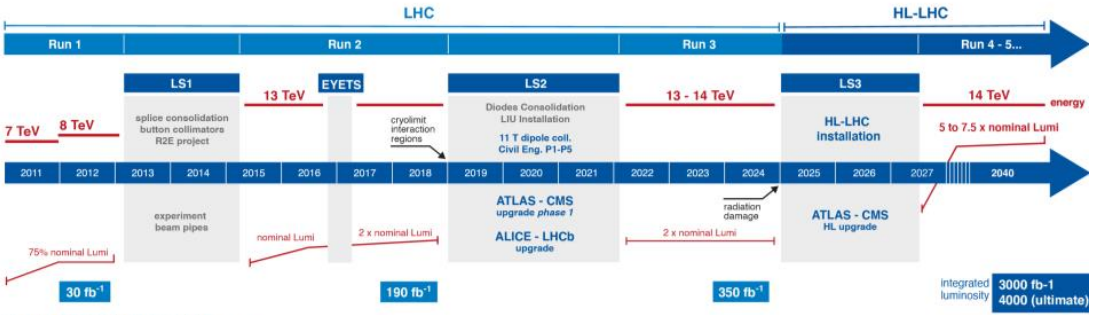

Figure 9.25.: Time scale for the data-taking (Run) and maintenance (Long Shutdown, LS) periods at the LHC and HL-LHC. [320]

the integrated luminosity by a factor of ten. Figure 9.25 shows the time scale for the previous data-taking periods Run 1 (2011–2013) and Run 2 (2015–2018), the planned Run 3 (2022–2024), the HL-LHC installation foreseen for 2025-2027, and future data-taking periods. The integrated luminosity is expected to reach more than $300\,\text{fb}^{-1}$ at the end of Run 3 and $3\,000\,\text{fb}^{-1}$ after Run 4 and 5.

The significance of the energy asymmetry at these luminosities was evaluated by repeating the pseudo-data measurements described in section 9.1.1 in three different scenarios. In all scenarios, the input distributions to the unfolding were scaled according to the expected luminosity. The expected increase of the centre-of-mass energy from 13 to 14 TeV, which would also increase the $t\bar{t}$ cross section by about 20% (see section 2.2.2) and partially offset the data/MC mismodelling described in section 9.4.1, was not taken into account. In the first scenario, "Stat. only", only the expected data statistical uncertainties were considered. Next, all systematic uncertainties were included, "Stat.+Syst. 1", except for the MC statistical uncertainties on the response matrix as in the nominal measurement, assuming that the systematic uncertainties will not be reduced during the future data-taking periods. For the last scenario, "Stat.+Syst. 2", the systematic uncertainty of the "Stat.+Syst. 1" scenario, obtained from subtraction in quadrature of the "Stat. only" and "Stat.+Syst. 1" uncertainties, was scaled in the same way as the expected statistical uncertainty was found to scale between the different luminosities and added in quadrature to the corresponding statistical uncertainty. To evaluate the significance with respect to the null hypothesis that the energy asymmetry is zero in all differential θ_j bins, it was assumed that the SM prediction from table 9.18 was measured and that the uncertainties were as obtained from the pseudo-data experiments.

Table 9.22 shows the expected uncertainties and significances of the energy asymmetry together with the SM prediction. Considering only the expected data statistical uncertainties, "Stat. only", the energy asymmetry could reach significances of up to $4\,\sigma$ and $12.5\,\sigma$ in the central θ_j bin after Run 3 and 5, respectively. Also the combined significance will be well above the required levels for an evidence and discovery. Assuming that the systematic uncertainties will stay at the current level, the significances will not increase above $3\,\sigma$. If they scale in the same way as the data statistical uncertainty, the significance in the central bin will come close to the level of an evidence at $300\,\text{fb}^{-1}$ and will be well above the level of a discovery at $3\,000\,\text{fb}^{-1}$.

Table 9.22.: Expected uncertainties and significances (in brackets) of the energy asymmetry for luminosities of 139, 300 and 3 000 fb^{-1} with expected data statistical uncertainties only ("Stat. only"), all systematic uncertainties except for MC statistical uncertainties on the response matrix ("Stat.+Syst. 1"), and with these systematic uncertainties assumed to scale in the same way as the statistical uncertainties ("Stat.+Syst. 2"). The significances Z were calculated from a goodness-of-fit test as described in section 9.1.1. The last line shows the SM prediction from table 9.18.

L[fb^{-1}]	Scenario	$\Delta A_E[10^{-2}](Z)$ inclusive	$0 \leq \theta_j < \frac{\pi}{4}$	$\frac{\pi}{4} \leq \theta_j < \frac{3\pi}{5}$	$\frac{3\pi}{5} \leq \theta_j \leq \pi$	Z Combination
139	Stat. only 139 fb^{-1}	0.77 (2.45)	1.54 (0.82)	1.34 (2.72)	1.32 (0.45)	2.13
	Stat.+Syst. 1 139 fb^{-1}	1.02 (1.86)	1.99 (0.64)	1.90 (1.93)	1.56 (0.38)	1.22
	Stat.+Syst. 2 139 fb^{-1}	1.02 (1.86)	1.99 (0.64)	1.90 (1.93)	1.56 (0.38)	1.22
300	Stat. only 300 fb^{-1}	0.52 (3.63)	1.05 (1.21)	0.92 (4.00)	0.89 (0.67)	3.63
	Stat.+Syst. 1 300 fb^{-1}	0.80 (2.35)	1.57 (0.81)	1.58 (2.32)	1.14 (0.52)	1.70
	Stat.+Syst. 2 300 fb^{-1}	0.69 (2.76)	1.36 (0.94)	1.29 (2.83)	1.05 (0.57)	2.27
3000	Stat. only 3000 fb^{-1}	0.17 (11.28)	0.33 (3.81)	0.29 (12.50)	0.28 (2.08)	> 8.2[1]
	Stat.+Syst. 1 3000 fb^{-1}	0.62 (3.04)	1.18 (1.07)	1.30 (2.80)	0.74 (0.80)	2.34
	Syst.+Syst. 2 3000 fb^{-1}	0.22 (8.56)	0.43 (2.96)	0.41 (8.84)	0.34 (1.77)	> 8.2[1]
		$A_E \pm \Delta A_E[10^{-2}]$ inclusive	$0 \leq \theta_j < \frac{\pi}{4}$	$\frac{\pi}{4} \leq \theta_j < \frac{3\pi}{5}$	$\frac{3\pi}{5} \leq \theta_j \leq \pi$	
	SM prediction	-1.89 ± 0.41	-1.27 ± 0.28	-3.66 ± 0.33	-0.59 ± 1.28	

[1] The significance of the combination was calculated with equations 9.4 and 9.2 using the scipy package [321] in Python. The precision in the cumulative distribution function calculation limits give a lower limit of the p-values of $\approx 2.2 \cdot 10^{-16}$, corresponding to a significance of $\lessapprox 8.2\sigma$. For the one-dimensional distributions in the individual bins, the significance was directly computed by $Z = |A_E|/\Delta A_E$ allowing for arbitrary large Z-values.

The impact of the systematic uncertainties by category was shown in table 9.21. The statistical uncertainty of the data-driven multijet estimate is sizeable in all three θ_j bins, but expected to reduce in the same way as the data statistical uncertainties. The $t\bar{t}$ modelling uncertainties on the other hand suffer from MC statistical uncertainties as discussed in section 8.3.1, which can be assumed to be reduced similarly if the simulation keeps pace with the data taking. The dominating $t\bar{t}$ ME/PS matching and FSR uncertainties might be mitigated considering higher order corrections to the ME as described in appendix B.1. The dominating detector related uncertainties on the jet energy resolution were obtained from in-situ measurements in data as described in section 8.2 and are thus also expected to decrease to some degree with more statistics. Overall, it seems realistic to expect significances somewhere between the two extreme scenarios "Stat.+Syst. 1" and "Stat.+Syst. 2".

10. SMEFT interpretation

The measurement of the energy asymmetry presented in chapter 9 was found to be consistent with the SM prediction. This chapter explores the sensitivity of the energy asymmetry to effective four-quark interactions in the framework of Standard Model Effective Field Theory (SMEFT) and provides a comparison with the rapidity asymmetry measurement. Section 10.1 gives a brief summary of the main concepts of SMEFT already described in section 2.4.3 and explains how the SMEFT predictions for the energy and rapidity asymmetries were obtained. Section 10.2 presents the one- and two-dimensional limits on Wilson coefficients obtained from fitting the SMEFT predictions to the measured asymmetries. Current global limits are discussed in section 10.3.

A preliminary SMEFT interpretation based on expected experimental uncertainties was published in reference [75]. The coefficient limits obtained from the differential energy asymmetry and their comparison with those obtained from the rapidity asymmetry were published in references [83] and [66], respectively.

10.1. Introduction

The Standard Model Effective Field Theory (SMEFT) represents a model-independent framework for new-physics interpretations by extending the SM Lagrangian with non-renormalisable, gauge invariant operators containing SM fields as described in section 2.4.3:

$$\mathcal{L}_{\text{SMEFT}} = \mathcal{L}_{\text{SM}} + \mathcal{L}^{(5)} + \mathcal{L}^{(6)} + \mathcal{L}^{(7)} + ... \qquad \mathcal{L}^{(d)} = \sum_{i=1}^{n_d} \frac{C_i^{(d)}}{\Lambda^{d-4}} O^{(d)} \tag{10.1}$$

This analysis focuses on the following six dimension-six operators:

$$\begin{aligned} O_{Qq}^{1,8} &= (\bar{Q}\gamma_\mu T^A Q)(\bar{q}_i \gamma^\mu T^A q_i), \quad O_{Qq}^{1,1} = (\bar{Q}\gamma_\mu Q)(\bar{q}_i \gamma^\mu q_i), \\ O_{tu}^{8} &= (\bar{t}\gamma_\mu T^A t)(\bar{u}_i \gamma^\mu T^A u_i), \qquad O_{tu}^{1} = (\bar{t}\gamma_\mu t)(\bar{u}_i \gamma^\mu u_i), \\ O_{tq}^{8} &= (\bar{q}_i \gamma^\mu T^A q_i)(\bar{t}\gamma_\mu T^A t), \qquad O_{tq}^{1} = (\bar{q}_i \gamma^\mu q_i)(\bar{t}\gamma_\mu t) \end{aligned} \tag{10.2}$$

with

$$\begin{aligned} q_i &= (u_L^i, d_L^i), \qquad u_i = u_R^i,\, d_i = d_R^i, \qquad i = 1, 2 \\ Q &= (t_L, b_L), \qquad t = t_R,\, b = b_R \end{aligned} \tag{10.3}$$

that provide a complete set of chiralities for both colour singlet and octet operators.

Cross sections and asymmetries depend on the Wilson coefficients C_i as in eq. 2.50:

$$\begin{aligned} \sigma &= \sigma_S^{\text{SM}} + \sum_k C_k \sigma_S^k + \sum_{k \le l} C_k C_l\, \sigma_S^{kl} \\ A &= \frac{\sigma_A}{\sigma_S} = \frac{\sigma_A^{\text{SM}} + \sum_k C_k \sigma_A^k + \sum_{k \le l} C_k C_l\, \sigma_A^{kl}}{\sigma_S^{\text{SM}} + \sum_k C_k \sigma_S^k + \sum_{k \le l} C_k C_l\, \sigma_S^{kl}} \end{aligned} \tag{10.4}$$

Table 10.1.: SM predictions for the inclusive and differential energy asymmetry A_E obtained from simulation at NLO in $t\bar{t}j$ with MADGRAPH5_aMCATNLO and the inclusive and differential rapidity asymmetry A_C calculated at NNLO with electroweak corrections [151] including MC statistical ("Stat.") and scale ("Syst.") uncertainties.

			A	Stat.	Syst.	Total unc.
A_E	inclusive		-1.89	0.14	0.38	0.41
	θ_j	0–$\pi/4$	-1.27	0.27	0.09	0.28
		$\pi/4$–$3\pi/5$	-3.66	0.23	0.24	0.33
		$3\pi/5$–π	-0.59	0.24	1.25	1.28
A_C	inclusive		0.64	0.01	0.06	0.06
	$m_{t\bar{t}}$	$< 500\,\text{GeV}$	0.55	0.02	0.06	0.06
		500–750 GeV	0.72	0.02	0.06	0.06
		750–1000 GeV	0.79	0.03	0.05	0.06
		1000–1500 GeV	0.96	0.05	0.08	0.09
		$\geq 1500\,\text{GeV}$	0.94	0.07	0.13	0.15

where $\sigma^k_{S,A}$ and $\sigma^{kl}_{S,A}$ correspond to $A_{\text{SM}} \times A_{\text{dim-6}}$ and $|A_{\text{dim-6}}|^2$ operator interferences, respectively.

The SM prediction at the particle level was obtained from simulation with MADGRAPH5_aMC@NLO 2.7+PYTHIA 8.2 at NLO in $t\bar{t}j$ production, while the SM-EFT interference and EFT-EFT contributions were generated at LO using the SMEFTATNLO package [152]; see section 6.2.2 for further details.

The rapidity asymmetry provides complementary information and was measured at the parton level inclusive and differential in $m_{t\bar{t}}$ [66]. The SM prediction was calculated at NNLO in $t\bar{t}$ production including electroweak corrections [151], while the operator contributions were calculated at NLO by E. Vryonidou and C. Zhan [152] using the SMEFTATNLO package. The SM predictions for the inclusive and differential asymmetries including MC statistical and scale uncertainties are listed in table 10.1; the scale uncertainty was obtained from the envelope of the individual scale variations and the total uncertainty is given by the sum in quadrature of the MC statistical and the scale uncertainties. The dependence of the asymmetries on the Wilson coefficients are illustrated in figures 2.30 and 2.31 in section 2.4.3.

The energy asymmetry was measured in the boosted phase space that probes invariant masses in the range of $600\,\text{GeV} \lessapprox m_{t\bar{t}} \lessapprox 1200\,\text{GeV}$ well above the $t\bar{t}$ production threshold as shown in figure 9.20. This corresponds to the $m_{t\bar{t}}$ region where the measured rapidity asymmetry is most sensitive to new physics. The two asymmetries are thus compared in similar phase-space regions where they feature a high theoretical sensitivity to four-quark operators.

10.2. Limits on Wilson coefficients

The sensitivity of the asymmetries to the various operator contributions is assessed with one- and two-parameter maximum-likelihood fits of the SMEFT prediction x^{SMEFT} depending on the Wilson coefficients C_i to the measured (expected) asymmetries $x^{\mathrm{d(e)}}$.

The maximum likelihood estimator (MLE) starts from the joint density or likelihood $L(x|\theta)$ of the observed data x conditioned on a set of n parameters θ. The estimate $\hat{\theta}$ is given by the value of θ that maximises the likelihood. The MLE is asymptotic normal, i.e. the estimator $\hat{\theta}$ is distributed according to a n-variate normal distribution $N(\hat{\theta}, \Sigma)$ with mean $\hat{\theta}$ and variance Σ. The asymptotic variance Σ is given by the negative inverse of the expected value of the Hessian matrix H of $\ln L$ [322]:

$$\Sigma(\hat{\theta})_{ij} = \left(\left\langle -H(\hat{\theta})_{ij} \right\rangle\right)^{-1} = \left(-\left\langle \frac{\partial^2 \ln L(\hat{\theta})}{\partial\theta_i \partial\theta_j} \right\rangle\right)^{-1} \tag{10.5}$$

The quantity $(\theta-\hat{\theta})^T\Sigma^{-1}(\theta-\hat{\theta})$ follows a χ^2 distribution with n degrees of freedom such that a confidence region at the $1-\alpha$ confidence level for a n-variate normal distribution $N(\hat{\theta}, \Sigma)$ is given by the parameter region satisfying:

$$(\theta - \hat{\theta})^T \Sigma^{-1} (\theta - \hat{\theta}) \leq \chi^2_{n,1-\alpha} \tag{10.6}$$

where $\chi^2_{n,1-\alpha}$ is the $1-\alpha$ quantile of the χ^2 distribution. The Taylor approximation of the log likelihood function in vicinity to its maximum value reads:

$$\ln L(\theta) = \ln L(\hat{\theta}) + \frac{1}{2}(\theta - \hat{\theta})^T H(\hat{\theta})(\theta - \hat{\theta}) \tag{10.7}$$

Approximating $\langle H \rangle$ by the actual value H and using that $\Sigma(\hat{\theta}) = -\langle H(\hat{\theta})\rangle^{-1}$ yields:

$$\ln L(\theta) = \ln L(\hat{\theta}) - \frac{1}{2}(\theta - \hat{\theta})^T \Sigma^{-1}(\hat{\theta})(\theta - \hat{\theta}) \tag{10.8}$$

The $1-\alpha$ confidence regions are thus given by all parameter combinations that satisfy $\ln L(\theta) \geq \ln L(\hat{\theta}) - \frac{1}{2}\chi^2_{n,1-\alpha}$, or, equivalently:

$$-2\ln L(\theta) \leq -2\ln L(\hat{\theta}) + \chi^2_{n,1-\alpha} \tag{10.9}$$

In the one-dimensional case, the boundary line intersects the likelihood curve at the points θ^+ and θ^- which are the upper and lower bounds of $\hat{\theta}$ at the given confidence level. In the two-dimensional case, the confidence regions are given by contours in $\Delta \ln L$.

In case the joint probability $L = L(\theta)$ is Gaussian distributed with mean $\mu = \mu(\theta)$ and covariance $C = C(\theta)$, the likelihood is given by:

$$L = \frac{1}{\sqrt{(2\pi)^n |C|}} \exp\left(-\frac{1}{2}(x-\mu)^T C^{-1}(x-\mu)\right) \tag{10.10}$$

with logarithm:

$$\ln L = -\frac{1}{2}(x-\mu)^T C^{-1}(x-\mu) - \frac{1}{2}\ln|C| - n\ln(2\pi) \tag{10.11}$$

and maximising L is equivalent to minimise $-2\ln L$:

$$-2\ln L = (x-\mu)^T C^{-1}(x-\mu) + n\ln(2\pi) + \ln(|C|) \tag{10.12}$$

and thus to minimise

$$\chi^2 = (x-\mu)^T C^{-1}(x-\mu) \tag{10.13}$$

if C does not depend on θ. In this analysis, the effect of C on θ is found to be small, such that C can be approximated as constant. Similar as the likelihood function, in vicinity to its minimum value, $\chi^2_{\text{min}} = \chi^2(\hat{\theta})$, the χ^2 function in eq. 10.8 can be approximated as:

$$\chi^2(\theta) = \chi^2(\hat{\theta}) + (\theta-\hat{\theta})^T \Sigma^{-1}(\hat{\theta})(\theta-\hat{\theta}) \tag{10.14}$$

such that the $1-\alpha$ confidence regions are given by all parameter combinations that satisfy $\chi^2(\theta) \leq \chi^2(\hat{\theta}) + \chi^2_{n,1-\alpha}$. In the one-dimensional case, the boundary line intersects the χ^2 curve at the upper and lower bounds of $\hat{\theta}$ at the given confidence level. In the two-dimensional case, the confidence regions are given by contours in $\Delta\chi^2$. The $\chi^2_{n,1-\alpha}$ quantiles for the 68.27 % and 95.45 % confidence levels are given by 1.0 and 4.0 for $n = 1$ and by 2.30 and 6.18 for $n = 2$, respectively. These confidence levels reflect the one and two σ confidence levels of the univariate Gaussian distribution used in typical error calculations and are referred to as 68% CL and 95% CL in the following.

Let $x^{\text{d(e)}}$ denote the measured (expected) asymmetries and x^{SMEFT} the SMEFT prediction depending on the Wilson coefficients C_i. The χ^2 function to be minimized then reads:

$$\chi^2 = (x^{\text{d(e)}} - x^{\text{SMEFT}})^\top C^{-1}(x^{\text{d(e)}} - x^{\text{SMEFT}})\,. \tag{10.15}$$

where the covariance matrix

$$C = C^{\text{d(e)}} + C^t, \qquad C^t = C^{\text{MC stat}} + C^{\text{scale}}, \tag{10.16}$$

contains the (expected) measurement uncertainties ($C^{\text{d(e)}}$), taking into account the correlations between the measured bins, and the theoretical uncertainties on the predictions (C^t) due to the limited sample size ($C^{\text{MC stat}}$) and scale uncertainties (C^{scale}). The covariance matrix for the (expected) measurement uncertainties ($C^{\text{d(e)}}$) contains the full correlations between the measured bins, while $C^{\text{MC stat}}$ is diagonal by definition. The scale uncertainties on the energy asymmetry in the individual bins are evaluated from nine different scale variations, obtained by independent up and down variations of the renormalisation and factorisation scales by a factor of 2. The covariance matrix C^{scale} is then built assuming no correlation between the bins. It has been checked that the impact of this assumption on the result is negligible, since the theoretical uncertainties are small compared to the measurement uncertainties except for the last θ_j bin.

Figure 10.1 shows the χ^2 values in dependence of the Wilson coefficients in one-parameter fits to the differential energy asymmetry. As described above, the 68% and 95% confidence bounds are given by the coefficient values at the intersections of the χ^2 curve with the $\chi^2_{\text{min}} + 1$ and $\chi^2_{\text{min}} + 4$ lines, respectively. The corresponding figures for the inclusive energy asymmetry and the inclusive and differential rapidity asymmetry are shown in figures C.1, C.2 and C.3 in appendix C, respectively.

Figure 10.2 and tables 10.2 and 10.3 show the bounds on the Wilson coefficients obtained from one-parameter fits to the inclusive and differential energy and rapidity

asymmetries. Differences in the bounds obtained from the rapidity asymmetry to those reported in reference [66] are due to a different treatment of MC statistical, scale, and PDF uncertainties in the fitting procedure. The differential energy asymmetry is found to be sensitive to four-quark operator coefficients in the range of $[-1, 1]\,(\mathrm{TeV}/\Lambda)^2$ at the 68% and of $[-2, 2]\,(\mathrm{TeV}/\Lambda)^2$ at the 95% confidence level. The sensitivity of the energy and rapidity asymmetries to the coefficients C_{Qq}^{11}, C_{tu}^{1} and C_{tu}^{8} is found to be comparable such that the energy asymmetry will play an important role in global fits which are sensitive to the charge asymmetries [52, 53, 323].

Table 10.2.: Bounds on individual Wilson coefficients $C\,(\,\mathrm{TeV}/\Lambda)^2$ from one-parameter fits to the measured and expected inclusive energy asymmetry and the inclusive rapidity asymmetry measured in reference [66]. The dashes (–) indicate that no bound was found within the range of $[-10.0, 10.0]$.

$C\,(\,\mathrm{TeV}/\Lambda)^2$	$A_E^{\mathrm{incl.}}$		$A_E^{\mathrm{incl.}}$ (expected)		$A_C^{\mathrm{incl.}}$	
	68% CL	95% CL	68% CL	95% CL	68% CL	95% CL
C_{Qq}^{11}	$[-0.38, 0.50]$	$[-0.72, 0.85]$	$[-0.60, 0.73]$	$[-0.93, 1.08]$	$[-0.65, 0.54]$	$[-0.87, 0.76]$
C_{Qq}^{18}	$[-0.88, 1.16]$	$[-1.66, 2.15]$	$[-1.37, 1.79]$	$[-2.19, 2.92]$	$[-3.43, 0.61]$	$[-3.99, 0.99]$
C_{tq}^{1}	$[-1.94, 1.52]$	$[-3.64, 2.75]$	$[-1.15, 0.86]$	$[-1.92, 1.51]$	$[-0.42, 0.52]$	$[-0.65, 0.77]$
C_{tq}^{8}	$[-4.20, 5.48]$	$[-,-]$	$[-2.35, 2.75]$	$[-4.15, 5.38]$	$[-2.92, 0.65]$	$[-3.58, 1.62]$
C_{tu}^{1}	$[-0.46, 0.58]$	$[-0.87, 1.01]$	$[-0.72, 0.85]$	$[-1.12, 1.27]$	$[-0.87, 0.62]$	$[-1.14, 0.91]$
C_{tu}^{8}	$[-0.92, 1.12]$	$[-1.66, 1.91]$	$[-1.40, 1.63]$	$[-2.07, 2.37]$	$[-3.22, 0.96]$	$[-3.81, 1.49]$

Table 10.3.: Bounds on individual Wilson coefficients $C\,(\,\mathrm{TeV}/\Lambda)^2$ from one-parameter fits to the measured and expected energy asymmetry differential in θ_j and the rapidity asymmetry differential in $m_{t\bar{t}}$ measured in reference [66].

$C\,(\,\mathrm{TeV}/\Lambda)^2$	A_E		A_E (expected)		A_C	
	68% CL	95% CL	68% CL	95% CL	68% CL	95% CL
C_{Qq}^{11}	$[-0.41, 0.47]$	$[-0.65, 0.67]$	$[-0.46, 0.45]$	$[-0.66, 0.65]$	$[-0.53, -0.29]$	$[-0.64, 0.40]$
C_{Qq}^{18}	$[-0.87, 1.24]$	$[-1.72, 2.10]$	$[-1.27, 1.35]$	$[-2.06, 2.22]$	$[0.04, 0.41]$	$[-0.24, 0.57]$
C_{tq}^{1}	$[-0.43, 0.52]$	$[-0.69, 0.75]$	$[-0.48, 0.50]$	$[-0.71, 0.73]$	$[-0.09, 0.15]$	$[-0.22, 0.27]$
C_{tq}^{8}	$[-1.41, 0.84]$	$[-2.01, 1.43]$	$[-1.47, 0.89]$	$[-2.03, 1.44]$	$[-0.35, 0.44]$	$[-0.71, 0.90]$
C_{tu}^{1}	$[-0.50, 0.56]$	$[-0.78, 0.81]$	$[-0.55, 0.54]$	$[-0.80, 0.79]$	$[-0.71, -0.40]$	$[-0.85, 0.32]$
C_{tu}^{8}	$[-1.00, 1.01]$	$[-1.71, 1.56]$	$[-1.27, 0.98]$	$[-1.85, 1.53]$	$[0.13, 0.65]$	$[-2.32, 0.87]$

Figures 10.3 and 10.4 show the Wilson coefficient bounds from two-parameter fits of the inclusive and differential energy asymmetry, respectively. The pairs of operators were chosen to investigate the effects of the colour structure and the quark chirality independently: the top row shows colour-singlet operators with different quark chiralities, the middle row shows the same chirality scenarios for colour-octet operators and the bottom row shows colour-singlet versus colour-octet operators with the same quark chiralities. Figures (a) and (c) demonstrate the difference between colour-singlet and colour-octet operators (C_{tq}^{1} vs. C_{tq}^{8}), such that no plot for C_{tu}^{1} vs. C_{tu}^{8} was included. The difference between left- and right-chiral quarks (C_{Qq}^{11} vs. C_{tu}^{1}) is illustrated in figure (b). The expected and observed bounds are very similar due to the good agreement between the measured and predicted energy asymmetry. The confidence regions of the measured

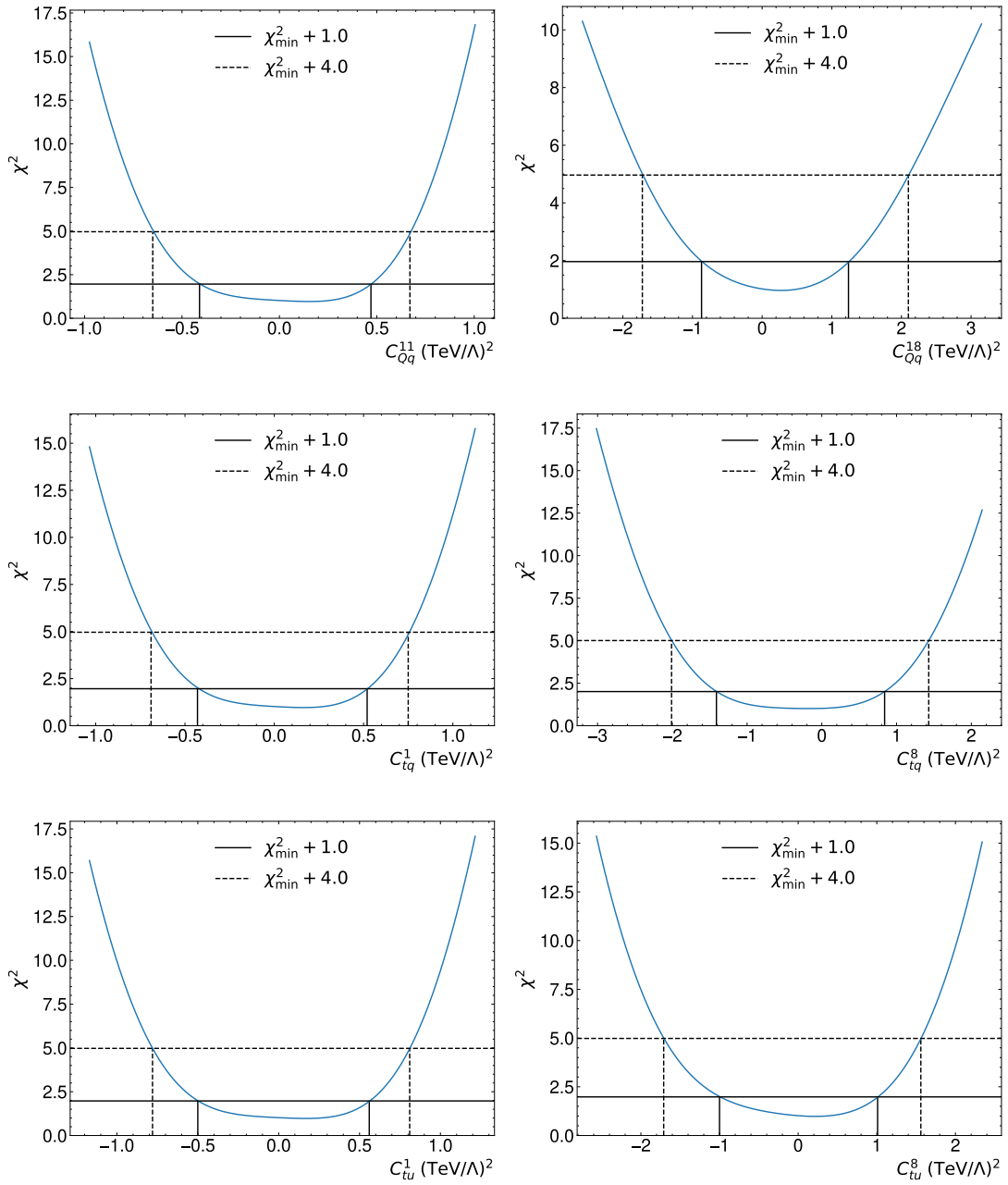

Figure 10.1.: χ^2 values vs. Wilson coefficients of the one-parameter χ^2 fits of the energy asymmetry differential in θ_j. Solid and dashed lines indicate the χ^2 values and associated Wilson coefficient values corresponding to the 68% and 95% confidence limits, respectively.

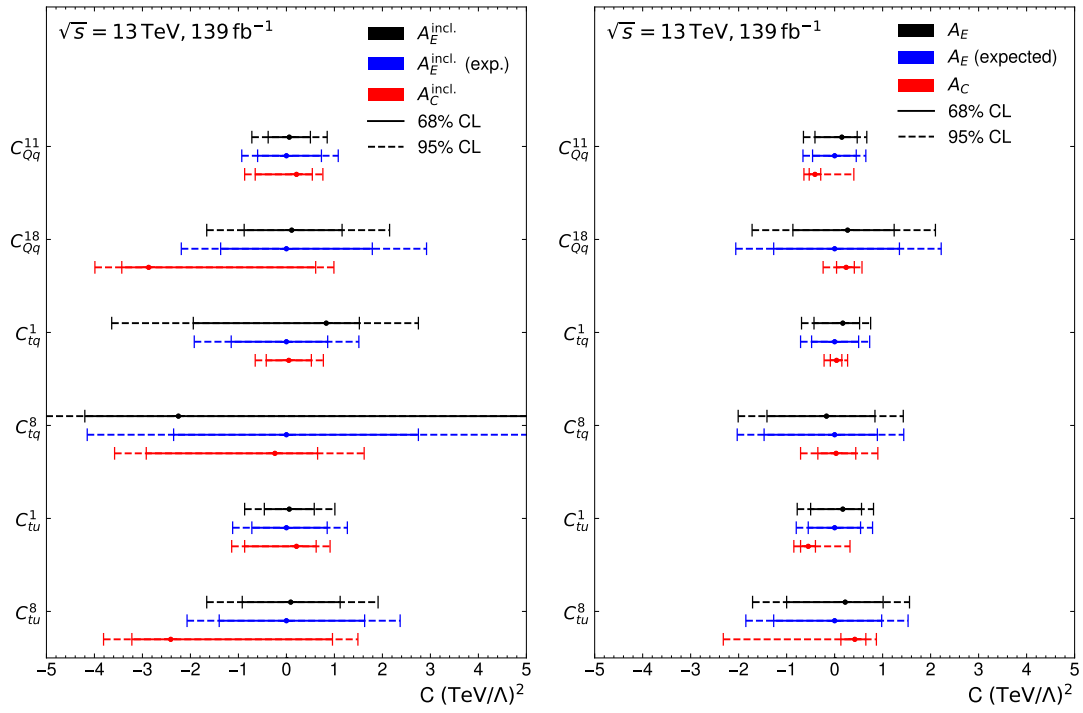

(a) (b)

Figure 10.2.: Bounds on the individual Wilson coefficients from one-parameter fits of the inclusive (a) and differential (b) energy and rapidity asymmetries. Black and blue lines correspond to the measured and expected energy asymmetries as published in figure 9 in reference [83], red lines correspond to the measured rapidity asymmetry [66]. Solid and dashed lines correspond to the 68% and 95% confidence level, respectively. Dots denote the best fit values.

asymmetry are centred near (0,0) for the same reason, while the best fit values from the expected asymmetry are exactly (0,0) and are thus not shown in the plots.

The energy asymmetry in $t\bar{t}j$ production exhibits a different QCD structure than the rapidity asymmetry in $t\bar{t}$ due to the extra jet such that these two asymmetries probe different directions in chiral and colour space. Figures 10.5 and 10.6 illustrate these complementarity. The two asymmetries probe similar areas in the parameter space for colour-singlet operators (top row), while the shapes of the bounds look very different for colour-octet operators (middle row). Specifically, the blind direction in the C_{Qq}^{18}-C_{tq}^{8} plane in figure 10.6c left by the rapidity asymmetry is broken by the energy asymmetry due to dimension-six operator interference with the SM amplitude. Differences in colour-singlet and colour-octet contributions to $t\bar{t}$ and $t\bar{t}j$ production lead to differently shaped bounds in the bottom row.

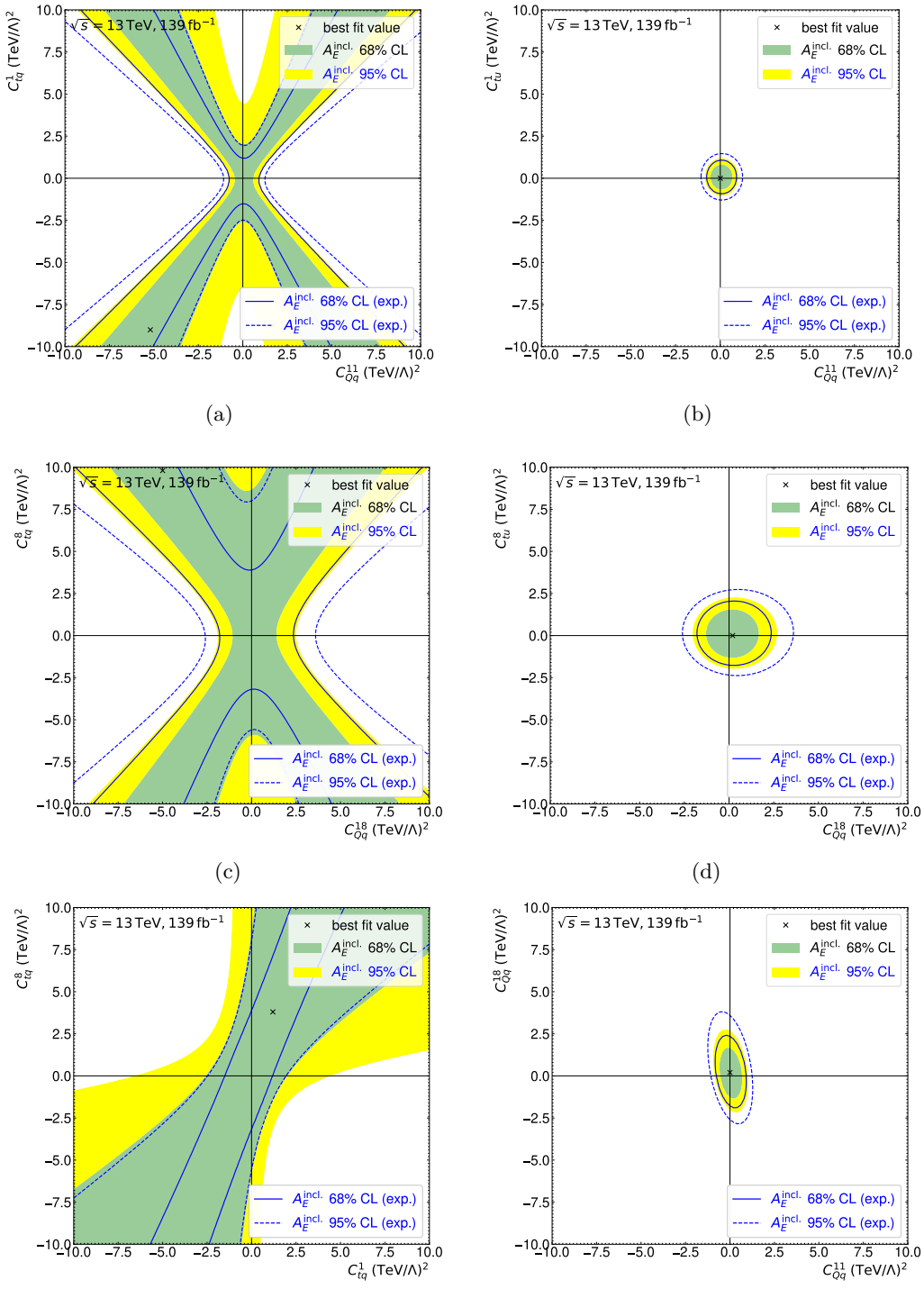

Figure 10.3.: Bounds on Wilson coefficients from two-parameter fits of the measured and expected inclusive energy asymmetry. The inner green and outer yellow areas show the 68% and 95% CL limits obtained from the measured energy asymmetry, respectively. The black cross denotes the minimum of the χ^2 fit. Solid and dashed blue contours show the expected 68% and 95% CL limits from the energy asymmetry, respectively.

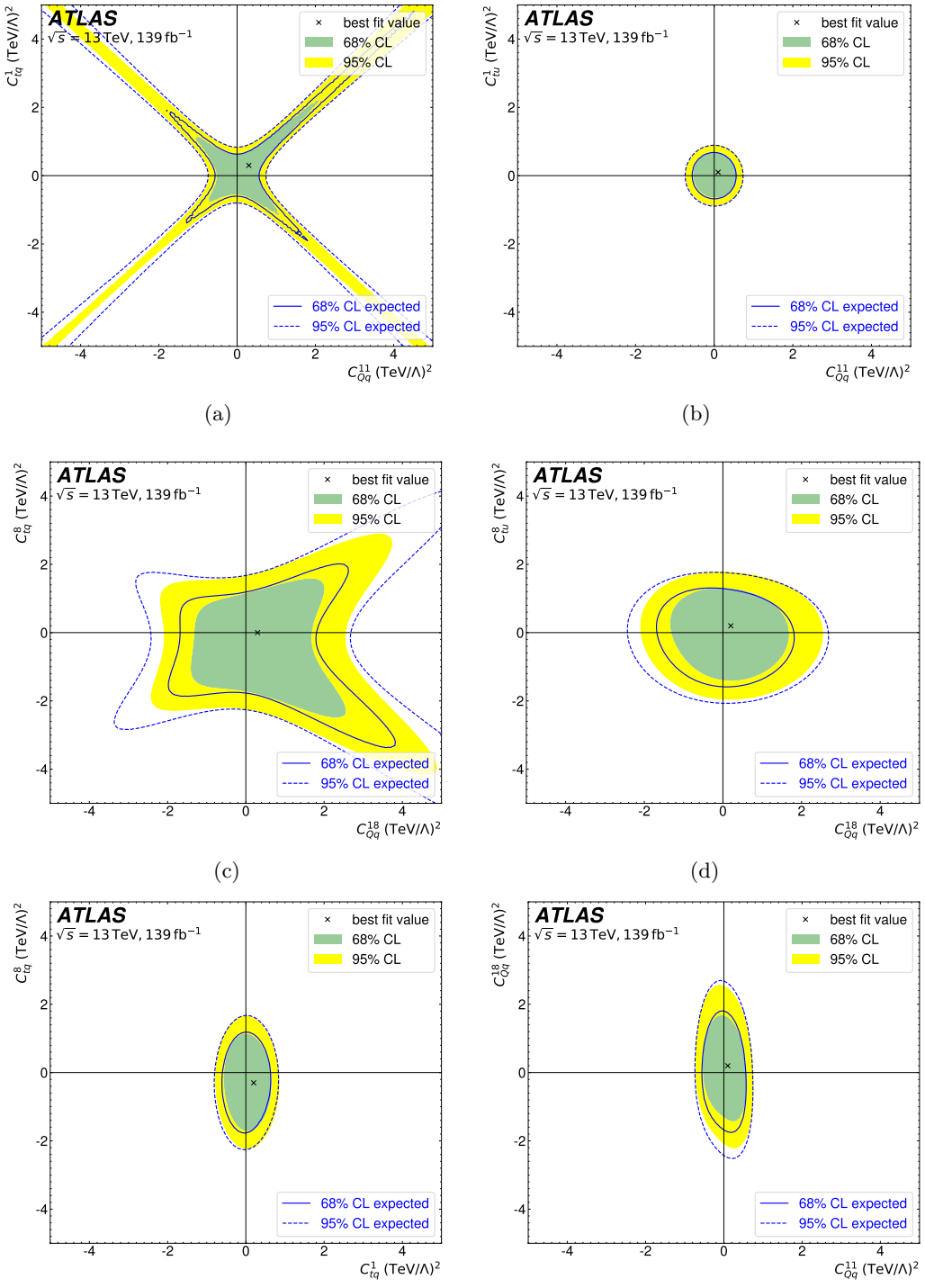

Figure 10.4.: Bounds on Wilson coefficients from two-parameter fits of the energy asymmetry A_E in all three θ_j bins, setting all other operator coefficients to zero. The inner green and outer yellow areas show the 68% and 95% CL limits obtained from the measured energy asymmetry, respectively. The black cross denotes the minimum of the χ^2 fit. Solid and dashed blue contours show the expected 68% and 95% CL limits from the energy asymmetry, respectively. This figure was published as figure 10 in reference [83].

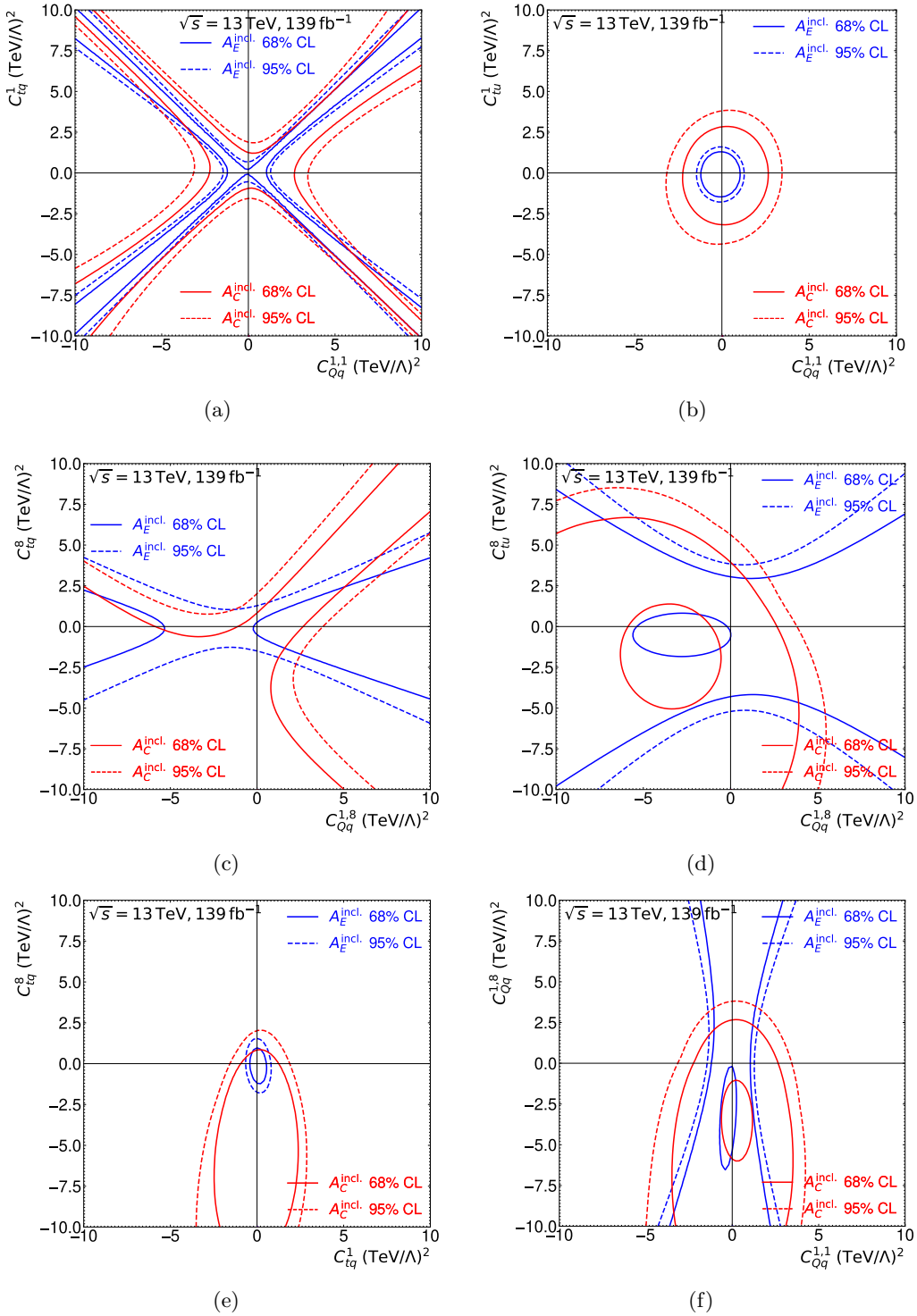

Figure 10.5.: Bounds on Wilson coefficients from two-parameter fits of the inclusive energy (blue) and rapidity (red) asymmetries, setting all other operator coefficients to zero. Solid and dashed contours show the 68% and 95% confidence bounds, respectively.

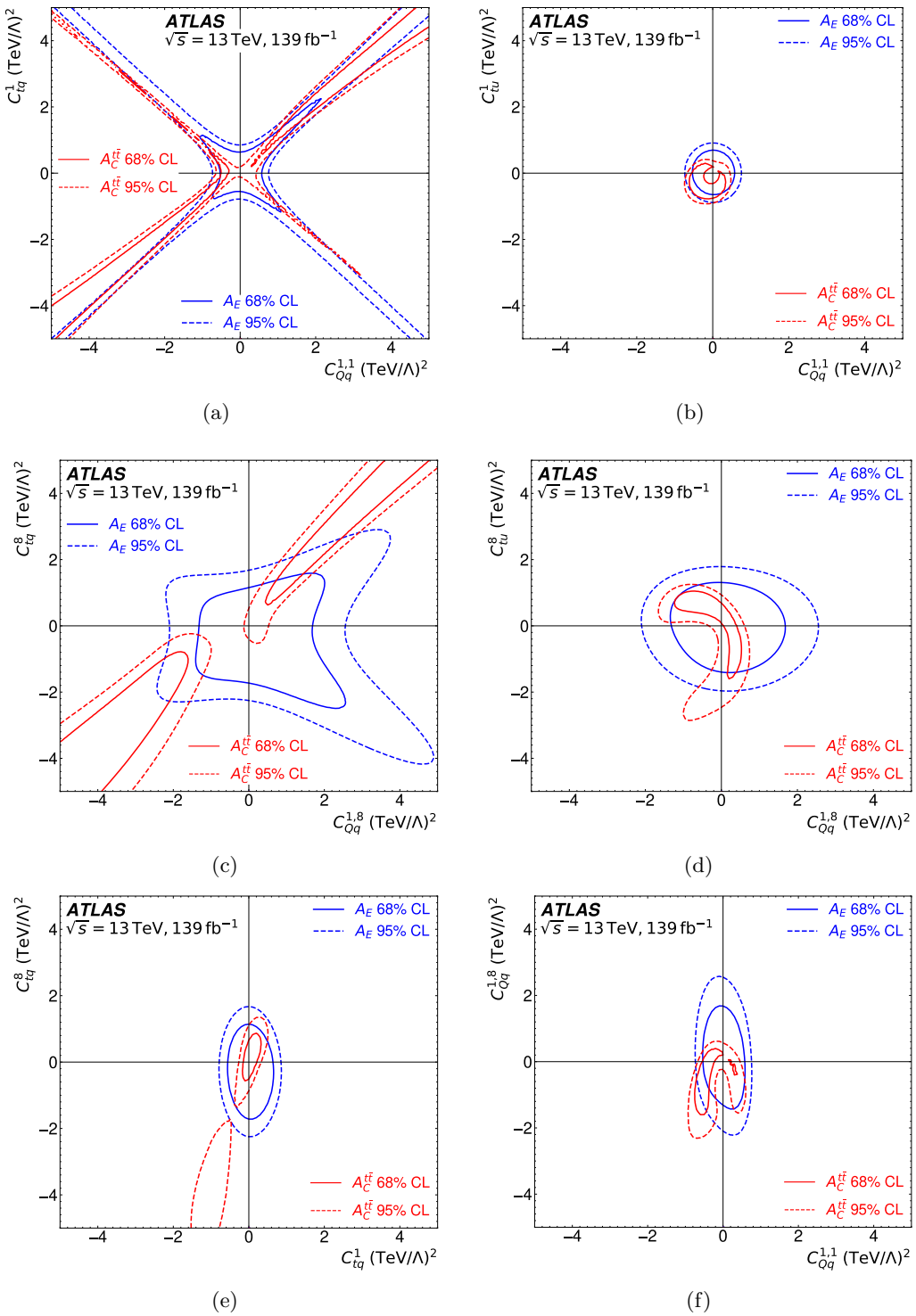

Figure 10.6.: Bounds on Wilson coefficients from two-parameter fits of the energy asymmetry A_E (blue) differential in θ_j and the rapidity asymmetry $A_C^{t\bar{t}}$ (red) differential in $m_{t\bar{t}}$ [65]. Solid and dashed contours show the 68% and 95% confidence bounds, respectively. This figure was published as figure 9 in reference [66].

Table 10.4.: Bounds on individual Wilson coefficients $C\,(\,\mathrm{TeV}/\Lambda)^2$ from the energy asymmetry, obtained from a combined fit to its values in all three θ_j bins: A_E^1, A_E^2, and A_E^3. The SMEFT predictions include operator contributions to σ_S and σ_A up to $\mathcal{O}(\Lambda^{-4})$ (left) and up to $\mathcal{O}(\Lambda^{-2})$ (right).

$C\,(\,\mathrm{TeV}/\Lambda)^2$	A_E (Λ^{-4})		A_E (Λ^{-2})	
	68% CL	95% CL	68% CL	95% CL
C_{Qq}^{11}	$[-0.41, 0.47]$	$[-0.65, 0.67]$	$[-0.68, 4.06]$	$[-3.36, 6.16]$
C_{Qq}^{18}	$[-0.87, 1.24]$	$[-1.72, 2.10]$	$[-1.26, 4.76]$	$[-3.24, 9.64]$
C_{tq}^{1}	$[-0.43, 0.52]$	$[-0.69, 0.75]$	$[-0.60, 5.76]$	$[-3.42, 9.36]$
C_{tq}^{8}	$[-1.41, 0.84]$	$[-2.01, 1.43]$	$[-1.86, 1.70]$	$[-3.30, 3.98]$
C_{tu}^{1}	$[-0.50, 0.56]$	$[-0.78, 0.81]$	$[-0.96, 5.82]$	$[-4.72, 8.88]$
C_{tu}^{8}	$[-1.00, 1.01]$	$[-1.71, 1.56]$	$[-1.30, 2.52]$	$[-3.02, 4.66]$

As shown in eq. 2.49 in section 2.4.3, corrections due to the interference between dimension-eight operators and the SM, $A_\mathrm{SM} \times A^{(8)}$, contribute to the squared amplitude at the same order in Λ as the dimension-six interference terms $A^{(6)} \times A^{(6)}$. Some analyses like the rapidity asymmetry measurement [65] therefore prefer to present the SMEFT results only to the order of Λ^2. To ease comparisons with such measurements and to evaluate the impact of $\mathcal{O}(\Lambda^{-2})$ versus $\mathcal{O}(\Lambda^{-4})$ operator contributions for the energy asymmetry, the bounds obtained from the energy asymmetry including operator contributions to the charge-symmetric and charge-asymmetric cross sections σ_S and σ_A up to $\mathcal{O}(\Lambda^{-2})$ and up to $\mathcal{O}(\Lambda^{-4})$ are compared in table 10.4. The bounds are clearly dominated by the $\mathcal{O}(\Lambda^{-4})$ contributions $\sigma_{\mathrm{S,A}}^{kl}$. Studies in dilepton production found large effects from both the inclusion of dimension-six squared terms and of dimension-eight terms [324] on the limits of four-fermion operators including leptons, while studies on Higgs measurements found the impact of dimension-eight operators including Higgs bosons to be at the order of a few percent [150].

10.3. Global fits

Figure 10.7 shows current bounds on the Wilson coefficients for top-quark operators from global fits [323] of observables in the top-quark sector such as the forward-backward [128] and rapidity [65] asymmetries, measurements of the tW [325], tZ [326], $t\bar{t}\gamma$ [327], ttW and ttZ [328] cross sections, searches for four-top events [329] as well as electroweak precision measurements. The limits were obtained with a χ^2 fit similar to that described in section 10.2 taking into account operator contributions up to order $\mathcal{O}(\Lambda)^{-2}$ and neglecting dimension-six $A^{(6)} \times A^{(6)}$ interference terms. The upper panel shows individual limits, setting all other operator coefficients to zero, while they were profiled or marginalised in the lower panel. The individual limits are of the order of $\mathcal{O}(0.1)$ for C_{Qq}^{31} and of $\mathcal{O}(1)$ for the other four-fermion operators and can be directly compared to the limits obtained from the energy asymmetry in table 10.4 which are of order $\mathcal{O}(5)$. Marginalising over all other operators increases the current limits by factors up to ten, resulting in the individual limits from the energy asymmetry being smaller than current global limits.

Figure 10.8 illustrates the interplay between the various top-quark observables in constraining the Wilson coefficients for four-fermion operators in two-parameter fits. In the C_{Qq}^{18}-C_{tq}^{8} plane, corresponding to figure 10.4c, the $t\bar{t}$ cross section and asymmetry observables exhibit blind directions orthogonal to each other and the $t\bar{t}V$ and $t\bar{t}H$ cross section measurements provide elliptical bounds with a similar size as those obtained from the energy asymmetry. Their combination yields much tighter bounds without any blind directions, showing that the energy asymmetry observable will provide a valuable input to global fits.

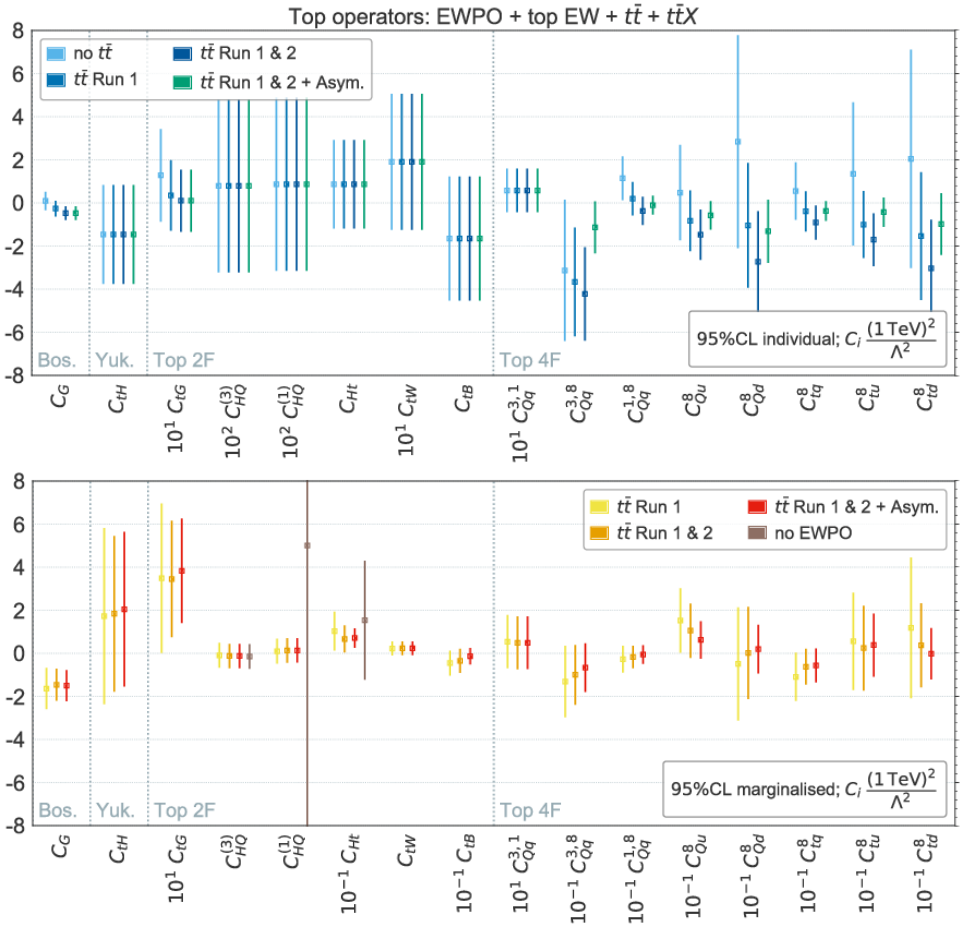

Figure 10.7.: 95% CL intervals for the individual (top panel) and marginalised (bottom panel) Wilson coefficients of top-quark operators from combined fits to top-quark data. [323]

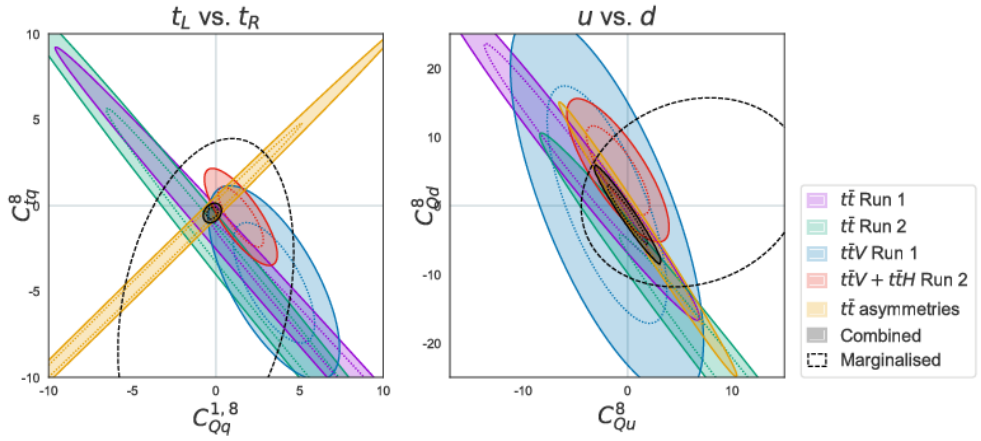

Figure 10.8.: Bounds on Wilson coefficients from two-parameter fits of various top-quark datasets for operators coupling to left- and right-handed top quarks (left) and to up- and down-type quarks (right) [323]. Dashed and solid lines correspond to 68% and 95% confidence levels, respectively.

11. Summary

In this thesis the first measurement of the top-antitop energy asymmetry and its interpretation in the Standard Model Effective Field Theory (SMEFT) framework were presented. The results were published in reference [83]. Phenomenological studies on the expected sensitivity of the energy asymmetry and a comparison with the rapidity asymmetry were published in references [75] and [66], respectively.

The measurement was based on proton-proton collision data collected by the ATLAS experiment during Run 2 from 2015–2018 at the Large Hadron Collider (LHC) with an integrated luminosity of $139\,\text{fb}^{-1}$ and a centre-of-mass energy of $\sqrt{s} = 13\,\text{TeV}$. The energy asymmetry was measured in jet-associated top-quark pair production events in the semi-leptonic decay channel in the boosted topology requiring the hadronically decaying top quark to have a transverse momentum above 350 GeV. The measurement was performed at the particle level using the Fully Bayesian Unfolding (FBU) method to correct the results for detector resolution and acceptance effects.

Both the inclusive and differential measurements of the energy asymmetries were found to be consistent with the SM prediction calculated at next-to-leading order in quantum chromodynamics including effects of parton shower and hadronisation. In the central bin of the scattering angle of the associated jet with respect to the beam axis, $\pi/4 \leq \theta_j \leq 3\pi/5$, where the energy asymmetry is expected to be the largest, the measured asymmetry of -0.043 ± 0.020 is found to be different from zero with a significance of $2.1\,\sigma$ and to be in good agreement with the SM prediction of -0.038 ± 0.003. The measurement uncertainties are dominated by the limited data statistics in the chosen phase-space region, $t\bar{t}$ modelling and jet energy resolution uncertainties. Assuming that the SM prediction is measured and that the systematic uncertainties scale in the same way as the data statistical uncertainties, the energy asymmetry in the central θ_j region is expected to reach significances close to $3\,\sigma$ and well above $5\,\sigma$ during Run 3 and at the HL-LHC, respectively.

The energy asymmetry observable was interpreted within the SMEFT framework and found to have a high sensitivity to the chiral and colour structure of four-quark operators with top quarks. One- and two-dimensional bounds on the Wilson coefficients of individual operators were extracted in fits of the SMEFT predictions to the measured asymmetries. The sensitivity to individual four-quark operators were found to be similar to that of other observables in the top-quark sector; as illustrated in the two-parameter fits of operator pairs with different chiral and colour structure, the energy asymmetry probes new directions in the parameter space of Wilson coefficients and breaks blind directions observed for the rapidity asymmetry. Therefore, the energy asymmetry is complementary to other observables such as differential cross sections and the rapidity asymmetry and will provide a valuable new input to global SMEFT fits.

A. Data and Monte Carlo samples

The data samples used in this analysis with the corresponding event numbers and the trigger configuration names are listed in tables A.1 and A.2, respectively. Tables A.3 to A.12 list the simulated signal and background samples. Shown are the dataset identifier (DSID), sample name, detector simulation type, simulation campaign, simulated cross section σ before filtering, filter efficiency ϵ_{Filter}, k-factor, total cross section and number of simulated events. "FS" and "AF" refer to the full and fast detector simulation, respectively, while "TRUTH" denotes samples at the particle level without detector simulation. The Monte Carlo samples were simulated independently for the 2015–2016, 2017 and 2018 data-taking periods in the "mc16a", "mc16d" and "mc16e" MC campaigns, respectively. The k-factor [121] corrects the simulated cross section for higher order corrections in perturbation theory. The total cross section σ_{tot} is given by the product of the simulated cross section with the filter efficiency and the k-factor, $\sigma_{\text{tot}} = k\epsilon_{\text{Filter}}\sigma$. Some of the samples were filtered by decay products, transverse momenta or the appearance of b- and c-jets at the particle level.

Table A.1.: Dataset names and event numbers for the data samples.

Dataset	Events
data15_13TeV.AllYear.physics_Main.PhysCont.DAOD_TOPQ1.grp15_v01_p4345	220,574,004
data16_13TeV.AllYear.physics_Main.PhysCont.DAOD_TOPQ1.grp16_v01_p4345	1,069,006,174
data17_13TeV.AllYear.physics_Main.PhysCont.DAOD_TOPQ1.grp17_v01_p4345	1,340,803,654
data18_13TeV.AllYear.physics_Main.PhysCont.DAOD_TOPQ1.grp18_v01_p4345	1,716,774,819

Table A.2.: Single-electron (e) and single-muon (mu) trigger [270, 271] configuration for the 2015 and 2016–2018 data-taking periods. The trigger names indicate the transverse energy threshold for electrons (e) and muons (mu) as well as the identification (lh) and isolation (i) requirements for the HLT. Triggers with the suffix "nod0" do not use the transverse impact parameter in the LH. Triggers with the "L1" tag are seeded from L1 objects, where the number denotes the transverse energy requirements for electrons (EM) and muons (MU). The abbreviations "V" and "H" indicate η-dependent transverse energy requirements and a veto against leakage of energy deposits into the hadronic calorimeter, respectively.

Year	Electrons	Muons
2015	e24_lhmedium_L1EM20VH e60_lhmedium e120_lhloose	mu20_iloose_L1MU15 mu50
2016–2018	e26_lhtight_nod0_ivarloose e60_lhmedium_nod0 e140_lhloose_nod0	mu26_ivarmedium mu50

Table A.3.: Cross sections, filter efficiencies, k-factors and event numbers for the $t\bar{t}$ samples. The $t\bar{t}$ samples contain only the semi-leptonic and di-leptonic decay channels. To evaluate systematic uncertainties due to final state radiation, sliced samples filtered by the scalar sum of transverse momenta of all particle-level jets H_T were used. The mass variation, ME/PS matching and PS samples are subdivided into semi-leptonic and di-leptonic $t\bar{t}$ decay channels.

DSID	Sample	Type	Campaign	σ [pb]	ϵ_{Filter}	k	σ_{tot} [pb]	Events
410470	PhPy8EG_A14_ttbar_hdamp258p75_nonallhad	FS	mc16d	729.77	0.5438	1.1398	452.37	149,327,000
410470	PhPy8EG_A14_ttbar_hdamp258p75_nonallhad	FS	mc16e	729.77	0.5438	1.1398	452.37	199,193,000
410470	PhPy8EG_A14_ttbar_hdamp258p75_nonallhad	FS	mc16a	729.77	0.5438	1.1398	452.37	119,432,000
407342	PhPy8EG_A14_ttbarHT1k5_hdamp258p75_nonallhad	FS	mc16d	729.77	0.0006	1.1398	0.51	2,434,350
407342	PhPy8EG_A14_ttbarHT1k5_hdamp258p75_nonallhad	FS	mc16e	729.77	0.0006	1.1398	0.51	8,835,000
407342	PhPy8EG_A14_ttbarHT1k5_hdamp258p75_nonallhad	FS	mc16a	729.77	0.0006	1.1398	0.51	1,984,550
407343	PhPy8EG_A14_ttbarHT1k_1k5_hdamp258p75_nonallhad	FS	mc16d	729.77	0.0036	1.1398	2.96	9,938,500
407343	PhPy8EG_A14_ttbarHT1k_1k5_hdamp258p75_nonallhad	FS	mc16e	729.77	0.0036	1.1398	2.96	13,136,000
407343	PhPy8EG_A14_ttbarHT1k_1k5_hdamp258p75_nonallhad	FS	mc16a	729.77	0.0036	1.1398	2.96	8,003,000
407344	PhPy8EG_A14_ttbarHT6c_1k_hdamp258p75_nonallhad	FS	mc16d	729.76	0.0257	1.1398	21.36	12,296,000
407344	PhPy8EG_A14_ttbarHT6c_1k_hdamp258p75_nonallhad	FS	mc16e	729.76	0.0257	1.1398	21.36	16,502,000
407344	PhPy8EG_A14_ttbarHT6c_1k_hdamp258p75_nonallhad	FS	mc16a	729.76	0.0257	1.1398	21.36	10,003,000
410470	PhPy8EG_A14_ttbar_hdamp258p75_nonallhad	AF	mc16d	729.77	0.5438	1.1398	452.37	149,845,000
410470	PhPy8EG_A14_ttbar_hdamp258p75_nonallhad	AF	mc16e	729.77	0.5438	1.1398	452.37	200,752,000
410470	PhPy8EG_A14_ttbar_hdamp258p75_nonallhad	AF	mc16a	729.77	0.5438	1.1398	452.37	119,916,000
410557	PowhegHerwig7EvtGen_H7UE_tt_hdamp258p75_704_SingleLep	AF	mc16d	730.14	0.4385	1.1392	364.76	120,732,000
410557	PowhegHerwig7EvtGen_H7UE_tt_hdamp258p75_704_SingleLep	AF	mc16e	730.14	0.4385	1.1392	364.76	161,049,000
410557	PowhegHerwig7EvtGen_H7UE_tt_hdamp258p75_704_SingleLep	AF	mc16a	730.14	0.4385	1.1392	364.76	96,426,000
410558	PowhegHerwig7EvtGen_H7UE_tt_hdamp258p75_704_dil	AF	mc16d	730.15	0.1055	1.1391	87.72	99,645,000
410558	PowhegHerwig7EvtGen_H7UE_tt_hdamp258p75_704_dil	AF	mc16e	730.15	0.1055	1.1391	87.72	132,917,000
410558	PowhegHerwig7EvtGen_H7UE_tt_hdamp258p75_704_dil	AF	mc16a	730.15	0.1055	1.1391	87.72	79,846,000
410480	PhPy8EG_A14_ttbar_hdamp517p5_SingleLep	AF	mc16d	729.74	0.4385	1.1398	364.74	120,673,000
410480	PhPy8EG_A14_ttbar_hdamp517p5_SingleLep	AF	mc16e	729.74	0.4385	1.1398	364.74	158,501,000
410480	PhPy8EG_A14_ttbar_hdamp517p5_SingleLep	AF	mc16a	729.74	0.4385	1.1398	364.74	96,924,000
410482	PhPy8EG_A14_ttbar_hdamp517p5_dil	AF	mc16d	729.74	0.1055	1.1398	87.72	99,704,000
410482	PhPy8EG_A14_ttbar_hdamp517p5_dil	AF	mc16e	729.74	0.1055	1.1398	87.72	133,138,000
410482	PhPy8EG_A14_ttbar_hdamp517p5_dil	AF	mc16a	729.74	0.1055	1.1398	87.72	79,976,000
411046	PowhegPythia8EvtGen_ttbar_172p00_SingleLep	AF	mc16d	739.77	0.4385	1.1416	370.30	149,992,000
411046	PowhegPythia8EvtGen_ttbar_172p00_SingleLep	AF	mc16e	739.77	0.4385	1.1416	370.30	195,928,000
411046	PowhegPythia8EvtGen_ttbar_172p00_SingleLep	AF	mc16a	739.77	0.4385	1.1416	370.30	119,887,000
411054	PowhegPythia8EvtGen_ttbar_172p00_dilep	AF	mc16d	77.95	1.0000	1.1416	88.98	74,875,000
411054	PowhegPythia8EvtGen_ttbar_172p00_dilep	AF	mc16e	77.95	1.0000	1.1416	88.98	97,961,000
411054	PowhegPythia8EvtGen_ttbar_172p00_dilep	AF	mc16a	77.95	1.0000	1.1416	88.98	59,999,000
411049	PowhegPythia8EvtGen_ttbar_173p00_SingleLep	AF	mc16d	719.93	0.4385	1.1378	359.16	149,968,000
411049	PowhegPythia8EvtGen_ttbar_173p00_SingleLep	AF	mc16e	719.93	0.4385	1.1378	359.16	195,999,000
411049	PowhegPythia8EvtGen_ttbar_173p00_SingleLep	AF	mc16a	719.93	0.4385	1.1378	359.16	119,993,000
411057	PowhegPythia8EvtGen_ttbar_173p00_dilep	AF	mc16d	75.86	1.0000	1.1378	86.31	74,999,000
411057	PowhegPythia8EvtGen_ttbar_173p00_dilep	AF	mc16e	75.86	1.0000	1.1378	86.31	97,989,000
411057	PowhegPythia8EvtGen_ttbar_173p00_dilep	AF	mc16a	75.86	1.0000	1.1378	86.31	59,909,000
411288	PhPy8EG_A14_ttbar_hdamp258p75_MECoff_nonallhad	AF	mc16d	729.33	0.5438	1.1405	452.37	124,992,000
411288	PhPy8EG_A14_ttbar_hdamp258p75_MECoff_nonallhad	AF	mc16e	729.33	0.5438	1.1405	452.37	165,959,000
411288	PhPy8EG_A14_ttbar_hdamp258p75_MECoff_nonallhad	AF	mc16a	729.33	0.5438	1.1405	452.37	99,994,000
410464	aMcAtNloPy8EvtGen_MEN30NLO_A14N23LO_ttbar_noShWe_SingleLep	AF	mc16d	711.43	0.4404	1.1691	366.27	119,984,000
410464	aMcAtNloPy8EvtGen_MEN30NLO_A14N23LO_ttbar_noShWe_SingleLep	AF	mc16e	711.43	0.4404	1.1691	366.27	159,922,000
410464	aMcAtNloPy8EvtGen_MEN30NLO_A14N23LO_ttbar_noShWe_SingleLep	AF	mc16a	711.43	0.4404	1.1691	366.27	97,000,000
410465	aMcAtNloPy8EvtGen_MEN30NLO_A14N23LO_ttbar_noShWe_dil	AF	mc16d	712.02	0.1072	1.1681	89.13	99,939,000
410465	aMcAtNloPy8EvtGen_MEN30NLO_A14N23LO_ttbar_noShWe_dil	AF	mc16e	712.02	0.1072	1.1681	89.13	124,656,000
410465	aMcAtNloPy8EvtGen_MEN30NLO_A14N23LO_ttbar_noShWe_dil	AF	mc16a	712.02	0.1072	1.1681	89.13	139,966,000

Table A.4.: Cross sections, filter efficiencies, k-factors and event numbers for the W+jets ($W \to e\nu_e$ and $W \to \mu\nu_\mu$) samples filtered by the $\max(H_T, P_T(V))$, where H_T denotes the sum of the transverse momenta of all particle-level jets and $P_T(V)$ the transverse momentum of the W boson, and the appearance of b- and c-jets at the particle level.

DSID	Sample	Type	Campaign	σ [pb]	ϵ_{Filter}	k	σ_{tot} [pb]	Events
364170	Sherpa_221_NNPDF30NNLO_Wenu_MAXHTPTV0_70_CVetoBVeto	FS	mc16d	19156.00	0.8246	0.9702	15325.87	14,961,987
364170	Sherpa_221_NNPDF30NNLO_Wenu_MAXHTPTV0_70_CVetoBVeto	FS	mc16e	19156.00	0.8246	0.9702	15325.87	20,104,467
364170	Sherpa_221_NNPDF30NNLO_Wenu_MAXHTPTV0_70_CVetoBVeto	FS	mc16a	19156.00	0.8246	0.9702	15325.87	12,205,680
364171	Sherpa_221_NNPDF30NNLO_Wenu_MAXHTPTV0_70_CFilterBVeto	FS	mc16d	19145.00	0.1310	0.9702	2432.33	29,449,776
364171	Sherpa_221_NNPDF30NNLO_Wenu_MAXHTPTV0_70_CFilterBVeto	FS	mc16e	19145.00	0.1310	0.9702	2432.33	73,804,414
364171	Sherpa_221_NNPDF30NNLO_Wenu_MAXHTPTV0_70_CFilterBVeto	FS	mc16a	19145.00	0.1310	0.9702	2432.33	45,669,245
364172	Sherpa_221_NNPDF30NNLO_Wenu_MAXHTPTV0_70_BFilter	FS	mc16d	19143.00	0.0442	0.9702	820.59	44,278,204
364172	Sherpa_221_NNPDF30NNLO_Wenu_MAXHTPTV0_70_BFilter	FS	mc16e	19143.00	0.0442	0.9702	820.59	64,133,724
364172	Sherpa_221_NNPDF30NNLO_Wenu_MAXHTPTV0_70_BFilter	FS	mc16a	19143.00	0.0442	0.9702	820.59	41,060,000
364173	Sherpa_221_NNPDF30NNLO_Wenu_MAXHTPTV70_140_CVetoBVeto	FS	mc16d	945.69	0.6803	0.9702	624.14	10,493,507
364173	Sherpa_221_NNPDF30NNLO_Wenu_MAXHTPTV70_140_CVetoBVeto	FS	mc16e	945.69	0.6803	0.9702	624.14	13,946,535
364173	Sherpa_221_NNPDF30NNLO_Wenu_MAXHTPTV70_140_CVetoBVeto	FS	mc16a	945.69	0.6748	0.9702	619.14	8,439,699
364174	Sherpa_221_NNPDF30NNLO_Wenu_MAXHTPTV70_140_CFilterBVeto	FS	mc16d	946.40	0.2427	0.9702	222.82	7,724,762
364174	Sherpa_221_NNPDF30NNLO_Wenu_MAXHTPTV70_140_CFilterBVeto	FS	mc16e	946.40	0.2427	0.9702	222.82	10,319,801
364174	Sherpa_221_NNPDF30NNLO_Wenu_MAXHTPTV70_140_CFilterBVeto	FS	mc16a	946.08	0.2414	0.9702	221.62	6,212,305
364175	Sherpa_221_NNPDF30NNLO_Wenu_MAXHTPTV70_140_BFilter	FS	mc16d	945.63	0.0834	0.9702	76.47	13,977,668
364175	Sherpa_221_NNPDF30NNLO_Wenu_MAXHTPTV70_140_BFilter	FS	mc16e	945.63	0.0834	0.9702	76.47	17,336,777
364175	Sherpa_221_NNPDF30NNLO_Wenu_MAXHTPTV70_140_BFilter	FS	mc16a	945.63	0.0834	0.9702	76.47	11,237,955
364176	Sherpa_221_NNPDF30NNLO_Wenu_MAXHTPTV140_280_CVetoBVeto	FS	mc16d	339.79	0.5987	0.9702	197.36	7,557,262
364176	Sherpa_221_NNPDF30NNLO_Wenu_MAXHTPTV140_280_CVetoBVeto	FS	mc16e	339.79	0.5987	0.9702	197.36	10,124,453
364176	Sherpa_221_NNPDF30NNLO_Wenu_MAXHTPTV140_280_CVetoBVeto	FS	mc16a	339.79	0.5987	0.9702	197.36	6,060,935
364177	Sherpa_221_NNPDF30NNLO_Wenu_MAXHTPTV140_280_CFilterBVeto	FS	mc16d	339.80	0.2880	0.9702	94.96	10,958,986
364177	Sherpa_221_NNPDF30NNLO_Wenu_MAXHTPTV140_280_CFilterBVeto	FS	mc16e	339.80	0.2880	0.9702	94.96	14,555,629
364177	Sherpa_221_NNPDF30NNLO_Wenu_MAXHTPTV140_280_CFilterBVeto	FS	mc16a	339.80	0.2880	0.9702	94.96	8,731,687
364178	Sherpa_221_NNPDF30NNLO_Wenu_MAXHTPTV140_280_BFilter	FS	mc16d	339.70	0.1108	0.9702	36.52	19,040,059
364178	Sherpa_221_NNPDF30NNLO_Wenu_MAXHTPTV140_280_BFilter	FS	mc16e	339.70	0.1108	0.9702	36.52	19,329,693
364178	Sherpa_221_NNPDF30NNLO_Wenu_MAXHTPTV140_280_BFilter	FS	mc16a	339.69	0.1109	0.9702	36.55	14,885,415
364179	Sherpa_221_NNPDF30NNLO_Wenu_MAXHTPTV280_500_CVetoBVeto	FS	mc16d	72.07	0.5469	0.9702	38.24	3,796,298
364179	Sherpa_221_NNPDF30NNLO_Wenu_MAXHTPTV280_500_CVetoBVeto	FS	mc16e	72.07	0.5469	0.9702	38.24	5,236,025
364179	Sherpa_221_NNPDF30NNLO_Wenu_MAXHTPTV280_500_CVetoBVeto	FS	mc16a	72.07	0.5469	0.9702	38.24	3,162,604
364180	Sherpa_221_NNPDF30NNLO_Wenu_MAXHTPTV280_500_CFilterBVeto	FS	mc16d	72.10	0.3199	0.9702	22.38	2,475,430
364180	Sherpa_221_NNPDF30NNLO_Wenu_MAXHTPTV280_500_CFilterBVeto	FS	mc16e	72.10	0.3199	0.9702	22.38	3,292,193
364180	Sherpa_221_NNPDF30NNLO_Wenu_MAXHTPTV280_500_CFilterBVeto	FS	mc16a	72.10	0.3199	0.9702	22.38	1,985,740
364181	Sherpa_221_NNPDF30NNLO_Wenu_MAXHTPTV280_500_BFilter	FS	mc16d	72.08	0.1386	0.9702	9.70	4,678,654
364181	Sherpa_221_NNPDF30NNLO_Wenu_MAXHTPTV280_500_BFilter	FS	mc16e	72.08	0.1386	0.9702	9.70	6,224,670
364181	Sherpa_221_NNPDF30NNLO_Wenu_MAXHTPTV280_500_BFilter	FS	mc16a	72.08	0.1386	0.9702	9.70	3,751,380
364182	Sherpa_221_NNPDF30NNLO_Wenu_MAXHTPTV500_1000	FS	mc16d	15.05	1.0000	0.9702	14.60	4,987,723
364182	Sherpa_221_NNPDF30NNLO_Wenu_MAXHTPTV500_1000	FS	mc16e	15.05	1.0000	0.9702	14.60	6,617,665
364182	Sherpa_221_NNPDF30NNLO_Wenu_MAXHTPTV500_1000	FS	mc16a	15.05	1.0000	0.9702	14.60	3,998,328
364183	Sherpa_221_NNPDF30NNLO_Wenu_MAXHTPTV1000_E_CMS	FS	mc16d	1.23	1.0000	0.9702	1.20	6,343,903
364183	Sherpa_221_NNPDF30NNLO_Wenu_MAXHTPTV1000_E_CMS	FS	mc16e	1.23	1.0000	0.9702	1.20	4,733,767
364183	Sherpa_221_NNPDF30NNLO_Wenu_MAXHTPTV1000_E_CMS	FS	mc16a	1.23	1.0000	0.9702	1.20	2,856,070
364156	Sherpa_221_NNPDF30NNLO_Wmunu_MAXHTPTV0_70_CVetoBVeto	FS	mc16d	19151.00	0.8246	0.9702	15322.24	17,281,437
364156	Sherpa_221_NNPDF30NNLO_Wmunu_MAXHTPTV0_70_CVetoBVeto	FS	mc16e	19151.00	0.8246	0.9702	15322.24	22,966,620
364156	Sherpa_221_NNPDF30NNLO_Wmunu_MAXHTPTV0_70_CVetoBVeto	FS	mc16a	19151.00	0.8246	0.9702	15322.24	13,759,181
364157	Sherpa_221_NNPDF30NNLO_Wmunu_MAXHTPTV0_70_CFilterBVeto	FS	mc16d	19144.00	0.1311	0.9702	2435.73	26,843,617
364157	Sherpa_221_NNPDF30NNLO_Wmunu_MAXHTPTV0_70_CFilterBVeto	FS	mc16e	19145.00	0.1302	0.9702	2418.77	83,211,370
364157	Sherpa_221_NNPDF30NNLO_Wmunu_MAXHTPTV0_70_CFilterBVeto	FS	mc16a	19145.00	0.1302	0.9702	2418.77	51,058,149
364158	Sherpa_221_NNPDF30NNLO_Wmunu_MAXHTPTV0_70_BFilter	FS	mc16d	19143.00	0.0452	0.9702	839.40	61,724,699
364158	Sherpa_221_NNPDF30NNLO_Wmunu_MAXHTPTV0_70_BFilter	FS	mc16e	19143.00	0.0452	0.9702	839.40	41,721,519
364158	Sherpa_221_NNPDF30NNLO_Wmunu_MAXHTPTV0_70_BFilter	FS	mc16a	19143.00	0.0452	0.9702	839.40	37,948,493
364159	Sherpa_221_NNPDF30NNLO_Wmunu_MAXHTPTV70_140_CVetoBVeto	FS	mc16d	945.99	0.6743	0.9702	618.89	11,711,699
364159	Sherpa_221_NNPDF30NNLO_Wmunu_MAXHTPTV70_140_CVetoBVeto	FS	mc16e	945.99	0.6743	0.9702	618.89	15,623,527
364159	Sherpa_221_NNPDF30NNLO_Wmunu_MAXHTPTV70_140_CVetoBVeto	FS	mc16a	945.99	0.6743	0.9702	618.89	9,380,737
364160	Sherpa_221_NNPDF30NNLO_Wmunu_MAXHTPTV70_140_CFilterBVeto	FS	mc16d	946.08	0.2427	0.9702	222.74	8,483,694
364160	Sherpa_221_NNPDF30NNLO_Wmunu_MAXHTPTV70_140_CFilterBVeto	FS	mc16e	946.08	0.2427	0.9702	222.74	11,259,835
364160	Sherpa_221_NNPDF30NNLO_Wmunu_MAXHTPTV70_140_CFilterBVeto	FS	mc16a	946.12	0.2436	0.9702	223.58	6,774,270
364161	Sherpa_221_NNPDF30NNLO_Wmunu_MAXHTPTV70_140_BFilter	FS	mc16d	944.91	0.0846	0.9702	77.58	15,776,664
364161	Sherpa_221_NNPDF30NNLO_Wmunu_MAXHTPTV70_140_BFilter	FS	mc16e	944.91	0.0846	0.9702	77.58	20,710,000
364161	Sherpa_221_NNPDF30NNLO_Wmunu_MAXHTPTV70_140_BFilter	FS	mc16a	944.91	0.0846	0.9702	77.58	12,450,003

Table A.5.: Cross sections, filter efficiencies, k-factors and event numbers for the W+jets ($W \to \mu\nu_\mu$ and $W \to \tau\nu_\tau$) samples filtered by the $\max(H_T, P_T(V))$, where H_T denotes the sum of the transverse momenta of all particle-level jets and $P_T(V)$ the transverse momentum of the W boson, and the appearance of b- and c-jets at the particle level.

DSID	Sample	Type	Campaign	σ [pb]	ϵ_{Filter}	k	σ_{tot} [pb]	Events
364162	Sherpa_221_NNPDF30NNLO_Wmunu_MAXHTPTV140_280_CVetoBVeto	FS	mc16d	339.71	0.5999	0.9702	197.74	8,179,012
364162	Sherpa_221_NNPDF30NNLO_Wmunu_MAXHTPTV140_280_CVetoBVeto	FS	mc16e	339.71	0.5999	0.9702	197.74	11,116,095
364162	Sherpa_221_NNPDF30NNLO_Wmunu_MAXHTPTV140_280_CVetoBVeto	FS	mc16a	339.71	0.5999	0.9702	197.74	6,613,735
364163	Sherpa_221_NNPDF30NNLO_Wmunu_MAXHTPTV140_280_CFilterBVeto	FS	mc16d	339.80	0.2926	0.9702	96.45	11,859,442
364163	Sherpa_221_NNPDF30NNLO_Wmunu_MAXHTPTV140_280_CFilterBVeto	FS	mc16e	339.80	0.2926	0.9702	96.45	15,794,675
364163	Sherpa_221_NNPDF30NNLO_Wmunu_MAXHTPTV140_280_CFilterBVeto	FS	mc16a	339.80	0.2926	0.9702	96.45	9,406,889
364164	Sherpa_221_NNPDF30NNLO_Wmunu_MAXHTPTV140_280_BFilter	FS	mc16d	339.68	0.1108	0.9702	36.52	17,347,246
364164	Sherpa_221_NNPDF30NNLO_Wmunu_MAXHTPTV140_280_BFilter	FS	mc16e	339.68	0.1108	0.9702	36.52	27,246,901
364164	Sherpa_221_NNPDF30NNLO_Wmunu_MAXHTPTV140_280_BFilter	FS	mc16a	339.67	0.1090	0.9702	35.91	16,368,765
364165	Sherpa_221_NNPDF30NNLO_Wmunu_MAXHTPTV280_500_CVetoBVeto	FS	mc16d	72.08	0.5478	0.9702	38.31	4,306,136
364165	Sherpa_221_NNPDF30NNLO_Wmunu_MAXHTPTV280_500_CVetoBVeto	FS	mc16e	72.08	0.5478	0.9702	38.31	5,742,890
364165	Sherpa_221_NNPDF30NNLO_Wmunu_MAXHTPTV280_500_CVetoBVeto	FS	mc16a	72.08	0.5478	0.9702	38.31	3,449,628
364166	Sherpa_221_NNPDF30NNLO_Wmunu_MAXHTPTV280_500_CFilterBVeto	FS	mc16d	72.11	0.3201	0.9702	22.40	2,692,191
364166	Sherpa_221_NNPDF30NNLO_Wmunu_MAXHTPTV280_500_CFilterBVeto	FS	mc16e	72.11	0.3201	0.9702	22.40	3,583,664
364166	Sherpa_221_NNPDF30NNLO_Wmunu_MAXHTPTV280_500_CFilterBVeto	FS	mc16a	72.11	0.3201	0.9702	22.40	2,144,286
364167	Sherpa_221_NNPDF30NNLO_Wmunu_MAXHTPTV280_500_BFilter	FS	mc16d	72.06	0.1314	0.9702	9.18	5,177,294
364167	Sherpa_221_NNPDF30NNLO_Wmunu_MAXHTPTV280_500_BFilter	FS	mc16e	72.06	0.1314	0.9702	9.18	6,840,532
364167	Sherpa_221_NNPDF30NNLO_Wmunu_MAXHTPTV280_500_BFilter	FS	mc16a	72.06	0.1314	0.9702	9.18	4,066,926
364168	Sherpa_221_NNPDF30NNLO_Wmunu_MAXHTPTV500_1000	FS	mc16d	15.01	1.0000	0.9702	14.56	5,457,286
364168	Sherpa_221_NNPDF30NNLO_Wmunu_MAXHTPTV500_1000	FS	mc16e	15.01	1.0000	0.9702	14.56	7,239,697
364168	Sherpa_221_NNPDF30NNLO_Wmunu_MAXHTPTV500_1000	FS	mc16a	15.01	1.0000	0.9702	14.56	4,359,820
364169	Sherpa_221_NNPDF30NNLO_Wmunu_MAXHTPTV1000_E_CMS	FS	mc16d	1.23	1.0000	0.9702	1.20	3,888,319
364169	Sherpa_221_NNPDF30NNLO_Wmunu_MAXHTPTV1000_E_CMS	FS	mc16e	1.23	1.0000	0.9702	1.20	5,166,821
364169	Sherpa_221_NNPDF30NNLO_Wmunu_MAXHTPTV1000_E_CMS	FS	mc16a	1.23	1.0000	0.9702	1.20	3,105,465
364184	Sherpa_221_NNPDF30NNLO_Wtaunu_MAXHTPTV0_70_CVetoBVeto	FS	mc16d	19155.00	0.8246	0.9702	15324.52	1,767,128
364184	Sherpa_221_NNPDF30NNLO_Wtaunu_MAXHTPTV0_70_CVetoBVeto	FS	mc16e	19155.00	0.8246	0.9702	15324.52	2,340,521
364184	Sherpa_221_NNPDF30NNLO_Wtaunu_MAXHTPTV0_70_CVetoBVeto	FS	mc16a	19155.00	0.8246	0.9702	15324.52	1,310,669
364185	Sherpa_221_NNPDF30NNLO_Wtaunu_MAXHTPTV0_70_CFilterBVeto	FS	mc16d	19154.00	0.1296	0.9702	2407.83	1,650,427
364185	Sherpa_221_NNPDF30NNLO_Wtaunu_MAXHTPTV0_70_CFilterBVeto	FS	mc16e	19154.00	0.1296	0.9702	2407.83	2,109,645
364185	Sherpa_221_NNPDF30NNLO_Wtaunu_MAXHTPTV0_70_CFilterBVeto	FS	mc16a	19154.00	0.1296	0.9702	2407.83	1,250,406
364186	Sherpa_221_NNPDF30NNLO_Wtaunu_MAXHTPTV0_70_BFilter	FS	mc16d	19152.00	0.0451	0.9702	838.57	1,314,693
364186	Sherpa_221_NNPDF30NNLO_Wtaunu_MAXHTPTV0_70_BFilter	FS	mc16e	19152.00	0.0451	0.9702	838.57	1,737,074
364186	Sherpa_221_NNPDF30NNLO_Wtaunu_MAXHTPTV0_70_BFilter	FS	mc16a	19147.00	0.0451	0.9702	837.80	980,322
364187	Sherpa_221_NNPDF30NNLO_Wtaunu_MAXHTPTV70_140_CVetoBVeto	FS	mc16d	946.09	0.6760	0.9702	620.49	1,762,597
364187	Sherpa_221_NNPDF30NNLO_Wtaunu_MAXHTPTV70_140_CVetoBVeto	FS	mc16e	946.09	0.6760	0.9702	620.49	2,339,109
364187	Sherpa_221_NNPDF30NNLO_Wtaunu_MAXHTPTV70_140_CVetoBVeto	FS	mc16a	945.58	0.6756	0.9702	619.80	1,356,740
364188	Sherpa_221_NNPDF30NNLO_Wtaunu_MAXHTPTV70_140_CFilterBVeto	FS	mc16d	946.61	0.2425	0.9702	222.72	1,326,193
364188	Sherpa_221_NNPDF30NNLO_Wtaunu_MAXHTPTV70_140_CFilterBVeto	FS	mc16e	946.61	0.2425	0.9702	222.72	1,771,736
364188	Sherpa_221_NNPDF30NNLO_Wtaunu_MAXHTPTV70_140_CFilterBVeto	FS	mc16a	946.72	0.2422	0.9702	222.47	1,037,610
364189	Sherpa_221_NNPDF30NNLO_Wtaunu_MAXHTPTV70_140_BFilter	FS	mc16d	945.87	0.0862	0.9702	79.07	1,200,293
364189	Sherpa_221_NNPDF30NNLO_Wtaunu_MAXHTPTV70_140_BFilter	FS	mc16e	945.87	0.0862	0.9702	79.07	2,393,282
364189	Sherpa_221_NNPDF30NNLO_Wtaunu_MAXHTPTV70_140_BFilter	FS	mc16a	945.87	0.0839	0.9702	77.00	924,617
364190	Sherpa_221_NNPDF30NNLO_Wtaunu_MAXHTPTV140_280_CVetoBVeto	FS	mc16d	339.69	0.5988	0.9702	197.36	3,054,676
364190	Sherpa_221_NNPDF30NNLO_Wtaunu_MAXHTPTV140_280_CVetoBVeto	FS	mc16e	339.69	0.5988	0.9702	197.36	4,050,948
364190	Sherpa_221_NNPDF30NNLO_Wtaunu_MAXHTPTV140_280_CVetoBVeto	FS	mc16a	339.69	0.5988	0.9702	197.36	2,362,416
364191	Sherpa_221_NNPDF30NNLO_Wtaunu_MAXHTPTV140_280_CFilterBVeto	FS	mc16d	339.84	0.2848	0.9702	93.90	1,897,546
364191	Sherpa_221_NNPDF30NNLO_Wtaunu_MAXHTPTV140_280_CFilterBVeto	FS	mc16e	339.84	0.2848	0.9702	93.90	2,506,525
364191	Sherpa_221_NNPDF30NNLO_Wtaunu_MAXHTPTV140_280_CFilterBVeto	FS	mc16a	339.84	0.2848	0.9702	93.90	1,485,137
364192	Sherpa_221_NNPDF30NNLO_Wtaunu_MAXHTPTV140_280_BFilter	FS	mc16d	339.68	0.1060	0.9702	34.93	4,081,522
364192	Sherpa_221_NNPDF30NNLO_Wtaunu_MAXHTPTV140_280_BFilter	FS	mc16e	339.68	0.1060	0.9702	34.93	5,330,113
364192	Sherpa_221_NNPDF30NNLO_Wtaunu_MAXHTPTV140_280_BFilter	FS	mc16a	339.60	0.1068	0.9702	35.19	3,119,840
364193	Sherpa_221_NNPDF30NNLO_Wtaunu_MAXHTPTV280_500_CVetoBVeto	FS	mc16d	72.08	0.5617	0.9702	39.28	1,314,622
364193	Sherpa_221_NNPDF30NNLO_Wtaunu_MAXHTPTV280_500_CVetoBVeto	FS	mc16e	72.08	0.5617	0.9702	39.28	1,748,621
364193	Sherpa_221_NNPDF30NNLO_Wtaunu_MAXHTPTV280_500_CVetoBVeto	FS	mc16a	72.08	0.5617	0.9702	39.28	1,029,446
364194	Sherpa_221_NNPDF30NNLO_Wtaunu_MAXHTPTV280_500_CFilterBVeto	FS	mc16d	71.99	0.3186	0.9702	22.25	866,411
364194	Sherpa_221_NNPDF30NNLO_Wtaunu_MAXHTPTV280_500_CFilterBVeto	FS	mc16e	71.99	0.3186	0.9702	22.25	1,148,434
364194	Sherpa_221_NNPDF30NNLO_Wtaunu_MAXHTPTV280_500_CFilterBVeto	FS	mc16a	71.99	0.3186	0.9702	22.25	676,860
364195	Sherpa_221_NNPDF30NNLO_Wtaunu_MAXHTPTV280_500_BFilter	FS	mc16d	71.94	0.1360	0.9702	9.49	598,966
364195	Sherpa_221_NNPDF30NNLO_Wtaunu_MAXHTPTV280_500_BFilter	FS	mc16e	71.94	0.1360	0.9702	9.49	795,832
364195	Sherpa_221_NNPDF30NNLO_Wtaunu_MAXHTPTV280_500_BFilter	FS	mc16a	71.94	0.1360	0.9702	9.49	470,132
364196	Sherpa_221_NNPDF30NNLO_Wtaunu_MAXHTPTV500_1000	FS	mc16d	15.05	1.0000	0.9702	14.60	1,277,353
364196	Sherpa_221_NNPDF30NNLO_Wtaunu_MAXHTPTV500_1000	FS	mc16e	15.05	1.0000	0.9702	14.60	1,692,433
364196	Sherpa_221_NNPDF30NNLO_Wtaunu_MAXHTPTV500_1000	FS	mc16a	15.05	1.0000	0.9702	14.60	996,931
364197	Sherpa_221_NNPDF30NNLO_Wtaunu_MAXHTPTV1000_E_CMS	FS	mc16d	1.23	1.0000	0.9702	1.20	1,071,504
364197	Sherpa_221_NNPDF30NNLO_Wtaunu_MAXHTPTV1000_E_CMS	FS	mc16e	1.23	1.0000	0.9702	1.20	1,423,232
364197	Sherpa_221_NNPDF30NNLO_Wtaunu_MAXHTPTV1000_E_CMS	FS	mc16a	1.23	1.0000	0.9702	1.20	848,117

Table A.6.: Cross sections, filter efficiencies, k-factors and event numbers for the Z+jets ($Z \to e^+e^-$ and $Z \to \mu^+\mu^-$) samples filtered by the $\max(H_T, P_T(V))$, where H_T denotes the sum of the transverse momenta of all particle-level jets and $P_T(V)$ the transverse momentum of the Z boson, and the appearance of b- and c-jets at the particle level.

DSID	Sample	Type	Campaign	σ [pb]	ϵ_{Filter}	k	σ_{tot} [pb]	Events
364114	Sherpa_221_NNPDF30NNLO_Zee_MAXHTPTV0_70_CVetoBVeto	FS	mc16d	1982.80	0.8213	0.9751	1587.83	6,702,760
364114	Sherpa_221_NNPDF30NNLO_Zee_MAXHTPTV0_70_CVetoBVeto	FS	mc16e	1982.80	0.8213	0.9751	1587.83	8,888,833
364114	Sherpa_221_NNPDF30NNLO_Zee_MAXHTPTV0_70_CVetoBVeto	FS	mc16a	1981.60	0.8212	0.9751	1586.73	5,381,032
364115	Sherpa_221_NNPDF30NNLO_Zee_MAXHTPTV0_70_CFilterBVeto	FS	mc16d	1981.70	0.1136	0.9751	219.48	4,500,095
364115	Sherpa_221_NNPDF30NNLO_Zee_MAXHTPTV0_70_CFilterBVeto	FS	mc16e	1981.70	0.1136	0.9751	219.48	5,983,718
364115	Sherpa_221_NNPDF30NNLO_Zee_MAXHTPTV0_70_CFilterBVeto	FS	mc16a	1981.70	0.1135	0.9751	219.26	3,615,019
364116	Sherpa_221_NNPDF30NNLO_Zee_MAXHTPTV0_70_BFilter	FS	mc16d	1981.90	0.0658	0.9751	127.09	7,615,132
364116	Sherpa_221_NNPDF30NNLO_Zee_MAXHTPTV0_70_BFilter	FS	mc16e	1981.90	0.0658	0.9751	127.09	10,116,269
364116	Sherpa_221_NNPDF30NNLO_Zee_MAXHTPTV0_70_BFilter	FS	mc16a	1982.00	0.0658	0.9751	127.08	6,114,299
364117	Sherpa_221_NNPDF30NNLO_Zee_MAXHTPTV70_140_CVetoBVeto	FS	mc16d	110.71	0.6943	0.9751	74.95	5,868,887
364117	Sherpa_221_NNPDF30NNLO_Zee_MAXHTPTV70_140_CVetoBVeto	FS	mc16e	110.71	0.6943	0.9751	74.95	7,904,152
364117	Sherpa_221_NNPDF30NNLO_Zee_MAXHTPTV70_140_CVetoBVeto	FS	mc16a	110.64	0.6927	0.9751	74.74	4,739,028
364118	Sherpa_221_NNPDF30NNLO_Zee_MAXHTPTV70_140_CFilterBVeto	FS	mc16d	110.47	0.1907	0.9751	20.54	2,038,740
364118	Sherpa_221_NNPDF30NNLO_Zee_MAXHTPTV70_140_CFilterBVeto	FS	mc16e	110.47	0.1907	0.9751	20.54	2,717,950
364118	Sherpa_221_NNPDF30NNLO_Zee_MAXHTPTV70_140_CFilterBVeto	FS	mc16a	110.50	0.1893	0.9751	20.40	1,635,478
364119	Sherpa_221_NNPDF30NNLO_Zee_MAXHTPTV70_140_BFilter	FS	mc16d	110.53	0.1190	0.9751	12.82	6,303,483
364119	Sherpa_221_NNPDF30NNLO_Zee_MAXHTPTV70_140_BFilter	FS	mc16e	110.53	0.1190	0.9751	12.82	8,333,397
364119	Sherpa_221_NNPDF30NNLO_Zee_MAXHTPTV70_140_BFilter	FS	mc16a	110.46	0.1155	0.9751	12.44	5,030,096
364120	Sherpa_221_NNPDF30NNLO_Zee_MAXHTPTV140_280_CVetoBVeto	FS	mc16d	40.65	0.6161	0.9751	24.42	5,179,585
364120	Sherpa_221_NNPDF30NNLO_Zee_MAXHTPTV140_280_CVetoBVeto	FS	mc16e	40.65	0.6161	0.9751	24.42	6,921,428
364120	Sherpa_221_NNPDF30NNLO_Zee_MAXHTPTV140_280_CVetoBVeto	FS	mc16a	40.65	0.6159	0.9751	24.41	4,145,660
364121	Sherpa_221_NNPDF30NNLO_Zee_MAXHTPTV140_280_CFilterBVeto	FS	mc16d	40.67	0.2329	0.9751	9.24	3,145,197
364121	Sherpa_221_NNPDF30NNLO_Zee_MAXHTPTV140_280_CFilterBVeto	FS	mc16e	40.67	0.2329	0.9751	9.24	4,180,857
364121	Sherpa_221_NNPDF30NNLO_Zee_MAXHTPTV140_280_CFilterBVeto	FS	mc16a	40.67	0.2321	0.9751	9.20	2,518,391
364122	Sherpa_221_NNPDF30NNLO_Zee_MAXHTPTV140_280_BFilter	FS	mc16d	40.68	0.1534	0.9751	6.08	13,412,665
364122	Sherpa_221_NNPDF30NNLO_Zee_MAXHTPTV140_280_BFilter	FS	mc16e	40.68	0.1534	0.9751	6.08	17,748,452
364122	Sherpa_221_NNPDF30NNLO_Zee_MAXHTPTV140_280_BFilter	FS	mc16a	40.68	0.1524	0.9751	6.04	10,658,094
364123	Sherpa_221_NNPDF30NNLO_Zee_MAXHTPTV280_500_CVetoBVeto	FS	mc16d	8.67	0.5688	0.9751	4.81	2,118,516
364123	Sherpa_221_NNPDF30NNLO_Zee_MAXHTPTV280_500_CVetoBVeto	FS	mc16e	8.67	0.5688	0.9751	4.81	2,899,488
364123	Sherpa_221_NNPDF30NNLO_Zee_MAXHTPTV280_500_CVetoBVeto	FS	mc16a	8.67	0.5635	0.9751	4.76	1,695,492
364124	Sherpa_221_NNPDF30NNLO_Zee_MAXHTPTV280_500_CFilterBVeto	FS	mc16d	8.67	0.2662	0.9751	2.25	1,063,718
364124	Sherpa_221_NNPDF30NNLO_Zee_MAXHTPTV280_500_CFilterBVeto	FS	mc16e	8.67	0.2662	0.9751	2.25	1,476,924
364124	Sherpa_221_NNPDF30NNLO_Zee_MAXHTPTV280_500_CFilterBVeto	FS	mc16a	8.67	0.2653	0.9751	2.24	851,055
364125	Sherpa_221_NNPDF30NNLO_Zee_MAXHTPTV280_500_BFilter	FS	mc16d	8.68	0.1765	0.9751	1.49	4,321,440
364125	Sherpa_221_NNPDF30NNLO_Zee_MAXHTPTV280_500_BFilter	FS	mc16e	8.68	0.1765	0.9751	1.49	5,724,591
364125	Sherpa_221_NNPDF30NNLO_Zee_MAXHTPTV280_500_BFilter	FS	mc16a	8.68	0.1758	0.9751	1.49	3,460,436
364126	Sherpa_221_NNPDF30NNLO_Zee_MAXHTPTV500_1000	FS	mc16d	1.81	1.0000	0.9751	1.76	3,229,858
364126	Sherpa_221_NNPDF30NNLO_Zee_MAXHTPTV500_1000	FS	mc16e	1.81	1.0000	0.9751	1.76	4,335,753
364126	Sherpa_221_NNPDF30NNLO_Zee_MAXHTPTV500_1000	FS	mc16a	1.81	1.0000	0.9751	1.76	2,610,525
364127	Sherpa_221_NNPDF30NNLO_Zee_MAXHTPTV1000_E_CMS	FS	mc16d	0.15	1.0000	0.9751	0.15	1,129,386
364127	Sherpa_221_NNPDF30NNLO_Zee_MAXHTPTV1000_E_CMS	FS	mc16e	0.15	1.0000	0.9751	0.15	1,507,440
364127	Sherpa_221_NNPDF30NNLO_Zee_MAXHTPTV1000_E_CMS	FS	mc16a	0.15	1.0000	0.9751	0.15	903,024
364100	Sherpa_221_NNPDF30NNLO_Zmumu_MAXHTPTV0_70_CVetoBVeto	FS	mc16d	1981.70	0.8216	0.9751	1587.66	7,219,692
364100	Sherpa_221_NNPDF30NNLO_Zmumu_MAXHTPTV0_70_CVetoBVeto	FS	mc16e	1981.70	0.8216	0.9751	1587.66	9,662,509
364100	Sherpa_221_NNPDF30NNLO_Zmumu_MAXHTPTV0_70_CVetoBVeto	FS	mc16a	1982.50	0.8214	0.9751	1587.92	5,793,208
364101	Sherpa_221_NNPDF30NNLO_Zmumu_MAXHTPTV0_70_CFilterBVeto	FS	mc16d	1982.60	0.1136	0.9751	219.67	4,806,857
364101	Sherpa_221_NNPDF30NNLO_Zmumu_MAXHTPTV0_70_CFilterBVeto	FS	mc16e	1982.60	0.1136	0.9751	219.67	6,426,808
364101	Sherpa_221_NNPDF30NNLO_Zmumu_MAXHTPTV0_70_CFilterBVeto	FS	mc16a	1982.20	0.1132	0.9751	218.78	3,857,324
364102	Sherpa_221_NNPDF30NNLO_Zmumu_MAXHTPTV0_70_BFilter	FS	mc16d	1981.80	0.0660	0.9751	127.56	7,818,785
364102	Sherpa_221_NNPDF30NNLO_Zmumu_MAXHTPTV0_70_BFilter	FS	mc16e	1981.80	0.0660	0.9751	127.56	10,759,929
364102	Sherpa_221_NNPDF30NNLO_Zmumu_MAXHTPTV0_70_BFilter	FS	mc16a	1981.70	0.0651	0.9751	125.74	6,473,862
364103	Sherpa_221_NNPDF30NNLO_Zmumu_MAXHTPTV70_140_CVetoBVeto	FS	mc16d	109.07	0.6883	0.9751	73.20	6,330,824
364103	Sherpa_221_NNPDF30NNLO_Zmumu_MAXHTPTV70_140_CVetoBVeto	FS	mc16e	109.07	0.6883	0.9751	73.20	8,417,457
364103	Sherpa_221_NNPDF30NNLO_Zmumu_MAXHTPTV70_140_CVetoBVeto	FS	mc16a	109.14	0.6899	0.9751	73.42	5,057,345
364104	Sherpa_221_NNPDF30NNLO_Zmumu_MAXHTPTV70_140_CFilterBVeto	FS	mc16d	108.99	0.2003	0.9751	21.28	2,156,610
364104	Sherpa_221_NNPDF30NNLO_Zmumu_MAXHTPTV70_140_CFilterBVeto	FS	mc16e	108.99	0.2003	0.9751	21.28	2,862,596
364104	Sherpa_221_NNPDF30NNLO_Zmumu_MAXHTPTV70_140_CFilterBVeto	FS	mc16a	108.98	0.1903	0.9751	20.22	1,724,792
364105	Sherpa_221_NNPDF30NNLO_Zmumu_MAXHTPTV70_140_BFilter	FS	mc16d	109.05	0.1137	0.9751	12.09	6,607,119
364105	Sherpa_221_NNPDF30NNLO_Zmumu_MAXHTPTV70_140_BFilter	FS	mc16e	109.05	0.1137	0.9751	12.09	8,792,719
364105	Sherpa_221_NNPDF30NNLO_Zmumu_MAXHTPTV70_140_BFilter	FS	mc16a	109.03	0.1173	0.9751	12.48	5,285,898

Table A.7.: Cross sections, filter efficiencies, k-factors and event numbers for the Z+jets ($Z \to \mu^+\mu^-$ and $Z \to \tau^+\tau^-$) samples filtered by the $\max(H_T, P_T(V))$, where H_T denotes the sum of the transverse momenta of all particle-level jets and $P_T(V)$ the transverse momentum of the Z boson, and the appearance of b- and c-jets at the particle level.

DSID	Sample	Type	Campaign	σ [pb]	ϵ_{Filter}	k	σ_{tot} [pb]	Events
364106	Sherpa_221_NNPDF30NNLO_Zmumu_MAXHTPTV140_280_CVetoBVeto	FS	mc16d	39.89	0.5930	0.9751	23.07	5,461,489
364106	Sherpa_221_NNPDF30NNLO_Zmumu_MAXHTPTV140_280_CVetoBVeto	FS	mc16e	39.89	0.5930	0.9751	23.07	7,247,930
364106	Sherpa_221_NNPDF30NNLO_Zmumu_MAXHTPTV140_280_CVetoBVeto	FS	mc16a	39.87	0.6112	0.9751	23.76	4,369,473
364107	Sherpa_221_NNPDF30NNLO_Zmumu_MAXHTPTV140_280_CFilterBVeto	FS	mc16d	39.85	0.2353	0.9751	9.14	3,311,566
364107	Sherpa_221_NNPDF30NNLO_Zmumu_MAXHTPTV140_280_CFilterBVeto	FS	mc16e	39.85	0.2353	0.9751	9.14	4,404,437
364107	Sherpa_221_NNPDF30NNLO_Zmumu_MAXHTPTV140_280_CFilterBVeto	FS	mc16a	39.86	0.2336	0.9751	9.08	2,646,164
364108	Sherpa_221_NNPDF30NNLO_Zmumu_MAXHTPTV140_280_BFilter	FS	mc16d	39.88	0.1555	0.9751	6.05	14,011,026
364108	Sherpa_221_NNPDF30NNLO_Zmumu_MAXHTPTV140_280_BFilter	FS	mc16e	39.88	0.1555	0.9751	6.05	18,594,357
364108	Sherpa_221_NNPDF30NNLO_Zmumu_MAXHTPTV140_280_BFilter	FS	mc16a	39.89	0.1557	0.9751	6.06	11,157,922
364109	Sherpa_221_NNPDF30NNLO_Zmumu_MAXHTPTV280_500_CVetoBVeto	FS	mc16d	8.53	0.5602	0.9751	4.66	2,193,398
364109	Sherpa_221_NNPDF30NNLO_Zmumu_MAXHTPTV280_500_CVetoBVeto	FS	mc16e	8.53	0.5604	0.9751	4.66	2,960,446
364109	Sherpa_221_NNPDF30NNLO_Zmumu_MAXHTPTV280_500_CVetoBVeto	FS	mc16a	8.53	0.5602	0.9751	4.66	1,781,451
364110	Sherpa_221_NNPDF30NNLO_Zmumu_MAXHTPTV280_500_CFilterBVeto	FS	mc16d	8.52	0.2663	0.9751	2.21	1,118,128
364110	Sherpa_221_NNPDF30NNLO_Zmumu_MAXHTPTV280_500_CFilterBVeto	FS	mc16e	8.52	0.2663	0.9751	2.21	1,492,652
364110	Sherpa_221_NNPDF30NNLO_Zmumu_MAXHTPTV280_500_CFilterBVeto	FS	mc16a	8.53	0.2658	0.9751	2.21	893,654
364111	Sherpa_221_NNPDF30NNLO_Zmumu_MAXHTPTV280_500_BFilter	FS	mc16d	8.53	0.1767	0.9751	1.47	4,522,195
364111	Sherpa_221_NNPDF30NNLO_Zmumu_MAXHTPTV280_500_BFilter	FS	mc16e	8.53	0.1767	0.9751	1.47	5,992,059
364111	Sherpa_221_NNPDF30NNLO_Zmumu_MAXHTPTV280_500_BFilter	FS	mc16a	8.53	0.1746	0.9751	1.45	3,616,771
364112	Sherpa_221_NNPDF30NNLO_Zmumu_MAXHTPTV500_1000	FS	mc16d	1.79	1.0000	0.9751	1.74	3,419,348
364112	Sherpa_221_NNPDF30NNLO_Zmumu_MAXHTPTV500_1000	FS	mc16e	1.79	1.0000	0.9751	1.74	4,648,897
364112	Sherpa_221_NNPDF30NNLO_Zmumu_MAXHTPTV500_1000	FS	mc16a	1.79	1.0000	0.9751	1.74	2,732,759
364113	Sherpa_221_NNPDF30NNLO_Zmumu_MAXHTPTV1000_E_CMS	FS	mc16d	0.15	1.0000	0.9751	0.14	1,174,753
364113	Sherpa_221_NNPDF30NNLO_Zmumu_MAXHTPTV1000_E_CMS	FS	mc16e	0.15	1.0000	0.9751	0.14	1,566,503
364113	Sherpa_221_NNPDF30NNLO_Zmumu_MAXHTPTV1000_E_CMS	FS	mc16a	0.15	1.0000	0.9751	0.14	936,488
364128	Sherpa_221_NNPDF30NNLO_Ztautau_MAXHTPTV0_70_CVetoBVeto	FS	mc16d	1982.10	0.8213	0.9751	1587.33	1,017,014
364128	Sherpa_221_NNPDF30NNLO_Ztautau_MAXHTPTV0_70_CVetoBVeto	FS	mc16e	1982.10	0.8213	0.9751	1587.33	1,344,971
364128	Sherpa_221_NNPDF30NNLO_Ztautau_MAXHTPTV0_70_CVetoBVeto	FS	mc16a	1982.10	0.8213	0.9751	1587.33	782,423
364129	Sherpa_221_NNPDF30NNLO_Ztautau_MAXHTPTV0_70_CFilterBVeto	FS	mc16d	1981.70	0.1095	0.9751	211.67	691,925
364129	Sherpa_221_NNPDF30NNLO_Ztautau_MAXHTPTV0_70_CFilterBVeto	FS	mc16e	1981.70	0.1095	0.9751	211.67	930,495
364129	Sherpa_221_NNPDF30NNLO_Ztautau_MAXHTPTV0_70_CFilterBVeto	FS	mc16a	1981.70	0.1095	0.9751	211.67	543,372
364130	Sherpa_221_NNPDF30NNLO_Ztautau_MAXHTPTV0_70_BFilter	FS	mc16d	1981.90	0.0658	0.9751	127.07	1,228,194
364130	Sherpa_221_NNPDF30NNLO_Ztautau_MAXHTPTV0_70_BFilter	FS	mc16e	1981.90	0.0658	0.9751	127.07	1,622,409
364130	Sherpa_221_NNPDF30NNLO_Ztautau_MAXHTPTV0_70_BFilter	FS	mc16a	1981.90	0.0658	0.9751	127.07	954,222
364131	Sherpa_221_NNPDF30NNLO_Ztautau_MAXHTPTV70_140_CVetoBVeto	FS	mc16d	110.70	0.6926	0.9751	74.77	1,285,196
364131	Sherpa_221_NNPDF30NNLO_Ztautau_MAXHTPTV70_140_CVetoBVeto	FS	mc16e	110.70	0.6926	0.9751	74.77	1,705,834
364131	Sherpa_221_NNPDF30NNLO_Ztautau_MAXHTPTV70_140_CVetoBVeto	FS	mc16a	110.70	0.6926	0.9751	74.77	1,009,262
364132	Sherpa_221_NNPDF30NNLO_Ztautau_MAXHTPTV70_140_CFilterBVeto	FS	mc16d	110.46	0.1906	0.9751	20.53	440,219
364132	Sherpa_221_NNPDF30NNLO_Ztautau_MAXHTPTV70_140_CFilterBVeto	FS	mc16e	110.46	0.1906	0.9751	20.53	584,851
364132	Sherpa_221_NNPDF30NNLO_Ztautau_MAXHTPTV70_140_CFilterBVeto	FS	mc16a	110.46	0.1890	0.9751	20.36	345,662
364133	Sherpa_221_NNPDF30NNLO_Ztautau_MAXHTPTV70_140_BFilter	FS	mc16d	110.70	0.1183	0.9751	12.77	1,427,228
364133	Sherpa_221_NNPDF30NNLO_Ztautau_MAXHTPTV70_140_BFilter	FS	mc16e	110.70	0.1183	0.9751	12.77	1,897,428
364133	Sherpa_221_NNPDF30NNLO_Ztautau_MAXHTPTV70_140_BFilter	FS	mc16a	110.70	0.1183	0.9751	12.77	1,118,668
364134	Sherpa_221_NNPDF30NNLO_Ztautau_MAXHTPTV140_280_CVetoBVeto	FS	mc16d	40.76	0.6188	0.9751	24.59	1,398,483
364134	Sherpa_221_NNPDF30NNLO_Ztautau_MAXHTPTV140_280_CVetoBVeto	FS	mc16e	40.76	0.6188	0.9751	24.59	1,862,521
364134	Sherpa_221_NNPDF30NNLO_Ztautau_MAXHTPTV140_280_CVetoBVeto	FS	mc16a	40.76	0.6170	0.9751	24.52	1,098,513
364135	Sherpa_221_NNPDF30NNLO_Ztautau_MAXHTPTV140_280_CFilterBVeto	FS	mc16d	40.71	0.2343	0.9751	9.30	839,847
364135	Sherpa_221_NNPDF30NNLO_Ztautau_MAXHTPTV140_280_CFilterBVeto	FS	mc16e	40.71	0.2343	0.9751	9.30	1,115,942
364135	Sherpa_221_NNPDF30NNLO_Ztautau_MAXHTPTV140_280_CFilterBVeto	FS	mc16a	40.71	0.2343	0.9751	9.30	665,034
364136	Sherpa_221_NNPDF30NNLO_Ztautau_MAXHTPTV140_280_BFilter	FS	mc16d	40.74	0.1560	0.9751	6.20	1,510,717
364136	Sherpa_221_NNPDF30NNLO_Ztautau_MAXHTPTV140_280_BFilter	FS	mc16e	40.74	0.1560	0.9751	6.20	2,014,235
364136	Sherpa_221_NNPDF30NNLO_Ztautau_MAXHTPTV140_280_BFilter	FS	mc16a	40.74	0.1560	0.9751	6.20	1,202,662
364137	Sherpa_221_NNPDF30NNLO_Ztautau_MAXHTPTV280_500_CVetoBVeto	FS	mc16d	8.68	0.5638	0.9751	4.77	2,589,058
364137	Sherpa_221_NNPDF30NNLO_Ztautau_MAXHTPTV280_500_CVetoBVeto	FS	mc16e	8.68	0.5638	0.9751	4.77	3,415,053
364137	Sherpa_221_NNPDF30NNLO_Ztautau_MAXHTPTV280_500_CVetoBVeto	FS	mc16a	8.68	0.5638	0.9751	4.77	2,049,788
364138	Sherpa_221_NNPDF30NNLO_Ztautau_MAXHTPTV280_500_CFilterBVeto	FS	mc16d	8.67	0.2643	0.9751	2.24	317,411
364138	Sherpa_221_NNPDF30NNLO_Ztautau_MAXHTPTV280_500_CFilterBVeto	FS	mc16e	8.67	0.2643	0.9751	2.24	427,068
364138	Sherpa_221_NNPDF30NNLO_Ztautau_MAXHTPTV280_500_CFilterBVeto	FS	mc16a	8.67	0.2643	0.9751	2.24	253,964
364139	Sherpa_221_NNPDF30NNLO_Ztautau_MAXHTPTV280_500_BFilter	FS	mc16d	8.68	0.1762	0.9751	1.49	711,443
364139	Sherpa_221_NNPDF30NNLO_Ztautau_MAXHTPTV280_500_BFilter	FS	mc16e	8.68	0.1762	0.9751	1.49	945,093
364139	Sherpa_221_NNPDF30NNLO_Ztautau_MAXHTPTV280_500_BFilter	FS	mc16a	8.68	0.1762	0.9751	1.49	559,719
364140	Sherpa_221_NNPDF30NNLO_Ztautau_MAXHTPTV500_1000	FS	mc16d	1.81	1.0000	0.9751	1.76	1,094,790
364140	Sherpa_221_NNPDF30NNLO_Ztautau_MAXHTPTV500_1000	FS	mc16e	1.81	1.0000	0.9751	1.76	1,446,521
364140	Sherpa_221_NNPDF30NNLO_Ztautau_MAXHTPTV500_1000	FS	mc16a	1.81	1.0000	0.9751	1.76	868,245
364141	Sherpa_221_NNPDF30NNLO_Ztautau_MAXHTPTV1000_E_CMS	FS	mc16d	0.15	1.0000	0.9751	0.14	425,481
364141	Sherpa_221_NNPDF30NNLO_Ztautau_MAXHTPTV1000_E_CMS	FS	mc16e	0.15	1.0000	0.9751	0.14	565,548
364141	Sherpa_221_NNPDF30NNLO_Ztautau_MAXHTPTV1000_E_CMS	FS	mc16a	0.15	1.0000	0.9751	0.14	337,612

Table A.8.: Cross sections, filter efficiencies, k-factors and event numbers for the single-top Wt and s-channel samples. The POHWEG+PYTHIA samples are subdivided into events with top and antitop quarks.

DSID	Sample	Type	Campaign	σ [pb]	ϵ_{Filter}	k	σ_{tot} [pb]	Events
410644	PowhegPythia8EvtGen_A14_singletop_schan_lept_top	FS	mc16d	2.03	1.0000	1.0150	2.06	2,498,000
410644	PowhegPythia8EvtGen_A14_singletop_schan_lept_top	FS	mc16e	2.03	1.0000	1.0150	2.06	3,305,000
410644	PowhegPythia8EvtGen_A14_singletop_schan_lept_top	FS	mc16a	2.03	1.0000	1.0150	2.06	2,000,000
410645	PowhegPythia8EvtGen_A14_singletop_schan_lept_antitop	FS	mc16d	1.27	1.0000	1.0150	1.29	2,500,000
410645	PowhegPythia8EvtGen_A14_singletop_schan_lept_antitop	FS	mc16e	1.27	1.0000	1.0150	1.29	3,317,000
410645	PowhegPythia8EvtGen_A14_singletop_schan_lept_antitop	FS	mc16a	1.27	1.0000	1.0150	1.29	2,000,000
410646	PowhegPythia8EvtGen_A14_Wt_DR_inclusive_top	FS	mc16d	37.94	1.0000	0.9450	35.85	12,475,000
410646	PowhegPythia8EvtGen_A14_Wt_DR_inclusive_top	FS	mc16e	37.94	1.0000	0.9450	35.85	16,573,000
410646	PowhegPythia8EvtGen_A14_Wt_DR_inclusive_top	FS	mc16a	37.94	1.0000	0.9450	35.85	9,987,000
410647	PowhegPythia8EvtGen_A14_Wt_DR_inclusive_antitop	FS	mc16d	37.91	1.0000	0.9460	35.86	12,456,000
410647	PowhegPythia8EvtGen_A14_Wt_DR_inclusive_antitop	FS	mc16e	37.91	1.0000	0.9460	35.86	16,556,000
410647	PowhegPythia8EvtGen_A14_Wt_DR_inclusive_antitop	FS	mc16a	37.91	1.0000	0.9460	35.86	9,994,000
410658	PhPy8EG_A14_tchan_BW50_lept_top	FS	mc16d	36.99	1.0000	1.1910	44.06	31,170,000
410658	PhPy8EG_A14_tchan_BW50_lept_top	FS	mc16e	36.99	1.0000	1.1910	44.06	41,631,900
410658	PhPy8EG_A14_tchan_BW50_lept_top	FS	mc16a	36.99	1.0000	1.1910	44.06	24,755,500
410659	PhPy8EG_A14_tchan_BW50_lept_antitop	FS	mc16d	22.17	1.0000	1.1830	26.23	30,911,000
410659	PhPy8EG_A14_tchan_BW50_lept_antitop	FS	mc16e	22.17	1.0000	1.1830	26.23	41,414,850
410659	PhPy8EG_A14_tchan_BW50_lept_antitop	FS	mc16a	22.17	1.0000	1.1830	26.23	24,725,500
410654	PowhegPythia8EvtGen_A14_Wt_DS_inclusive_top	FS	mc16d	36.78	1.0000	0.9710	35.71	6,249,000
410654	PowhegPythia8EvtGen_A14_Wt_DS_inclusive_top	FS	mc16e	36.78	1.0000	0.9710	35.71	8,270,800
410654	PowhegPythia8EvtGen_A14_Wt_DS_inclusive_top	FS	mc16a	36.78	1.0000	0.9710	35.71	4,969,000
410655	PowhegPythia8EvtGen_A14_Wt_DS_inclusive_antitop	FS	mc16d	37.53	1.0000	0.9520	35.73	6,247,000
410655	PowhegPythia8EvtGen_A14_Wt_DS_inclusive_antitop	FS	mc16e	37.53	1.0000	0.9520	35.73	8,291,800
410655	PowhegPythia8EvtGen_A14_Wt_DS_inclusive_antitop	FS	mc16a	37.53	1.0000	0.9520	35.73	4,974,000
410644	PowhegPythia8EvtGen_A14_singletop_schan_lept_top	AF	mc16d	2.03	1.0000	1.0150	2.06	2,500,000
410644	PowhegPythia8EvtGen_A14_singletop_schan_lept_top	AF	mc16e	2.03	1.0000	1.0150	2.06	3,319,000
410644	PowhegPythia8EvtGen_A14_singletop_schan_lept_top	AF	mc16a	2.03	1.0000	1.0150	2.06	1,999,000
410645	PowhegPythia8EvtGen_A14_singletop_schan_lept_antitop	AF	mc16d	1.27	1.0000	1.0150	1.29	2,500,000
410645	PowhegPythia8EvtGen_A14_singletop_schan_lept_antitop	AF	mc16e	1.27	1.0000	1.0150	1.29	3,320,000
410645	PowhegPythia8EvtGen_A14_singletop_schan_lept_antitop	AF	mc16a	1.27	1.0000	1.0150	1.29	2,000,000
410646	PowhegPythia8EvtGen_A14_Wt_DR_inclusive_top	AF	mc16d	37.94	1.0000	0.9450	35.85	6,250,000
410646	PowhegPythia8EvtGen_A14_Wt_DR_inclusive_top	AF	mc16e	37.94	1.0000	0.9450	35.85	8,298,000
410646	PowhegPythia8EvtGen_A14_Wt_DR_inclusive_top	AF	mc16a	37.94	1.0000	0.9450	35.85	5,000,000
410647	PowhegPythia8EvtGen_A14_Wt_DR_inclusive_antitop	AF	mc16d	37.91	1.0000	0.9460	35.86	6,250,000
410647	PowhegPythia8EvtGen_A14_Wt_DR_inclusive_antitop	AF	mc16e	37.91	1.0000	0.9460	35.86	8,300,000
410647	PowhegPythia8EvtGen_A14_Wt_DR_inclusive_antitop	AF	mc16a	37.91	1.0000	0.9460	35.86	5,000,000
410658	PhPy8EG_A14_tchan_BW50_lept_top	AF	mc16d	36.99	1.0000	1.1910	44.06	6,235,000
410658	PhPy8EG_A14_tchan_BW50_lept_top	AF	mc16e	36.99	1.0000	1.1910	44.06	8,295,000
410658	PhPy8EG_A14_tchan_BW50_lept_top	AF	mc16a	36.99	1.0000	1.1910	44.06	4,980,000
410659	PhPy8EG_A14_tchan_BW50_lept_antitop	AF	mc16d	22.17	1.0000	1.1830	26.23	6,228,000
410659	PhPy8EG_A14_tchan_BW50_lept_antitop	AF	mc16e	22.17	1.0000	1.1830	26.23	8,292,000
410659	PhPy8EG_A14_tchan_BW50_lept_antitop	AF	mc16a	22.17	1.0000	1.1830	26.23	4,990,000
412002	aMcAtNloPythia8EvtGen_HThalfscale_tW_inclusive	AF	mc16d	73.83	1.0000	0.9711	71.70	12,410,000
412002	aMcAtNloPythia8EvtGen_HThalfscale_tW_inclusive	AF	mc16e	73.83	1.0000	0.9711	71.70	12,365,000
412002	aMcAtNloPythia8EvtGen_HThalfscale_tW_inclusive	AF	mc16a	73.83	1.0000	0.9711	71.70	9,960,000
412004	aMcAtNloPy8EG_tchan_NLO	AF	mc16d	64.33	1.0000	1.0950	70.44	12,484,000
412004	aMcAtNloPy8EG_tchan_NLO	AF	mc16e	64.33	1.0000	1.0950	70.44	16,532,000
412004	aMcAtNloPy8EG_tchan_NLO	AF	mc16a	64.33	1.0000	1.0950	70.44	9,989,000
412005	aMcAtNloPythia8EvtGen_A14_singletop_schan_lept	AF	mc16d	3.33	1.0000	1.0051	3.35	5,539,000
412005	aMcAtNloPythia8EvtGen_A14_singletop_schan_lept	AF	mc16e	3.33	1.0000	1.0051	3.35	9,191,000
412005	aMcAtNloPythia8EvtGen_A14_singletop_schan_lept	AF	mc16a	3.33	1.0000	1.0051	3.35	4,081,000

Table A.9.: Cross sections, filter efficiencies, k-factors and event numbers for the single-top t-channel samples. The POHWEG+PYTHIA samples are subdivided into events with top and antitop quarks.

DSID	Sample	Type	Campaign	σ [pb]	ϵ_{Filter}	k	σ_{tot} [pb]	Events
411032	PowhegHerwig7EvtGen_H7UE_704_tchan_lept_antitop	AF	mc16d	22.19	1.0000	1.1840	26.28	6,232,000
411032	PowhegHerwig7EvtGen_H7UE_704_tchan_lept_antitop	AF	mc16e	22.19	1.0000	1.1840	26.28	8,078,000
411032	PowhegHerwig7EvtGen_H7UE_704_tchan_lept_antitop	AF	mc16a	22.19	1.0000	1.1840	26.28	5,000,000
411033	PowhegHerwig7EvtGen_H7UE_704_tchan_lept_top	AF	mc16d	37.02	1.0000	1.1930	44.16	6,218,500
411033	PowhegHerwig7EvtGen_H7UE_704_tchan_lept_top	AF	mc16e	37.02	1.0000	1.1930	44.16	8,300,000
411033	PowhegHerwig7EvtGen_H7UE_704_tchan_lept_top	AF	mc16a	37.02	1.0000	1.1930	44.16	5,000,000
411034	PhHerwig7EG_H7UE_singletop_schan_lept_top	AF	mc16d	2.03	1.0000	1.0160	2.06	2,500,000
411034	PhHerwig7EG_H7UE_singletop_schan_lept_top	AF	mc16e	2.03	1.0000	1.0160	2.06	3,320,000
411034	PhHerwig7EG_H7UE_singletop_schan_lept_top	AF	mc16a	2.03	1.0000	1.0160	2.06	2,000,000
411035	PhHerwig7EG_H7UE_singletop_schan_lept_antitop	AF	mc16d	1.27	1.0000	1.0160	1.29	2,500,000
411035	PhHerwig7EG_H7UE_singletop_schan_lept_antitop	AF	mc16e	1.27	1.0000	1.0160	1.29	3,319,000
411035	PhHerwig7EG_H7UE_singletop_schan_lept_antitop	AF	mc16a	1.27	1.0000	1.0160	1.29	2,000,000
411036	PowhegHerwig7EvtGen_H7UE_Wt_DR_inclusive_top	AF	mc16d	37.96	1.0000	0.9448	35.86	6,250,000
411036	PowhegHerwig7EvtGen_H7UE_Wt_DR_inclusive_top	AF	mc16e	37.96	1.0000	0.9448	35.86	8,278,000
411036	PowhegHerwig7EvtGen_H7UE_Wt_DR_inclusive_top	AF	mc16a	37.96	1.0000	0.9448	35.86	5,000,000
411037	PowhegHerwig7EvtGen_H7UE_Wt_DR_inclusive_antitop	AF	mc16d	37.93	1.0000	0.9448	35.83	6,250,000
411037	PowhegHerwig7EvtGen_H7UE_Wt_DR_inclusive_antitop	AF	mc16e	37.93	1.0000	0.9448	35.83	8,299,000
411037	PowhegHerwig7EvtGen_H7UE_Wt_DR_inclusive_antitop	AF	mc16a	37.93	1.0000	0.9448	35.83	5,000,000

Table A.10.: Cross sections, filter efficiencies, k-factors and event numbers for the ttX samples.

DSID	Sample	Type	Campaign	σ [pb]	ϵ_{Filter}	k	σ_{tot} [pb]	Events
346343	PhPy8EG_A14NNPDF23_NNPDF30ME_ttH125_allhad	FS	mc16d	0.24	1.0000	1.0000	0.24	6,493,000
346343	PhPy8EG_A14NNPDF23_NNPDF30ME_ttH125_allhad	FS	mc16e	0.24	1.0000	1.0000	0.24	8,254,000
346343	PhPy8EG_A14NNPDF23_NNPDF30ME_ttH125_allhad	FS	mc16a	0.24	1.0000	1.0000	0.24	4,982,000
346344	PhPy8EG_A14NNPDF23_NNPDF30ME_ttH125_semilep	FS	mc16d	0.52	0.4384	1.0000	0.23	6,500,000
346344	PhPy8EG_A14NNPDF23_NNPDF30ME_ttH125_semilep	FS	mc16e	0.52	0.4384	1.0000	0.23	8,280,000
346344	PhPy8EG_A14NNPDF23_NNPDF30ME_ttH125_semilep	FS	mc16a	0.52	0.4384	1.0000	0.23	4,993,000
346345	PhPy8EG_A14NNPDF23_NNPDF30ME_ttH125_dilep	FS	mc16d	0.05	1.0000	1.0000	0.05	6,490,000
346345	PhPy8EG_A14NNPDF23_NNPDF30ME_ttH125_dilep	FS	mc16e	0.05	1.0000	1.0000	0.05	8,281,000
346345	PhPy8EG_A14NNPDF23_NNPDF30ME_ttH125_dilep	FS	mc16a	0.05	1.0000	1.0000	0.05	4,991,000
410155	aMcAtNloPythia8EvtGen_MEN30NLO_A14N23LO_ttW	FS	mc16d	0.55	1.0000	1.1000	0.60	7,497,000
410155	aMcAtNloPythia8EvtGen_MEN30NLO_A14N23LO_ttW	FS	mc16e	0.55	1.0000	1.1000	0.60	12,042,000
410155	aMcAtNloPythia8EvtGen_MEN30NLO_A14N23LO_ttW	FS	mc16a	0.55	1.0000	1.1000	0.60	7,497,000
410156	aMcAtNloPythia8EvtGen_MEN30NLO_A14N23LO_ttZnunu	FS	mc16d	0.15	1.0000	1.1100	0.17	1,500,000
410156	aMcAtNloPythia8EvtGen_MEN30NLO_A14N23LO_ttZnunu	FS	mc16e	0.15	1.0000	1.1100	0.17	2,001,000
410156	aMcAtNloPythia8EvtGen_MEN30NLO_A14N23LO_ttZnunu	FS	mc16a	0.16	1.0000	1.1100	0.17	1,500,000
410157	aMcAtNloPythia8EvtGen_MEN30NLO_A14N23LO_ttZqq	FS	mc16d	0.53	1.0000	1.1100	0.59	3,000,000
410157	aMcAtNloPythia8EvtGen_MEN30NLO_A14N23LO_ttZqq	FS	mc16e	0.53	1.0000	1.1100	0.59	3,587,000
410157	aMcAtNloPythia8EvtGen_MEN30NLO_A14N23LO_ttZqq	FS	mc16a	0.53	1.0000	1.1100	0.59	3,000,000
410218	aMcAtNloPythia8EvtGen_MEN30NLO_A14N23LO_ttee	FS	mc16d	0.04	1.0000	1.1200	0.04	1,337,000
410218	aMcAtNloPythia8EvtGen_MEN30NLO_A14N23LO_ttee	FS	mc16e	0.04	1.0000	1.1200	0.04	2,168,000
410218	aMcAtNloPythia8EvtGen_MEN30NLO_A14N23LO_ttee	FS	mc16a	0.04	1.0000	1.1200	0.04	1,410,000
410219	aMcAtNloPythia8EvtGen_MEN30NLO_A14N23LO_ttmumu	FS	mc16d	0.04	1.0000	1.1200	0.04	1,339,000
410219	aMcAtNloPythia8EvtGen_MEN30NLO_A14N23LO_ttmumu	FS	mc16e	0.04	1.0000	1.1200	0.04	2,173,000
410219	aMcAtNloPythia8EvtGen_MEN30NLO_A14N23LO_ttmumu	FS	mc16a	0.04	1.0000	1.1200	0.04	1,410,000
410220	aMcAtNloPythia8EvtGen_MEN30NLO_A14N23LO_tttautau	FS	mc16d	0.04	1.0000	1.1200	0.04	900,000
410220	aMcAtNloPythia8EvtGen_MEN30NLO_A14N23LO_tttautau	FS	mc16e	0.04	1.0000	1.1200	0.04	958,000
410220	aMcAtNloPythia8EvtGen_MEN30NLO_A14N23LO_tttautau	FS	mc16a	0.04	1.0000	1.1200	0.04	935,000

Table A.11.: Cross sections, filter efficiencies, k-factors and event numbers for the VV samples.

DSID	Sample	Type	Campaign	σ [pb]	ϵ_{Filter}	k	σ_{tot} [pb]	Events
363355	Sherpa_221_NNPDF30NNLO_ZqqZvv	FS	mc16d	15.56	0.2799	0.2798	1.22	107,211
363355	Sherpa_221_NNPDF30NNLO_ZqqZvv	FS	mc16e	15.56	0.2799	0.2798	1.22	175,412
363355	Sherpa_221_NNPDF30NNLO_ZqqZvv	FS	mc16a	15.56	0.2800	0.2798	1.22	82,768
363356	Sherpa_221_NNPDF30NNLO_ZqqZll	FS	mc16d	15.56	0.1416	0.1396	0.31	3,468,216
363356	Sherpa_221_NNPDF30NNLO_ZqqZll	FS	mc16e	15.57	0.1414	0.1396	0.31	5,744,150
363356	Sherpa_221_NNPDF30NNLO_ZqqZll	FS	mc16a	15.56	0.1416	0.1396	0.31	6,920,351
363357	Sherpa_221_NNPDF30NNLO_WqqZvv	FS	mc16d	6.80	1.0000	1.0000	6.80	86,129
363357	Sherpa_221_NNPDF30NNLO_WqqZvv	FS	mc16e	6.80	1.0000	1.0000	6.80	140,270
363357	Sherpa_221_NNPDF30NNLO_WqqZvv	FS	mc16a	6.80	1.0000	1.0000	6.80	58,972
363358	Sherpa_221_NNPDF30NNLO_WqqZll	FS	mc16d	3.43	1.0000	1.0000	3.43	16,951,525
363358	Sherpa_221_NNPDF30NNLO_WqqZll	FS	mc16e	3.43	1.0000	1.0000	3.43	5,642,855
363358	Sherpa_221_NNPDF30NNLO_WqqZll	FS	mc16a	3.43	1.0000	1.0000	3.43	3,397,388
363359	Sherpa_221_NNPDF30NNLO_WpqqWmlv	FS	mc16d	24.71	1.0000	1.0000	24.71	16,605,664
363359	Sherpa_221_NNPDF30NNLO_WpqqWmlv	FS	mc16e	24.70	1.0000	1.0000	24.70	5,533,983
363359	Sherpa_221_NNPDF30NNLO_WpqqWmlv	FS	mc16a	24.71	1.0000	1.0000	24.71	3,326,177
363360	Sherpa_221_NNPDF30NNLO_WplvWmqq	FS	mc16d	24.72	1.0000	1.0000	24.72	6,613,136
363360	Sherpa_221_NNPDF30NNLO_WplvWmqq	FS	mc16e	24.72	1.0000	1.0000	24.72	5,490,378
363360	Sherpa_221_NNPDF30NNLO_WplvWmqq	FS	mc16a	24.72	1.0000	1.0000	24.72	3,298,446
363489	Sherpa_221_NNPDF30NNLO_WlvZqq	FS	mc16d	11.42	1.0000	1.0000	11.42	16,765,285
363489	Sherpa_221_NNPDF30NNLO_WlvZqq	FS	mc16e	11.42	1.0000	1.0000	11.42	5,574,774
363489	Sherpa_221_NNPDF30NNLO_WlvZqq	FS	mc16a	11.42	1.0000	1.0000	11.42	3,342,337
364250	Sherpa_222_NNPDF30NNLO_llll	FS	mc16d	1.25	1.0000	1.0000	1.25	19,788,881
364250	Sherpa_222_NNPDF30NNLO_llll	FS	mc16e	1.25	1.0000	1.0000	1.25	14,110,846
364250	Sherpa_222_NNPDF30NNLO_llll	FS	mc16a	1.25	1.0000	1.0000	1.25	9,793,164
364253	Sherpa_222_NNPDF30NNLO_lllv	FS	mc16d	4.57	1.0000	1.0000	4.57	19,514,661
364253	Sherpa_222_NNPDF30NNLO_lllv	FS	mc16e	4.57	1.0000	1.0000	4.57	16,269,844
364253	Sherpa_222_NNPDF30NNLO_lllv	FS	mc16a	4.57	1.0000	1.0000	4.57	9,431,765
364254	Sherpa_222_NNPDF30NNLO_llvv	FS	mc16d	12.50	1.0000	1.0000	12.50	21,607,019
364254	Sherpa_222_NNPDF30NNLO_llvv	FS	mc16e	12.50	1.0000	1.0000	12.50	17,931,874
364254	Sherpa_222_NNPDF30NNLO_llvv	FS	mc16a	12.50	1.0000	1.0000	12.50	10,808,079
364255	Sherpa_222_NNPDF30NNLO_lvvv	FS	mc16d	3.23	1.0000	1.0000	3.23	5,982,610
364255	Sherpa_222_NNPDF30NNLO_lvvv	FS	mc16e	3.23	1.0000	1.0000	3.23	4,958,682
364255	Sherpa_222_NNPDF30NNLO_lvvv	FS	mc16a	3.23	1.0000	1.0000	3.23	2,985,330

Table A.12.: Cross sections, filter efficiencies, k-factors and event numbers for the $t\bar{t}j$ samples.

DSID	Sample	Type	Campaign	σ [pb]	ϵ_{Filter}	k	σ_{tot} [pb]	Events
500336	aMCPy8EG_ttj_SM_madspin	TRUTH	-	26.61	0.4307	1.0000	11.46	299,930,000
500337	aMCPy8EG_ttj_SM	TRUTH	-	26.62	0.4379	1.0000	11.66	49,992,000
500934	MGPy8EG_ttj_SMEFTSM	TRUTH	-	28.77	0.4377	1.0000	12.59	29,910,000
500935	MGPy8EG_ttj_SMEFTint_cQq11	TRUTH	-	-0.17	0.4378	1.0000	-0.08	29,960,000
500936	MGPy8EG_ttj_SMEFTint_cQq81	TRUTH	-	0.92	0.4378	1.0000	0.40	29,920,000
500937	MGPy8EG_ttj_SMEFTint_ctq1	TRUTH	-	0.17	0.4380	1.0000	0.08	29,850,000
500938	MGPy8EG_ttj_SMEFTint_ctq8	TRUTH	-	0.65	0.4378	1.0000	0.28	29,940,000
500939	MGPy8EG_ttj_SMEFTint_ctu8	TRUTH	-	0.32	0.4377	1.0000	0.14	29,980,000
500940	MGPy8EG_ttj_SMEFTint_ctu1	TRUTH	-	-0.11	0.4377	1.0000	-0.05	29,920,000
500941	MGPy8EG_ttj_SMEFTsq_cQq11cQq11	TRUTH	-	4.60	0.4377	1.0000	2.01	29,930,000
500942	MGPy8EG_ttj_SMEFTsq_cQq11cQq81	TRUTH	-	5.61	0.4378	1.0000	2.46	29,930,000
500943	MGPy8EG_ttj_SMEFTsq_cQq11ctq1	TRUTH	-	9.31	0.4376	1.0000	4.07	29,930,000
500944	MGPy8EG_ttj_SMEFTsq_cQq11ctq8	TRUTH	-	5.48	0.4378	1.0000	2.40	29,850,000
500945	MGPy8EG_ttj_SMEFTsq_cQq11ctu8	TRUTH	-	5.11	0.4378	1.0000	2.24	29,780,000
500946	MGPy8EG_ttj_SMEFTsq_cQq11ctu1	TRUTH	-	7.71	0.4378	1.0000	3.38	29,840,000
500947	MGPy8EG_ttj_SMEFTsq_cQq81cQq81	TRUTH	-	1.34	0.4377	1.0000	0.59	29,920,000
500948	MGPy8EG_ttj_SMEFTsq_cQq81ctq1	TRUTH	-	5.92	0.4377	1.0000	2.59	29,920,000
500949	MGPy8EG_ttj_SMEFTsq_cQq81ctq8	TRUTH	-	2.29	0.4377	1.0000	1.00	29,930,000
500950	MGPy8EG_ttj_SMEFTsq_cQq81ctu8	TRUTH	-	1.89	0.4377	1.0000	0.83	29,840,000
500951	MGPy8EG_ttj_SMEFTsq_cQq81ctu1	TRUTH	-	4.45	0.4377	1.0000	1.95	29,980,000
500952	MGPy8EG_ttj_SMEFTsq_ctq1ctq1	TRUTH	-	4.58	0.4377	1.0000	2.00	29,810,000
500953	MGPy8EG_ttj_SMEFTsq_ctq1ctq8	TRUTH	-	5.79	0.4378	1.0000	2.54	29,970,000
500954	MGPy8EG_ttj_SMEFTsq_ctq1ctu8	TRUTH	-	5.08	0.4378	1.0000	2.23	29,720,000
500955	MGPy8EG_ttj_SMEFTsq_ctq1ctu1	TRUTH	-	7.69	0.4376	1.0000	3.36	29,800,000
500956	MGPy8EG_ttj_SMEFTsq_ctq8ctq8	TRUTH	-	0.88	0.4377	1.0000	0.39	29,880,000
500957	MGPy8EG_ttj_SMEFTsq_ctq8ctu8	TRUTH	-	1.39	0.4378	1.0000	0.61	29,870,000
500958	MGPy8EG_ttj_SMEFTsq_ctq8ctu1	TRUTH	-	3.99	0.4376	1.0000	1.75	29,870,000
500959	MGPy8EG_ttj_SMEFTsq_ctu8ctu8	TRUTH	-	0.50	0.4377	1.0000	0.22	29,890,000
500960	MGPy8EG_ttj_SMEFTsq_ctu1ctu8	TRUTH	-	3.38	0.4376	1.0000	1.48	29,960,000
500961	MGPy8EG_ttj_SMEFTsq_ctu1ctu1	TRUTH	-	3.11	0.4377	1.0000	1.36	29,870,000
500934	MGPy8EG_ttj_SMEFTSM	AF	mc16a	28.77	0.4377	1.0000	12.59	20,000,000
500935	MGPy8EG_ttj_SMEFTint_cQq11	AF	mc16a	0.00	1.0000	1.0000	0.00	3,000,000
500937	MGPy8EG_ttj_SMEFTint_ctq1	AF	mc16a	0.17	0.4380	1.0000	0.08	3,000,000
500941	MGPy8EG_ttj_SMEFTsq_cQq11cQq11	AF	mc16a	4.60	0.4377	1.0000	2.01	3,000,000
500943	MGPy8EG_ttj_SMEFTsq_cQq11ctq1	AF	mc16a	9.31	0.4376	1.0000	4.07	3,000,000
500952	MGPy8EG_ttj_SMEFTsq_ctq1ctq1	AF	mc16a	4.58	0.4377	1.0000	2.00	2,984,000

B. Further studies

B.1. NNLO reweighting

The agreement between data and prediction was found to improve by considering calculations at NNLO instead of NLO in QCD [330]; thus the $t\bar{t}$ modelling is expected to improve after reweighting the $t\bar{t}$ samples simulated at NLO to match their kinematic distributions to that predicted in calculations at NNLO accuracy.

The NNLO reweighting was performed using an iterative reweighting procedure [331, 332] based on NNLO-QCD+NLO-EW predictions of the transverse momenta of the top and antitop quarks, $p_T(t)$ and $p_T(\bar{t})$, as well as the mass $m_{t\bar{t}}$ and transverse momentum $p_T(t\bar{t})$ of the top-antitop-quark system taken from [333]. Both the prediction and simulation were obtained at the parton level after parton shower defined in section 3.3.

In the first step, the ratio between the $p_T(t\bar{t})$ distributions from the prediction and the MC simulation is taken and assigned as a scale factor to each simulated MC event. Starting from the reweighted MC sample, the $m_{t\bar{t}}$ distribution is reweighted in the same way. In the last step, the geometric average of the weights obtained for the $p_T(t)$ and $p_T(\bar{t})$ is used to reweight the MC sample once more. These three steps are repeated three times to reduce the residual difference between the MC simulation and the prediction below NNLO uncertainty for all four variables. The resulting set of weights, depending on the MC generator and the kinematic variables $p_T(t)$, $p_T(\bar{t})$, $p_T(t\bar{t})$ and $m_{t\bar{t}}$, were then applied to the $t\bar{t}$ events in this analysis.

Figure B.1 shows a comparison of data to the pre-marginalisation predictions for the ΔE vs. θ_j distribution used in the unfolding at NLO and at NNLO in $t\bar{t}$ production. Taking NNLO corrections into account, the data/prediction agreement improves; normalisation discrepancy reduces from about 10% to less than 5%, while the shape remains similar. Given that the $t\bar{t}$ normalisation does not affect the energy asymmetry measurement and that the reweighting procedure is still in an early stage of development, it was not applied to this analysis.

B.2. W+jets modeling

The W+jets background constitutes the largest background contribution of about 5% as shown in table 9.16 and discussed in section 9.4.1. The W+jets modeling is checked in a control region close to the signal region enriched with W+jets events. In this control region, events with top-tagged large-R jets are vetoed, and the highest-p_T large-R jet is considered as the hadronically decaying top-quark candidate. The events are further required to have exactly one b-tagged small-R jet. Figure B.2 shows a comparison of data to the pre-marginalisation ΔE vs. θ_j distribution in this control region. The purity of $t\bar{t}$ events decreases to 34% compared to 87% in the signal region, and the fraction of W+jets events increases from 5% to 44%. The number of $t\bar{t}$ events passing both the particle- and detector-level events (fiducial $t\bar{t}$ signal) is below 0.2% and not

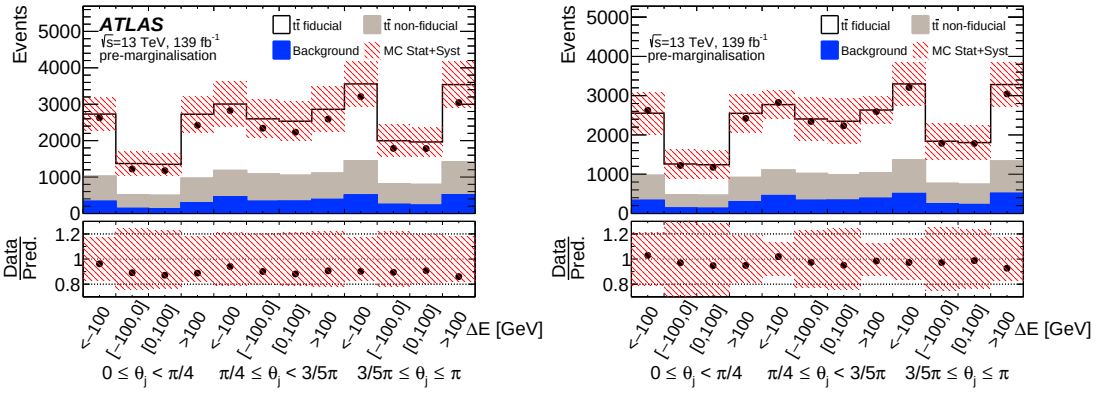

(a) NLO (b) NNLO

Figure B.1.: Comparison of ATLAS data (black markers) to the pre-marginalisation distribution for the ΔE vs. θ_j observable used in the unfolding at NLO [83] (left) and at NNLO (right) in $t\bar{t}$ production. The event numbers correspond to the optimised cross section as defined in eq. 2.39.

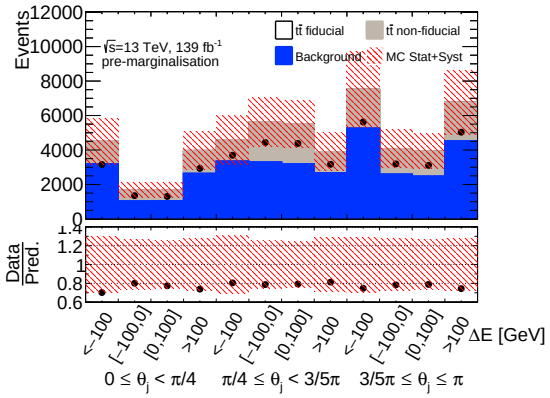

Figure B.2.: Comparison of ATLAS data (black dots) to the pre-marginalisation ΔE vs. θ_j distribution in the W+jets enriched control region. A goodness-of-fit test provides a reduced χ^2 value of 0.61, corresponding to a p-value of 0.83. All observed discrepancies are thus well covered by the systematic uncertainties.

visible in the figure. The data is just covered within the systematic uncertainties in all bins, a goodness-of-fit test performed as described in section 9.1.1, taking into account all systematic uncertainties and their correlation structure between the bins, yields a reduced χ^2 value of 0.61, corresponding to a p-value of 0.83. The W+jets background is thus considered to modelled well enough for this analysis, with all discrepancies to data being covered by its systematic uncertainties.

C. SMEFT figures

Figures C.1, C.2 and C.3 show the χ^2 values obtained from eq. 10.15 for the inclusive energy and rapidity asymmetries and the differential energy asymmetry, respectively, in dependence of the Wilson coefficients in one-parameter fits. The 68% and 95% confidence bounds of the coefficients are given by the intersections of the χ^2 curves with the $\chi^2_{\text{min}} + 1$ and $\chi^2_{\text{min}} + 4$ lines, respectively, as described in section 10.2.

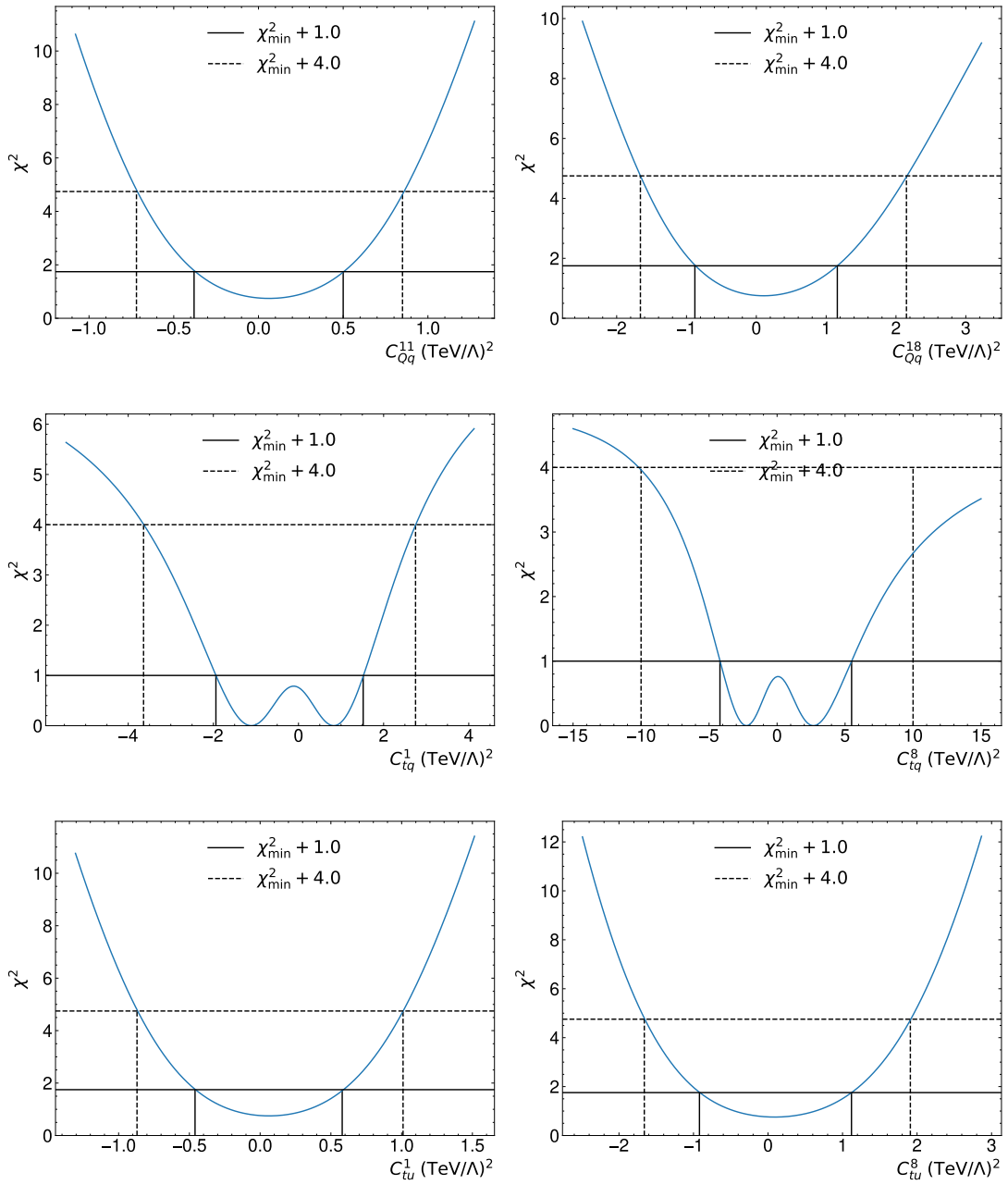

Figure C.1.: χ^2 values vs. Wilson coefficients of the one-parameter χ^2 fits of the inclusive energy asymmetry. Solid and dashed lines indicate the χ^2 values and associated Wilson coefficient values corresponding to the 68% and 95% confidence limits, respectively.

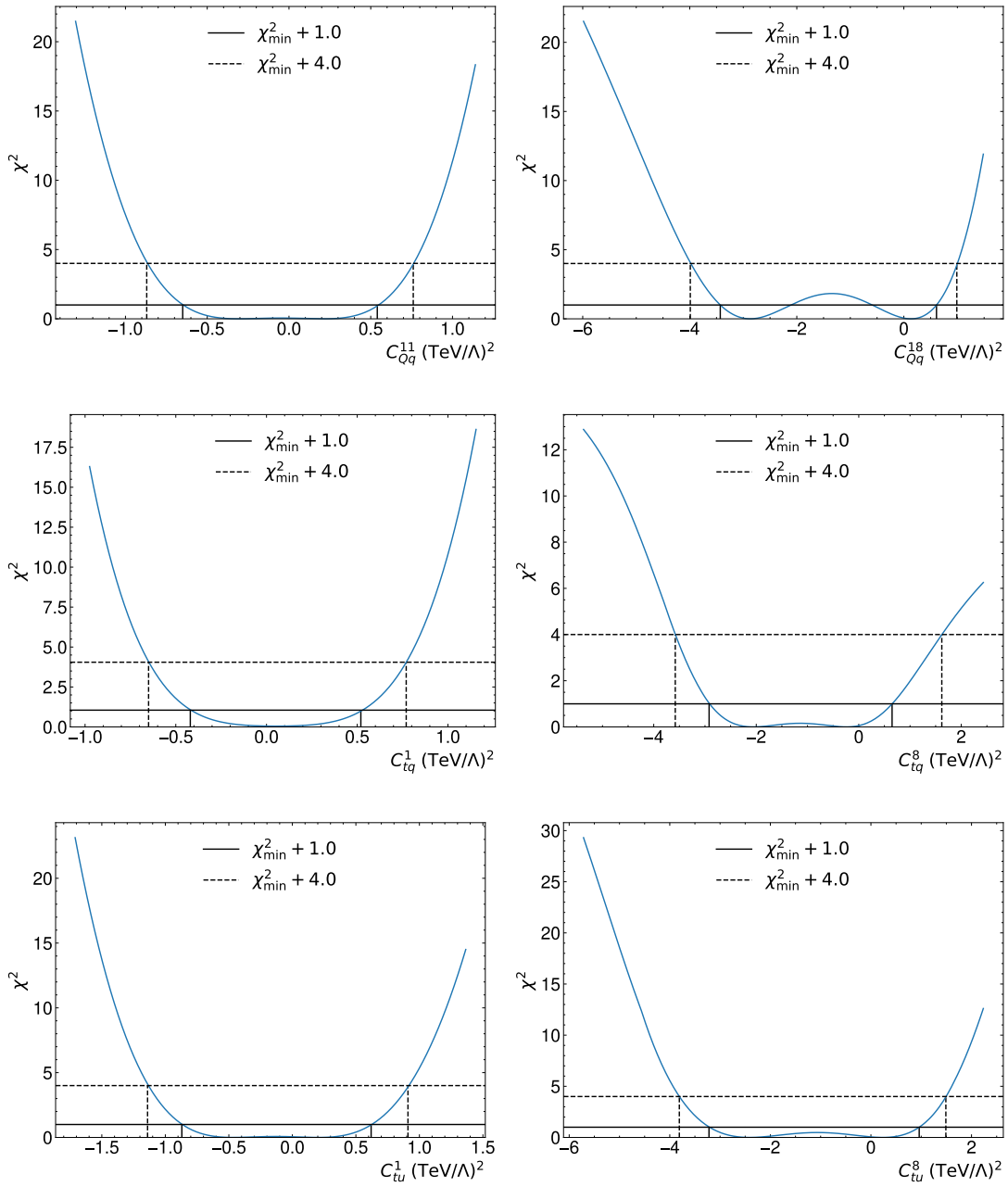

Figure C.2.: χ^2 values vs. Wilson coefficients of the one-parameter χ^2 fits of the inclusive rapidity asymmetry measured in reference [66]. Solid and dashed lines indicate the χ^2 values and associated Wilson coefficient values corresponding to the 68% and 95% confidence limits, respectively.

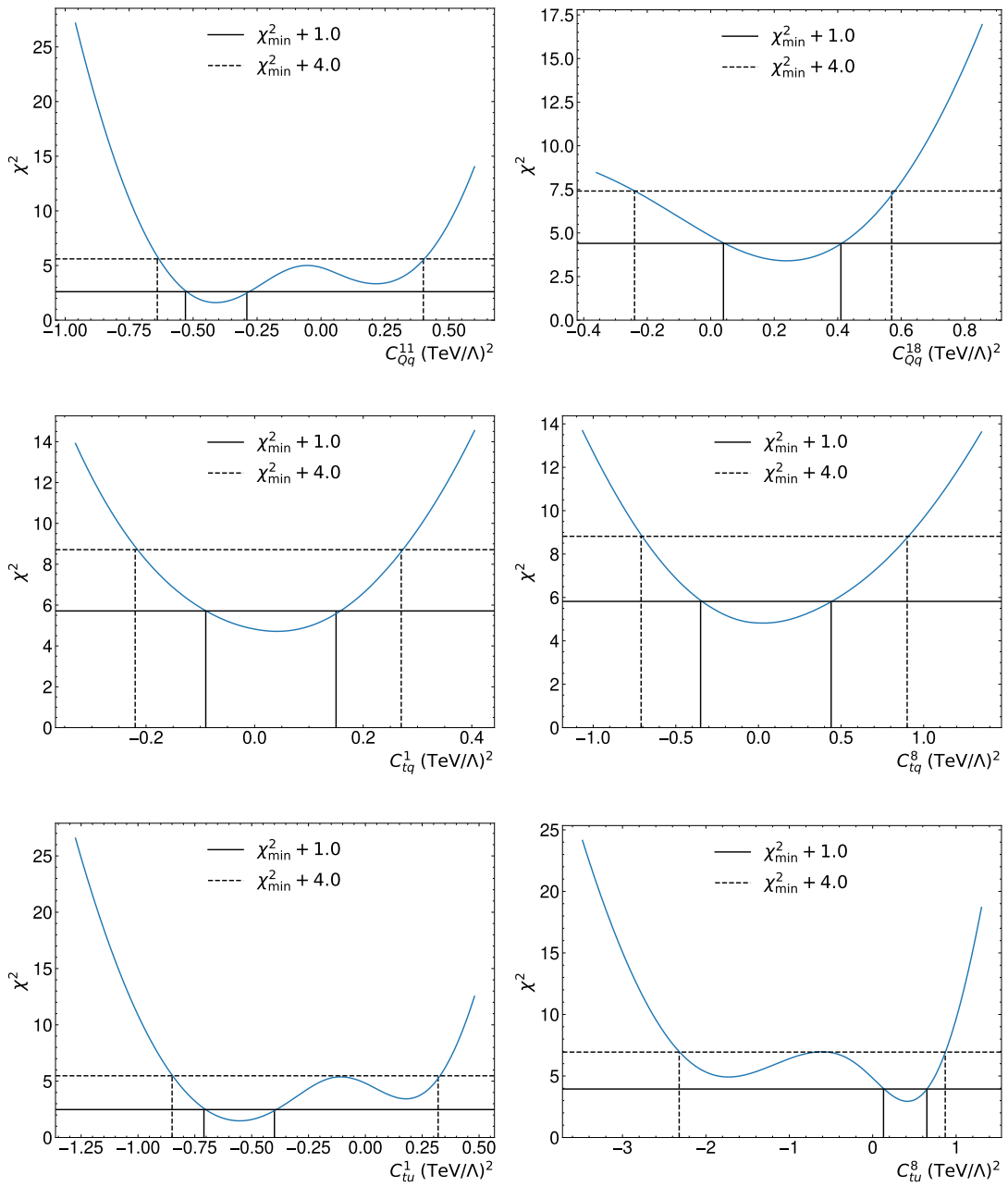

Figure C.3.: χ^2 values vs. Wilson coefficients of the one-parameter χ^2 fits of the rapidity asymmetry differential in $m_{t\bar{t}}$ measured in reference [66]. Solid and dashed lines indicate the χ^2 values and associated Wilson coefficient values corresponding to the 68% and 95% confidence limits, respectively.

Acknowledgements

Personal data has been removed from the electronic version for privacy reasons.

List of Figures

List of Tables

Bibliography

[1] J. Jeans, Physics and Philosophy, Cambridge University Press (1942).

[2] L.G. Marciano, Die Vorsokratiker 1–3, De Gruyter (2011–2013).

[3] D. Mendelejeff, Ueber die Beziehungen der Eigenschaften von Atomgewichten der Elemente, Zeitschrift für Chemie 12 (1869) 405.

[4] J.J. Thomson, Cathode rays, Phil. Mag. 44 (1897) 293.

[5] E. Rutherford, The scattering α and β particles by matter and the structure of the atom, Phil. Mag. 21 (1911) 669.

[6] E. Rutherford, Collision of α particles with light atoms. An anomalous Effect in Nitrogen, Philos. Mag. 37 (1919) 581.

[7] J. Chadwick, Possible Existence of a Neutron, Nature 129 (1932) 312.

[8] W. Heisenberg, Über den Bau der Atomkerne, Z. Physik 77 (1932) 1.

[9] P.A.M. Dirac, The quantum theory of the electron, Proc. of the Royal Society A 117 (1928).

[10] C.D. Anderson, The Positive Electron, Phys. Rev. 43 (1933) 491.

[11] H. Yukawa, On the Interaction of Elementary Particles, Proc. Phys. Math. Soc. Jap. 17 (1935) 48.

[12] C.M.G. Lattes et al., Processes Involving Charged Mesons, Nature 159 (1947) 694.

[13] W. Pauli, Offener Brief an die Gruppe der Radioaktiven bei der Gauverein-Tagung zu Tübingen, Pauli Letter Collection 259 (1930).

[14] F. Reines and C.L. Cowan, Detection of the Free Neutrino, Phys. Rev. 92 (1953) 830.

[15] M. Gell-Mann, The Eightfold Way: A Theory of strong interaction symmetry, California Institute of Technoloy Synchrotron Laboratory Report CTSL-20 (1961).

[16] M. Gell-Mann, A schematic model of baryons and mesons, Phys. Lett. 8 (1964) 214.

[17] O.W. Greenberg, Spin and Unitary-Spin Independence in a Paraquark Model of Baryons and Mesons, Phys. Rev. Lett. 13 (1964) 598.

[18] M. Breidenbach et al., Observed Behavior of Highly Inelastic Electron-Proton scattering, Phys. Rev. Lett. 23 (1969) 935.

[19] E.D. Bloom et al., High-Energy Inelastic *e-p* Scattering at 6° and 10°, Phys. Rev. Lett. 23 (1969) 930.

[20] J.D. Bjorken and E.A. Paschos, Inelastic Electron-Proton and γ-Proton Scattering and the Structure of the Nucleon, Phys. Rev. 185 (1969) 1975.

[21] R. Brandelik et al., Evidence for planar events in e^+e^- annihilation at high energies, Phys. Lett. B 86 (1979) 243.

[22] D.P. Barber et al., Discovery of Three-Jet Events and a Test of Quantum Chromodynamics at PETRA, Phys. Rev. Lett. 43 (1979) 830.

[23] PLUTO Collaboration, Evidence for gluon bremsstrahlung in e^+e^- annihilations at high energies, Phys. Lett. B 86 (1979) 418.

[24] JADE Collaboration, Observation of planer three-jet events in e^+e^- annihilation and evidence for gluon bremsstrahlung, Phys. Lett. B 91 (1980) 142.

[25] S.L. Glashow, The renormalizability of vector meson interactions, Nuclear Physics 10 (1959) 107.

[26] A. Salam and J.C. Ward, Weak and electromagnetic interactions, Il Nuvo Cimento 11 (1959) 568.

[27] S. Weinberg, A Model of Leptons, Phys. Rev. Lett. 19 (1967) 1264 .

[28] UA1 Collaboration, Experimental observation of isolated large transverse energy electrons with associated missing energy at $\sqrt{s} = 540\,\text{GeV}$, Phys. Lett. B 122 (1983) 103.

[29] UA2 Collaboration, Observation of single isolated electrons of high transverse momentum in events with missing transverse energy at the CERN *pp* collider, Phys. Lett. B 122 (1983) 476.

[30] UA1 Collaboration, Experimental observation of lepton pairs of invariant mass around 95 GeV/c^2 at the CERN SPS collider, Phys. Lett. B 126 (1983) 398.

[31] UA2 Collaboration, Evidence for $Z^0 \to e^+e^-$ at the CERN *pp* collider, Phys. Lett. B 129 (1983) 130.

[32] P.W. Higgs, Broken Symmetries and the Masses of Gauge Bosons, Phys. Rev. Lett. 13 (1964) 508.

[33] F. Englert and R. Brout, Broken Symmetry and the Mass of Gauge Vector Mesons, Phys. Rev. Lett. 13 (1964) 321.

[34] ATLAS Collaboration, Observation of a new particle in the search for the Standard Model Higgs boson with the ATLAS detector at the LHC, Phys.Lett. B716 (2012) 1-29, arXiv:1207.7214 [hep-ex].

[35] CMS Collaboration, Observation of a new boson at a mass of 125 GeV with the CMS experiment at the LHC, Phys. Lett. B 716 (2012) 30-61, arXiv:1207.7235 [hep-ex].

[36] R.L. Workman et al. (Particle Data Group), Review of Particle Physics, Prog. Theor. Exp. Phys 2022 (2022) 083C01.

[37] P. Ramond, Dual Theory for Free Fermions, Phys. Rev. D 3 (1971) 2415.

[38] J. Wess and B. Zumino, Supergauge transformations in four dimensions, Nucl. Phys. B 70 (1974) 39.

[39] S.P. Martin, A Supersymmetry primer, Adv. Ser. Direct. High Energy Phys. 18 (1998) 1, Adv. Ser. Direct. High Energy Phys. 21 (2010) 1, arXiv:hep-ph/9709356.

[40] G. Veneziano, Construction of a crossing-simmetric, Regge-behaved amplitude for linearly rising trajectories, Nuovo Cimento A 57 (1968) 190.

[41] M. Green, J. Schwarz, E. Witten, Superstring Theory, Cambridge University Press (1987).

[42] J. Polchinski, String Theory: An Introduction to the Bosonic String, Cambridge University Press (2005).

[43] CDF Collaboration, Observation of Top Quark Production in $\bar{p}p$ Collisions with the Collider Detector at Fermilab, Phys. Rev. Lett. 74 (1995) 2626.

[44] ATLAS Collaboration, Measurement of the top quark mass in the $t\bar{t} \to$ lepton+jets channel from $\sqrt{s} = 8\,\text{TeV}$ ATLAS data and combination with previous results, Eur. Phys. J. C 79 (2019) 290, arXiv:1810.01772 [hep-ex].

[45] C. Degrande et al., Non-resonant New Physics in Top Pair Production at Hadron Colliders, JHEP 1103 (2011) 125, arXiv:1010.6304 [hep-ph].

[46] A. Buckley et al., A global fit of top quark effective theory to data, Phys. Rev. D 92 (2015) 091501, arXiv:1506.08845 [hep-ph].

[47] A. Buckley et al., Constraining top quark effective theory in the LHC Run II era, JHEP 04 (2016) 015, arXiv:1512.03360 [hep-ph].

[48] O.B. Bylund, F. Maltoni, I. Tsinikos, E. Vryonidou and C. Zhang, Probing top quark neutral couplings in the Standard Model Effective Field Theory at NLO QCD, JHEP 05 (2016) 052, arXiv:1601.08193 [hep-ph].

[49] M. Schulze and Y. Soreq, Pinning down electroweak dipole operators of the top quark, Eur. Phys. J. C 76 (2016) 466, arXiv:1603.08911 [hep-ph].

[50] C. Englert, L. Moore, K. Nordström and M. Russell, Giving top quark effective operators a boost, Phys. Lett. B 763 (2016) 9, arXiv:1607.04304 [hep-ph].

[51] C. Englert, M. Russell and C.D. White, Effective Field Theory in the top sector: do multijets help?, Phys. Rev. D 99 (2019) 035019, arXiv:1809.09744 [hep-ph].

[52] N.P. Hartland et al., A Monte Carlo global analysis of the Standard Model Effective Field Theory: the top quark sector, JHEP 04 (2019) 100, arXiv:1901.05965 [hep-ph].

[53] I. Brivio et al., O new physics, where art thou? A global search in the top sector, JHEP 02 (2020) 131, arXiv:1910.03606 [hep-ph].

[54] P. Ferrario and G. Rodrigo, Massive color-octect bosons and the charge asymmetries of top quarks at hadron colliders, Phys. Rev. D 78 (2008) 094018, arXiv:0809.3354 [hep-ph].

[55] A. Djouadi et al., Forward-backward asymmetry of top quark production at the Tevatron in warped extra dimensional models, Phys. Rev. D 82 (2010) 071702(R), arXiv:0906.0604 [hep-ph].

[56] I. Dorsner et al., Light colored scalars from grand unification and the forward-backward asymmetry in $t\bar{t}$ production, Phys. Rev. D 81 (2010) 055009, arXiv:0912.0972 [hep-ph].

[57] P.H. Frampton, J. Shu,and K. Wang, Axigluon as possible explanation for $p\bar{p} \to t\bar{t}$ forward-backward asymmetry, Phys. Lett. B 683 (2010) 294, arXiv:0911.2955 [hep-ph].

[58] J.H. Kühn and G. Rodrigo, Charge asymmetry of heavy quarks at hadron colliders, Phys. Rev. D 59 (1999) 054017, arXiv:hep-ph/9807420.

[59] CDF Collaboration, Measurement of the top quark forward-backward production asymmetry and its dependence on event kinematic properties, Phys. Rev. D 87 (2013) 092002, arXiv:1211.1003 [hep-ex].

[60] D0 Collaboration, Forward-backward asymmetry in top quark-antiquark production, Phys. Rev. D 84 (2011) 112005, arXiv:1107.4995 [hep-ex].

[61] ATLAS Collaboration, Measurement of the charge asymmetry in top-quark pair production in the lepton-plus-jets final state in pp collision data at $\sqrt{s} = 8\,\text{TeV}$ with the ATLAS detector, Eur. Phys. J. C 76 (2016) 87, arXiv:1509.02358 [hep-ex], Erratum: Eur. Phys. J. C 77 (2017) 564.

[62] ATLAS Collaboration, Measurement of the charge asymmetry in highly boosted top-quark pair production in $\sqrt{s} = 8$ TeV pp collision data collected by the ATLAS experiment, Phys. Lett. B 756 (2016) 52-71, arXiv:1512.06092 [hep-ex].

[63] ATLAS Collaboration, Measurements of the charge asymmetry in top-quark pair production in the dilepton final state at $\sqrt{s} = 8$ TeV with the ATLAS detector, Phys. Rev. D 94 (2016) 032006, arXiv:1604.05538 [hep-ex].

[64] ATLAS and CMS Collaborations, Combination of inclusive and differential $t\bar{t}$ charge asymmetry measurements using ATLAS and CMS data at $\sqrt{s} = 7\,\text{TeV}$ and 8 TeV, JHEP 04 (2018) 033, arXiv:1709.05327 [hep-ex].

[65] ATLAS Collaboration, Inclusive and differential measurement of the charge asymmetry in $t\bar{t}$ events at 13 TeV with the ATLAS detector, ATLAS-CONF-2019-026 (2019).

[66] ATLAS Collaboration, Evidence for the charge asymmetry in $pp \to t\bar{t}$ production at $\sqrt{s} = 13$ TeV with the ATLAS detector, CERN preprint ID: CERN-EP-2022-166 (2022), arXiv:2208.12095 [hep-ex].

[67] CMS Collaboration, Inclusive and differential measurements of the $t\bar{t}$ charge asymmetry in pp collisions at $\sqrt{s} = 8$TeV, Phys. Lett. B 757 (2016) 154, arXiv:1507.03119 [hep-ex].

[68] CMS Collaboration, Measurements of $t\bar{t}$ charge asymmetry using dilepton final states in pp collisions at $\sqrt{s} = 8$TeV, Phys. Lett. B 760 (2016) 365, arXiv:1603.06221v2 [hep-ex] .

[69] M.T. Bowen, S.D. Ellis and D. Rainwater, Standard Model Top Quark Asymmetry at the Fermilab Tevatron, Phys. Rev. D 73 (2006) 014008, arXiv:hep-ph/0509267.

[70] S. Dittmaier, P. Uwer and S. Weinzierl, Next-to-Leading Order QCD Corrections to $t\bar{t}$ Production at Hadron Colliders, Phys. Rev. Lett. 98 (2007) 262002, arXivhep-ph/0703120.

[71] S. Dittmaier, P. Uwer and S. Weinzierl, Hadronic top-quark pair production in association with a hard jet at next-to-leading order QCD: Phenomenological studies for the Tevatron and the LHC, Eur. Phys. J. C 59 (2009) 625, arXiv:0810.0452 [hep-ph].

[72] K. Melnikov and M. Schulze, NNLO QCD corrections to top quark pair production in association with one hard jet at hadron colliders, Nucl. Phys. B 840 (2010) 129, arXiv:1004.3284 [hep-ph].

[73] S. Berge and S. Westhoff, Top-Quark Charge Asymmetry Goes Forward: Two New Observables for Hadron Colliders, JHEP 07 (2013) 179, arXiv:1305.3272 [hep-ph].

[74] S. Berge and S. Westhoff, Observing the Top Energy Asymmetry at the LHC, Phys. Rev. D 95 (2017) 014035, arXiv:1608.00574 [hep-ph].

[75] A. Basan et al., Measuring the top energy asymmetry at the LHC: QCD and SMEFT interpretations, JHEP 03 (2020) 184, arXiv:2001.07225 [hep-ph].

[76] S. Berge and S. Westhoff, Top-Quark Charge Asymmetry with a Jet Handle, Phys. Rev. D 86 (2012) 094036, arXiv:1208.4104 [hep-ph].

[77] M.I. Gresham, I.W. Kim and K.M. Zurek, Searching for Top Flavor Violating Resonances, Phys. Rev. D 84 (2011) 034025, arXiv:1102.0018 [hep-ph].

[78] P. Ferrario and G. Rodrigo, Heavy colored resonances in $t\bar{t}$+jet at the LHC, JHEP 02 (2010) 051, arXiv:0912.0687 [hep-ph].

[79] S. Alte, S. Berge, and H. Spiesberger, Top Quark Charge Asymmetry: Searching for Light Axigluons in top pair+jet Production at the LHC, JHEP 09 (2014) 084, arXiv:1406.0501 [hep-ph].

[80] W. Buchmüller, D. Wyler, Effective Lagrangian Analysis of New Interactions and Flavor Conservation, Nucl. Phys. B 268 (1986) 621.

[81] C.N. Leung, S.T. Love and S. Rao, Low-energy manifestations of a new interactions scale: Operator analysis, Z. Phys. C 31 (1986) 433.

[82] I. Brivio and M. Trott, The Standard Model as an Effective Field Theory, Phys. Rept. 793 (2019) 1, arXiv:1706.08945 [hep-ph].

[83] ATLAS Collaboration, Measurement of the energy asymmetry in $t\bar{t}j$ production at 13 TeV with the ATLAS experiment and interpretation in the SMEFT framework, Eur. Phys. J. C 82 (2022) 374, arXiv:2110.05453 [hep-ex].

[84] A. Basan, Top-antitop energy asymmetry in jet-associated top-quark pair production at ATLAS, 148th LHCC Meeting: 11th LHC students poster session, CERN-LHCC-2021-019 (2021), `https://indico.cern.ch/event/1091653/`.

[85] A. Basan, ATLAS Highlight – 1: Energy asymmetry, LHC TOP Working Group Meeting (2021), `https://indico.cern.ch/event/1092350`.

[86] M.D. Schwartz, Quantum Field Theory and the Standard Model, Cambridge University Press (2014).

[87] E. Noether, Invariante Variationsprobleme, Nachrichten von der Gesellschaft der Wissenschaften zu Göttingen, Mathematisch-Physikalische Klasse (1918) 235-257.

[88] W. Pauli, Über den Zusammenhang des Abschlusses der Elektronengruppen im Atom mit der Komplexstruktur der Spektren, Z. Physik 21 (1925) 765.

[89] W. Pauli, The Connection Between Spin and Statistics, Phys. Rev. 58 (1940) 716.

[90] D. Griffiths, Introduction to Elementary Particles, WILEY-VCH Verlag GmbH & Co. (2008).

[91] F. Halzen and A.D. Martin, Quarks and Leptons: An Introductory Course in Modern Particle Physics, John Wiley & Sons, Inc. (1984).

[92] P.A. Zyla et al. (Particle Data Group), Review of Particle Physics, Prog. Theor. Exp. Phys. 2020 (2020) 083C01 and 2021 update.

[93] J.M. Pendlebury et al., A Revised Experimental Upper Limit on the Electric Dipole Moment of the Neutron, Phys. Rev. D 92 (2015) 092003, arXiv:1509.04411 [hep-ex].

[94] B. Graner et al., Reduced Limit on the Permanent Electric Dipole Moment of ^{199}Hg, Phys. Rev. Lett. 116 (2016) 161601, arXiv:1601.04339 [physics.atom-ph].

[95] F.J. Dyson, The S Matrix in Quantum Electrodynamics, Phys. Rev. 75 (1949) 1736.

[96] S. L. Glashow, Partial-symmetries of weak interactions, Nuclear Physics 22 4 (1961) 579.

[97] A. Salam, Weak and Electromagnetic Interactions, Conf. Proc. C 680519 (1968) 367.

[98] CERN, The Higgs boson, 2014, `http://cds.cern.ch/record/1998491`.

[99] G. Barr et al., Particle Physics in the LHC Era, Oxford University Press (2016).

[100] E. Eichten et al., Charmonium: The model, Phys. Rev. D 21 (1980) 313.

[101] N. Brambilla and A. Vairo, Quark Confinement and the Hadron Spectrum, HEPHY-PUB 696/98, UWThPh-1998-33 (1999), arXiv:hep-ph/9904330.

[102] B. Andersson et al., Parton fragmentation and string dynamics, Physics Reports 97 2-3 (1983) 31.

[103] W. Pauli and F. Villars, On the Invariant Regularization in Relativistic Quantum Theory, Rev. Mod. Phys. 21 (1949) 434.

[104] E.C.G. Stueckelberg and A. Peterman, Normalization of constants in the quanta theory, Helv. Phys. Acta 26 (1953) 499.

[105] M. Gell-Mann and F.E. Low, Quantum electrodynamics at small distances, Phys. Rev. 95 (1954) 1300.

[106] C.G. Callan, Broken scale invaraince in scalar field theory, Phys. Rev. D 2 (1970) 1541.

[107] K. Symanzik, Small distance behaviour in field theory and power counting, Commun. Math. Phys 18 (1970) 227.

[108] G.'t Hooft, M.Veltman, Regularization and renormalization of gauge fields, Nucl. Phys. B 44 (1972) 189.

[109] J.C. Ward, An Identity in Quantum Electrodynamics, Phys. Rev. 78 (1950) 182.

[110] Y. Takahashi, On the generalized ward identity, Il Nuovo Cimento 6 (1957) 371.

[111] M. Thomson, Modern Particle Physics, Cambridge University Press (2013).

[112] OPAL collaboration, Tests of the Standard Model and Constraints on New Physics from Measurements of Fermion-Pair Production at 189-209 GeV at LEP, Eur. Phys. J.C 33 (2004) 173, arXiv:hep-ex/0309053.

[113] R. P. Feynman, Very High-Energy Collisions of Hadrons, Phys. Rev.Lett. 23 (1969) 1415.

[114] V.N. Gribov and L.N. Lipatov, Deep inelastic ep scattering in perturbation theory, Sov. J. Nucl. Phys. 15 (1972) 438.

[115] L.N. Lipatov, The parton model and perturbation theory, Sov. J. Nucl. Phys. 20 (1975) 95.

[116] G. Altarelli and G. Parisi, Asymptotic freedom in parton language, Nucl. Phys. B 126 (1977) 298.

[117] Yu.L. Dokshitzer, Calculation of the Structure Functions for Deep Inelastic Scattering and e+ e- Annihilation by Perturbation Theory in Quantum Chromodynamics, Sov. Phys. JETP 46 (1977) 641.

[118] NNPDF Collaboration, Parton distributions for the LHC Run II, JHEP 04 (2015) 40, arXiv:1410.8849 [hep-ph].

[119] S.D. Drell and T.M. Yan, Partons and their applications at high energies, Ann. Phys. 66 (1971) 578.

[120] J.C. Collins, The theorems of perturbative QCD, Ann. Rev. Nucl. Part. Sd. 37 (1987) 383.

[121] J.M. Campbell, J.W. Huston, W.J. Stirling, Hard Interactions of Quarks and Gluons: a Primer for LHC Physics, Rept. Prog. Phys. 70 (2007) 89, arXiv:hep-ph/0611148.

[122] Deutsches Elektronen-Synchrotron DESY, The most precise picture of the proton, News from the DESY research center, 2015/07/02, `https://www.desy.de/news/news_search/index_eng.html?openDirectAnchor=829`.

[123] J.M. Campbell et al., Report of the Showmass 2013 energy frontier QCD working group, ANL-HEP-CP-13-48, FERMILAB-FN-0967-CMS-T (2013), arXiv:1310.5189 [hep-ph].

[124] ATLAS Collaboration, Measurement of the $t\bar{t}$ production cross-section in the lepton-jets channel at $\sqrt{s} = 13$ TeV with the ATLAS experiment, ATLAS-CONF-2019-044 (2019).

[125] CMS Collaboration, Measurement of the $t\bar{t}$ production cross section, the top quark mass, and the strong coupling constant using dilepton events in pp collistions at $\sqrt{s} = 13$ TeV, Eur. Phys. J. C 79 (2019) 368, arXiv:1812.10505 [hep-ex].

[126] M. Czakon, P. Fiedler and A. Mitov, The total top quark pair production cross-section at hadron colliders through $O(\alpha_S^4)$, Phys. Rev. Lett. 110 (2013) 252004, arXiv:1303.6254 [hep-ph].

[127] I. Bigi et al., Production and decay properties of ultra-heavy quarks, Phys. Lett. B 181 (1986) 157.

[128] CDF Collaboration, D0 Collaboration, Combined Forward-Backward Asymmetry Measurements in Top-Antitop Quark Production at the Tevatron, Phys. Rev. Lett. 120 (2018) 042001, arXiv:1709.04894 [hep-ex].

[129] R. Diener, S. Godfrey and T.A.W. Martin, Using Final State Pseudorapidities to Improve s-channel Resonance Observables at the LHC, Phys. Rev. D 80 (2009) 075014, arXiv:0909.2022v2 [hep-ph] .

[130] S. Jung, A. Pierce and J.D. Wells, Top quark asymmetry from a non-Abelian horizontal symmetry, Phys. Rev. D 83 (2011) 114039, arXiv:1103.4835 [hep-ph].

[131] ATLAS Collaboration, Measurement of the charge asymmetry in top-quark pair production in the lepton-plus-jets final state in pp collision data at $\sqrt{s} = 8\,\text{TeV}$ with the ATLAS detector, Eur. Phys. J. C 76 (2016) 87, arXiv:1509.02358 [hep-ex].

[132] G.F. Giudice, Naturalness after LHC8, CERN-PH-TH-2013-180 (2013), arXiv:1307.7879 [hep-ph].

[133] AMS Collaboration, Search for antihelium in cosmic rays, Phys. Lett. B 461 (1999) 387, arXiv:hep-ex/0002048.

[134] L. Canetti, M. Drewes and M. Shaposhnikov, Matter and antimatter in the universe, New J. Phys. 14 (2012) 095012, arXiv:1204.4186 [hep-ph].

[135] A.D. Sakharov, Violation of CP Invariance, C Asymmetry, and Baryon Asymmetry of the Universe, JETP Lett.-USSR 5 (1967) 24.

[136] M. Kobayashi and T. Maskawa, CP Violation in the Renormalizable Theory of Weak Interaction, Prog. Theor. Phys. 49 (1973) 652-657.

[137] V.C. Rubin, W.K. Ford and N. Thonnard, Rotational properties of 21 SC galaxies with a large range of luminosities and radii, from NGC 4605 (R=4kpc) to UGC 2885 (R=122kpc), Astrophys. J. 238 (1980) 471.

[138] Planck Collaboration, Planck 2013 results. XVI. Cosmological parameters, Astron. Astrophys. 571 (2014) A16, arXiv:1303.5076 [astro-ph.CO].

[139] D.H. Weinberg et al., Observational Probes of Cosmic Acceleration, Phys. Rept. 530 2 (2013) 87, arXiv:1201.2434 [astro-ph.CO].

[140] S.L. Glashow and P.H. Frampton, Chiral Color: An Alternative to the Standard Model, Phys. Lett. B 190 (1987) 157.

[141] C.T. Hill, Topcolor: top quark condensation in a gauge extension of the standard model, Phys. Lett. B 266 (1991) 419.

[142] D.A. Dicus, C.D. McMullen, and S. Nandi, Collider implications of Kaluza-Klein excitations of the gluons, Phys. Rev. D 65 (2002) 076007, arXiv:hep-ph/0012259.

[143] R. Chivukula, Hadron Collider Production of Massive Color-Octet Vector Bosons at Next-to-Leading Order, Phys. Rev. D 87 (2013) 094011, arXiv:1303.1120 [hep-ph].

[144] E. Fermi, Versuch einer Theorie der β-Strahlen, Z. Physik 88 (1934) 161.

[145] S. Weinberg, Baryon- and Lepton-Nonconserving Processes, Phys. Rev. Lett. 43 (1979) 1566.

[146] B. Grzadkowski, M. Iskrzynski, M. Misiak, J. Rosiek, Dimension-Six Terms in the Standard Model Lagrangian, JHEP 10 (2010) 085, arXiv:1008.4884 [hep-ph].

[147] L. Lehman and A. Martin, Low-derivative operators of the Standard Model effective field theory via Hilbert series methods, JHEP02(2016)081, arXiv:1510.00372 [hep-ph].

[148] D. Barducci et al., Interpreting top-quark LHC measurements in the standard-model effective field theory, CERN-LPCC-2018-01 (2018), arXiv:1802.07237 [hep-ph].

[149] J.H. Kühn and G. Rodrigo, Charge asymmetries of top quarks at hadron colliders revisited, JHEP 01 (2012) 063, arXiv:1109.6830 [hep-ph].

[150] C. Hays, A. Martin, V. Sanz et al., On the impact of dimension-eight SMEFT operators on Higgs measurements, JHEP 02 (2019) 123, arXiv:1808.00442 [hep-ph].

[151] M. Czakon et al., Top-quark charge asymmetry at the LHC and Tevatron through NNLO QCD and NLO EW, Phys. Rev. D 98 (2018) 014003, arXiv:1711.03945 [hep-ph], `https://www.precision.hep.phy.cam.ac.uk/results/ttbar-nnloqcd-nloew/`.

[152] C. Degrande et al., Automated one-loop computations in the standard model effective field theory, Phys. Rev. D 103 (2021) 096024, arXiv:2008.11743 [hep-ph].

[153] CERN, About CERN, 2012, `http://cds.cern.ch/record/1997225`.

[154] CERN, CERN council, `https://council.web.cern.ch/`, [Online, accessed: 17/05/2020].

[155] CERN, About CERN, `https://home.cern/about`, [Online, accessed: 17/05/2020].

[156] ATLAS Collaboration, The ATLAS Experiment at the CERN Large Hadron Collider, JINST 3 (2008) S08003.

[157] CMS Collaboration, The CMS Experiment at the CERN LHC, JINST 3 (2008) S08004.

[158] ALICE Collaboration, The ALICE experiment at the CERN LHC, JINST 3 (2008) S08002.

[159] LHCb Collaboration, The LHCb Detector at the LHC, JINST 3 (2008) S08005.

[160] L. Evans and P. Bryant, LHC Machine, JINST 3 (2008) S08001.

[161] CERN, LEP design report, CERN-LEP-84-01 (1984).

[162] CERN, First beam in the lhc-accelerating science, Press release (2008), `https://home.cern/news/press-release/cern/first-beam-lhc-accelerating-science`, [Online, accessed 17/05/2020].

[163] E. Mobs, The CERN accelerator complex. Complexe des accélérateurs du CERN, OPEN-PHO-ACCEL-2016-009 (2016).

[164] TOTEM Collaboration, The TOTEM experiment at the CERN Large Hadron Collider, JINST 3 (2008) S08007.

[165] LHCf Collaboration, The LHCf detector at the CERN Large Hadron Collider, JINST 3 (2008) S08006.

[166] MoEDAL Collaboration, Technical Design Report of the MoEDAL Experiment, CERN-LHCC-2009-006, MoEDAL-TDR-001 (2009).

[167] ATLAS Collaboration, Luminosity determination in pp collisions at $\sqrt{s} = 13$ TeV using the ATLAS detector at the LHC, ATLAS-CONF-2019-021 (2019).

[168] ATLAS Collaboration, ATLAS data quality operations and performance for 2015–2018 data-taking, JINST 15 (2020) P04003, arXiv:1911.04632 [physics.ins-det].

[169] ATLAS Collaboration, Luminosity Public Results Run 2, `https://twiki.cern.ch/twiki/bin/view/AtlasPublic/LuminosityPublicResultsRun2`, [Online, accessed: 15/05/2020].

[170] Z. Marshall, Simulation of Pile-up in the ATLAS Experiment, ATL-SOFT-PROC-2013-030 (2013).

[171] J. Pequenao, Computer generated image of the whole ATLAS detector, CERN-GE-0803012 (2008).

[172] T.S. Virdee, Physics requirements for the design of the ATLAS and CMS experiments at the Large Hadron Collider, Phil. Trans. R. Soc. A (2012) 370876–891.

[173] ATLAS Collaboration, Atlas inner detector: Technical design report 1, CERN-LHCC-97-016; ATLAS-TDR-4 (1999).

[174] ATLAS Collaboration, Atlas pixel detector electronics and sensors, JINST 3 (2008) P07007.

[175] K. Potamianos, The upgraded Pixel detector and the commissioning of the Inner Detector tracking of the ATLAS experiment for Run-2 at the Large Hadron Collider, PoS EPS-HEP2015 (2015) 261, arXiv:1608.07850 [physics.ins-det].

[176] B. Abbott et al., Production and integration of the ATLAS Insertable B-Layer, JINST 13 (2018) T05008.

[177] ATLAS Collaboration, Operation and performance eof the ATLAS semiconductor tracker, JINST 9 (2014) P08009.

[178] ATLAS Collaboration, The ATLAS TRT Barrel Detector, JINST 3 (2008) P02014.

[179] ATLAS Collaboration, The ATLAS TRT end-cap detectors, JINST 3 (2008) P10003.

[180] ATLAS Collaboration, The alignment of the ATLAS Inner Detector in Run 2, PoS LHCP2016 (2016) 196.

[181] J. Pequenao, Computer generated image of the ATLAS inner detector, CERN-GE-0803014 (2008).

[182] H. Kolanoski and N. Wermes, Teilchendetektoren, Springer Spektrum (2016).

[183] J. Pequenao, Computer Generated image of the ATLAS calorimeter, CERN-GE-0803015 (2008).

[184] ATLAS Collaboration, Muon reconstruction performance of the ATLAS detector in proton-proton collision data at $\sqrt{s} = 13$ TeV, Eur. Phys. J. C (2016) 76:292 , https://doi.org/10.1140/epjc/s10052-016-4120-y.

[185] J. Pequenao, Computer generated image of the ATLAS Muons subsystem, CERN-GE-0803017 (2008).

[186] ATLAS Collaboration, Performance of the ATLAS trigger system in 2015, Eur. Phys. J. C 77 (2017) 317, arXiv:1611.09661 [hep-ex].

[187] W.P. Vazquez, ATLAS Collaboration, The ATLAS Data Acquisition System: from Run 1 to Run 2, Nuclear and Particle Physics Proceedings 273–275 (2016) 939–944, ATL-DAQ-PROC-2014-035 (2014).

[188] K. Bos et al., LHC Computing Grid: Technical Design Report, CERN-LHCC-2005-024 (2005).

[189] CERN, Update of the Computing Models of the WLCG and the LHC Experiments, CERN-LHCC-2014-014 (2014).

[190] E. Gardi et al., LHC Phenomenology, Scottish Graduate Series, Springer International Publishing (2015).

[191] J. Bellm et al., Herwig 7.0/Herwig++ 3.0 release note, Eur. Phys. J. C 76 (2016) 196, arXiv:1512.01178 [hep-ph].

[192] E. Bothmann et al., Event Generation with Sherpa 2.2, SciPost Phys. 7 (2019) 034, arXiv:1905.09127 [hep-ph].

[193] T. Sjöstrand et al., An Introduction to Pythia 8.2, Comp. Phys. Comm. 191 (2015) 159, arXiv:1410.3012 [hep-ph].

[194] T. Sjöstrand et al., PYTHIA 6.2 Physics and Manual, LU TP 01–21 (2002), arXiv:hep-ph/0108264.

[195] T. Binoth et al., LHC Physics, CRC Press (2012).

[196] S. Catani, F. Krauss, R. Kuhn, and B. Webber, QCD Matrix Elements + Parton Showers, JHEP 0111 (2001) 063, arXiv:hep-ph/0109231.

[197] L. Lonnblad, Correcting the Colour-Dipole Cascade Model with Fixed Order Matrix Elements, JHEP 0205 (2002) 046, arXiv:hep-ph/0112284.

[198] J. Alwall et al., Comparative study of various algorithms for the merging of parton showers and marix elements in hadronic collisions, Eur. Phys. J. C 53 (2008) 473, arXiv:0706.2569 [hep-ph].

[199] S. Frixione and B.R. Webber, Matching NLO QCD computations and parton shower simulations, JHEP 0206 (2002) 029, arXiv:hep-ph/0204244.

[200] S. Frixione, P. Nason and C. Oleari, Matching NLO QCD computations with Parton Shower simulations: the POWHEG method, JHEP 08 (2006) 077, arXiv:hep-ph/0606275.

[201] A. Buckley et al., General-purpose event generators for LHC physics, Physics Reports 504, Issue 5 (2011), arXiv:1101.2599 [hep-ph].

[202] B.R. Webber, A QCD model for Jet Fragmentation Including Soft Gluon Interference, Nucl. Phys. B238 (1984) 492.

[203] J.C. Winter, F. Krauss and G. Soff, A modified cluster-hadronization model, Eur. Phys. J. C36 (2004) 381, arXiv:hep-ph/0311085.

[204] T. Sjöstrand and M.v. Zijl, A Multiple Interaction Model for the Event Structure in Hadron Collisions, Phys.Rev.D 36 (1987) 2019.

[205] M. Bähr, S. Gieseke and M.H. Seymour, Simulation of multiple partonic interactions in Herwig++, JHEP 07 (2008) 076, arXiv:0803.3633 [hep-ph].

[206] D.J. Lange, The EvtGen particle decay simulation package, Nucl. Instrum. Meth. A462 (2001) 152.

[207] P. Golonka et al., The tauola-photos-F environment for the TUOLA and PHOTOS packages, relse II, Comput. Phys. Commun. 174 (2006) 818, arXiv:hep-ph/0312240.

[208] M. Dobbs and J. Hansen, The HepMC C++ Monte Carlo event record for high energy physics, Comput. Phys. Commun. 134 (2001) 41.

[209] ATLAS Collaboration, The ATLAS Simulation Infrastructure, Eur. Phys. J. C 70 (2010) 823, arXiv:1005.4568 [physics.ins-det].

[210] S. Agostinelli et al., GEANT4 – a simulation toolkit, Nucl.Instrum.Meth.A 506 (2003) 250.

[211] ATLAS Collaboration, Performance of pile-up mitigation techniques for jets in pp collisions at $\sqrt{s} = 8$ TeV using the ATLAS detector, Eur. Phys. J. C 76 (2016) 581.

[212] ATLAS Collaboration, Fast Simulation for ATLAS: Atlfast-II and ISF, J. Phys.: Conf. Ser. 396 (2012) 022031.

[213] T. Yamanaka and ATLAS Collaboration, The ATLAS calorimeter simulation FastCaloSim, J. Phys.: Conf. Ser. 331 (2011) 032053.

[214] W. Buttinger, Using Event Weights to account for differences in Instantaneous Luminosity and Trigger Prescale in Monte Carlo and Data, ATL-COM-SOFT-2015-119 (2015), [Internal].

[215] T. Cornelissen et al., Concepts, Design and Implementation of the ATLAS New Tracking (NEWT), ATL-COM-SOFT-2007-002 (2007).

[216] ATLAS Collaboration, Performance of the ATLAS Silicon Pattern Recognition Algorithm in Data and Simulation at $\sqrt{s} = 7\,\text{TeV}$, ATLAS-CONF-2010-072 (2010).

[217] ATLAS Collaboration, Performance of the atlas track reconstruction algorithms in dense environments in lhc run 2, Eur. Phys. J. C 77 (2017) 673, arXiv:1704.07983 [hep-ex].

[218] ATLAS Collaboration, Reconstruction of primary vertices at the ATLAS experiment in Run 1 proton-proton collisions at the LHC, Eur. Phys. J. C 77 (2017) 332, arXiv:1611.10235 [hep-ex].

[219] ATLAS Collaboration, Vertex Reconstruction Performance of the ATLAS Detector at $\sqrt{s} = 13$ TeV, ATL-PHYS-PUB-2015-026 (2015).

[220] ATLAS Collaboration, ATLAS b-jet identification performance and efficiency measurement with $t\bar{t}$ events in pp collisions at $\sqrt{s} = 13$ TeV, Eur. Phys. J. C 79 (2019) 970, arXiv:1907.05120 [hep-ex].

[221] ATLAS Collaboration, Electron and photon performance measurements with the ATLAS detector using the 2015–2017 LHC proton–proton collision data, JINST 14 (2019) P12006, arXiv:1908.00005 [hep-ex].

[222] ATLAS Collaboration, Electron reconstruction and identification in the ATLAS experiment using the 2015 and 2016 LHC proton–proton collision data at $\sqrt{s} = 13\,\text{TeV}$, Eur. Phys. J. C 79 (2019) 639, arXiv:1902.04655 [physics.ins-det].

[223] T. Cornelissen et al., The global χ^2 track fitter in ATLAS, J. Phys.: Conf. Ser. 119 (2008) 032013.

[224] R. Frühwirth, A Gaussian-mixture approximation of the Bethe-Heitler model of electron energy loss by bremsstrahlung, Comp. Phys. Comm. 154 (2003) 131.

[225] ATLAS Collaboration, Electron and photon energy calibration with the ATLAS detector using 2015–2016 LHC proton–proton collision data, JINST 14 (2019) P03017, arXiv:1812.03848 [hep-ex].

[226] ATLAS Collaboration, Muon reconstruction performance of the ATLAS detector in proton–proton collision data at $\sqrt{s} = 13\,\text{TeV}$, Eur. Phys. J. C 76 (2016) 292, arXiv:1603.05598 [hep-ex].

[227] ATLAS Collaboration, Muon reconstruction and identification efficiency in ATLAS using the full Run 2 *pp* collision data set at $\sqrt{s} = 13\,\text{TeV}$, Eur. Phys. J. C 81 (2021) 578, arXiv:2012.00578 [hep-ex].

[228] ATLAS Collaboration, Measurement of the muon reconstruction performance of the ATLAS detector using 2011 and 2012 LHC proton-proton collision data, Eur. Phys. J. C 74 (2014) 3130, arXiv:1404.4562 [hep-ex].

[229] ATLAS Collaboraiton, Expected performance of the ATLAS experiment: detector, trigger and physics, SLAC-R-980; CERN-OPEN-2008-020 (2009), arXiv:0901.0512 [hep-ex].

[230] ATLAS Collaboration, Muon isolation summary, ANA-MUON-2018-03-INT2 (2018), [Internal].

[231] ATLAS Collaboraiton, Search for new physics using events with b-jets and a pair of same charge leptons in pp collisions from 2015-16 at $\sqrt{s} = 13$ TeV with the ATLAS detector, ATL-COM-PHYS-2016-1474 (2016), [Internal].

[232] ATLAS Collaboration, Topological cell clustering in the ATLAS calorimeters and its performance in LHC Run 1, Eur. Phys. J. C 77 (2017) 490, arXiv:1603.02934 [hep-ex].

[233] ATLAS Collaboration, In situ calibration of large-radius jet energy and mass in 13 TeV proton–proton collisions with the ATLAS detector, Eur. Phys. J. C 79 (2019) 135, arXiv:1807.09477 [hep-ex].

[234] ATLAS Collaboration, Jet energy scale and resolution measured in proton–proton collisions at $\sqrt{s} = 13\,\text{TeV}$ with the ATLAS detector, Eur. Phys. J. C 81 (2020) 689, arXiv:2007.02645 [hep-ex].

[235] ATLAS Collaboration, Jet reconstruction and performance using particle flow with the ATLAS Detector, Eur. Phys. J. C 77 (2017) 466, arXiv:1703.10485 [hep-ex].

[236] M. Cacciari, G.P. Salam and G. Soyez, The anti-k_t jet clustering algorithm, JHEP 04 (2008) 063, arXiv:0802.1189 [hep-ph].

[237] S. Catani, Y.L. Dokshitzer, M.H. Seymour and B.R. Webber, Longitudinally invariant Kt clustering algorithms for hadron hadron collisions, Nucl. Phys. B 406 (1993) 187.

[238] S.D. Ellis and D.E. Soper, Successive combination jet algorithm for hadron collisions, Phys. Rev. D 48 (1993) 3160.

[239] Y.L. Dokshitzer, G.D. Leder, S. Moretti and B.R. Webber, Better jet clustering algorithms, JHEP 08 (1997) 001.

[240] ATLAS Collaboration, Measurement of the ATLAS Detector Jet Mass Response using Forward Folding with 80 fb^{-1} of $\sqrt{s} = 13$ TeV pp data., ATLAS-CONF-2020-022 (2020).

[241] ATLAS Collaboration, Measurement of large radius jet mass reconstruction performance at $\sqrt{s} = 8$ TeV using the ATLAS detector, ATLAS-CONF-2016-008 (2016).

[242] ATLAS Collaboration, Performance of jet substructure techniques for large-R jets in proton-proton collisions at $\sqrt{s} = 7$ TeV using the ATLAS detector, JHEP 09 (2013) 076, arXiv:1306.4945 [hep-ex].

[243] ATLAS Collaboration, Jet Mass Resolutions in ATLAS using Run 2 Monte Carlo Simulation, ATL-PHYS-PUB-2018-015 (2018).

[244] M. Cacciari, G.P. Salam and G. Soyez, The catchment area of jets, JHEP 04 (2008) 005, arXiv0802.1188 [hep-ph].

[245] ATLAS Collaboration, Performance of the ATLAS Secondary Vertex b-tagging Algorithm in 7 TeV Collision Data, ATLAS-CONF-2010-042 (2010).

[246] ATLAS Collaboration, Optimisation and performance studies of the ATLAS b-tagging algorithms for the 2017-18 LHC run, ATL-PHYS-PUB-2017-013 (2017).

[247] ATLAS Collaboration, Secondary vertex finding for jet flavor identification with the ATLAS detector, ATL-PHYS-PUB-2017-011 (2017).

[248] ATLAS Collaboration, Topological b-hadron decay reconstruction and identification of b-jets with the JetFitter package in the ATLAS experiment at the LHC, ATL-PHYS-PUB-2018-025 (2018).

[249] ATLAS Collaboration, Monte Carlo to Monte Carlo scale factors for flavour tagging efficiency calibration, ATL-PHYS-PUB-2020-009 (2020).

[250] ATLAS Collaboration, Performance of top-quark and W-boson tagging with ATLAS in Run 2 of the LHC, Eur. Phys. J. C 79 (2019) 375, arXiv:1808.07858 [hep-ex].

[251] ATLAS Collaboration, Jet mass reconstruction with the ATLAS Detector in early Run 2 data, ATLAS-CONF-2016-035 (2016).

[252] A.J. Larkoski, G.P. Salam and J. Thaler, Energy Correlation Functions for Jet Substructure, JHEP 06 (2013) 108, arXiv:1305.0007 [hep-ph].

[253] I. M. A.J. Larkoski and D. Neill, Power Counting to Better Jet Observables, JHEP 12 (2014) 009, arXiv:1409.6298 [hep-ph].

[254] J. Thaler and K.V. Tilburg, Identifying Boosted Objects with N-subjettiness, JHEP 03 (2011) 015, arXiv:1011.2268 [hep-ph].

[255] J. Thaler K.V. Tilburg, Maximizing boosted top identification by minimizing N-subjettiness, JHEP 02 (2012) 093, arXiv:1108.2701 [hep-ph].

[256] J. Thaler and L.-T. Wang, Strategies to identify boosted tops, JHEP 07 (2008) 092, arXiv:0806.0023.

[257] ATLAS Collaboration, Atlas LXR Cross Reference, `https://acode-browser.usatlas.bnl.gov/lxr/source/athena/Reconstruction/Jet/JetSubStructureMomentTools/Root/NSubjettinessTool.cxx`, [Online, accessed: 16/04/2020].

[258] J. Thaler et al., rFASTJETSVN1251, `https://phab.hepforge.org/source/fastjetsvn/browse/contrib/contribs/Nsubjettiness/tags/2.2.5/`, [Online, accessed: 04/10/2022].

[259] ATLAS Collaboration, Identification of high transverse momentum top quarks in pp collisions at $\sqrt{s} = 8$ TeV with the ATLAS detector, JHEP 06 (2016) 093, arXiv:1603.03127 [hep-ex].

[260] ATLAS Collaboration, Boosted hadronic vector boson and top quark tagging with ATLAS using Run 2 data, ATL-PHYS-PUB-2020-017 (2020).

[261] ATLAS Collaboration, Performance of pile-up mitigation techniques for jets in *pp* collisions at $\sqrt{s} = 8\,\text{TeV}$ using the ATLAS detector, Eur. Phys. J. C 76 (2016) 581, arXiv:1510.03823 [hep-ex].

[262] ATLAS Collaboration, Tagging and suppression of pileup jets with the ATLAS detector, ATLAS-CONF-2014-018 (2014).

[263] ATLAS Collaboration, Performance of missing transverse momentum reconstruction with the ATLAS detector using proton-proton collisions at $\sqrt{s} = 13$ TeV, Eur. Phys. J. C 78 (2018) 903, arXiv:1802.08168 [hep-ex].

[264] ATLAS Collaboration, E_T^{miss} performance in the ATLAS detector using 2015-2016 LHC p-p collisions, ATLAS-CONF-2018-023 (2018).

[265] ATLAS Collaboration, Recommendations of the Physics Objects and Analysis Harmonisation Study Groups 2014, ATL-COM-PHYS-2014-451 (2014), [Internal].

[266] ATLAS Collaboration, Measurements of top-quark pair differential and double-differential cross-sections in the ℓ+jets channel with *pp* collisions at $\sqrt{s} = 13\,\text{TeV}$ using the ATLAS detector, Eur. Phys. J. C 79 (2019) 1028, arXiv:1908.07305 [hep-ex], Erratum: Eur. Phys. J. C 80 (2020) 1092.

[267] ATLAS Collaboration, Proposal for truth particle observable definitions in physics measurements, ATL-PHYS-PUB-2015-013 (2015).

[268] A. Basan, Top-antitop energy asymmetry in jet-associated top-quark pair production at ATLAS, unpublished master thesis, Johannes Gutenberg University Mainz (2018).

[269] A. Basan, Rivet analyses reference for the energy asymmetry in ttj @ 13 TeV, ATLAS_2021_I1941095 (2021).

[270] ATLAS Collaboration, Performance of electron and photon triggers in ATLAS during LHC Run 2, Eur. Phys. J. C 80 (2020) 47, arXiv:1909.00761 [hep-ex].

[271] ATLAS Collaboration, Performance of the ATLAS muon triggers in Run 2, JINST 15 (2020) P09015, arXiv:2004.13447 [hep-ex].

[272] T. Chwalek, Measurement of W-Boson Helicity-Fractions in Top-Quark Decays with the CDF II Experiment and Prospects for an Early tt Cross-Section Measurement with the CMS Experiment, CERN-THESIS-2010-255 (2010).

[273] ATLAS Collaboration, The ATLAS Experiment's main offline software repository, `https://gitlab.cern.ch/atlas/athena`, [Online, accessed: 04/10/2022].

[274] ATLAS Collaboration, ATLAS Software Documentation, `https://atlassoftwaredocs.web.cern.ch/ABtutorial`, [Online, accessed: 04/10/2022].

[275] A. Basan, Gitlab repository for the top-antitop energy asymmetry measurement, `https://gitlab.cern.ch/atlas-phys-top-energyAsymmetry`, [Internal].

[276] J.M. Campbell et al., Top-pair production and decay at NLO matched with parton showers, JHEP 04 (2015) 114, arXiv:1412.1828 [hep-ph].

[277] ATLAS Collaboration, Studies on top-quark Monte Carlo modelling for Top 2016, ATL-PHYS-PUB-2016-020 (2016).

[278] ATLAS Collaboration, ATLAS Pythia 8 tunes to 7 TeV data, ATL-PHYS-PUB-2014-021 (2014).

[279] J. Butterworth et al., PDF4LHC recommendations for LHC Run II, J. Phys. G: Nucl. Part. Phys. 43 (2016) 023001, arXiv:1510.03865 [hep-ph].

[280] P. M. L. Harland-Lang, A. Martin and R. Thorne, Parton distributions in the LHC era: MMHT 2014 PDFs, Eur. Phys. J. C 75 (2015) 204, arXiv:1412.3989 [hep-ph].

[281] J. Alwall et al., The automated computation of tree-level and next-to-leading order differential cross sections, and their matching to parton shower simulations, JHEP 07 (2014) 079, arXiv:1405.0301 [hep-ph].

[282] M. Czakon and A. Mitov, TOP++: A program for the calculation of the top-pair cross-section at hadron colliders, Comput. Phys. Commun. 185 (2014) 2930, arXiv:1112.5675 [hep-ph].

[283] M. Beneke, P. Falgari, S. Klein and C. Schwinn, Hadronic top-quark pair production with NNLL threshold resummation, Nucl. Phys. B 855 (2012) 695, arXiv:1109.1536 [hep-ph].

[284] M. Cacciari, M. Czakon, M. Mangano, A. Mitov and P. Nason, Top-pair production at hadron colliders with next-to-next-to-leading logarithmic soft-gluon resummation, Phys. Lett. B 710 (2012) 612, arXiv:1111.5869 [hep-ph].

[285] P. Bärnreuther, M. Czakon and A. Mitov, Physics at the Tevatron: Next-to-Next-to-Leading Order QCD Corrections to $q\bar{q} \to t\bar{t}X$, Phys. Rev. Lett. 109 (2012) 132001, arXiv:1204.5201 [hep-ph].

[286] M. Czakon and A. Mitov, NNLO corrections to top-pair production at hadron colliders: the all-fermionic scattering channels, JHEP 12 (2012) 054, arXiv:1207.0236 [hep-ph].

[287] M. Czakon and A. Mitov, NNLO corrections to top pair production at hadron colliders: the quark-gluon reaction, JHEP 01 (2013) 080, arXiv:1210.6832 [hep-ph].

[288] M. Czakon, P. Fiedler and A. Mitov, Total Top-Quark Pair-Production Cross Section at Hadron Colliders Through $O(\alpha_S^4)$, JHEP 01 (2013) 080, arXiv:1210.6832 [hep-ph].

[289] M. Aliev et al., HATHOR – HAdronic Top and Heavy quarks crOss section calculatoR, Comput. Phys. Commun. 182 (2011) 1034, arXiv:1007.1327 [hep-ph].

[290] P. Kant et al., HatHor for single top-quark production: Updated predictions and uncertainty estimates for single top-quark production in hadronic collisions, Comput. Phys. Commun. 191 (2015) 74, arXiv:1406.4403 [hep-ph].

[291] P. M. e. a. S. Frixione, E. Laenen, Single-top hadroproduction in association with a W boson, JHEP 07 (2008) 029, arXiv0805.3067 [hep-ph].

[292] ATLAS Collaboration, Estimation of non-prompt and fake lepton backgrounds in final states with top quarks produced in proton–proton collisions at $\sqrt{s} =$ 8 TeV with the ATLAS Detector, ATLAS-CONF-2014-058 (2014).

[293] ATLAS Collaboration, Muon reconstruction and identification efficiency in ATLAS using the full Run 2 pp collision data set at $\sqrt{s} = 13\,\text{TeV}$, Eur. Phys. J. C 81 (2021) 578, arXiv:2012.00578 [hep-ex].

[294] G. Choudalakis, Fully Bayesian Unfolding, 2012, arXiv:1201.4612 [physics.data-an].

[295] R. Barlow and C. Beeston, Fitting using finite Monte Carlo samples, Comp. Phys. Comm. 77 (1993) 219.

[296] K. Cranmer, G. Lewis, L. Moneta et al., HistFactory: A tool for creating statistical models for use with RooFit and RooStats, Tech. Rep. CERN-OPEN-2012-016 (2012).

[297] P. Diaconis, The Markov Chain Monte Carlo Revolution, Bull. Amer. Math. Soc. 46 (2009) 179.

[298] N. Metropolis, A. Rosenbluth, M. Rosenbluth et al., Equation of State Calculations by Fast Computing Machines, J. Chem. Phys. 21, 1087 (1953).

[299] A. Klenke, Probability Theory, 3rd edition, Springer (2020).

[300] O. Martin, Bayesian Analysis with Python, Second Edition, Packt Publishing (2018).

[301] S. Duane, A. Kennedy, B.J. Pendleton and D. Roweth, Hybrid Monte Carlo, Phys. Lett. B. 195 (1987) 216.

[302] R. Neal, MCMC Using Hamiltonian dynamics, Handbook of Markov Chain Monte Carlo, CRC Press (2011), arXiv:1206.1901 [stat.CO].

[303] M.D. Hoffman and A. Gelman, The no-u-turn sampler: Adaptively setting path lengths in hamiltonian monte carlo, 2011, arXiv:1111.4246 [stat.CO].

[304] Y. Nesterov, Prime-dual subgradient methods for convex problems, Mathematical Programming 120 (2009) 221.

[305] A. Gelman and D. Rubin, Inference from iterative simulation using multiple sequences, Statistical Science 7 (1992) 457.

[306] S. Brooks and A. Gelman, General Methods for Monitoring Convergence of Iterative Simulations, Journal of Computational and Graphical Statistics 7 (1998) 434.

[307] C. Helsens, F. Rubbo and D. Gerbaudo, Implementation of the Fully Bayesian Unfolding algorithm, 2018, `https://github.com/pyFBU/fbu`.

[308] J. Salvatier, T.V. Wiecki and C. Fonnesbeck, Probabilistic programming in Python using PyMC3, PeerJ Computer Science (2016) 2:e55.

[309] ATLAS Collaboration, ATLAS Collaboration, Measurement of $W\pm$ and Z-boson production cross sections in pp collisions at $\sqrt{s} = 13\,\text{TeV}$ with the ATLAS detector, Phys. Lett. B 759 (2016) 601, arXiv:1603.09222 [hep-ex].

[310] ATLAS Collaboration, Studies on top-quark Monte Carlo modelling with Sherpa and MG5_aMC@NLO, ATL-PHYS-PUB-2017-007 (2017).

[311] ATLAS Collaboration, ATLAS simulation of boson plus jets processes in Run 2, ATL-PHYS-PUB-2017-006 (2017).

[312] G. Avoni et al., The new LUCID-2 detector for luminosity measurement and monitoring in ATLAS, JINST 13 (2018) P07017.

[313] G. Bohm and G. Zech, Introduction to Statistics and Data Analysis for Physicists, Verlag Deutsches Elektronen-Synchrotron Hamburg (2014).

[314] G. Cowan, Statistical Data Analysis, Cambridge University Press (1998).

[315] O. Behnke et al., Data Analysis in High Energy Physics, WILEY-VCH (2013).

[316] L. Lista, Statistical Methods for Data Analysis in Particle Physics, Springer Nature (2017).

[317] R. Barlow, Practical Statistics for Particle Physics, CERN-2020-0005 (2020), arXiv:1905.12362 [physics.data-an].

[318] ATLAS Collaboration, ATLAS Insertable B-Layer Technical Design Report, ATLAS-TDR-19 (2010).

[319] ATLAS Collaboration, Study of top-quark pair modelling and uncertainties using ATLAS measurements at $\sqrt{s} = 13\,\text{TeV}$, ATL-PHYS-PUB-2020-023 (2020).

[320] O. Aberle, I.B. Alonso, O. Brüning et al., High-Luminosity Large Hadron Collider (HL-LHC): Technical design report, CERN Yellow Reports: Monographs 10 (2020), CERN-2020-010.

[321] P. Virtanen, R. Gommers, T.E. Oliphant et al., SciPy 1.0: Fundamental Algorithms for Scientific Computing in Python, Nature Methods 17 (2020) 261.

[322] W. Greene, Econometric Analysis, Seventh Edition, Pearson Education Limited (2012).

[323] J. Ellis, M. Madigan, K. Mimasu, V. Sanz and T. You, Top, Higgs, Diboson and Electroweak Fit to the Standard Model Effective Field Theory, JHEP 04 (2021) 279, arXiv:2012.02779 [hep-ph].

[324] R. Boughezal and E. Mereghetti and F. Petriello, Dilepton production in the SMEFT at $\mathcal{O}(1/\Lambda^4)$, Phys. Rev. D 104 (2021) 095022, arXiv:2106.05337 [hep-ph].

[325] ATLAS Collaboration, Measurement of the cross-section for producing a W boson in association with a single top quark in pp collisions at $\sqrt{s} = 13\,\text{TeV}$ with ATLAS, JHEP 01 (2018) 63, arXiv:1612.07231 [hep-ex].

[326] ATLAS Collaboration, Measurement of the production cross-section of a single top quark in association with a Z boson in proton–proton collisions at 13 TeV with the ATLAS detector, Phys. Lett. B 780 (2018) 557, arXiv:1710.03659 [hep-ex].

[327] ATLAS Collaboration, Measurements of inclusive and differential cross-sections of combined $t\bar{t}\gamma$ and $tW\gamma$ production in the $e\mu$ channel at 13 TeV with the ATLAS detector, JHEP 09 (2020) 049, arXiv:2007.06946 [hep-ex].

[328] ATLAS Collaboration, Measurement of the $t\bar{t}Z$ and $t\bar{t}W$ cross sections in proton-proton collisions at $\sqrt{s} = 13\,\text{TeV}$ with the ATLAS detector, Phys. Rev. D 99 (2019) 072009, arXiv:1901.03584 [hep-ex].

[329] ATLAS Collaboration, Search for four-top-quark production in the single-lepton and opposite-sign dilepton final states in pp collisions at $\sqrt{s} = 13\,\text{TeV}$ with the ATLAS detector, Phys. Rev. D 99 (2019) 052009, arXiv:1811.02305 [hep-ex].

[330] ATLAS Collaboration, Measurements of top-quark pair differential cross-sections in the lepton+jets channel in pp collisions at $\sqrt{s} = 8$ TeV using the ATLAS detector, Eur. Phys. J. C76 (2016) 538, arXiv:1511.04716 [hep-ex].

[331] M. Pinamonti, TTbarNNLOReweighter package, `https://gitlab.cern.ch/pinamont/TTbarNNLOReweighter`, [Internal].

[332] M. Pinamonti, $t\bar{t}$ Reweighting Reloaded, Top Reconstruction and Modelling Weekly (2020), `https://indico.cern.ch/event/940116/contributions/3950096/attachments/2082894/3498732/Pinamonti_30jul2020_topModelling.pdf`, [Internal].

[333] M. Czakon et al., Top-pair production at the LHC through NNLO QCD and NLO EW, JHEP 10 (2017) 186, arXiv:1705.04105 [hep-ph].

Alexander Basan

Alexander Basan

Personal data has been removed from the electronic version for privacy reasons.

Education

since 2018, Doctorate in Physics
Johannes Gutenberg University Mainz

2013–2018, M.Sc. Physics
Johannes Gutenberg University Mainz

2013–2017, M.Sc. International Economics & Public Policy
Johannes Gutenberg University Mainz

2014–2015, Study abroad
Lund University, Sweden

2010–2013, B.Sc. Physics
Johannes Gutenberg University Mainz

2009, General University Entrance Qualification
Gymnasium am Kurfürstlichen Schloss Mainz

Publications, posters and talks

2022, Evidence for the charge asymmetry in $pp \to t\bar{t}$ production at $\sqrt{s} = 13$ TeV with the ATLAS detector
ATLAS Collaboration, CERN-EP-2022-166 (2022)
https://arxiv.org/abs/2208.12095

2022, Measurement of the energy asymmetry in $t\bar{t}j$ production at 13 TeV with the ATLAS experiment and interpretation in the SMEFT framework
ATLAS Collaboration, Eur. Phys. J. C 82 (2022) 374
https://doi.org/10.1140/epjc/s10052-022-10101-w

2021, Talk, ATLAS Highlight – 1: Energy asymmetry
LHC TOP Working Group Meeting, CERN, 1–3 December 2021
https://indico.cern.ch/event/1092350

2021, Poster, Top-antitop energy asymmetry in jet-associated top-quark pair production at ATLAS
148th LHCC Meeting, 18 November 2021
https://indico.cern.ch/event/1091653

2021, Talk, Top quark precision measurements with the ATLAS experiment at the LHC
Phenomenology Symposium 2021, Pittsburgh, 24–26 May 2021
https://cds.cern.ch/record/2767499

2020, Measuring the top energy asymmetry at the LHC: QCD and SMEFT interpretations
A. Basan et al., J. High Energ. Phys. 03 (2020) 184
https://doi.org/10.1007/JHEP03(2020)184

2020, Technical Design Report: A High-Granularity Timing Detector for the ATLAS Phase-II Upgrade
ATLAS Collaboration, CERN-LHCC-2020-007 (2020)
https://cds.cern.ch/record/2719855